Formability of Aluminum Alloy Sheet at Elevated Temperature

by

Reza Bagheriasl

A thesis
presented to the University of Waterloo
in fulfilment of the
thesis requirement for the degree of
Doctor of Philosophy
in
Mechanical Engineering

Waterloo, Ontario, Canada, 2012

I hereby declare that I am the sole author of this thesis. This is a true copy of the thesis, including any required final revisions, as accepted by my examiners.

I understand that my thesis may be made electronically available to the public.

Abstract

An experimental and numerical study of the isothermal and non-isothermal warm formability of an AA3003 aluminum alloy brazing sheet is presented. Forming limit diagrams were determined using warm limiting dome height (LDH) experiments with *in situ* strain measurement based on digital image correlation (DIC) techniques. Forming limit curves (FLCs) were developed at several temperature levels (room temperature, 100°C, 200°C, 250°C, and 300°C) and strain-rates (0.003, 0.018, and $0.1s^{-1}$). The formability experiments demonstrated that temperature has a significant effect on formability, whereas forming speed has a mild effect within the studied range. Elevating the temperature to 250°C improved the formability more than 200% compared to room temperature forming, while forming at lower speeds increased the limiting strains by 10% and 17% at room temperature and 250°C, respectively.

Non-isothermal deep draw experiments were developed considering an automotive heat exchanger plate. A parametric study of the effects of die temperature, punch speed, and blank holder force on the formability of the part was conducted. The introduction of non-isothermal conditions in which the punch is cooled and the flange region is heated to 250°C resulted in a 61% increase in draw depth relative to room temperature forming.

In order to develop effective numerical models of warm forming processes, a constitutive model is proposed for aluminum alloy sheet to account for temperature and strain rate dependency, as well as plastic anisotropy. The model combines the Barlat YLD2000 yield criterion (Barlat et al., 2003) to capture sheet anisotropy and the Bergstrom (1982) hardening rule to account for temperature and strain rate dependency. Stress-strain curves for AA3003 aluminum alloy brazing sheet tested at elevated temperatures and a range of strain rates were used to fit the Bergstrom parameters, while measured R-values were used to fit the yield function parameters. The combined constitutive model was implemented within a user defined material subroutine that was linked to the LS-DYNA finite element code. Finite element models were developed based on the proposed material model and the results were compared with experimental data. Isothermal uniaxial tensile tests were simulated and the

predicted responses were compared with measured data. The tensile test simulations accurately predicted material behaviour.

The user material subroutine and forming limit criteria were then applied to simulate the isothermal warm LDH tests, as well as isothermal and non-isothermal warm deep drawing experiments. Two deep draw geometries were considered, the heat exchanger plate experiments developed as part of this research and the 100 mm cylindrical cup draw experiments performed by McKinley et al. (2010). The strain distributions, punch forces and failure location predicted for all three forming operations were in good agreement with the experimental results. Using the warm forming limit curves, the models were able to accurately predict the punch depths to failure as well as the location of failure initiation for both the isothermal and non-isothermal deep draw operations.

Acknowledgements

This thesis would not have been possible without the help and support of many individuals, and I would like to take this opportunity to thank all of them here. First of all I would like to thank Professor Michael Worswick for the opportunity to do this research and for the positive and open working environment he provided. He not only served as my supervisor but was also a constant source of encouragement, providing invaluable guidance while allowing me to cultivate and build upon my ideas. His way of supervising is incredibly supportive and stimulating and I enjoyed every bit of this research.

I gratefully acknowledge the financial support of this work provided by DANA Long Manufacturing, the Natural Sciences and Engineering Research Council (NSERC), and the Ontario Research Fund (ORF). I would particularly like to thank Dr Mark Kozdras and Dr Sooky Winkler of DANA Long Manufacturing for their assistance, expertise and encouragement throughout the project.

The experimental effort of this research required the development, manufacture, procurement and installation of specialized equipment. I would like to thank Eckhard Budziarek, Andy Barber, Tom Gawel, Neil Griffett, and Jason Benninger. They are invaluable resources in the lab and their knowledge and experience was much appreciated in the development of the experimental apparatus. The numerical effort and umat development presented in this thesis benefited immensely from the help and advice provided by Dr. Kamyar Ghavam and Dr Hari Simha. I would also like to thank Jonathan McKinley, who initiated the experimental work within this research project. His help at the start of my studies was invaluable.

I thank Laurie Wilfong for all her help, patience, knowledgeable guidance and administrative support. I am also grateful to the MME administration staff. I would like to thank Page Burton for her invaluable help with proofreading this thesis.

I also wish to acknowledge the friendship and help of the forming group at the University of Waterloo, especially Alexander Bardelcik, Jose Imbert, Dariush Tari, and Srihari Kurukuri.

And finally I would like to offer my sincerest gratitude to the most important people in my life: the three generations of my family who supported me in so many ways throughout this long process. I am very thankful to my parents for their continuous and endless support, inspiration and motivation. To my little angel Nicki - although now, as I write this, she is still too young to understand what her father did, one day she will. The research did not get more difficult with her around, maybe in a way it became easier. Shadi, yes we did it. The work is finally done and I emphasize that WE did it. Thank you for your limitless support during the hard times, you make me enjoy life with your sweet caring and unconditional love.

Table of Contents

List of figures

List of tables

1 Introduction

Aluminum has a density that is only one-third that of steel; however, when alloyed with other metals, it has an excellent strength-to-weight ratio and shows outstanding performance in terms of recyclability, corrosion resistance, durability, ductility, formability and conductivity. This unique combination of properties has garnered significant attention from automotive and aerospace manufacturers seeking to incorporate high strength, lightweight materials into their vehicle assemblies, without sacrificing safety and performance. While widespread adoption of these alloys has been limited by poor room temperature workability and formability, recent studies have indicated that the forming limit can be increased considerably at elevated temperatures. Warm forming technology has been recognized as a promising alternative for aluminum alloy sheet manufacturing. However, because aluminum has a low heat capacity, critical challenges remain in controlling process parameters such as the forming speed and temperature. Warm forming of aluminum alloys has been studied for several decades with earlier efforts concentrating on forming experiments and characterizing material behaviour. More recent research has shifted towards numerical simulations and failure prediction.

1.1 Aluminium alloys and their applications

Aluminum alloys have been used by the automotive and aerospace industries for decades. These alloys are attractive because they are light weight, have good corrosion resistance, thermal and electrical conductivity, and can be formed in a soft condition, then heat treated to achieve a temper comparable to structural steel. However, replacing structural steels with aluminum alloys and expanding aluminum applications in general requires improved formability. The formability of aluminum alloys at room temperature is generally lower than at either cryogenic or elevated temperatures. At cryogenic temperatures, many aluminum alloys experience significantly increased tensile elongation due to enhanced work hardening, while at elevated temperatures this phenomenon is mainly caused by increased strain-rate hardening.

The International Alloy Designation System is the most widely accepted naming scheme for wrought alloys; it designates a four-digit number to each alloy, where the first digit indicates the major alloying elements. Table 1.1 summarizes characteristics and current applications of aluminum alloys by their series (Kaufman, 2000).

Table 1.1 Aluminum alloys; characteristics and applications

Series	Alloying elements	Major characteristics	Industrial application samples
1000	Pure aluminum (minimum 99.0%)	Strain hardenable High formability, corrosion resistance, and electrical conductivity Ultimate tensile strength: 70 to 185 MPa (10–27 ksi) Readily joined by welding, brazing, and soldering	Chemical piping (1060) Aluminium foil for foods (1175) Electrical conductor wire (1350) Space mirror
2000	Copper	Heat treatable, can be precipitation hardened High strength at room and elevated temperatures Ultimate tensile strength: 190 to 430 MPa (27–62 ksi) Usually joined mechanically, but some alloys are weldable	External body sheet panel (2008) Vehicle hood, deck lids (2036) Aircraft wing structure (2024) Aircraft engine components (2618)
3000	Manganese	High formability and corrosion resistance with medium strength Ultimate tensile strength: 110 to 285 MPa (16–41 ksi) Readily joined by all commercial procedures	Air conditioner tube and heat exchanger (3003) Can bodies (3004) Building sheet, siding (3005,3105)
4000	Silicon	Heat treatable Medium strength, with good flow characteristics Ultimate tensile strength: 175 to 380 MPa (25–55 ksi) Easily joined, especially by brazing and soldering	Forged aircraft piston Weld filler alloy (4043)
5000	Magnesium	Strain hardenable Moderate strength, with excellent corrosion resistance, toughness, and weldability Representative alloys: 5052, 5083, and 5754 Ultimate tensile strength: 125 to 350 MPa (18–51 ksi)	Auto body and frame (5182, 5754) Auto inner panel (5083) Truck trailer bodies (5456) Offshore station tanks (5083)
6000	Magnesium-Silicon	Heat treatable Moderate strength, with high corrosion resistance, and excellent extrudability Ultimate tensile strength: 125 to 400 MPa (18–58 ksi) Readily welded by GMAW and GTAW methods	External vehicle body (6111) Truck beams (6070) Auto door beams (6061, 6063)
7000	Zinc	Heat treatable Very high strength; special high-toughness versions Ultimate tensile strength: 220 to 610 MPa (32–88 ksi) Mechanically joined	Auto bumpers (7029, 7129) Aircraft wing and fuselage skin (7050, 7475) Aircraft wing structure (7050)
8000	Lithium and other elements	Heat treatable High strength, conductivity, and hardness Ultimate tensile strength: 120 to 240 (17–35 ksi)	Aerospace applications

1.2 Aluminum alloys for passenger vehicles

Increasing environmental concerns and global demand for improved fuel economy have placed intense pressure on car manufacturers to produce lighter vehicles with dramatically reduced emissions and fuel consumption ratings (Cole and Sherman, 1995). Aluminum alloys are likely candidates to facilitate these lightweighting initiatives, and with widespread

application are expected to figure prominently in future vehicle generations (Carle and Blount, 1999) and ultimately improve the sustainability of transportation industries. Figure 1.1 illustrates likely applications for aluminum alloys within passenger vehicles.

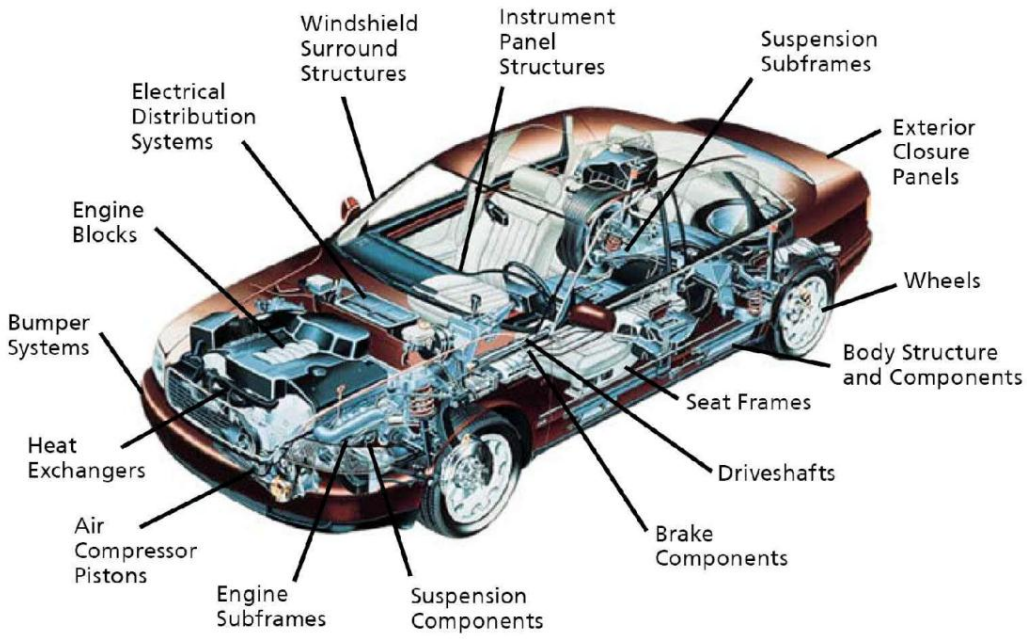

Figure 1.1 Aluminum alloy applications in passenger cars [The Aluminum Association Inc.]

Figure 1.2 illustrates the increased usage of aluminum alloys within North American vehicles over the last three decades, from 36kg per unit in 1973 to 148kg per unit, and an overall average of 2267 tons, in 2007 (Ducker Worldwide). Figure 1.2 also depicts the anticipated rise in aluminum content through 2015, reaching 170kg per vehicle and a total of over 2730 tons across North American fleets. Figure 1.3 shows the relative proportion of aluminum content against other materials used in light weight vehicles, rising slightly from 7.7% in 2005 to an anticipated 10% in 2015. Based on these figures, it seems aluminum will continue to have a meager showing by comparison with steel (54.9% and 52.9% in 2005 and 2015, respectively); however, this discrepancy can largely be attributed to the limited formability aluminum exhibits under conventional, room temperature methods. Advancing new forming methods that address this issue will narrow the gap between these two materials.

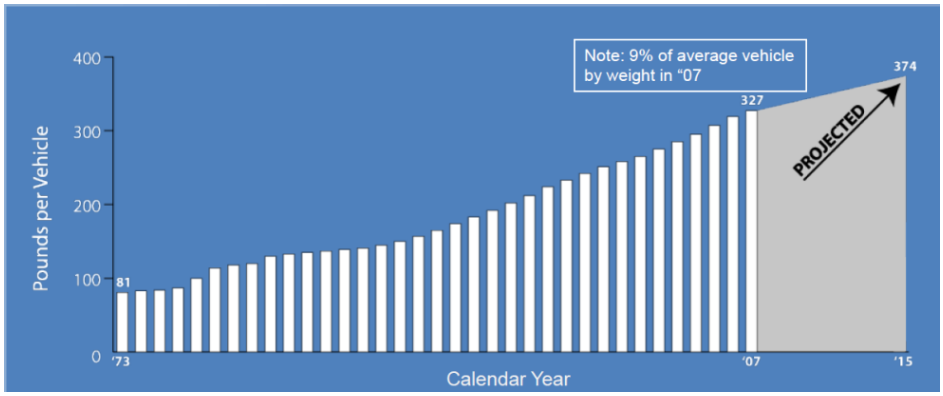

Figure 1.2 Steady growth of aluminum usage 1973-2015 [Ducker Worldwide Institute]

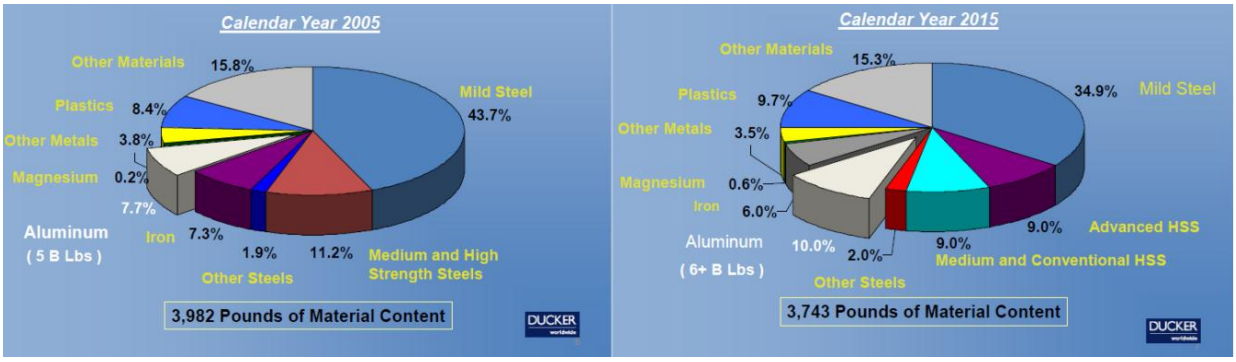

Figure 1.3 Recent (left) and expected (right) material content of light weight North American vehicles [Ducker Worldwide Institute]

In the automotive industry, aluminum alloys were initially applied in casting products such as engines, wheels, and exhaust decor; however, wrought aluminum products have found additional applications, primarily in: i) sheets, including exterior panels such as hoods and heat insulators, ii) thermal systems, such as heat exchanger fins and air-condition tubes, iii) extrusions, including bumper beams, and iv) forgings, including suspension parts (Figure 1.1).

Replacing steel parts with aluminum alloys in automotive applications will help reduce global greenhouse gas levels considerably. Carbon dioxide (CO_2) emissions are a major contributor to global warming, leading to increased atmospheric temperatures and changes in global climate patterns. Schwarz et al. (2001) showed that CO_2 emission ratios can be reduced by incorporating lightweight materials such as aluminum into new transportation designs. For every kg of aluminum added 2 kg of steel is replaced, leading to a net reduction of 10 kg of CO_2 over the average lifetime of a vehicle (Ungureanu et al., 2007). Vehicle weight reduction strongly influences fuel consumption as well. Mordike and Ebert (2001) reported that every

10% reduction in weight achieved improves fuel economy by 6–8%, which equates to roughly 2.5 extra miles per gallon (1.0 extra kilometer per liter).

1.3 Forming limit diagram (FLD)

Forming Limit Diagrams (FLDs), also known as Keeler-Goodwin diagrams (Keeler and Backofen, 1963 and Goodwin, 1968) are used to describe forming limits under a range of forming conditions, from balanced biaxial tension, through plane strain, to combined tensile/compressive strain states. Nakazima et al. (1968) can be credited with first introducing the use of strips of varying widths to measure forming limit strains; however, it was Hecker et al. (1978) who established the method commonly used today: gridded specimens of varying widths are firmly clamped and stretched with a 100 mm or 4 in (101.6 mm) diameter punch, under well-lubricated conditions, until localized necking is observed or the maximum load is sensed. Distorted circles in the vicinity of the neck are used to measure strain ratios, and data from each test specimen provides one point on the forming limit curve (FLC).

Dinda et al. (1981) combined Nakazima's method with Hecker's grid technique to generate FLDs. Ayres et al. (1979) and Harvey et al. (1984) introduced a computer-image analysis technique to alleviate the tedium and uncertainties associated with manual measurement of circles. Vogel and Lee (1989) and Kapij et al. (1990) measured surface strains by taking images of two different views of the sample surface. Regardless of the technique used, it remains difficult to select definitive circles from a range of specimens. Bragard (1989) introduced parabolic interpolation to mitigate this issue; however, his method has yet to achieve widespread application.

Formability experiments date back over a century, with the Erichsen and Olsen tests taking broad prominence in Europe and North America, respectively. Neither method accurately predicts actual press performance largely because there is some draw-in, and the biaxiality of the stress state is hard to maintain. Moreover, the small punch radius used introduces an overemphasis on bending performance and produces results that are greatly dependent on sheet thickness (Hecker, 1974; Ayres et al., 1979). The Fukui test (1960) gives a combined measure of stretchability and drawability. Fukui et al. (1960) used a 60° conical die and a hemispherical punch (Figure 1.4) to force an unsupported 50 or 60-mm circular blank into a

cone-shape die until it breaks in the ball contact area. The base diameter is then measured for comparison with other cups.

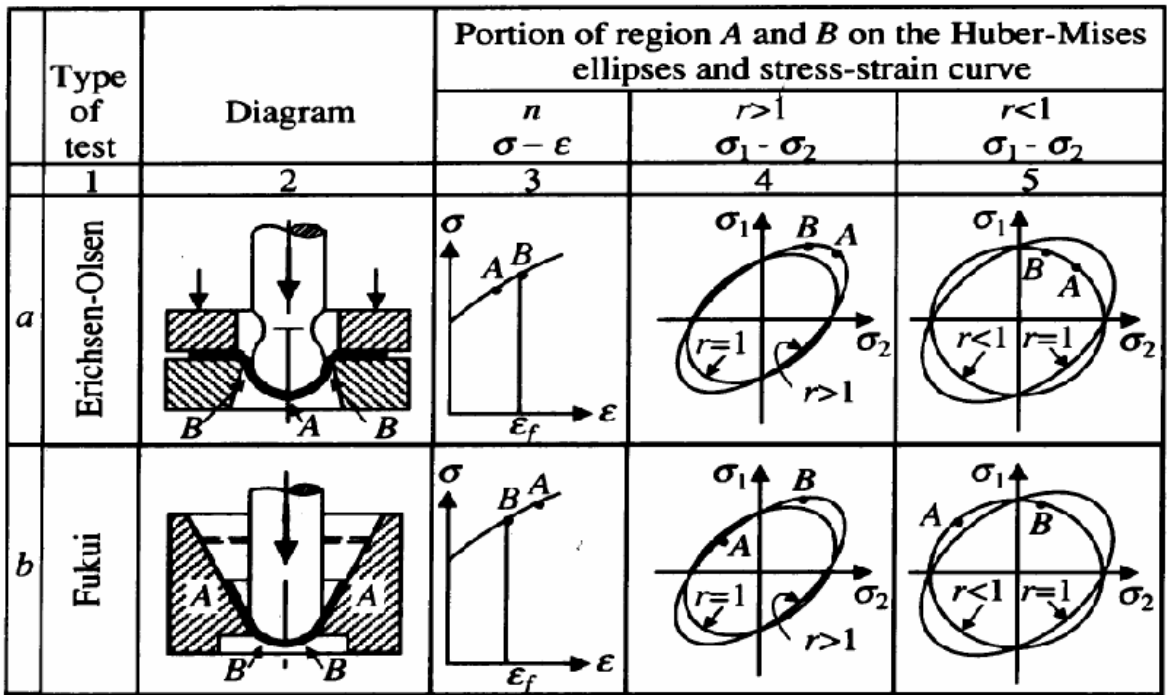

Figure 1.4 schematic of Erichsen-Olsen and Fukui test (Schey, 1992)

Variants of the original FLD determination experiments have emerged and gradually changed over time. For example, relatively large hemispherical punches have been used to stretch sheet specimens to failure. In these experiments, varying the width of the specimen changes the strain path (stress state). Gosh (1975) proposed that gridded blanks of different widths, which produce near-plane strain conditions, can be used to evaluate sheet formability. He plotted critical minor strain, which he measured next to the necking area, against specimen width, and, in a second plot, mapped critical strain in the press-formed part. Comparison of the two plots determines the specimen width that accurately reproduces critical minor strain in the press-formed part, which can then be used in dome tests to evaluate sheet quality. Ayres et al. (1979) and Story (1982) later applied this method, and showed the predicted behaviour correlates well with press performance. This encouraged a significant cooperative effort by the North American Deep Drawing Research Group (NADDRG), leading to a recommended standard practice (1987). Typically, the punch used is a hemisphere measuring 100 mm or 101.6 mm (4 in) in diameter. Smaller punches can be used (Vetger et al., 1985); however, decreasing punch diameter increases limit strain. The ratio of sheet thickness to punch radius

has an important effect on limit strain (Story, 1982), thus absolute Limiting Dome Height (LDH) values should not be compared for sheets of different thicknesses. More important is the lock bead configuration, which has an important role to ensure pure stretching. The tooling incorporates a circular lock bead with a conforming female die.

1.4 Warm formability of aluminum alloy sheet

As previously discussed, aluminum alloys have high strength-to-weight ratios and good corrosion resistance but demonstrate limited applicability due to the low formability of aluminum sheets. This issue can be overcome by introducing elevated temperatures to the forming process that are close to, but below the recrystallization temperature (Tebbe and Kridli, 2004). Warm forming has been studied for many years, dating back to the 1970s and 1980s (Shehata et al., 1978; Wilson, 1988). Shehata et al. (1978) showed that formability gains achieved for AA5082 and AA5005 can be attributed to increases in strain hardening at the elevated temperatures. Schmoeckel (1994) and Schmoeckel et al. (1995) studied the drawability of 5000 series aluminum alloys at elevated temperatures. Temperature has been identified to have a significant influence on the stamping process.

1.4.1 Formability improvement with temperature

Studies have been undertaken to characterize the effect of temperature on the formability of aluminum alloy sheet and the resulting quality of warm formed parts. Formability depends strongly on the composition of the aluminum alloy in question. For example, aluminum–magnesium alloys generally demonstrate good formability, although 5000 series alloys sometimes develop stretcher lines after forming that result in an undesirable surface quality; hence these alloys are often used to form automotive inner panels. Van den Boogaard et al. (2004) showed that warm forming can eliminate these undesirable surface defects.

Li and Ghosh (2004) investigated the biaxial warm forming behaviour of three aluminum alloys, AA5754, AA5182 and AA6111-T4, across the temperature range 200-350°C. They formed rectangular parts at a rapid rate of 1 s^{-1} using heated tooling under both isothermal and non-isothermal conditions; while all three alloys demonstrated improved formability at elevated temperatures, AA5754 and AA5182 showed considerably greater improvement than AA6111-T4. Apart from these alloy-specific effects, their results also showed that

temperature strongly impacts formability. They were able to achieve additional formability gains by applying a gradient of temperature between the die and punch. They also derived forming limit diagrams (FLD) for each alloy under warm forming conditions and used them to accurately predict part depth. FLDs for AA5754, AA5182 and AA6111-T4 are shown in Figure 1.5, indicating that all three alloys demonstrated increased formability with increased forming temperature, with AA5754 being particularly sensitive to temperature effects.

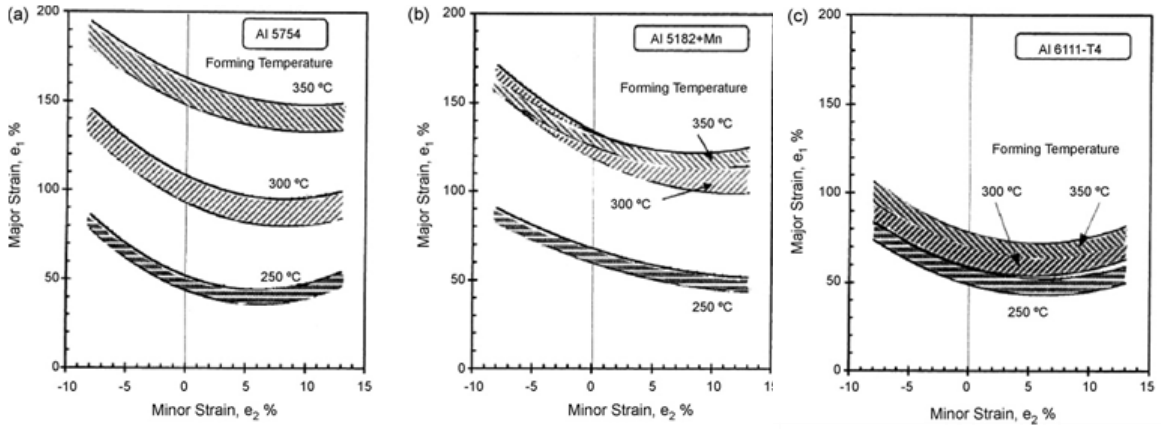

Figure 1.5 The effect of warm temperatures on FLDs [Li and Ghosh, 2004]

Kim et al. (2006) studied rectangular cup drawing of aluminum alloy sheets at elevated temperatures using a thermal-mechanical coupled finite element analysis. They examined the applicability, accuracy and repeatability of three different failure criteria (maximum load, minimum load, and thickness ratio) to identify the onset of failure during numerical simulation. They used a simplified thickness ratio as a necking criterion which was in good agreement with experimental measurements, and established FLDs at three different warm forming temperature levels (250, 300 and 350°C). They concluded that limit strain increases with increasing forming temperatures. Furthermore, increased formability depended on establishing a high temperature gradient between the die and punch ($T_{die} > T_{punch}$).

Wang et al. (2011) evaluated the formability of aluminum alloy AA7075 at elevated temperatures using simple tension, deep draw, and stretch forming experiments. Different temperatures and forming speeds were investigated. They showed that temperatures below 140°C do not alter the properties of AA7075, and that, according to their deep draw and stretch forming results, formability is very poor at these low temperatures. They also observed that at 260°C, the total elongation begins to decrease, and that the strain-rate sensitivity factor

(*m* value) is higher at 180 °C than at 140 °C or 220 °C. They observed the best deep drawing formability near 180 °C and the best stretch formability near 220 °C.

1.4.2 Non isothermal forming

Partial heating in the holder or die area has been shown to produce a much better effect on formability than uniformly heated tools (Schmoeckel, 1994). Schmoeckel et al. (1995) demonstrated that the limiting drawing ratio (LDR) of aluminum alloys increases with temperature. Specifically, formability can be improved by applying a uniform temperature increase, but the best results are obtained by applying temperature gradients.

Takuda et al. (2002) studied the deformation behaviour and the temperature change in cylindrical deep drawing of an aluminum alloy sheet at elevated temperatures using a combination of rigid-plastic and heat conduction finite element methods. They demonstrated that in order to obtain higher LDRs, an appropriate distribution of flow stress depending on temperature must be applied to the sheet. In their study, both the numerical results and experiments showed that the LDR in warm deep drawing increases with the die profile radius.

Yoshihara et al. (2004) examined the spin formability of Al–Mg alloy using an NC control machine operating at 300°C with a main shaft rotational frequency of 300 rpm and feed per revolution of 180 mm/min. They also developed a new deep drawing process and localized heating and cooling technique (Yoshihara et al., 2003a, b) to improve formability. They concluded that the deep drawability of the alloy can be increased by applying an appropriate temperature distribution with their local heating and cooling technique and with variable blank holder pressure control.

Van den Boogaard and Hu´etink (2006) studied cylindrical cup deep drawing at different temperature gradients and observed that the formability of Al–Mg alloy sheets can be improved by increasing the temperature in some parts of the sheet and cooling other regions.

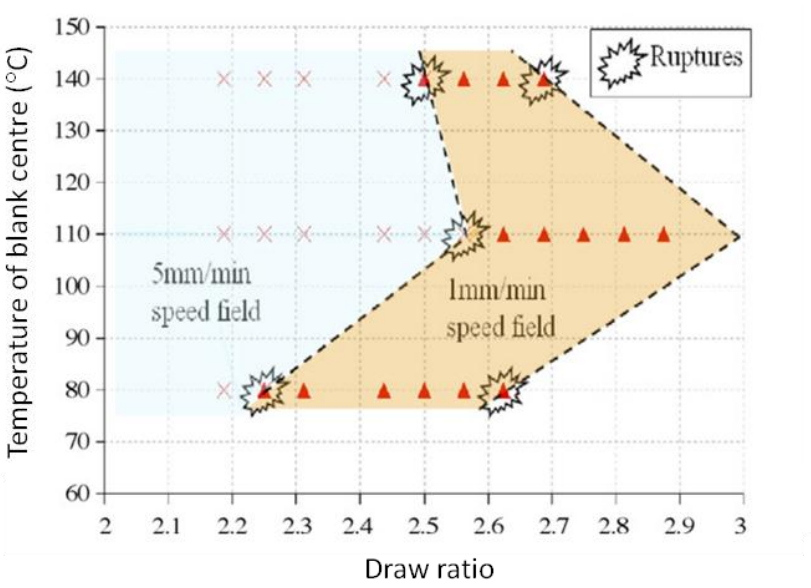

Figure 1.6 WDD test results considering both successes and rupture [Palumbo and Tricarico, 2007]

Palumbo and Tricarico (2007) investigated the effectiveness of the warm deep drawing (WDD) process for AA5754-O forming, specifically considering the effects of temperature at the blank centre, forming speed, and the use of grease lubricant. They found that the temperature of the centre of the blank strongly affects the formability of AA5754 (Figure 1.6), as does forming speed. They obtained the limit value of punch speeds under different thermal conditions; for example, for a thermal gradient roughly equal to 60°C superimposed between the blank holder and 75mm diameter blank centre, they estimated a punch speed limit value of 10 mm/min. They concluded that evaluation of optimal conditions to improve AA5754-O formability requires consideration of: (i) the strengthening effect using a cold punch in the punch profile radius area; (ii) material softening in the flange area; and (iii) the worsening of lubrication conditions in the flange area (which has an opposite effect on the punch load).

Kaya et al (2008) experimentally evaluated non-isothermal deep drawing of AA5754 and AA5052 alloys, using a heated die (310° C) and a cooled punch (65°C). Variable punch speeds throughout the punch stroke were produced using a servo toolset. They observed that increasing the die temperature reduces thinning at the bottom of the cup, whereas increasing the punch speed has the opposite effect. The slower initial punch velocity also decreased the tendency for necking at the bottom of the cup. Kaya et al. suggested that accurate finite element analysis of warm forming requires: material properties as a function of temperature

and strain-rate; accurate heat transfer coefficients between the tooling and the blank; and the coefficient of friction as a function of temperature and pressure.

1.4.3 Material anisotropy

Further investigations were performed to study the effect of temperature on yield surface and material anisotropy. Naka et al. (2003) investigated the effects of temperature on yield locus for AA5083 sheet. They obtained yield surfaces at elevated temperatures by performing biaxial tensile tests using cruciform specimens at a strain-rate of $10s^{-1}$. Their results show that the size of the yield surface is strongly temperature dependent and drastically decreases with increasing temperature (Figure 1.7). Their experimental results revealed that yield functions such as Barlat YLD2000 (Barlat et al., 2003) and Logan–Hosford (Logan and Hosford, 1980) fit well with warm deformation of aluminum alloy sheet, while Hill's (Hill, 1993) or von Mises' (von Mises, 1913) criteria are not suitable for the prediction of plastic deformation of this material. They also found that the r-values become larger with the temperature rise which is beneficial to reducing localized necking.

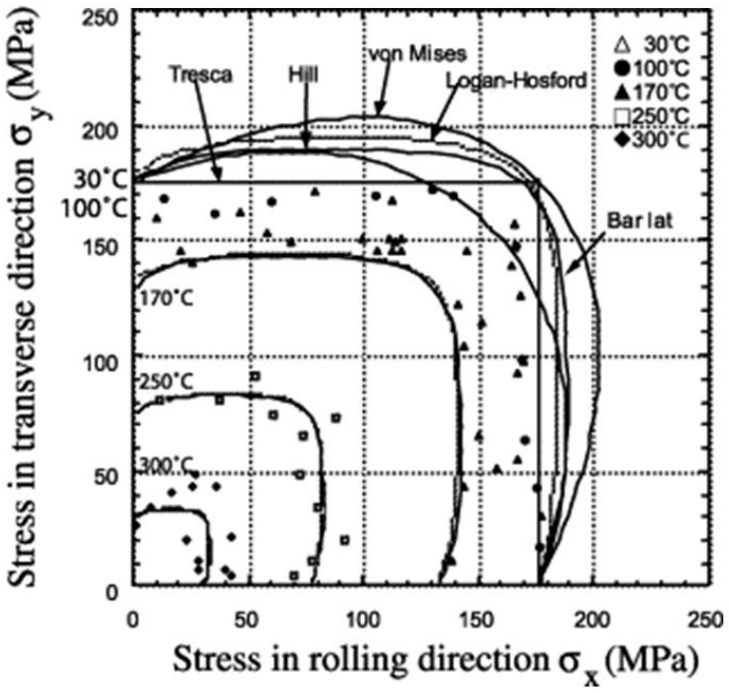

Figure 1.7 Comparison of experimental yield loci and those predicted by the von Mises, Hill, Tresca, Logan–Hosford and Barlat criteria under biaxial stress conditions for Al–Mg alloy sheet [Naka et al., 2003]

Abedrabbo et al. (2007) developed a temperature-dependent anisotropic material model for FEA and forming simulation for AA5182-O and AA5754-O. The model was able to simulate the forming of complex parts at elevated temperatures. In addition to the temperature, the forming speed (strain-rate), the die and punch corner radii and other geometric parameters of the die set-up had an effect on the formability of the aluminum alloy sheet. They concluded that the most important factor for an accurate finite element simulation is the material model and adoption of Barlat-type yield surfaces (Barlat et al. 1989, 1991, 1997, 2003) which provide accurate descriptions of aluminum alloy behaviour. They also derived stress- and strain-based FLDs for AA5182 at elevated temperatures (Figure 1.8)

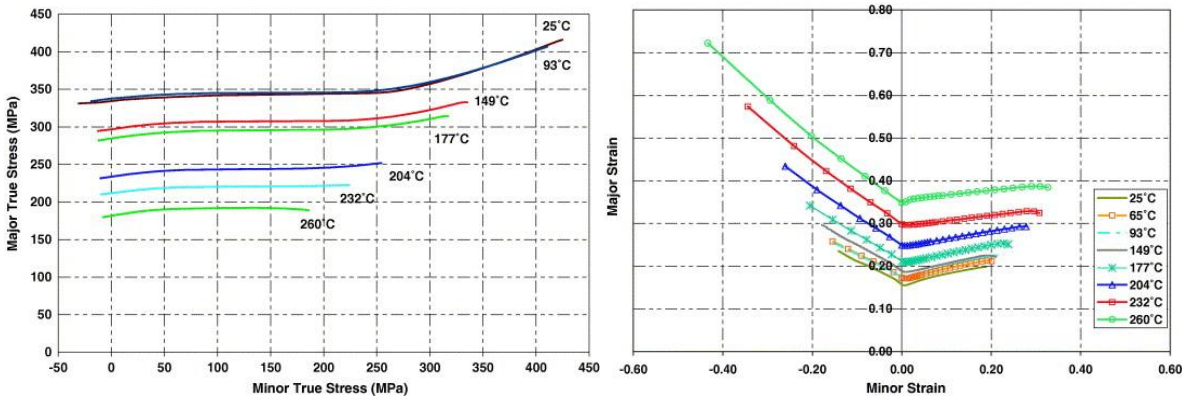

Figure 1.8 Stress- and strain-based FLDs for AA5182-O based on the M–K model, Barlat's YLD2000-2d anisotropic yield function, and Voce hardening law at elevated temperatures [Abedrabbo et al., 2007]

1.4.4 Strain-rate sensitivity

Naka and Yoshida (1999) investigated the effects of forming speed and temperature on the deep drawability of AA5083-O using various forming speeds (0.2–500mm/min) and die temperatures (between 20°C and 180°C, the punch was water cooled during the tests). They found: i) that the LDR increases with increasing die temperature because the deformation resistance to flange reduction decreases with temperature rise and ii) the LDR decreases with increasing forming speed at all temperatures (Figure 1.9). This behaviour was attributed to the fact that the flow stress in the flange of the heated blank increases with increasing strain-rate. In addition, the cooled blank at the punch corner becomes less formable at higher rates of deformation.

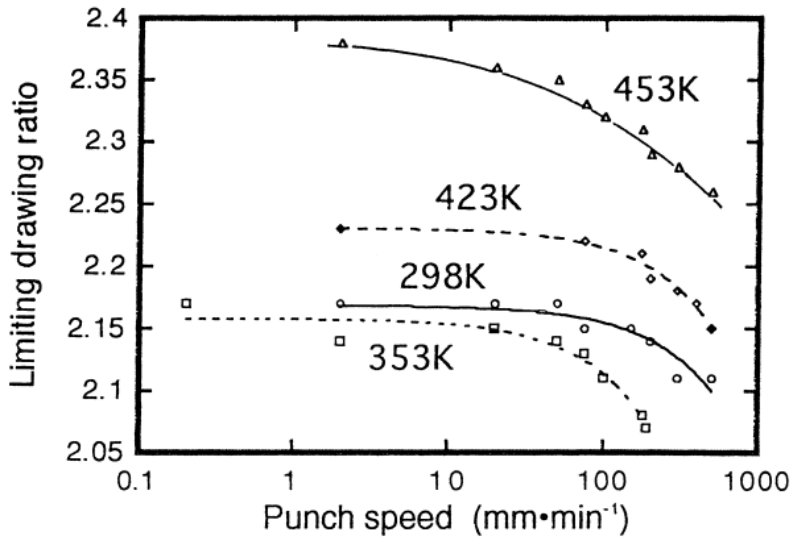

Figure 1.9 Effect of punch speed on the LDR of AA5083-O at various die temperatures [Naka and Yoshida, 1999]

Naka et al. (2001) experimentally investigated the effects of forming speed and temperature on the FLD of AA5083-O by stretch-forming the alloyed sheet at various forming speeds (0.2–200mm/min) and temperatures (between 20°C and 300°C). It was found that the forming limit strain increased drastically with decreased forming speed at temperatures ranging from 150°C to 300°C. They also found that the FLD was not sensitive to speed at room temperature. Furthermore, the high strain-rate hardening characteristic of the material served to improve formability at low forming speeds, both above 300°C and below 200°C.

Li and Ghosh (2003) studied uniaxial tensile deformation behaviour of AA5182, AA5754, and AA6111-T4 at elevated temperatures, ranging from 200 to 350°C, and strain-rates from 0.015 to 1.5S^{-1}. They found that the total elongation in uniaxial tension increased with increasing temperature and decreased with increasing strain-rate. They report enhancement of ductility at elevated temperatures primarily through increased post-uniform elongation which becomes dominant at elevated temperatures and/or at slow strain-rates. The increase in strain-rate sensitivity with increasing temperature accounts for the ductility improvement at elevated temperatures. They used the uniaxial tensile test results to rank the relative formability of different sheet alloys. They showed that strain hardening 5000 series alloys (AA5182 and AA5754) respond better to elevated forming temperatures than the precipitation hardening alloy (AA6111-T4).

Spigarelli et al. (2004) investigated uniaxial compression of an aluminum alloy between 120°C and 180°C and compared the deformation response in compression with uniaxial tensile data. They realized that at higher strain-rates the compressive strength of the alloy is higher than its tensile strength but at lower strain-rates this difference vanishes.

Smerd et al. (2005) investigated the strain-rate sensitivity of AA5754 and AA5182 aluminum alloy sheet at room and elevated temperatures. They used the split Hopkinson bar apparatus to identify the constitutive response and damage evolution produced at high strain-rates of 600, 1100, and $1500S^{-1}$. They showed that, for the range of strain-rates and temperatures considered, the quasi-static and dynamic stress-strain responses were low for both alloys. They further demonstrated that AA5182 is not strain-rate sensitive at room temperature while AA5754 showed a mild increase in flow stress with strain-rate. For both materials, ductility did not change between temperatures of 23 and 150°C, when tested at a strain-rate of $1500S^{-1}$; however, the final elongation decreased at 300°C.

Picu et al. (2005) investigated the mechanical behaviour of AA5182-O and observed the dynamic strain aging effect at temperatures between −80 and 110°C for strain-rates lower than $0.1S^{-1}$. Moreover, they determined the strain-rate sensitivity exponent, *m*, as a function of temperature and plastic strain (Figure 1.10).

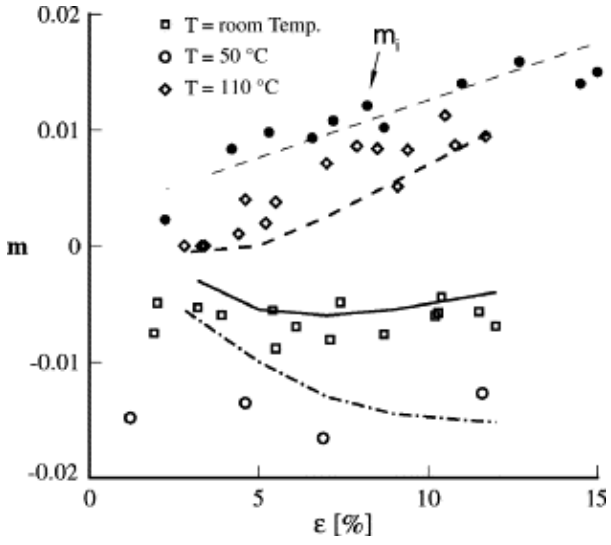

Figure 1.10 Variation of the strain-rate sensitivity parameter (m) with strain at three temperatures for AA5182-O [Picu et al., 2005]

1.4.5 Effect of alloying element

The number of commercially available 5000 series aluminum alloys for passenger vehicles is very limited. Currently, AA5052 and AA5754 are the most commonly used alloys for these applications. AA5052 offers a good combination of desirable mechanical properties, corrosion resistance, and formability; however, it cannot be used at temperatures above 120°C due to poor creep resistance. In order to achieve a better overall understanding of alloys and to identify the most promising compositions, most researchers examine and evaluate microstructural features, tensile properties, and creep resistance. Zhang et al. (1998) presented new Al–Mg alloys with good creep resistance, desirable formability, and low cost. They also studied the effect of small additions of Ca and Sr on tensile and creep properties. Romhanji et al. (1998) assessed the formability of Al–Mg6.8 type alloy sheet with either a fully re-crystallized or partially annealed structure, which showed yield strengths of 175 and 283MPa, respectively. Using the Limiting Dome Height (LDH) test, they found the increase in strength caused formability degradation of 42% under plane strain deformation; measured Forming Limit Curves (FLC) confirmed this finding, showing a slightly lower degradation of 35%. They compared these results with known values of high-strength formable alloys and showed that the re-crystallized condition demonstrated a better stretch formability than the un-recrystallized, partially annealed alloy.

Bolt et al. (2001) also studied the formability of 5000 series aluminum alloys, comparing box-shaped and conical rectangular products made from AA1050, 5754 and 6016 type aluminum alloys, at temperatures between 100 and 250°C. They showed that the maximum height of box shaped, deep-drawn products increased by 25% when a die temperature of 175°C is used; conical stretched-drawn products improved by 65% at 250°C. They also found that the formability of AA6016-T4 begins to increase at lower temperatures than that of AA5754-O. For example, a die temperature of 175°C increases the maximum height of stretched-drawn AA6016-T sheet products by 30%, and only 11% for 5754-O sheet.

Altan (2002) showed that an aluminum alloy with 6% magnesium can demonstrate a 300% total elongation at roughly 250°C.

1.4.6 Die design geometry

Jain et al. (1998) used experimental and numerical methods to investigate the LDRs and other axisymmetric deep drawing characteristics of AA5754-O and AA6111-T4 as a function of die profile radii. Punch load versus displacement, flange draw-in, strain distribution along the cup profile, flange wrinkling, wall ironing, and fracture characteristics were experimentally assessed for both alloys as a function of the die profile radius. They used cup depth as an index to describe the deep drawability of both alloys, and in this way showed that AA5754-O has a better formability than AA6111-T4. They explained the differences in the deep drawing behaviour of the two alloys in terms of: i) the competition between work hardening in the flange at the die profile radius versus that at the punch profile radius; ii) the bendability of the two materials and their fracture characteristics. They also demonstrated a decrease in LDR and flange draw-in to be a function of the die profile radius.

Namoco et al. (2007) applied an embossing and restoration process to deep drawing of AA5052 and AA6061 and showed that applying embossing or restoration in the flange area reduces the deformation force. They decreased the resistance to drawing in the flange region by embossing and increased the strength of the punch shoulder area with restorations to increase the drawability of the sheet and LDR.

1.5 Numerical simulation of warm forming

Recently, warm forming research has begun to focus on the development of numerical models to predict the temperature and strain-rate dependent behaviour of aluminum alloys and their formability during the warm forming process.

Takuda et al. (2002) performed axisymmetric finite element simulations of the warm deep drawing of AA5182-0 and compared their results to experiments. Uniaxial tensile tests were performed at temperatures from 20°C to 320°C to characterize the material. There were large gains in elongation to failure and a decrease in flow stress above 150°C. The average Lankford parameter $\bar{R}$, was found to be constant at 0.7 for all temperatures which is contrary to the results of Naka (2003). Deep drawing experiments by Takuda et al. (2002) were performed using a 33 mm diameter punch. The dies and blank were heated in an oven before forming; the punch was kept at room temperature. At low temperatures, failure occurred at the punch radius, while at higher temperatures failure occurred in the cup wall due to the

relatively higher strength of the colder material in contact with the punch. Room temperature deep drawing was unsuccessful, with an LDR of 2.4. Warm deep drawing was achieved with an LDR of 2.68. The material behaviour was modeled as rigid-plastic using power-law plasticity (equation (1-1)) with *K* (strength parameter) and *n* (strain hardening exponent) as functions of temperature. Heat transfer between the blank and the tooling was set to 1,400 $W/m^2\ K$ and the coefficient of friction (COF or μ) was assumed to be 0.05. Five elements were used over the sheet thickness of 1mm.

$$\sigma = K\varepsilon^n \tag{1-1}$$

Keum et al. (2001) undertook a finite element study of AA5052-H32 non-isothermal warm forming. Tensile tests were performed at temperatures from 18°C to 300°C to characterize the material, and a rate sensitive power-law type constitutive equation was used (equation (1-2))

$$\sigma = K\varepsilon^n\dot{\varepsilon}^{\mathrm{m}} \tag{1-2}$$

in which *K*, *n*, and *m* were expressed as functions of temperature. Barlat's yield function (Barlat and Chung, 1993) was used to represent planar anisotropy, with the parameters introduced as a function of temperature. The coefficient of friction was set to 0.08. The model was found to predict trends adequately; however, Keum et al. concluded that a strain-rate sensitive constitutive model is necessary for accurate warm forming simulations of aluminum alloy sheet.

Abedrabbo et al. (2006, 2007) developed a temperature and strain-rate dependant anisotropic finite element model for warm forming using a user defined material model (UMAT) in LS-DYNA. AA3003, AA5182, and AA5754 were characterized from 25°C to 260°C by means of uniaxial, isothermal tensile tests. Tests were performed using biaxial extensometers at 0°, 45°, and 90° with respect to the rolling direction to determine the effect of temperature on the yield surface and the degree of planar anisotropy. Jump rate tests were performed to determine the strain-rate sensitivity as a function of temperature. Bulge tests were performed at room temperature in order to determine the behaviour of the material under biaxial stretching. Their numerical models used a power-law hardening rule and Barlat's Yld96 (Barlat, et al. 1997), and later Yld2000 (Barlat et al. 2003), yield functions. Hardening parameters *K*, *n*, and *m* were expressed as functions of temperature (equation (1-3)). *K* and *n* both decrease linearly, while strain-rate sensitivity increases exponentially, with temperature.

$$\bar{\sigma}(\bar{\varepsilon}^p, \dot{\varepsilon}, T) = K(T)(\bar{\varepsilon}^p + \varepsilon_0)^{n(T)} \left(\frac{\dot{\varepsilon}}{\varepsilon_{sr0}}\right)^{m(T)} \quad (1\text{-}3)$$

where ε_{sr0} is a constant which is a strain rate normalization factor. The average R-value increased from less than unity at room temperature to over 2 at 260°C, indicating a large increase in the resistance to thinning. The spread between the lowest (R_0) and the highest (R_{45}) R-values also increased with temperature. M-K analysis (Marciniak and Kuczynski, 1967) was used to develop temperature-dependant failure limit curves using the anisotropic yield function, which showed that failure strains increased with temperature. Stress- and strain-based FLCs were also developed. Stress-based FLDs were found to be more accurate in forming simulations because they are not strain path dependant. LDH experiments were performed with heated dies. The 101.6mm diameter punch was not actively heated or cooled. The forming depth increased at higher temperatures (200°C) for all materials. Coupled thermal-mechanical simulations were able to accurately predict punch force and failure location.

McKinley et al. (2008) performed a combined experimental and numerical study of the effects that die and punch temperatures have on the formability of AA3003-H111. They ran numerical simulations of the warm forming process using a coupled thermal-mechanical FEA model. The temperature-dependant material model used Barlat's YLD2000 anisotropic plane-stress yield function. Numerical results were in good agreement against the experiments. They used strain and stress based FLDs to determine both the location and failure depth for the numerical models.

Choi et al. (2007) developed analytical models for hydro-mechanical deep drawing tests to investigate the effects of process conditions such as temperature, hydraulic pressure, BHF and forming speed on formability. Their experimental results were in very good agreement with numerical models (Figure 1.11).

Van den Boogaard et al. (2003) also investigated the effect of forming condition on sheet formability using implicit and explicit finite element simulations. They found that the computation time for implicit finite element analyses tended to increase disproportionately with increasing problem size (Figure 1.12). Sheet metal deformation is considered a biaxial rather than tensile deformation and biaxial data should be evaluated for accurate material

modeling. To accurately simulate warm forming of aluminum sheet a material model is required that incorporates temperature and strain-rate dependency (Van den Boogaard and Hu´ etink, 2004).

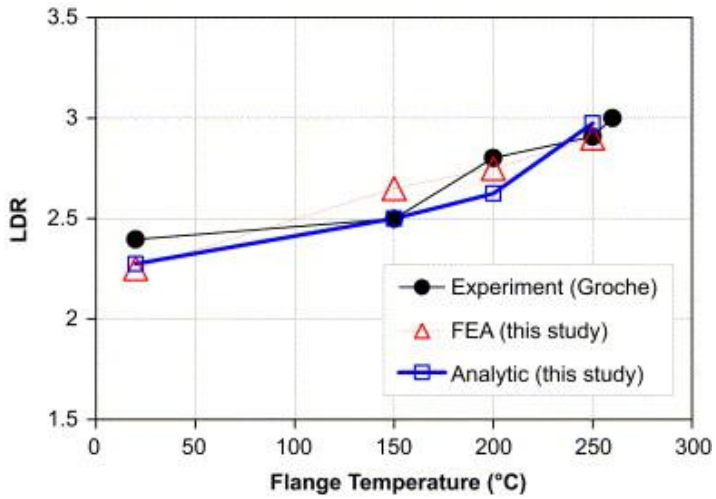

Figure 1.11 Comparison of LDRs under different flange temperatures [Choi et al., 2007]

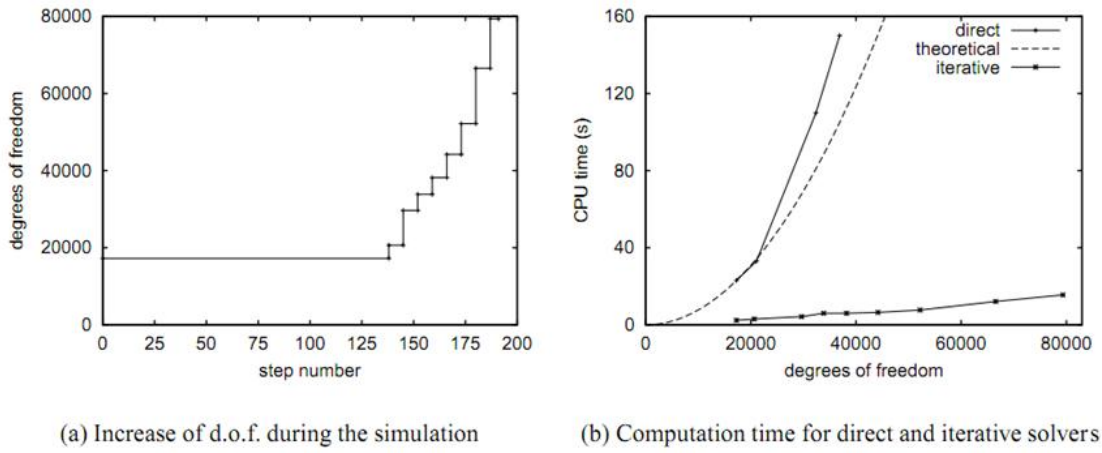

(a) Increase of d.o.f. during the simulation (b) Computation time for direct and iterative solvers

Figure 1.12 Evolution of d.o.f. and CPU time in front door panel simulation [Boogaard et al, 2003]

1.5.1 Hardening rules for warm forming of aluminum alloys

Considerable research has been undertaken to identify the proper flow rule that best fits the behaviour of aluminum alloys formed at high temperatures. Van den Boogaard and Huetink (2006) developed a coupled thermal-mechanical, anisotropic, temperature, and strain-rate dependent finite element model to describe aluminum alloy forming behaviour. They used a physically based constitutive model developed by Bergstrom (1982), which decomposed the

flow stress into three components: strain and strain-rate independent stress; dynamic stress that depends on strain-rate and temperature; and work hardening. The work hardening component is a function of dislocation density which is in turn dependent on the rate of dislocation immobilization and dynamic recovery achieved by remobilization and annihilation. The anisotropic Vegter (2006) yield function was used. Deep drawing experiments were performed with a 25°C punch and dies at 25°C, 175°C, and 250°C. The finite element simulations underestimated the maximum punch force achieved during deep drawing; however, trends experienced with changing temperature were well predicted.

Palumbo and Tricarico (2007) used the Bergstrom model, as developed by van den Boogaard (2006), to model warm deep drawing of AA5754 using coupled thermal-mechanical finite element analysis. Deep drawing experiments were performed with a cooled punch and heated dies. Axisymmetric simulations were performed with various coefficients of friction and punch speeds. The calculated punch force had reasonable agreement with the experiments.

Kurukuri et al. (2009, 2011) developed an improved physically-based constitutive model, they call the Nes model (Nes, 1998). The Nes model improves upon the Bergstrom model by incorporating a multi-parameter description of microstructure. The dislocations are stored in finite cells, as shown in Figure 1.13, and both dislocation density and cell size are tracked. This enables improved strain-rate dependence and more accurate localization prediction. However, Kurukuri recommends investigating friction in detail to further improve warm forming simulations. One drawback of the NES model lies in the requirement to fully define 30 independent parameters.

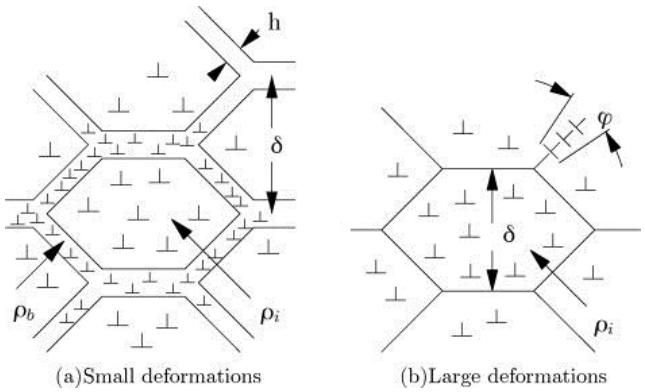

Figure 1.13 Schematic presentation of the dislocation cell structure: (a) small deformations and (b) large deformations [Kurukuri et al., 2009]

Recent studies have looked at warm forming simulation of elastoplastic hardening materials with anisotropy using temperature and strain-rate dependent hardening rules. For example, Farrokh and Khan (2009) proposed a new formulation for flow stress in terms of temperature, strain-rate and grain size for ultra-fine grained and nanocrystalline copper and aluminum. Khan and Baig (2011) studied finite deformation anisotropic responses of AA5182-O at elevated temperatures over different strain-rates. They showed that the strain-rate sensitivity of AA5182-O alloy changes from negative at room temperature to positive at 200°C. They also showed that the modified Khan–Huang–Liang (KHL) constitutive model (1999) is able to predict the strain-rate and temperature dependent responses reasonably well.

1.5.2 Yield functions for warm forming of aluminum

Initial efforts to improve the yield surface description of metals beyond the classical Tresca (Hershey, 1954) and von Mises (von Mises, 1913) surfaces began in the 1940's. Hershey (1954) showed that the most popular isotropic yield conditions, which were proposed by Tresca and von Mises, may be expressed in terms of the principal values of the stress (σ_i) or the deviatoric stress (S_i) tensors as

$$\phi = |\sigma_1 - \sigma_2|^a + |\sigma_2 - \sigma_3|^a + |\sigma_3 - \sigma_1|^a = |S_1 - S_2|^a + |S_2 - S_3|^a + |S_3 - S_1|^a = 2\bar{\sigma}^a \qquad (1\text{-}4)$$

where $\bar{\sigma}$ defines the effective stress. In this equation, a=2 reduces to von Mises, whereas $a = 1$ leads to the Tresca yield condition. The main advantage of Hershey's formula is that good approximations of yield loci can be obtained using the Bishop-Hill crystal plasticity model and by setting $a = 6$ and $a = 8$ for BCC and FCC materials, respectively (Hershey, 1954; Logan and Hosford, 1980).

Hill (1948) proposed an extension of the isotropic von Mises criterion to address orthotropic materials, such that

$$\phi = F(\sigma_{yy} - \sigma_{zz})^2 + G(\sigma_{zz} - \sigma_{xx})^2 + H(\sigma_{xx} - \sigma_{yy})^2 + 2(L\sigma_{yz}^2 + M\sigma_{zx}^2 + N\sigma_{xy}^2) = \bar{\sigma}^2 \qquad (1\text{-}5)$$

where *F,G,H,L,M* and *N* are material constants. Hill (1979) and Mellor (1981) showed that this yield surface format is well suited for steels, but is inappropriate for non-ferrous materials. Hill (1990) proposed a non-quadratic yield criterion to describe non-steel materials and derived four special cases from the general form. The most widely used expression of this

yield criterion applies to materials exhibiting planar isotropy (with an average Lankford coefficient, $\bar{r}$) for plane stress states

$$\phi = |\sigma_1 + \sigma_2|^a + (1+2\bar{r})|\sigma_1 - \sigma_2|^a = 2(1+\bar{r})\bar{\sigma}^a \qquad (1\text{-}6)$$

He also proposed other non-quadratic plane stress yield criteria (Hill, 1990, 1993).

Hosford (1972) also used Hershey's isotropic criterion (1954) as described in equation (1-4) and proposed the following generalized format for orthotropic materials

$$\phi = \mathrm{F}|\sigma_{yy} - \sigma_{zz}|^a + \mathrm{G}|\sigma_{zz} - \sigma_{xx}|^a + \mathrm{H}|\sigma_{xx} - \sigma_{yy}|^a = \bar{\sigma}^a \qquad (1\text{-}7)$$

Barlat and Lian (1989) extended Hosford's (1979) yield criterion to describe the behaviour of orthotropic sheets considering planar anisotropy by folding in the effect of shear stress under plane stress conditions. This yield function showed similar results to that calculated by the Taylor/Bishop and Hill models. Lian et al. (1989) effectively applied this model to study the effect of yield surface shape on failure behaviour of sheet metals. Barlat et al. (1991) extended this method to tri-axial loading conditions by using a six-component yield function (often referred to as YLD91). Anisotropy is introduced by replacing the principal values of the stress tensor, σ_{ij}, with those of a stress tensor modified by weighting coefficients, S_{ij}. Karafillis and Boyce (1993) proposed a generalization of Hershey's criterion

$$\phi = (1-c)\left(|S_1 - S_2|^a + |S_2 - S_3|^a + |S_3 - S_1|^a\right) + \frac{3^a c}{2^{a-1}+1}\left(|S_1|^a + |S_2|^a + |S_3|^a\right) = 2\bar{\sigma}^a \qquad (1\text{-}8)$$

where c is a constant. They extended this model to orthotropic materials, thus generalizing YLD91 (Barlat et al., 1991).

Yoon et al. (2004) compared yield surface shapes and R-values for Al–5wt. % Mg and AA6016-T4 alloy sheet samples with the previously suggested yield functions (Figure 1.14). Barlat et al. (2005) proposed anisotropic yield functions based on linear transformations of the stress deviator in general terms. Two specific convex formulations were given to describe the anisotropic behaviour of metals and alloys for a full stress state (3D).

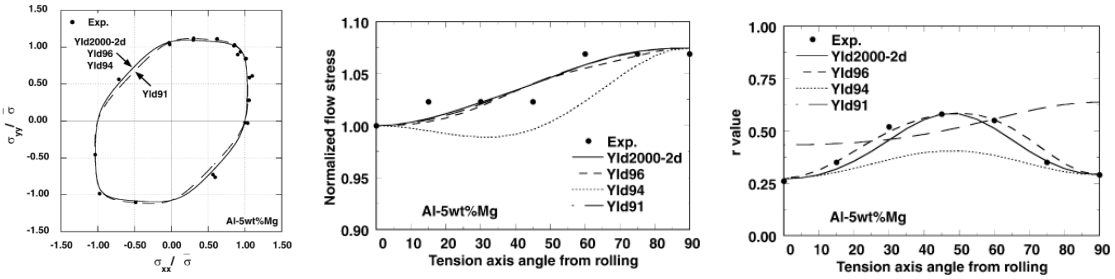

(a) (b) (c)

Figure 1.14 Yield surface shape (a), Normalized yield stress (b) and R-value anisotropy (c) for Al-5wt. % Mg alloy, [Yoon et al., 2004]

Further numerical studies have applied these yield surface functions to describe the forming behaviour of aluminum alloys at elevated temperatures. For example, Yu et al. (2007) developed a ductile fracture criterion based on Barlat's yield function (Barlat et al., 1989) and Hollomon's hardening equation, and simulated aluminum alloy sheet forming using Barlat's yield function (Barlat and Lian, 1989) and Hollomon's hardening equation. They calculated the critical punch stroke for several aluminum alloy sheets, X611-T4, 6111-T4 and 5754-O, using their ductile fracture criterion in a complex forming operation that combines deep drawing and stretching modes. The predictions were in good agreement with experiments. Barlat et al. (1997) measured the yield surfaces of binary aluminum–magnesium sheet samples with different microstructures, and proposed a generalized plastic yield description that predicts the behaviour of solute strengthened aluminum alloy sheets. Barlat et al. (2003) proposed a different plane stress yield function to describe the anisotropic behaviour of sheet metals, particularly aluminum alloy sheets. The anisotropy of this yield function was introduced using two linear transformations of the Cauchy stress tensor.

Considerable effort has been expended to characterize the anisotropic behaviour of aluminum alloys (Paquet et. al, 2011; Desmorat and Marull, 2011; Segurado et al., 2012). Fourmeau et al. (2011) studied the effect of plastic anisotropy on the mechanical behaviour of rolled aluminum plate under quasi-static loading conditions. They found that the Yld2004-18p anisotropic yield function (Barlat et al., 2005) provides an adequate description of the significant anisotropic behaviour typical of high-strength aluminum alloys. Yoon and Barlat (2011) showed that earing is produced by the combination of the contributions from *R*-value and yield stress directionalities. They presented a new analytical approach that predicts the earing profile and verified the results for three different aluminum alloys.

In order to capture material anisotropy in the plastic regime, an advanced material yield surface must be incorporated to capture the crystallographic nature of yielding in FCC aluminum alloys. This includes capturing material R-values which control thinning in textured sheet materials. The Barlat YLD2000 yield surface (Barlat et al., 2003) has been shown to accurately describe the anisotropic material behaviour of aluminum alloy sheet (Abedrabbo, 2007; Bagheriasl et al., 2011; Ghavam et al., 2011).

1.6 Prediction of formability under warm conditions

Naka et al. (2001) studied the effect of temperature and strain-rate on the forming limits of AA5083 aluminum sheet at elevated temperatures. They developed an analytical formability model based on M-K analysis (Marciniak and Kuczynski, 1967) to predict failure and forming limit strains. The M-K method assumes that a thickness imperfection develops into a neck. A sheet, as shown in Figure 1.15, is subjected to proportional loading until the thickness ratio between the imperfection and the rest of the sheet reaches a limit value, often assumed to be 0.8. Naka et al. (2001) used a power-law hardening rule (equation 1.2) to account for strain hardening (n) and strain-rate sensitivity (m). The analytical results had reasonable agreement with their experimental results.

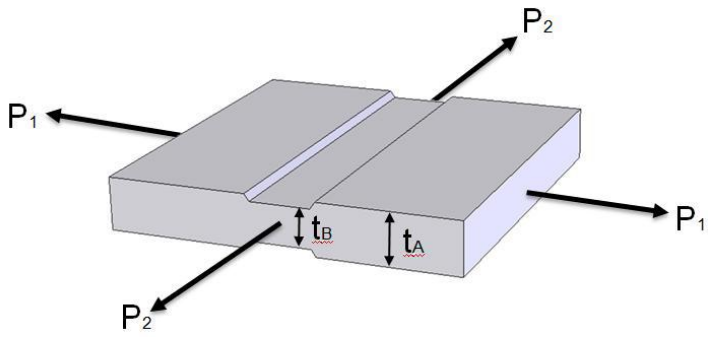

Figure 1.15 Illustration of M-K analysis. Biaxial loading of a flat plate with an imperfection

Ambrogio et al. (2005) studied the increase in deep drawing formability achieved by imposing a thermal gradient within the sheet. They used a damage-based criterion to predict ductile failure in the part, and calculated the stress and strain fields using the developed code. In particular, the prediction of ductile material failure was based on a number of commonly adopted diffuse damage criteria, i.e., Normalized Cockcroft & Latham (1968), Brozzo (1972), Freudenthal (1950) and Ayada (1987). They implemented these criteria into the FE

simulations and obtained predicted damage values for a fixed draw ratio at three different thermal conditions - warm, cold, and gradient. They realized that the damage values (shown in Table 1.2) correspond to a clear trend: in all cases a higher value of the predicted damage was shown to move from the "gradient imposed process" to the cold isothermal case, and this was true for each criterion. Conversely, when the "warm process" is considered, the success or failure of the process cannot be inferred from increases or decreases in the damage value. The critical threshold, in fact, may be dependent on the material temperature.

Table 1.2 Predicted levels of damage (Ambrogio et al. ,2005)

Criterion	DR* = 1.88			DR = 2.03			DR = 2.19		
Condition	cold	Warm	gradient	cold	warm	gradient	cold	warm	gradient
Cockcroft & Latham normalized	0.22	0.23	0.22	0.26	0.27	0.24	0.30	0.27	0.26
Brozzo	0.27	0.26	0.25	0.28	0.29	0.26	0.39	0.29	0.29
Freudental	26	24	22	29	18	25	31	30	29
Ayada	0.11	0.11	0.10	0.12	0.12	0.11	0.16	0.12	0.11

*DR: Drawing Ratio

Kim et.al (2006) used three simplified failure criteria (maximum load, minimum thickness, and thickness ratio) along with a coupled thermal-mechanical FEA to predict the formability of AA5182 sheet during warm drawing of rectangular cups. By comparing the FE simulations against experimental results obtained under warm conditions, they realized that the thickness ratio criterion produces a repeatable and more accurate prediction of necking-type failure than the other two criteria. They obtained predicted part depth values from FEA at various die-punch temperature combinations and showed that the numerical results are in good agreement with the experiments. Kim et al. also established FLDs for three different warm forming temperatures (250°C, 300°C, and 350°C). Both the FEA and experimental data showed that limit strain increases with increasing forming temperature (Figure 1.16).

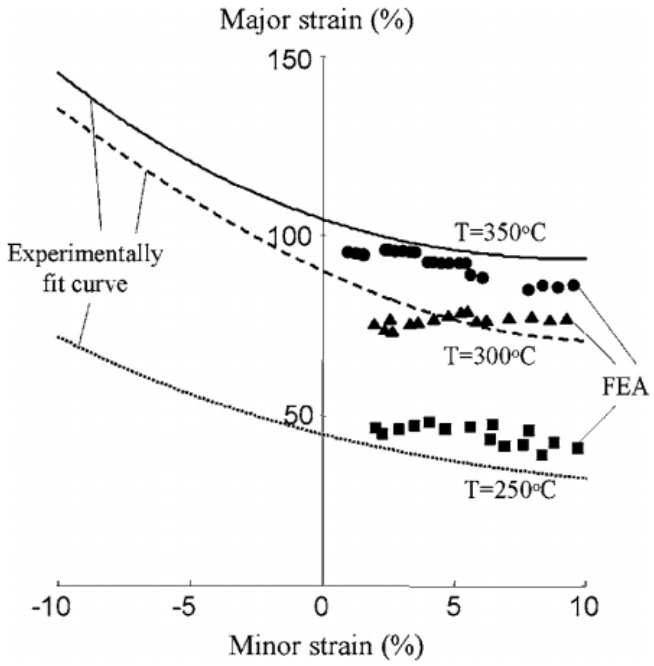

Figure 1.16 Comparison of FEA predictions based on thickness ratio criterion with experimental findings. Effect of forming temperature on FLDs [Kim et al, 2006]

Abedrabbo et al. (2006a, b) developed a temperature and strain-rate-dependent anisotropic finite element model for warm forming using a user defined material model (UMAT) in LS-DYNA. The constitutive model used in their UMAT consisted of a modified power-law hardening rule that includes the strain-rate sensitivity as proposed by Wagoner et al. (1988) and Barlat's YLD96 yield function. The hardening and anisotropy parameters were expressed as functions of temperature. They used M-K analysis to develop temperature-dependent failure limit curves using the anisotropic yield function, and showed that failure strains increase with temperature. They also performed LDH experiments for AA3003 and showed that the coupled thermal-mechanical LDH simulations were able to accurately predict both failure depth and location. Abedrabbo et al. (2007) later expanded their research to include AA5182 and AA5754. Both stress- and strain-based FLDs were developed using M-K analysis. The failure stress decreased with temperature; however, since the flow stress also decreased, this does not indicate a decrease in formability. Stress-based FLDs were found to

be more accurate in forming simulations because they are not strain path dependent (Stoughton and Zhu, 2004) and the resulting failure predictions were quite accurate.

1.7 Lubrication under warm forming conditions

Lubrication is an important parameter for aluminum alloy sheet forming; it not only contributes to better surface quality, but decreases friction at the tooling surface, thus extending the lifetime of the die by decreasing wear. An effective warm forming lubricant must provide sufficient lubricity at elevated temperatures ranging from 25°C to 250°C, sometimes higher. Very few findings have been reported on the use of forming lubricants at elevated temperatures. Effective and optimum lubricants for warm forming of aluminum alloy sheet are only just beginning to become available.

Doege et al. (1978) investigated the effects of warm lubricants on physical isolation, reduction of friction, cooling, and so on, during hot and warm forming processes. As a part of their studies, each lubricant's friction coefficient was determined as a function of the temperature of the billets, the tools, and the tool material by measuring the horizontal and vertical forces during heading. They showed that the coefficient of friction is higher at temperatures below 100°C than it is between 140 and 220°C. The low temperature behaviour is attributed to the water contained within the lubricant which does not evaporate immediately, preventing build-up of a lubricating film. At higher temperatures between 220 and 300 ° C, the coefficient of friction rises quickly, suggesting the wetting power of the lubricant is insufficient to handle forming activities in this range of temperature.

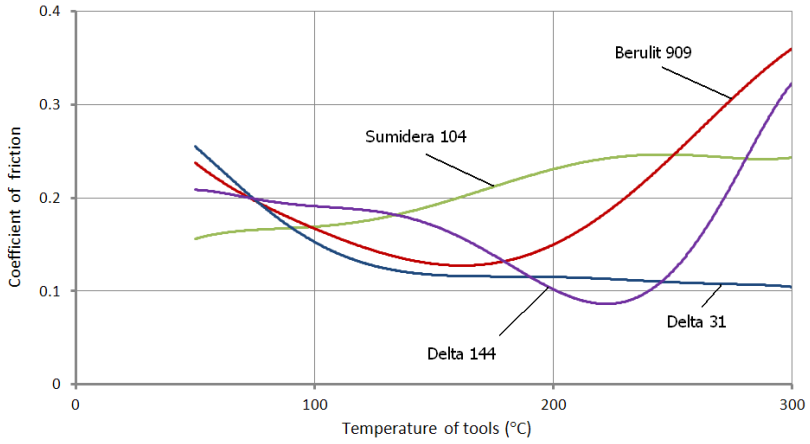

Figure 1.17 Influence of tool temperature on the coefficient of friction, for tool material X32CrMoV33 [Doege et al., 1978]

Naka et al. (1999, 2001) used both wax type lubricants and thin steel sheet to protect the aluminum blank in LDR experiments. However, they did not report on the effectiveness of the lubrication techniques used in their experiments.

While some researchers have measured the friction coefficient of the lubricant at room temperature (for example van den Boogaard et al., 2006), some warm forming studies do not report the lubricant used in the experiments or the friction model used to develop numerical simulations (Abedrabbo et al., 2006a, 2006b, 2007). Van den Boogaard et al. (2006) used a coefficient of friction of 0.06 below 90°C, 0.12 above 110°C, and linearly interpolated between 90°C and 110°C.

Palumbo et al. (2007) used the same Bergstrom material model as described by van den Boogaard (2006). They did not measure the coefficient of friction (COF) experimentally; however, they performed a parametric FE study of the effect of friction on warm deep drawing of AA5754-0. In their study, COFs between 0.2 and 0.3 were used for the punch to blank interaction, and COFs between 0.05 and 0.08 were used for the die and blank holder. It was determined that the punch to blank COF has little effect on punch load, while the required punch force increases as the COF increases between the die/blank holder and the blank.

Kaya et al. (2008) performed warm deep drawing experiments on AA1050, AA5754, and AA6016 sheet using PTFE (Teflon) film, a grease with 7.5% boron nitride, and a grease without boron nitride as lubricants. They observed that the Teflon film allowed for a more uniform sheet thickness than the other lubricants. The non-PTFE lubricants also generated smoke and left a burnt residue on the tooling.

Hanna (2009) studied tribological mechanisms during interaction of aluminum sheet with steel tools at high temperature. He showed that the tribological behaviour of AA5083 sheet sliding against a steel tool has a significant impact on the quality of components manufactured with elevated temperatures. He mentioned that adhesion of aluminum to forming tools is of concern since it directly influences the quality of the formed part.

1.8 Summary

The warm forming process has been used widely for the production of metal components; however, this forming technology requires further development prior to increased adoption by industry. In particular, methods to predict formability limits and failure are required for process design. In addition, previously published literature indicates that an accurate constitutive model requires both an accurate hardening law, accounting for thermal softening and rate-dependant hardening, and an appropriate anisotropic yield function. Aluminum alloys exhibit a complex dependence of flow stress on temperature and strain-rate. Reported constitutive fitting exercises have identified the Bergstrom (van den Boogaard et al., 2006; Bagheriasl et al., 2011a,b; Ghavam et al., 2011) or NES (Kurukiri et al., 2009) models as appropriate material models for use in numerical simulation of warm forming. In addition to capturing material hardening response, it is necessary to incorporate an advanced material yield surface function to capture the crystallographic nature of yielding in FCC aluminum alloys as well as R-values which control thinning in textured sheet materials. The Barlat-YLD2000 (Barlat et al., 2003) yield surface function has been shown to accurately describe the anisotropic material behaviour of aluminum alloy sheet. Many studies have reported application of the NES/Bergstrom model and the Barlat-YLD2000 yield surface function separately; however, there still exists a need to implement the Barlat-YLD2000 yield surface in conjunction with the Bergstrom constitutive model.

To facilitate widespread application of the warm forming process for manufacture of aluminum alloy sheet, a reliable method to determine forming limits at elevated temperature is required. The experimental evaluation of FLDs for sheet metal is time consuming and demands expensive equipment. The experimental work could be omitted in some cases by predicting FLDs with numerical simulations. A few studies have reported numerical investigation of aluminum alloy sheet forming limits at elevated temperatures; however, a thorough study of forming limits and a proper numerical model to capture warm formability behaviour is not available as yet.

1.9 Current work

The current research considers 3000 series aluminum alloys, which are non-heat treatable with an ultimate tensile strength of 110 to 280 MPa. A brazing sheet was considered that consisted of a modified AA3003 core with an AA4045 clad layer, fabricated using a co-casting technique. This sheet material, hereafter referred to as AA3003 brazing sheet, was studied in the O temper condition. The material is used for fabrication of heat exchangers, which represents a major application of the current research.

The overarching objective of the current research is to develop an understanding of the formability of the AA3003 brazing sheet at elevated temperatures and to develop numerical models that accurately predict the warm formability of this material. The literature review presented in this chapter revealed that very little information exists regarding the failure of aluminum alloy sheet in this form during forming at elevated temperatures. Thus, the specific objectives of this research are to:

- develop an accurate constitutive model of the deformation of AA3003 brazing sheet accounting for rate sensitivity, thermal softening and yield anisotropy; and,
- develop an accurate model of the formability of AA3003 brazing sheet at elevated temperature.

The balance of this thesis is organized as follows. Chapter 2 presents results from characterization of the constitutive behavior of the AA3003 material considered in this research and the constitutive model parameter identification effort. The uniaxial tensile stress-strain data was used to perform fitting of the Bergstrom (1982) constitutive model to this tensile data and to identify yield surface parameters required for the Barlat (2003) yield surface. Also the coefficients of friction for two lubricants used in forming experiments (Teflon Sheet and Dasco cast), were measured using twist compression tests.

The experimental characterization of the formability behaviour of AA3003 aluminum alloy sheet at elevated temperatures is presented in chapter 3, which describes the experimental procedure performed to develop strain-based FLDs at elevated temperatures. These FLDs were used later to predict the failure of the material studied using the developed numerical models. The failure knowledge that is the FLD at elevated temperature is needed by industries that form this alloy.

A second key element of this research was development of an accurate constitutive model of the deformation of AA3003 aluminum alloy sheet, accounting for rate sensitivity, thermal softening and yield anisotropy. This requirement motivated the development of a numerical model that incorporates a proper yield surface and flow stress functions for aluminum alloy sheets at elevated temperatures. Since none of the constitutive models implemented within current finite element codes were able to accurately model the material response of aluminum alloy sheet at elevated temperatures, a user defined material subroutine was developed, as described in Chapter 4. While the aforementioned studies have reported the application of the NES/Bergstrom model (van den Boogaard et al., 2006) and the Barlat-2000 yield surface separately; the current work considers the novel implementation of the Barlat YLD2000 yield surface (Barlat et al., 2003) in conjunction with the Bergstrom hardening model to accurately model aluminum alloy sheet during warm forming as described in this chapter. Tension test and stretch forming data is used to validate the predictions of the developed material model. Measured stress-strain curves were used to fit the material parameters. Numerical models of the tensile test were used to investigate whether the material model is capable of reproducing the stress-strain data. As the second validation, numerical models of stretch forming were compared against the measured data and the accuracy of models was investigated.

Chapters 5 and 6, describe the experimental and numerical study of two warm forming applications: warm deep drawing of circular cups, and warm forming of a cup shape feature part used in auto heat exchanger assemblies. In both cases, predictions are compared against experimental results.

Finally, conclusions and recommendations are presented in the last chapter.

2 Characterization of the Material Constitutive Response

This chapter presents results from characterization of the constitutive behaviour of the AA3003 sheet material considered in this research and the constitutive model parameter identification effort. The uniaxial tensile stress-strain data was taken from work presented by McKinley (2010) that was performed at the Novelis Kingston R&D Center (2008). As part of the current research, this data was used to perform fitting of the Bergstrom (1982) constitutive model to this tensile data in order to capture material strain rate sensitivity and thermal softening. The data was also used to identify yield surface parameters required for the Barlat (2003) yield surface. These parameters were determined as a function of temperature for use in subsequent simulation of warm forming behavior.

2.1 Uniaxial Tensile Characterization

Novelis Inc. (2008) provided experimental tensile data at five temperature levels, room temperature, 100°C, 150°C, 200°C, and 250°C, and at five strain rates, 0.0007, 0.0035, 0.007, 0.035, and $0.07s^{-1}$ (25 experimental conditions in total). The dimensions of the tensile test specimen are shown in Figure 2.1. The total gauge length is 56mm, the specimen width is 12.5mm and the thickness is 0.5mm.

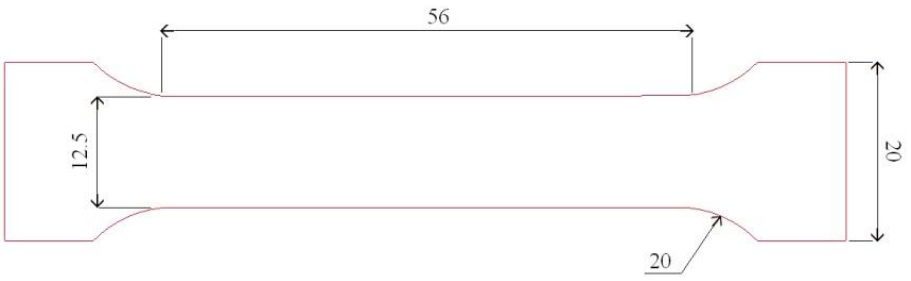

Figure 2.1 Geometry of tensile test sample (all dimensions are in mm)

Photographs of tensile samples at 250°C and different deformations, provided by Novelis Inc., are shown in Figure 2.2. Figure 2.3 shows the measured stress-strain data for the range of temperatures and strain rates considered. At room temperature, this AA3003 aluminum alloy shows almost no rate sensitivity. At elevated temperatures, the material shows a strong

degree of thermal softening, but also pronounced strain rate sensitivity. The strain-rate sensitivity becomes important at temperatures above 150°C. The strain-rate affects both yield stress and total elongation. By increasing the strain-rate, the yield stress increases at 200°C and 250°C, while the total elongation decreases. The elongation is also seen to increase dramatically at higher temperatures. The post-uniform elongation is much larger at temperatures above 200°C than at lower temperatures. The total strain at failure is approximately 25% at room temperature and 100°C, while the total elongation increases by 30%-50% at 200°C and 40%-60% at 250°C, depending upon the strain rate. Much of this increase is attributed to the increased rate sensitivity which in turn promotes high levels of diffuse necking at high temperatures compared to room temperature conditions.

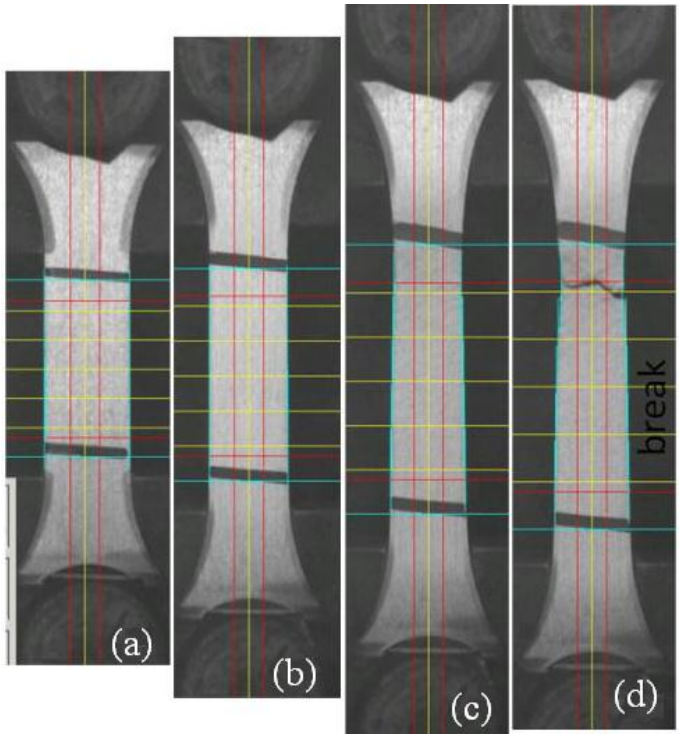

Figure 2.2 Longintudinal ASTM standard tensile test at 250°C before deformation (a), at 22% strain (b), at 54% strain(c), and at failure (d) [McKinley, 2010]

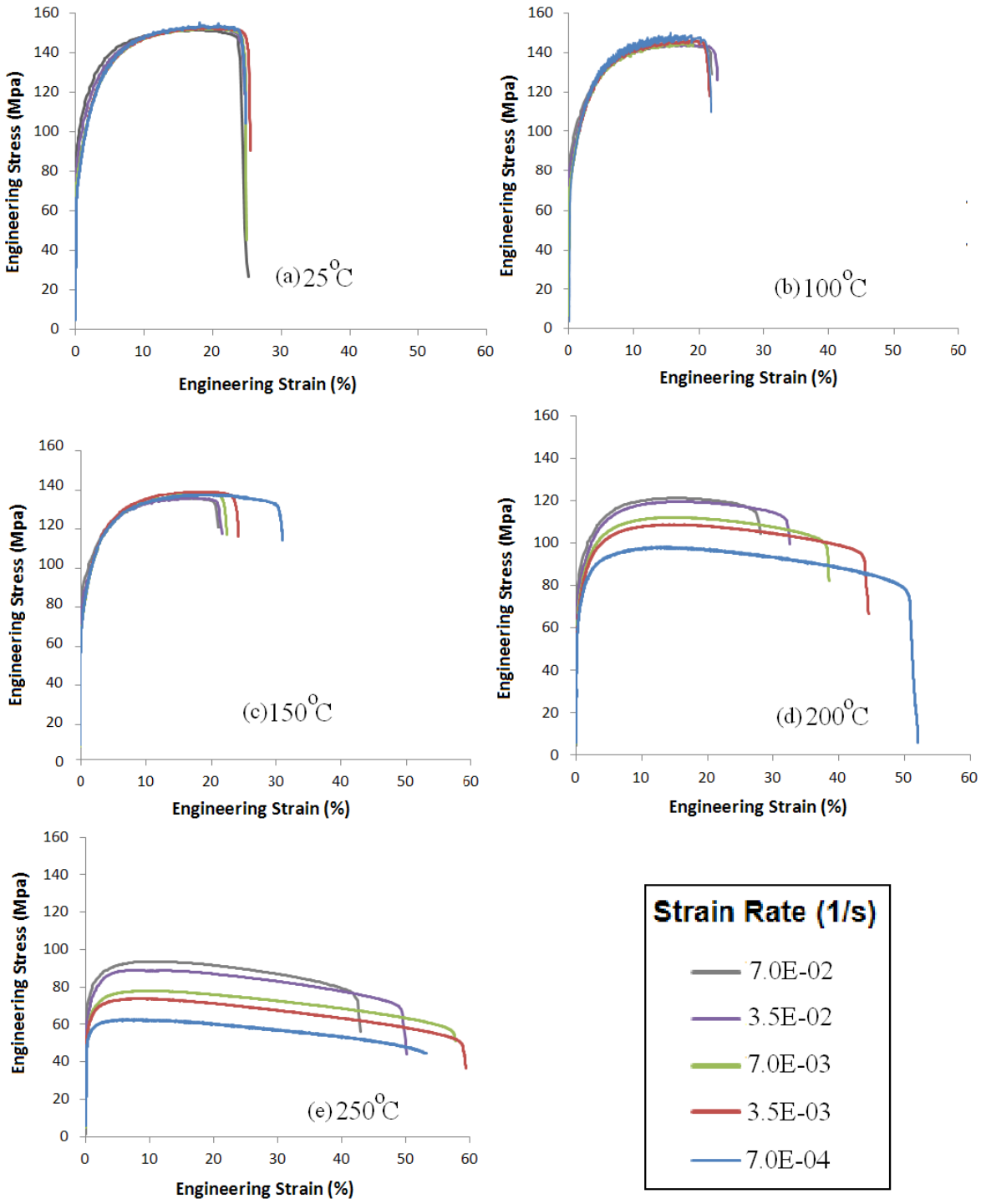

Figure 2.3 Engineering stress-strain curves of 0.5mm AA3003 performed at room temperature (a), 100°C (b), 150°C (c), 200°C (d), and 250°C (e)

The yield stress and R-values, which are defined as the ratio of the width strain, $\varepsilon_w = ln(w/w_0)$ to the thickness strain, $\varepsilon_t = ln(t/t_0)$ under uniaxial tension, in the longitudinal, transverse and diagonal directions, are shown in Table 2.1. The R-values are plotted *versus* test temperature in Figure 2.4 Anisotropy in a sheet material is determined by the grain structure imparted by the rolling process. There is significant anisotropy in the R-values, however there is no clear temperature dependent trend; in fact, the variation in R-values with temperature is low. The diagonal R-values, R_{45}, show the most variation with temperature from 0.741 to 0.779. A higher R-value indicates higher resistance to thinning, which is beneficial in forming. The R-values in the transverse direction, are the lowest and denote that the material experiences higher levels of thinning under transverse loading compared to loading in the rolling direction.

Table 2.1 Yield stresses and R-values at different temperatures for AA3003

Temperature	Yield Stress (MPa)				R-values		
C	σ_0	σ_{90}	σ_{45}	σ_b	R_0	R_{90}	R_{45}
25	78.66	71.29	75.87	73.58	0.694	0.5627	0.758
100	74.73	72.55	73.75	73.15	0.7122	0.5786	0.7642
150	69.77	69.1	70.27	69.685	0.7065	0.5807	0.7786
200	65.02	61.92	62.49	62.205	0.6981	0.6022	0.7584
250	52.8	52	51.4	51.7	0.6871	0.5906	0.7407

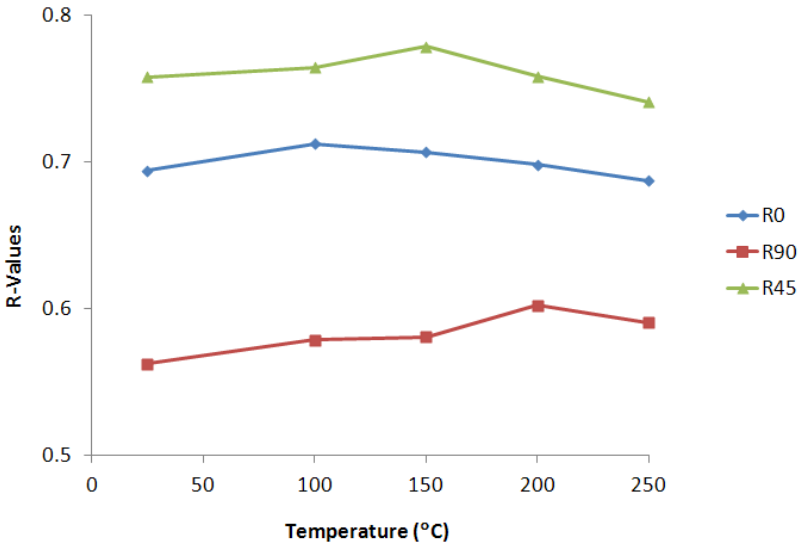

Figure 2.4 R-values versus temperature for AA3003-O

2.2 Flow Stress and Uniaxial Stress-Strain Response

An appropriate description of flow stress and work hardening of aluminum alloys, considering both temperature and strain rate dependency during deformation at elevated temperatures, is needed to support simulation of warm forming processes. Traditional, or phenomenological, models describe flow stress in terms of mathematical equations such as power laws, where experimental test data is fit to functions of strain that contain many empirical constants. These models often embody little or no material physics and the parameters are not defined according to physical processes or phenomena; however, because they have low computational requirements, they are used extensively in FEM codes. These models can provide excellent fits for a given deformation condition, but only in the experimental data range. A well-known phenomenological model based on the Nadai (1950) hardening law with strain rate and temperature effects was described by Van den Boogaard and Huétink, 2006; and Abedrabbo et al., 2007.

Physics-based models mathematically express the underlying science governing plastic deformation and may have a wider applicability. These models indirectly consider microstructure evolution and account for the effects of micro level processes on the macro level. Two well-known examples include the dislocation density-based material models developed by Bergström (1969, 1983) and Nes (1998). Both models assume similar basic concepts about dislocation density evolution processes, specifically with regard to storage and dynamic recovery processes. They have been used extensively in numerical studies and are considered appropriate for modelling aluminum alloys at elevated temperatures.

2.2.1 Bergstrom Constitutive Model

Given the strong coupled effect of temperature and strain rate on constitutive response, it was considered important to utilize a material model that captures these effects in simulations of warm forming operations. A previous fitting exercise by McKinley et al. (2009) using five different constitutive models; Zerilli-Armstrong, modified Johnson-Cook, Voce-Kocks, Bergstrom, and modified Voce hardening law, showed that only the Bergstrom and the modified Voce models were able to capture the temperature and strain rate dependent behaviour of the material accurately, with the Bergstrom being the preferred model as it was able to predict the temperature dependence of rate effects. In the current work, the flow stress

of aluminum alloy sheet is described by the physically-based Bergstrom (1969, 1983) model which takes into account both the evolution of dislocation density and dynamic recovery. In this model, flow stress ($\bar{\sigma}$) is composed of a simple temperature dependent term (σ_0), a dynamic stress term (σ^*) that depends on both strain rate and temperature, and finally by a work hardening term (σ_w) that depends on both dislocation density and temperature $\sigma_w(\rho, T)$. Flow stress is expressed by

$$\bar{\sigma} = \sigma_0(T) + \sigma^*(\dot{\varepsilon}, T) + \sigma_w(\rho, T) \tag{2.1}$$

The evolution of dislocation density ρ is responsible for work hardening. Also, the dynamic recovery term reflects both annihilation and remobilization of dislocations. Finally the flow stress can be expressed by

$$\bar{\sigma} = \left(1 - C_T \exp\left(-\frac{T_1}{T}\right)\right)\left(\sigma_0 + \alpha G_{ref} b\sqrt{\rho}\right) \tag{2.2}$$

where C_T and T_1 are fitting parameters, G_{ref} is the reference shear modulus, α is a scaling parameter of order 1, b is the Burgers vector ($2.857 \times 10^{-10} m$ (van den Boogaard, 2006), σ_0 is the strain rate independent term, and finally ρ is the dislocation density which evolves during the deformation from its initial value, as described by

$$\frac{d\rho}{d\varepsilon} = U(\rho) - \Omega(\dot{\varepsilon}, T)\rho \tag{2.3}$$

The function U, which describes the storage of mobile dislocations, and Ω, which describes the dynamic recovery due to remobilization and annihilation, are defined as follows

$$\begin{aligned} U &= U_0 \rho \\ \Omega &= \Omega_0 + C \exp\left(-\frac{mQ_v}{RT}\right)\dot{\varepsilon}^{-m} \end{aligned} \tag{2.4}$$

where R is the gas constant and Q_v is the activation energy for vacancy migration.

2.2.2 Constitutive Parameter Identification

The measured uniaxial stress-strain data was used to fit the Berstrom constitutive model parameters, described above. In the current work, a MATLAB parameter optimization program was developed to fit the material data using a least squares approximation. Typically, the code converts engineering stress-strain curves into true stress-strain curves, and then fits the constitutive model parameters by finding the local values of parameters that minimize a least squares error function. However, only engineering curves are presented here in order to illustrate the onset of necking (the ultimate tensile strength) and post uniform elongation.

In the case of the Bergström model (Bergstrom, 1982), some parameters can be selected beforehand; for example, the initial dislocation density (ρ_0) for aluminum alloys, the magnitude of the Burgers vector, the scaling parameter, α, and the shear modulus at room temperature (μ_0) were taken directly from the literature (van den Boogaard et al., 2006). The Bergstrom fit parameters are listed in Table 2.2. Figure 2.5 shows the predicted flow stress curves at different temperatures based on these parameters, which agree well with measured data for post-uniform stresses. As can be seen, the material exhibits negligible rate sensitivity at lower temperatures, but strong strain rate sensitivity and material softening at elevated temperatures.

Table 2.2 Bergstrom parameters

σ_0 = 71.5 MPa	C = 334220	Ω_0 = 67.1755	C_T = 198.62
μ_0 = 26354 MPa	m = 0.4239	Q_v =1.0917 $\times 10^5$ J/mol	T_1 = 3,418.8 K
b = 2.857 $\times 10^{-10}$ m	U_0 = 6.9492 $\times 10^8$ m-1	ρ_0 = 10 $\times 10^{11}$ m-2	α=1

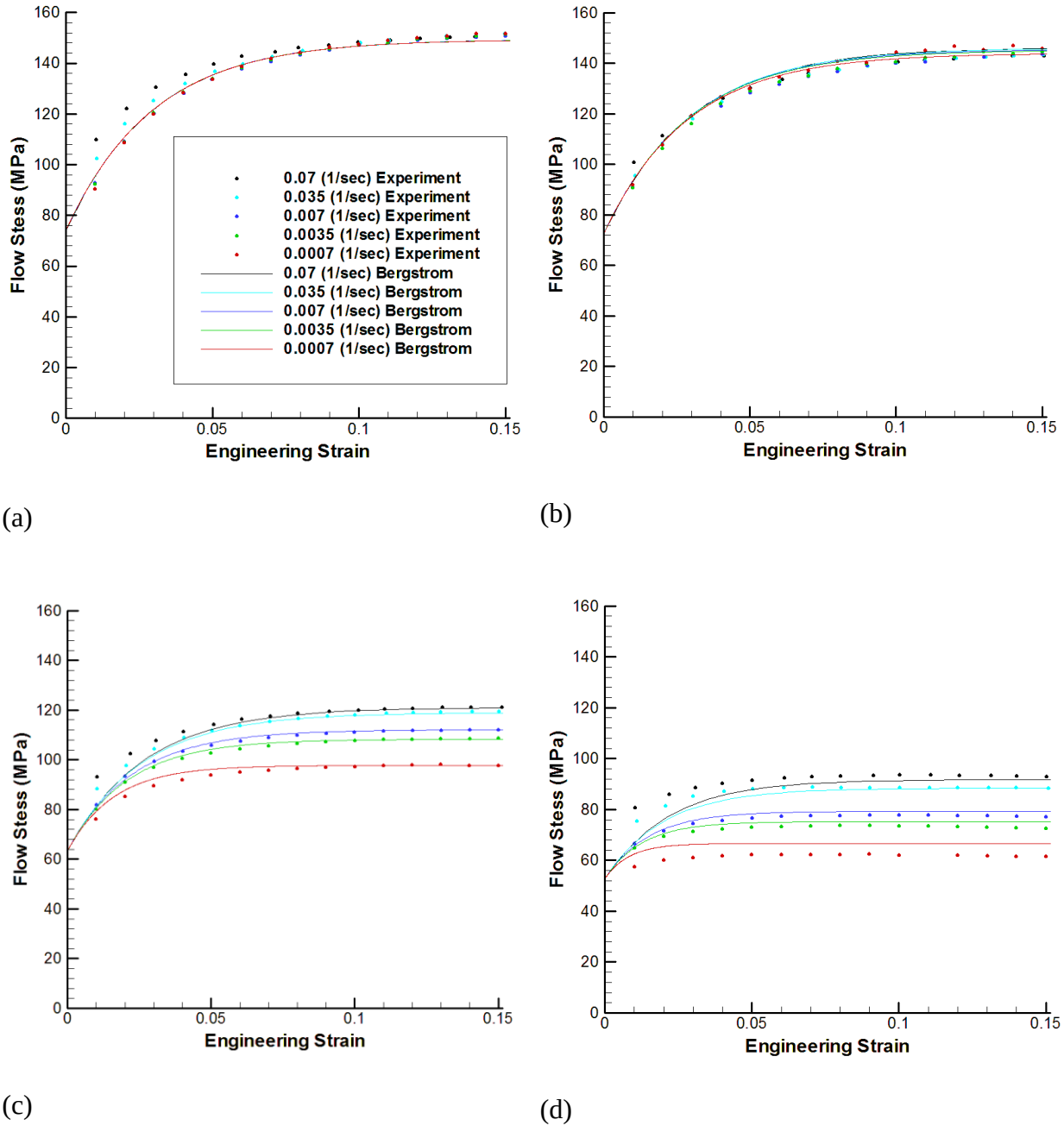

Figure 2.5 Stress-strain curves using fit parameters vs. experimental results for different temperatures and strain rates. (a) 25°C, (b) 100°C, (c) 200°C and (d) 250°C

2.3 Yield Surface Constitutive Parameters

A yield function must be defined for numerical computation of material behaviour during the forming process. The yield function ($\emptyset$) depends on the stress tensor and the deformation history. The equation ($\emptyset = 0$) defines the yield surface. If the stress state lies inside the yield surface, the material undergoes elastic deformation; however, if the stress state lies on the yield surface, plastic deformation may be observed. The rate of plastic deformation is perpendicular to the yield surface, such that $\Delta\varepsilon^p = \dot{\lambda}\frac{\partial\varphi}{\partial\sigma}$, where $\dot{\lambda}$ is a consistency parameter. Several factors can alter the size, position and shape of the yield surface, including plastic deformation and temperature changes. A change in size can be modelled with isotropic hardening or softening if the centre of the yield surface and the shape remain constant. This is the most commonly used hardening model. For isotropic hardening, only one history parameter is required, usually the equivalent plastic strain.

2.3.1 Barlat YLD2000

In the current work, the Barlat (2003) yield function is used to capture the anisotropic yield behavior of the AA3003 alloy. This anisotropic yield function for plane stress in the x-y plane in general format is expressed by Barlat (2003) as

$$\emptyset = \emptyset' + \emptyset'' = 2\bar{\sigma}^a \tag{2.5}$$

where

$$\emptyset' = \left|X_1' - X_2'\right|^a, \emptyset'' = \left|2X_2'' + X_1''\right|^a + \left|2X_1'' + X_2''\right|^a \tag{2.6}$$

with $a = 8$ for FCC materials. The $X_{1,2}'$ and $X_{1,2}''$ are the principal values of the linear transformations of the stress deviators X' and X'', which are defined as

$$\begin{bmatrix} X_{xx}' \\ X_{yy}' \\ X_{xy}' \end{bmatrix} = \begin{bmatrix} C_{11}' & C_{12}' & 0 \\ C_{21}' & C_{22}' & 0 \\ 0 & 0 & C_{66}' \end{bmatrix} \begin{bmatrix} S_{xx} \\ S_{yy} \\ S_{xy} \end{bmatrix} \text{ and} \tag{2.7}$$

$$\begin{bmatrix} X''_{xx} \\ X''_{yy} \\ X''_{xy} \end{bmatrix} = \begin{bmatrix} C''_{11} & C''_{12} & 0 \\ C''_{21} & C''_{22} & 0 \\ 0 & 0 & C'_{66} \end{bmatrix} \begin{bmatrix} S_{xx} \\ S_{yy} \\ S_{xy} \end{bmatrix}$$

where C' and C" are linear transformation matrices, S_{xx}, S_{yy}, S_{xy} are the components of the deviatoric stress tensor, and x and y represent the rolling and transverse directions of the sheet, respectively. The transformation can also be applied on the stress tensor σ as follows

$$\begin{aligned} X' &= C'S = C'T\sigma = L'\sigma \\ X'' &= C''S = C''T\sigma = L''\sigma \end{aligned} \tag{2.8}$$

where the transformation matrix, T, is

$$T = \begin{bmatrix} 2/3 & -1/3 & 0 \\ -1/3 & 2/3 & 0 \\ 0 & 0 & 1 \end{bmatrix} \tag{2.9}$$

As a result L' and L" can be expressed as

$$\begin{bmatrix} L'_{11} \\ L'_{12} \\ L'_{21} \\ L'_{22} \\ L'_{66} \end{bmatrix} = \begin{bmatrix} 2/3 & 0 & 0 \\ -1/3 & 0 & 0 \\ 0 & -1/3 & 0 \\ 0 & 2/3 & 0 \\ 0 & 0 & 1 \end{bmatrix} \begin{bmatrix} \alpha_1 \\ \alpha_2 \\ \alpha_7 \end{bmatrix} \text{ and}$$

$$\begin{bmatrix} L''_{11} \\ L''_{12} \\ L''_{21} \\ L''_{22} \\ L''_{66} \end{bmatrix} = \begin{bmatrix} -2 & 2 & 8 & -2 & 0 \\ 1 & -4 & -4 & 4 & 0 \\ 4 & -4 & -4 & 1 & 0 \\ -2 & 8 & 2 & -2 & 0 \\ 0 & 0 & 0 & 0 & 9 \end{bmatrix} \begin{bmatrix} \alpha_3 \\ \alpha_4 \\ \alpha_5 \\ \alpha_6 \\ \alpha_8 \end{bmatrix} \tag{2.10}$$

The independent coefficients, $\alpha_i, i = 1 - 8$, are all that is needed to describe the anisotropic behaviour of a material - they reduce to 1 in the isotropic case. Seven coefficients can be determined using measured data, namely $\sigma_0, \sigma_{45}, \sigma_{90}, \sigma_b, r_0, r_{45}$ and r_{90} (the strength and r-values in the sheet directions and biaxial yield strength, σ_b). The eighth coefficient can be determined by assuming $C''_{12} = C''_{21}$ or $L''_{12} = L''_{21}$, or by using additional input data such as

the ratio $r_b = \dot{\varepsilon}_{xx}/\dot{\varepsilon}_{yy}$, which characterizes the slope of the yield surface in balanced biaxial tension ($\sigma_{xx} = \sigma_{yy}$). This parameter, r_b, is similar to the r-value obtained in uniaxial tension, and can be determined by experimental measurement, calculation from another yield function such as Yld96 (Barlat et al., 1989), or computation from a polycrystal model if the crystallographic texture of the material is known. The yield function coefficients are calculated with a Newton–Raphson non-linear solver, as described by Barlat et al. (2003).

For the material model to account for changes in temperature, the anisotropy coefficients must be expressed as functions of temperatures; for example, $\emptyset = \bar{\sigma}(\sigma, T)$.

2.3.2 Yield Surface Parameter identification

In order to calculate the eight α_i anisotropy parameters, yield stress (σ_0, σ_{90}, σ_{45}) and r-values (r_0, r_{90}, r_b) in the longitudinal, transverse and diagonal directions, as well as the biaxial yield stress (σ_b), are required (Yoon et al., 2004). Since biaxial data was unavailable, σ_b was set equal to $(\sigma_{90} + \sigma_{45})/2$, following the approach of Abedrabbo et al. (2006) for the same material as in this research, but a different temper condition (AA3003-H111). Using these tabulated yield stresses and r-values (Table 2.1), one can find the eight anisotropy parameters at different temperatures (Table 2.3).

Table 2.3 Anisotropy parameters at different temperatures

C	α_1	α_2	$\alpha_3 = \alpha_6$	α_4	α_5	α_7	α_8
25	0.86346	1.13930	0.94163	1.09380	1.01080	1.01010	1.10150
100	0.96053	0.99171	0.96707	1.04170	1.00990	0.99095	1.05900
150	0.98445	0.94841	0.95792	1.02420	1.00680	0.97441	1.02210
200	0.92524	1.04990	0.98358	1.05790	1.01610	1.01400	1.10640
250	0.97386	0.97141	0.99096	1.03420	1.01470	1.00050	1.08640
Average	0.94151	1.02015	0.96823	1.05036	1.01166	0.99799	1.07508
Std. Dev.	0.04901	0.07651	0.01980	0.02722	0.00375	0.01593	0.03490

As can be seen from the table, variation of the α_i parameters with temperature is quite low. The strongest temperature dependency is observed for α_2, which varies in magnitude by 0.191 or 17%. In order to capture the dependence of the yield function shape on temperature, the simulations utilized fourth order functions (Table 2.4) that were fit to the experimental variation of α_i with respect to temperature.

Table 2.4 Temperature dependent anisotropy parameters for Barlat YLD 2000

$\alpha_1 = 1.39\times10^{-9}T^4 - 7.17\times10^{-7}T^3 + 0.0001152T^2 - 0.005536T + 0.9405$
$\alpha_2 = -2.44\times10^{-9}T^4 + 1.27\times10^{-6}T^3 - 0.0002086T^2 + 0.01064T + 0.9847$
$\alpha_3 = -5.98\times10^{-10}T^4 + 3.48\times10^{-7}T^3 - 6.72\times10^{-5}T^2 + 0.004978T + 0.854$
$\alpha_4 = -8.34\times10^{-10}T^4 + 4.39\times10^{-7}T^3 - 7.26\times10^{-5}T^2 + 0.003725T + 1.04$
$\alpha_5 = -2.10\times10^{-10}T^4 + 1.16\times10^{-7}T^3 - 2.09\times10^{-5}T^2 + 0.001359T + 0.9882$
$\alpha_6 = \alpha_3$
$\alpha_7 = -9.48\times10^{-10}T^4 + 5.18\times10^{-7}T^3 - 9.15\times10^{-5}T^2 + 0.00564T + 0.9185$
$\alpha_8 = -1.99\times10^{-9}T^4 + 1.09\times10^{-6}T^3 - 0.0001931T^2 + 0.0119T + 0.9084$

Figure 2.6 shows the Barlat YLD2000 yield criterion for AA3003 at different temperatures based on the anisotropy coefficients in Table 2.4. In Figure 2.6(a) the stresses are normalized with respect to σ0, the rolling direction yield stress for each temperature. An isotropic von Mises yield surface is plotted as well for comparison purposes. As expected, the quadratic von Mises yield surface lies outside of the Barlat surface and is isotropic with respect to stress. The plot of the Barlat yield loci exhibits the in-plane anisotropic behaviour of this material, which is stronger at room temperature as seen from the TD yield stress, which is lower than along the RD. As temperature increases, the degree of in-plane anisotropy reduces, at least in terms of the yield stresses; although, the difference in the r-values along different sheet orientations does not change significantly (Figure 2.4). Figure 2.6(b) shows the Barlat yield loci as a function of stress without normalization and serves to demonstrate the yield surface contraction with increasing temperature. In Figure 2.6(b), the yield surfaces are plotted for the temperatures at which the r-values and yield stresses are measured (Table 2.1). In Figure 2.6(c), yield surfaces are plotted at additional intermediate (interpolated) temperatures.

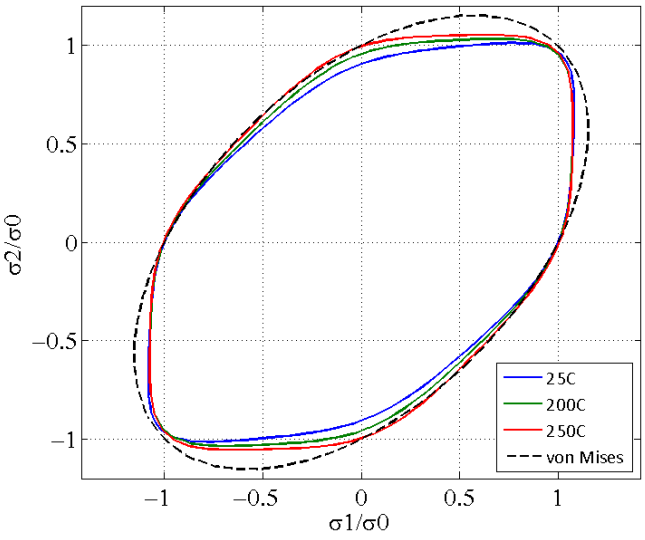

(a)

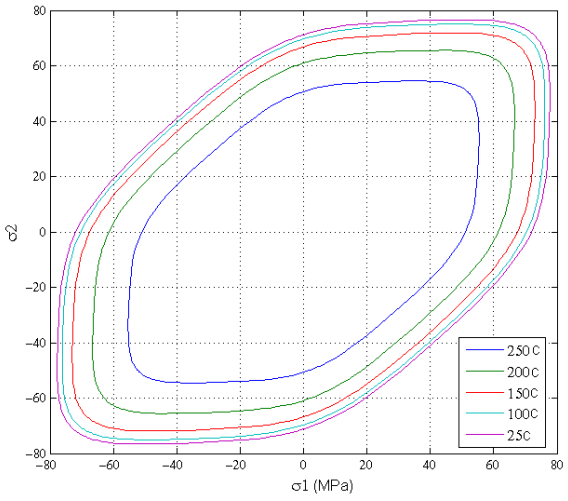

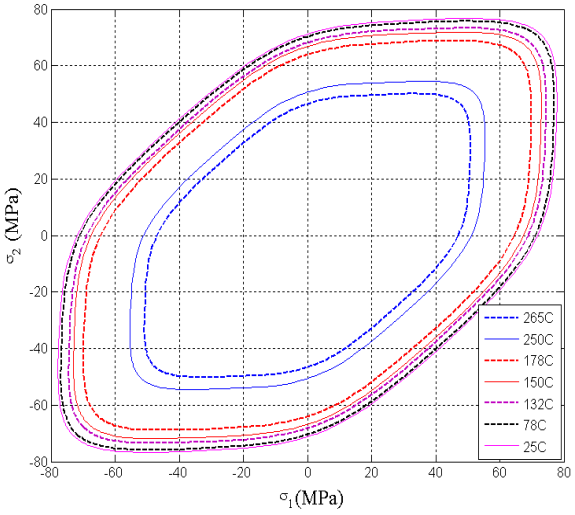

(b) (c)

Figure 2.6 AA3003 Yield surface at different temperatures : (a) normalized by the RD yield stress for each temperature, (b) without normalization at measurement temperature points, and (c) without normalization at temperatures other than measurement points.

2.4 Friction characterization

Friction is an important aspect of metal forming processes and must be accurately modelled in forming simulations. Two lubricants were used for warm forming experiments in the current research: Teflon sheet and Dasco Cast 1200. Dasco Cast 1200 is a water-based siloxane die casting mold lubricant and can be used at elevated temperatures up to 370°C. The coefficients of friction of these lubricants were measured using the twist compression test (TCT).

TCT (Figure 2.7) was developed by Schey (Schey 1990) to replicate the conditions found in metal forming. In fact Twist Compression Test is a tribometer designed to measure friction and evaluate adhesion in metal forming. The TCT is effective because of several critical features; the most important being that the contact pressures can be set to match the process. The TCT apparatus consists of a rotating tool which is pressed against a sample sheet. This test measures the transmitted torque between a rotating annular cylinder and a lubricated flat sheet specimen. The 25mm (1") diameter annular cylinder is driven by a hydraulic motor for smooth delivery of the applied torque at speeds up to 30RPM (38mm/s). The pressure may be adjusted up to 240MPa to best duplicate the tribological conditions of the metal forming process being studied. Data is collected electronically and the coefficient of friction is calculated from the ratio of transmitted torque to applied pressure. The twist compression test is well suited for metal forming because it can combine high interface pressures with a large sliding distance. The control variables in the TCT are interface pressure and sliding velocity.

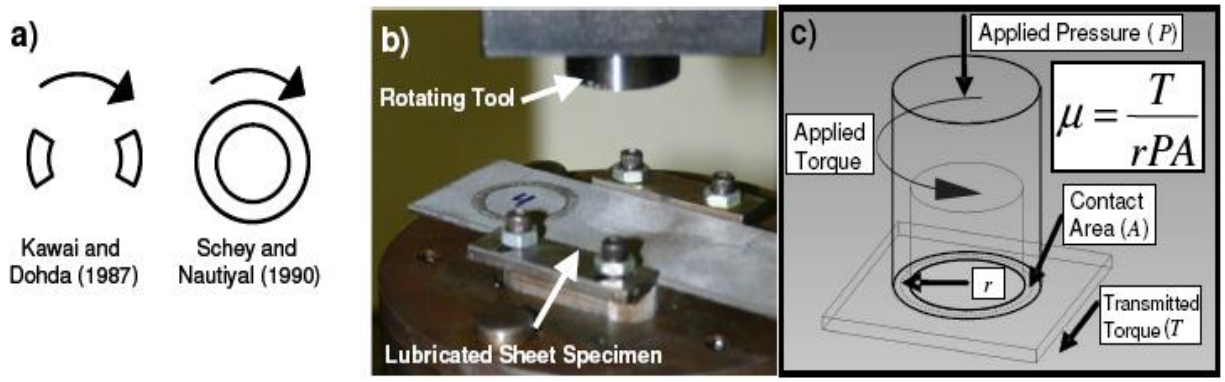

Figure 2.7 Twist compression test (a) Contact surface, (b) test apparatus, (c) Schematic diagram (Bardelcik 2006)

Both Teflon sheet and Dasco Cast lubricants were tested at room temperature as the current TCT apparatus is not designed for elevated temperatures. To use Dasco Cast at room temperature as a lubricant, it was sprayed on a pre-heated sample and then it was cooled down at room temperature to form a thin layer on the sample. It should be noted that the Dasco Cast is designed for elevated temperature usage and it does not adhere to the sample surface at room temperature.

Figure 2.8 shows the coefficient of friction as a function of time for a sample tested at a velocity of 1.6mm/s (1.2rpm) and with a contact pressure of 3.5MPa (500 psi) as an example. The figure shows that the coefficient of friction approaches a maximum value of 0.105 very fast and then it decreases and fluctuates around 0.075. Therefore the coefficient of static and dynamic friction can be obtained as 0.105 and 0.08 for the applied velocity and pressure.

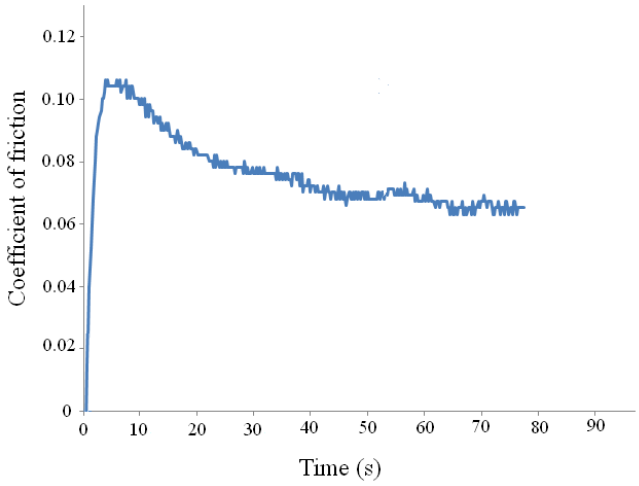

Figure 2.8 Test result for Dasco Cast by applying a velocity of 8mm/s (6rpm) and contact pressure of 3.5MPa (500 psi)

Each lubricant was tested at three sliding speeds; 1.6mm/s (1.2 rpm), 8mm/s (6.0 rpm), and 40mm/s (30 rpm). Three levels of contact pressure were applied for each sliding velocity; 3.5MPa (500psi), 7.0MPa (1000psi) and 10.5MPa (2000psi). Figure 2.9 displays the measured coefficient of friction for all combinations of contact pressure and sliding velocity. As seen, the Teflon sheet shows no sensitivity to sliding velocity and contact pressure. The average values of all measured COFs for Teflon sheet is 0.043 which is plotted as horizontal dashed line in Figure 2.9, Dasco Cast shows a higher level of sensitivity to sliding velocity. This can be a result of erosion of the lubricant layer at higher velocities. The average value of

measured COF at 1.6mm/s and 8.0mm/s sliding velocities is 0.080. Most forming experiments performed in this research consider a forming speed of 1.6mm/s and 8.0mm/s, therefore constant values of 0.043 and 0.080 based on TCT experiments at room temperature are used later in room temperature and elevated temperature numerical models.

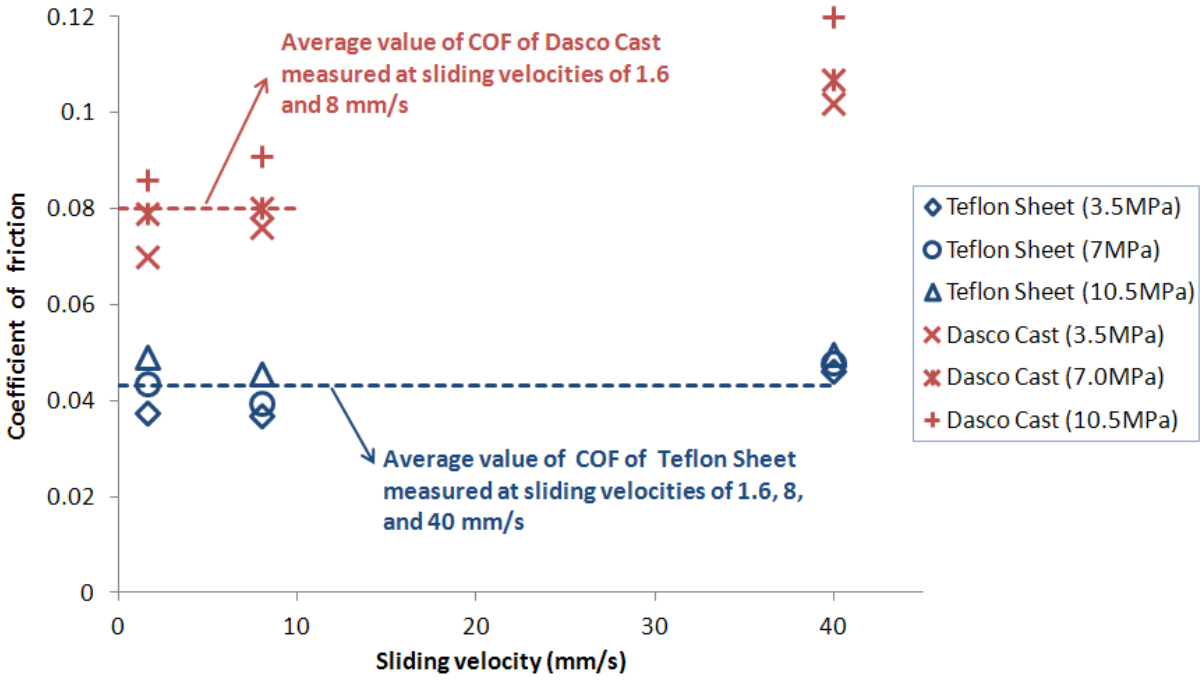

Figure 2.9 TCT results for Dasco Cast and Teflon Sheet, sliding velocities of 1.6, 8, and 40mm/s and contact pressure of 3.5, 7.0, and 10.5MPa. Horizontal lines show the average values of measured coefficients of friction for each lubricant

3 Development of forming limit diagrams at elevated temperatures

Several experimental test methods have been devised to characterize the formability of the sheet metal considered in this study. The most important concern while choosing an experimental characterization method is its applicability to manufacturing situations. More basic tests, such as the tension test and other in-plane forming tests, correlate poorly with manufacturing performance. So-called simulation experiments, on the other hand, have potential to correlate well with production data since they take into account the nature of the tooling/sheet contact interaction and therefore introduce process conditions that often determine success or failure. Common simulation experiments include: the limiting dome height (LDH), stretch-bend, and hole-expansion tests.

3.1 Forming limit diagrams at elevated temperatures

In the current work, FLDs were obtained experimentally at elevated temperatures and different forming speeds using digital image correlation analysis and standard LDH experiments. The test procedure and strain measurement techniques used in FLD development are explained below.

3.1.1 Experimental setup

The LDH test is a standard formability characterization method used for sheet metals (Section 1.3). In order to characterize the formability of aluminum alloys at elevated temperature, a warm tooling set was designed and fabricated to accommodate LDH experiments performed at temperatures up to 350°C. A schematic of the tooling is shown in Figure 3.1. The tooling is composed of three components: the die, punch, and clamp. The hemispherical punch is 101.6mm (4.0 in) in diameter. Both the clamp and die have flat surfaces with v-shaped lock beads and conforming female dies, as shown in Figure 3.1, and outer diameters of 228.6mm (9.0 in). The die entry profile radius is 6.35mm (0.25 in). The tooling is made of H13 tool steel hardened to 55 Rockwell C. Figure 3.1 also shows the locations of cartridge heaters embedded in the die and blank holder. They each contain four 15.8mm (5/8 in)-diameter, 1000 Watt resistance cartridge heaters. The punch contains six 9.5mm (3/8 in)-diameter, 600 Watt resistance cartridge heaters. Ceramic insulation is used to limit heat transfer between the tooling and the rest of the press.

During experimentation, the warm tooling was mounted on a double acting servo-hydraulic press at the University of Waterloo, shown in Figure 3.2. In order to ensure proper alignment and that the apparatus was properly secured to the moving platens on the press, the tooling was affixed to a die set. The die was held stationary while the punch and blank holder were moved by two hydraulic actuators. Load cells inserted between the actuators and their respective tooling measured the actuator force. The tool displacements were measured with linear variable differential transformers (LVDT).

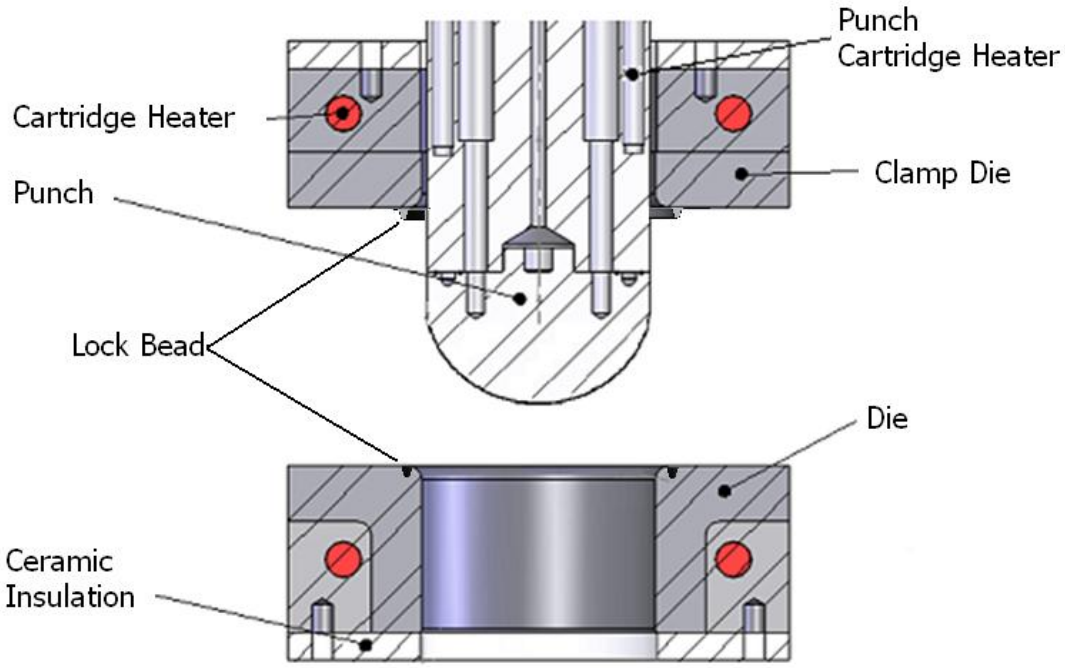

Figure 3.1 Schematic of LDH warm tooling

Figure 3.2 Servo-hydraulic press at the University of Waterloo

The maximum clamp and punch force capacities are 750 kN (168 kip) and 600 kN (134 kip), respectively. Each actuator was controlled by a MTS 407 controller. While the punch was operated under displacement control, the clamp die was operated under load control in which a constant clamping force was maintained during the forming process. The maximum punch velocity was approximately 40 mm/s and the punch stroke was about 120 mm, which is more than sufficient for these experiments. Thermocouples were embedded in the tooling near the tooling surface to allow precise surface temperature control. An external thermocouple was available to measure the temperature of the center of the blank as needed. A custom temperature control system was built at the University of Waterloo. The tooling was designed to maintain any temperature between room temperature and 350°C. The entire system was controlled by a Labview program. A data acquisition card attached to a PC was used to record the experimental data. The force and displacement of the punch and blank holder were recorded, as was the temperature of the die, clamp, and punch. A fourth thermocouple input was included for the optional measurement of the blank centre temperature using the external thermocouple.

3.1.2 Samples

The experiments were designed to produce limit strain data, contributing to the development of FLDs. According to ISO12004, at least five different strain paths are needed to plot an FLD. Different strain paths can be obtained by varying blank geometry (Nakazima et al., 1968). Thus, four specimen geometries were used to produce a range of minor strain in the samples. Figure 3.3 shows the so-called "dog-bone" or draw strain-state specimens, including: (i) 25.4mm (1in) wide dog-bone, (ii) 50.8mm (2in) wide dog-bone, (iii) 76.2mm (3in) wide dog-bone, and (iv) 203.2 x 203.2 mm (8in×8in) biaxial stretch specimen. Sample dimensions were designed for easy alignment and centering on the die. Figure 3.4 shows the 25.4mm wide dog-bone sample dimensions when placed on the die, as well as the position of the lock bead and inner and outer radii of the die. The sample can be properly centered on the die by aligning the four corners of the sample on the die's outer radius. Three-inch wide dog-bone samples (geometry iii) were used as plane strain specimens (the plane strain condition was experimentally observed by measuring the minor strain to be approximately zero). Friction limits the strain distribution in the course of stretching; thus, a Teflon sheet lubricant was inserted between the punch and test specimen surfaces during forming. In order to obtain the fifth strain path, as required in FLD development, 203.2mm x 203.2mm samples were used without lubricant.

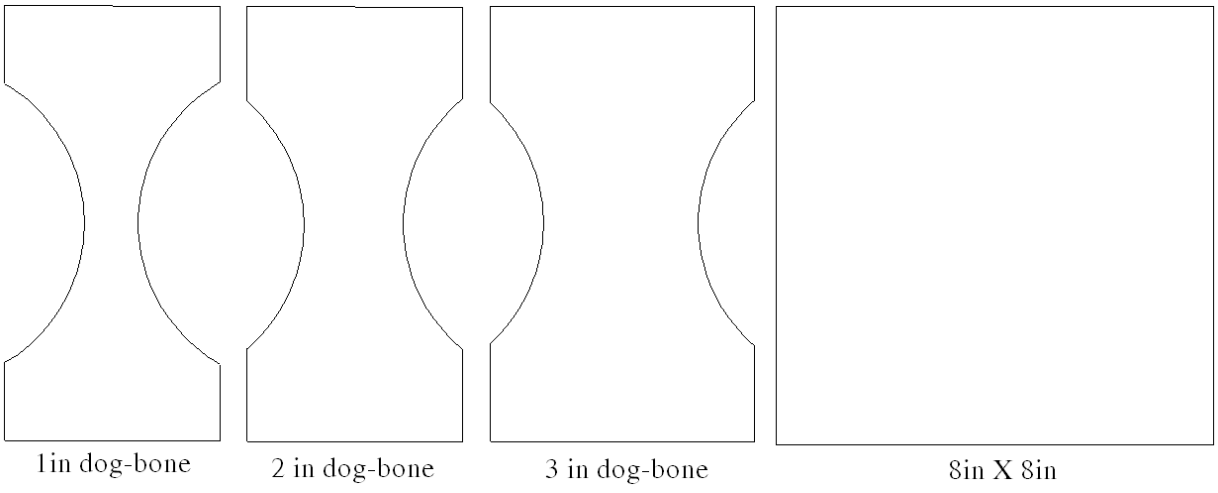

Figure 3.3 LDH specimen geometries

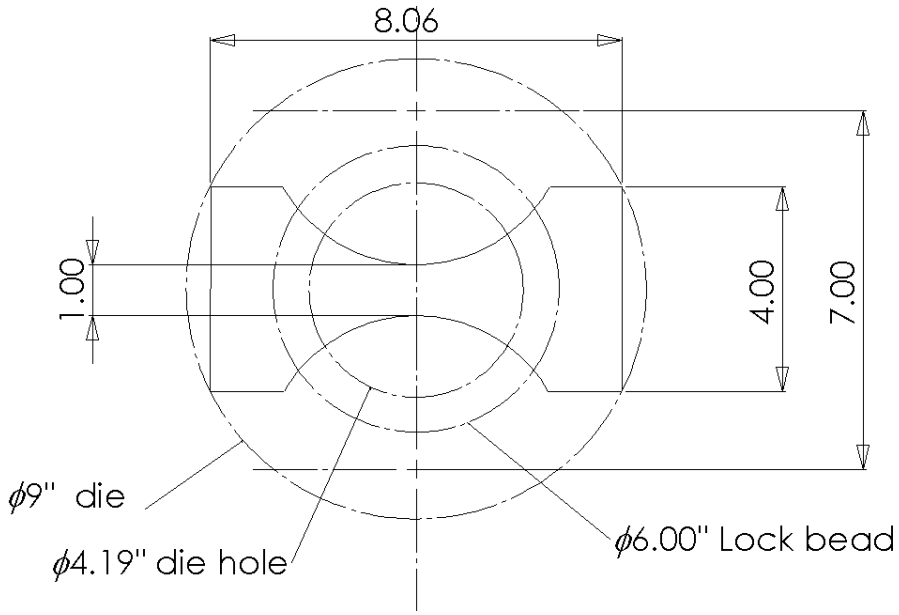

Figure 3.4 Alignment and centering of 1 in dog-bone sample on die (all dimensions in inches)

3.2 Strain measurement system

3.2.1 Grid analysis

Circle grid analysis is used widely to evaluate sheet metal formability and is considered a reliable method of strain measurement by sheet metal practitioners. It permits immediate and direct measurement of the maximum elongation of the sheet at any location. In this study, 2mm diameter circle grid patterns were etched onto the sheet prior to forming, as shown in Figure 3.5. During dome forming, the circles were deformed into ellipses, which were measured to determine major and minor limit strains. Each of the four sample geometries produced a distinct strain path, and, from this, the strain values and ratio of major-to-minor strain provided information on the type of deformation experienced in the failure area of the formed samples. For example, this data allowed us to determine whether the limit strains in the failure area denote drawing or stretching.

An optical strain measurement system originally proposed by Harvey (1984) was used to automatically acquire principal strain values for the deformed grids. By using a binary-image thresholding operation, the original circle is transformed into the inner and outer edges of the

deformed grid through convolution and recognition, and both are determined by least square elliptical regression. Then, the dimension of the deformed grid is obtained by calculating the mean dimension of the inner and outer edges, and used to calculate the limit strains along principal axes.

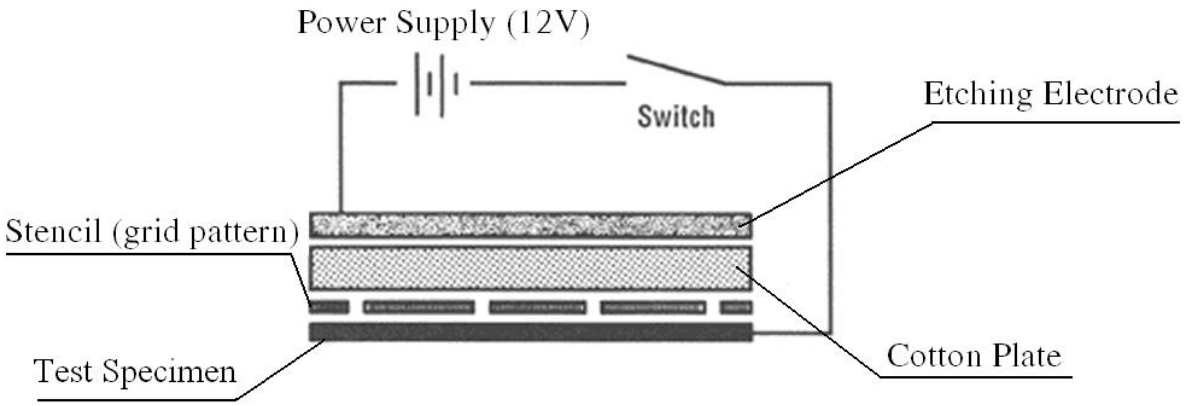

Figure 3.5 Equipment layout for electrochemical etching of grid patterns

3.2.2 Digital Image Correlation System (DIC)

A three dimensional 3D DIC system, VIC-3D, was also used to measure strain. Two high-resolution CCD cameras configured for three-dimensional computer vision were used *in situ* to capture the forming process. The DIC system was capable of automatic calibration, camera system disturbance correction and multi-image stitching. Specifications for the cameras are given in Table 3.1. In order to observe the blank during the forming process, cameras were placed under the die opening and LED lights were used to illuminate the test specimen. Both cameras were fastened to the die's fixed platen to ensure that the distance between the lenses and the sample's initial position remained constant. A schematic of the camera and tooling configuration is shown in Figure 3.6. The DIC system required that a random pattern of black and white speckles be applied to each sample, as described in the next section.

Table 3.1 DIC system specifications

Variable	Range
Measurement area	mm^2 to m^2
Strain measurement accuracy	up to 50με
Strain measurement range	0.005% to >2000%
Camera resolution	1624×1224, 14-bit
Maximum frame range	25 fps
Exposure time	20μs-10s
Analog data recording	4 channel, 16-bit A/D

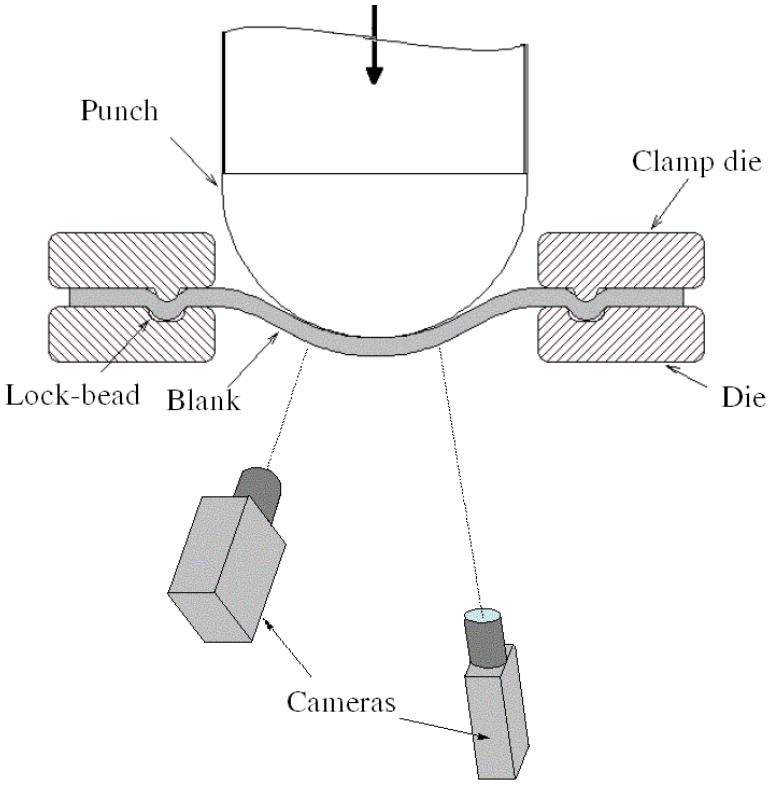

Figure 3.6 Schematic view of camera-tooling configuration

3.3 Test procedure

Each of the specimens was cleaned thoroughly with acetone prior to testing. They were then speckled on the side facing away from the punch (and towards the cameras). Speckling was applied only to the center area of the specimen (i.e., the area observed by the cameras through the die opening). Spray paint with matt finish was used to minimize specular reflections. Both white and black paints were resistant to high temperatures, up to 371°C (700K). On each sample, an arbitrary pattern of small black dots was applied over a thin layer of white paint. Both black and white paints were fast drying, requiring a maximum of thirty minutes to dry (as indicated by paint manufacturer instruction); however, a 24-hour drying time was required to completely eliminate specular reflections. Therefore, all samples were painted at least 24 hours before testing.

The speckled specimens (Figure 3.7) were placed on the pre-heated die and centered by aligning the four corners on the outer radius of the die. The clamping force was then applied to close the die and lock the sample in place using the lock-bead. The tooling was held in this position to allow heat to transfer between the tooling and the sample – two minutes was sufficient time to bring the temperature of the blank up to the tooling temperature (test temperature). The punch motion was then initiated at a specified speed to form the sheet. Image acquisition at 4 fps was initiated simultaneously with the beginning of the punch motion for all punch speeds. The test was terminated upon fracture of the specimen. Different test parameter configurations were used to study the effect of temperature and forming speed on the limiting strains. Table 3.2 displays the process variables considered in the LDH experiments.

Table 3.2 LDH experiment variables

Variable	Range
Temperature	25°C to 300°C
Clamping force	0 to 300kN
Sheet thickness	0.5mm
Test geometry	Dog-bones of 25.4mm, 50.8mm and 76.2mm minimum width Full width of 203.2mm×203.2mm
Punch speed	0 to 40mm/s
Lubricant	Teflon sheet

Experiments using punch speeds faster than 8mm/s were unable to capture necking and failure images with the low speed cameras; therefore, forming speeds of 0.32, 1.6 and 8mm/s were studied. The test results depend critically upon the absence of draw-in, which can be no more than 0.25 mm measured in the center of the lock beads, as specified by the previously mentioned NADDRG practice (1987). The required clamp force depends on bead design and friction on the binder surface. To estimate the required clamping force, 203.2mm × 203.2mm samples were stretched using a range of clamping forces. Clamping forces higher than 40kN resulted in failure in the lock-bead area, while forces lower than 10kN produced draw-in and increased both dome height and scatter. With the standard design and smooth (ground) surface of tooling, 30kN was identified to be appropriate for 0.5 mm thick 3003 aluminum alloy sheet (Figure 3.8). Hence a 30kN clamping force, which produces no sign of draw-in or fracture in the bead area, was applied in these experiments.

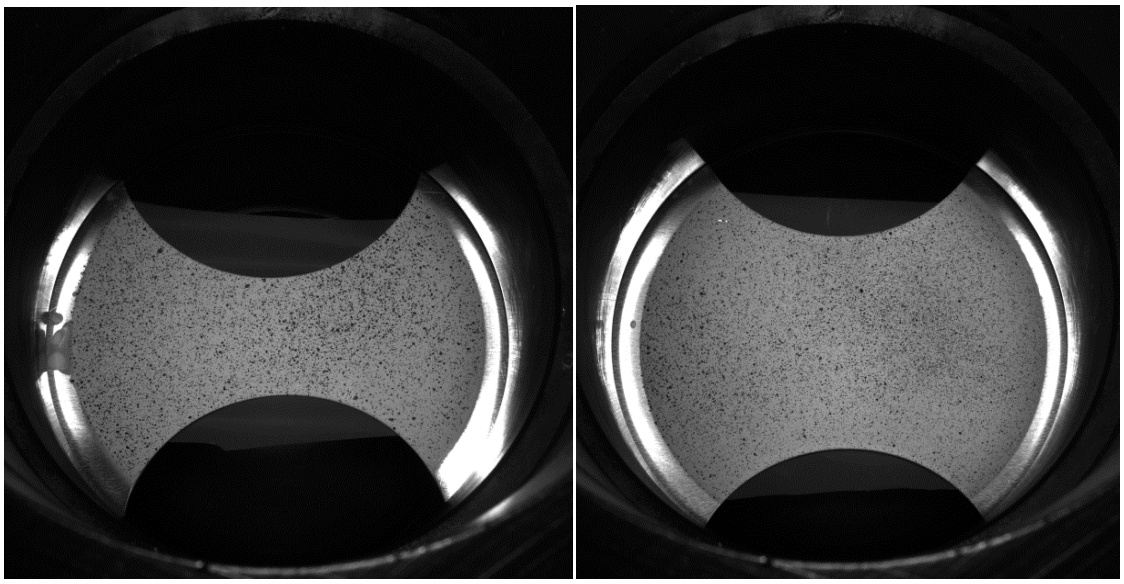

25.4mm wide dog-bone 50.8mm wide dog-bone

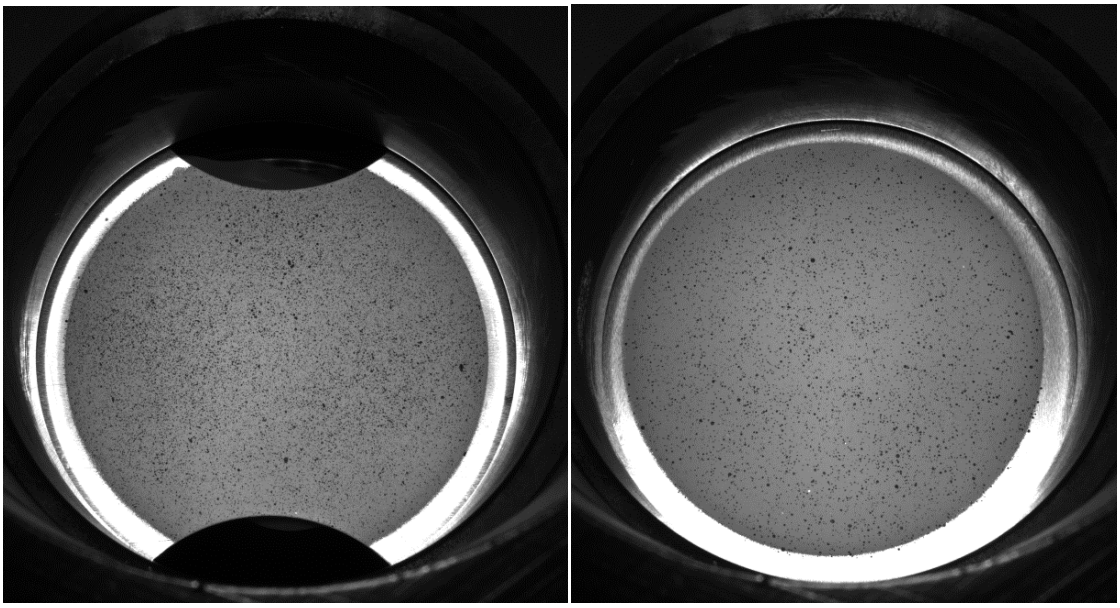

76.2mm wide dog-bone 203.2mm × 203.2mm

Figure 3.7 Speckled samples

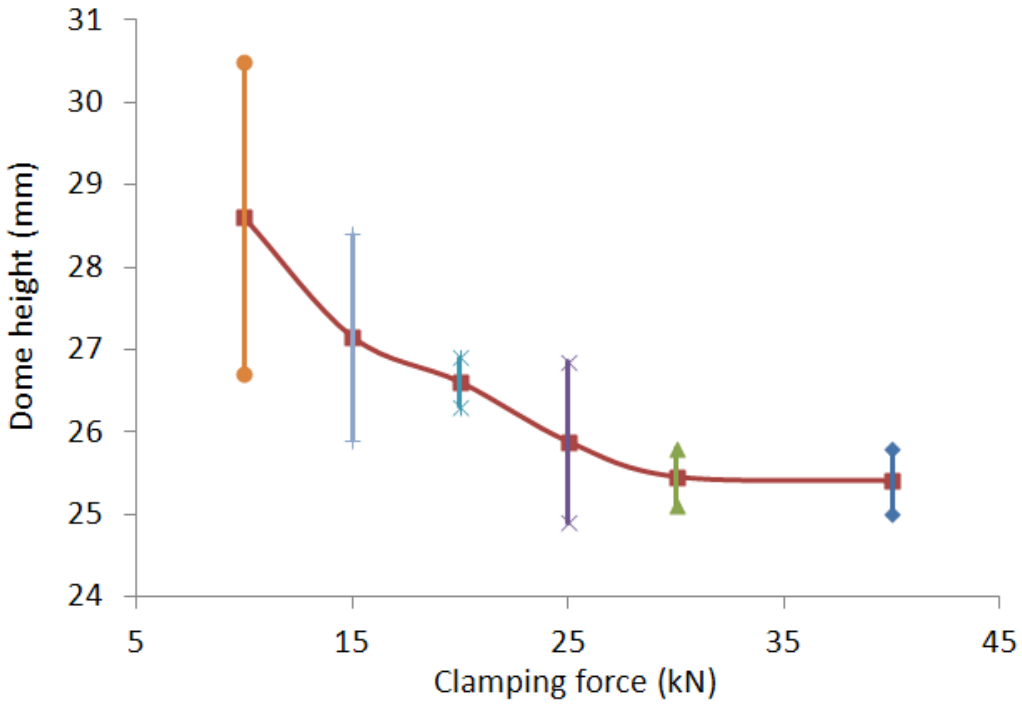

Figure 3.8 Effect of clamping force on LDH

3.4 Computation of limiting strains

In order to detect the onset of localized necking, about 140 images (70 from each of the cameras) were captured for each test. Faster imaging speeds were required for faster punch speeds. If the forming speed is slow, the onset of necking can be identified visually in the images. Figure 3.9 shows images of both necking and fracture of a specimen formed at room temperature, with a punch speed of 1.6mm/s and a clamping force of 30kN. The image captured just before the appearance of necking is selected for determination of limit strains though analyzed by the DIC system. Where the necking cannot be detected by visual inspection, the evolution of major strain along a line going from the pole through the fracture line was used to identify necking (described later). DIC analyses were performed using a subset size of 29 pixels and step size of 7 pixels. The subset size controls the area of the image that is used to track the displacement between images and has to be large enough to ensure that there is a sufficiently distinctive pattern contained in the area used for correlation. Different subset sizes were used as needed to reduce the projection error to an acceptable

level (maintain an optimal match confidence of 0.05 pixels for a given assumed noise level). A subset size of 29 pixels corresponds approximately to 2.5mm on the surface of the blank, which is close to the size of the circular grid used in the conventional strain circle technique (circle grid analyses were performed for room temperature and 250°C, punch speed of 1.6mm/s and a clamping force of 30kN to evaluate the accuracy of DIC results as used here). The step size controls the spacing of the points that are analyzed during correlation. If a step size of 1 pixel is chosen, a correlation analysis is performed at every pixel inside the area-of-interest. A step size of 2 pixels means that a correlation will be carried out at every other pixel in both the horizontal and vertical direction, etc. The analysis time varies inversely with the square of the step size. It was realized that a step size of 7 pixels results in an acceptable projection error; therefore, all DIC analyses were carried out using a step size of 7 pixels.

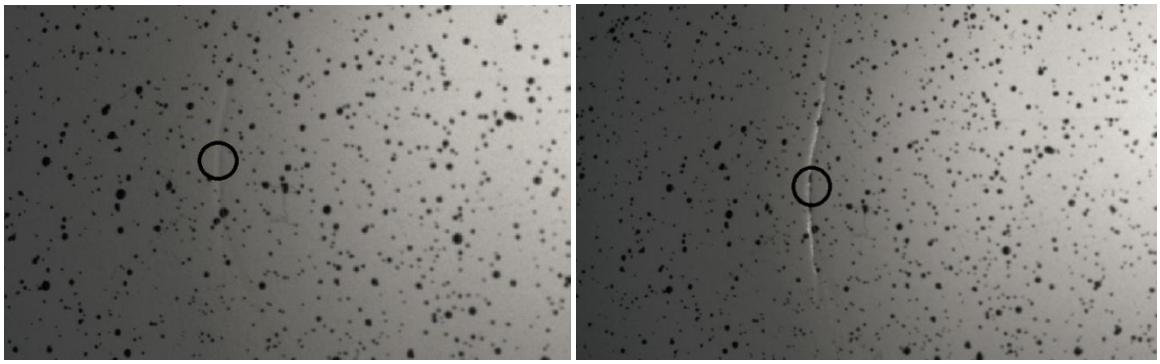

Figure 3.9 Detection of necking and failure by visual inspection

All analyses were performed using the incremental method (i.e., the total deformation is obtained by comparing successive images on a step-by-step basis) and strain fields were calculated during the forming process for all captured images. The results (major strain, minor strain, displacements, etc.) were presented in three-dimensional and two-dimensional plots. In two-dimensional presentation, the speckled sample appears in the background of a contour plot. Figure 3.10 shows 3-D and 2-D presentations of sheet thickness distribution for 76.2mm wide dog-bone sample.

The DIC system keeps the history of deformation and field variables during the forming process. Figure 3.11 shows contour plots of the major strain distribution for 76.2mm wide dog-bone samples formed at room temperature and 250°C, with a punch speed of 8mm/s and clamping force of 30kN. The plots for both temperature cases are presented at 11.9mm,

16.8mm, 21.7mm, and 26.6mm dome heights. Comparison of the strain distributions at room temperature and 250°C reveals that the major strains are growing faster with dome height at room temperature than those at 250°C. As can be seen from Figure 3.11, the room temperature sample offered a lower formability than warmer samples and failed at a dome height of 26.6mm. Elevating the temperature to 250°C improves formability and increases dome height considerably. The 250°C sample presented lower strain levels compared to room temperature samples tested at the same dome heights. It should be noted that the minor strains for 76.2mm wide dog-bones are very close to zero and consequently this geometry was adopted as the plane strain sample.

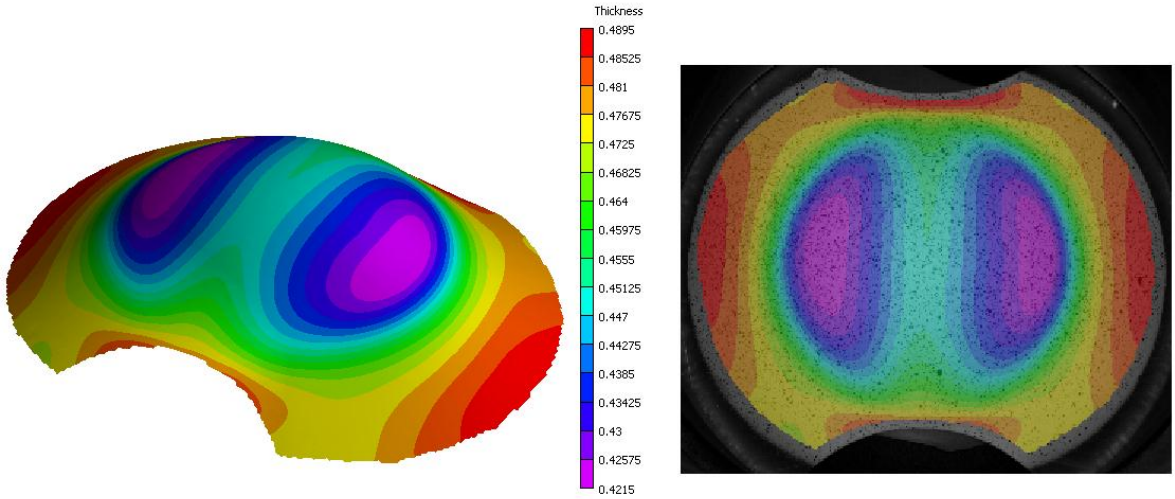

Figure 3.10 Two-dimensional and three-dimensional presentations of field variables (Contour plots of shell thickness are presented)

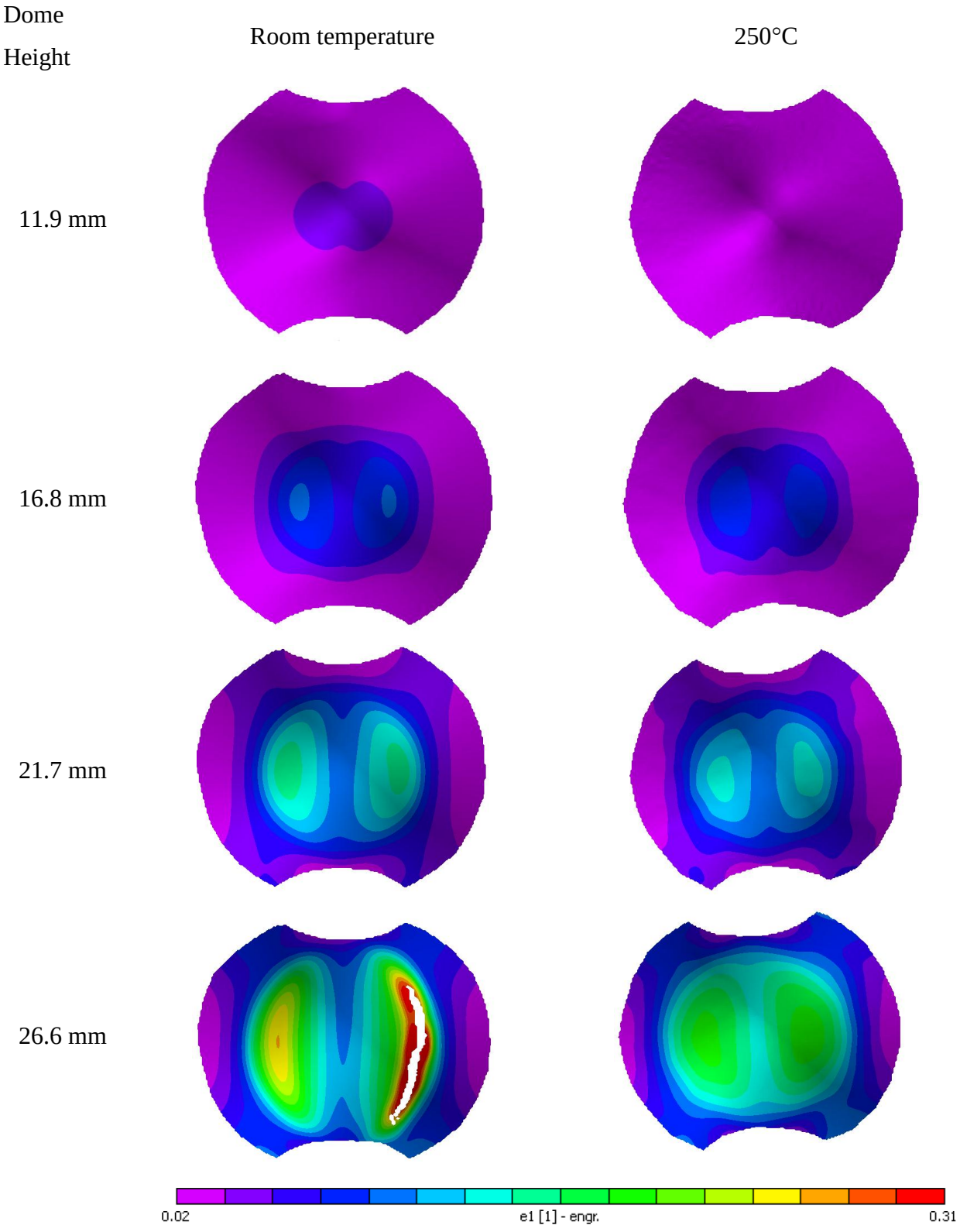

Figure 3.11 Contour plots of major strain distribution at different forming steps for a punch speed of 8mm/s and 30kN clamping force.

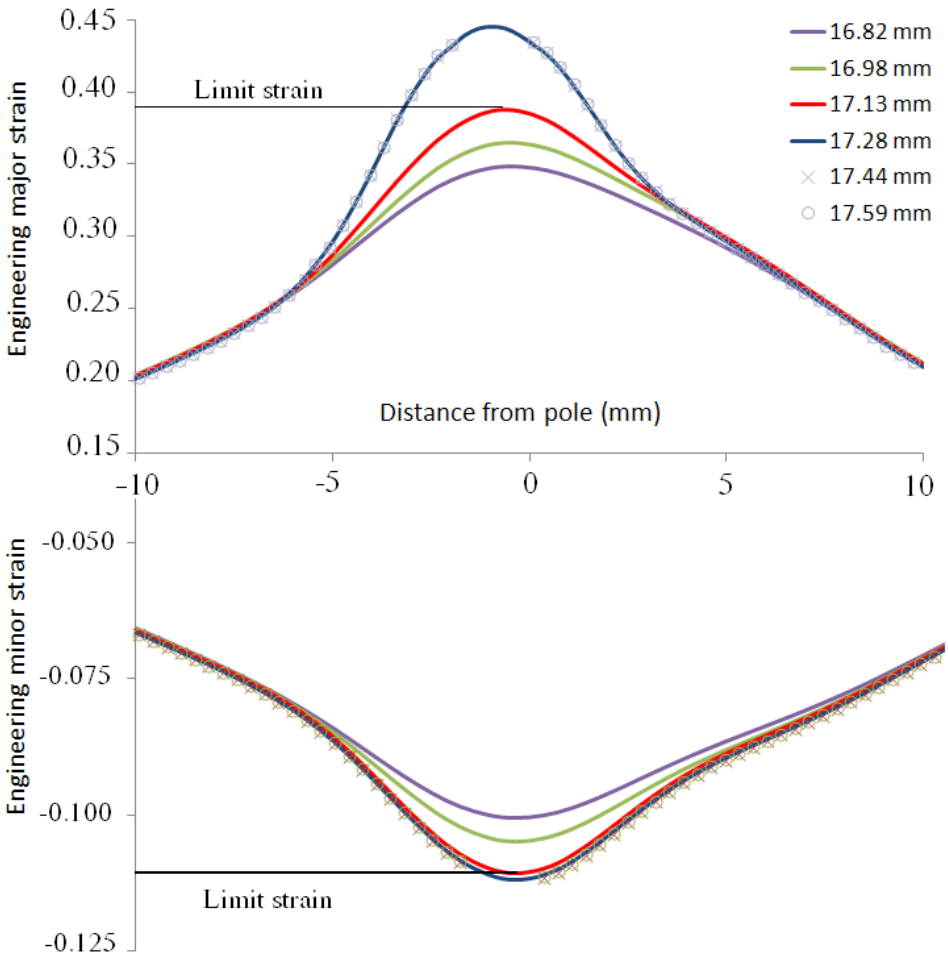

Figure 3.12 Evaluation of limiting strains by investigating the evolution of major strains

In order to generate accurate FLDs, limiting strains were determined by plotting major and minor strains, which were obtained from images captured prior to the onset of localized necking (usually 5 images before the localized necking or fracture is visible), along a line from the pole to the edge of the test specimen as shown in Figure 3.12. In order to capture the limiting strains accurately, a sharp increase at the peak point of the major strain graph (after which the minor strain remains almost constant) was taken as the onset of necking. Each test was repeated a minimum of three times to ensure results were repeatable and to minimize experimental errors. Limiting major and minor strains were obtained from images representing the forming step that occurs just before the onset of necking (safe dome height). These limiting strains are taken as single points on FLD. A set of such limiting strain points obtained in a similar manner from different specimen geometries would define the FLC for the material at each temperature level.

3.5 Results and discussion

3.5.1 Effect of temperature on dome height

Dome testing of 203.2mm×203.2mm biaxial stretch samples was performed at both room and elevated temperatures (i.e. 100°C, 200°C, 250°C and 300°C) to study the effect of temperature on LDH. A clamping force of 30kN (as was required to eliminate the draw-in and to avoid failure at the lock-bead area) and a punch speed of 1.6mm/s were used. For all tests, Teflon sheet lubricant was placed between the blank and the punch head to minimize friction. The variation of Teflon sheet lubricity with temperature is thought to be low; thus, it was assumed that the coefficient of friction at different temperatures remains constant. LDH was measured from images taken using the DIC system. First, the images were inspected to identify the frame corresponding to the onset of localized necking (Figure 3.9). The dome height corresponding to the image taken immediately prior to the necking image was considered the safe dome height. These measurements agreed well with punch force vs. punch displacement data recorded using the Labview program, which assumed that the sharp drop in punch force was indicative of material failure (Figure 3.13). In order to determine the dome height before necking using the load-drop criterion, the decrease in the value of the measured punch force at each time step was compared with the level of noise in the measured data (for example the maximum noise in load-displacement curve which corresponds to room temperature stretching of 25.4mm wide dog-bone was 0.57kN). The value of punch force at each time step was compared with the maximum punch force of all previous time steps. A time step was considered to correspond to the onset of necking if the decrease in the value of corresponding punch force was greater than the noise level. The decrease in slope of the punch force versus displacement response at elevated temperatures corresponds to material softening. The punch force vs. punch displacement measurements will be used later to verify the numerical models (Chapter 4).

Measurements of the dome height at onset of necking were repeated three times for each temperature case. Figure 3.14 shows the average measured dome height at necking vs. temperature using the DIC results as well as based on punch load-displacement response. The vertical lines at each temperature present the repeated measurements using DIC data. LDH measurement using both methods agreed well. As can be seen from DIC results, LDH

increased with forming temperature; however, scatter also increases at higher temperatures. Comparing the LDH at room temperature and 100°C shows that no formability improvement was gained below 100°C. Also, any improvement in dome height was not clearly observed after increasing the temperature from 250°C to 300°C. The maximum dome height measured at 250°C and 300°C was 42.6mm and 43.5mm, respectively; however, the average dome height decreased when the sample was heated to 300°C. Similar results can be seen from measurements based on punch load-displacement response, however the average LDH is overestimated at room temperature and underestimated at 300°C conditions compared to the DIC results by 5.6% and 4.7%, respectively.

It can be concluded from this data that, under these conditions, formability gains are negligible when the forming temperature is increased from 250°C to 300°C. The reason for the lack of improvement corresponding to this temperature increase is unclear; however, this may be due to a degradation of the response of the AA4045 clad layer at the higher temperature since it has a lower melting point (575°C) compared to that of the AA3003 655°C core. Alternatively, it is possible the Teflon sheet softens overly during forming at 300°C and loses its lubricity; however, to confirm this hypothesis, future work should consider friction measurements to characterize the friction coefficient of the Teflon sheet at elevated temperatures. Apart from the forming results at 300°C, these experiments confirm an overall trend that increasing forming temperatures enhance limiting dome height and subsequently improve the formability of AA3003.

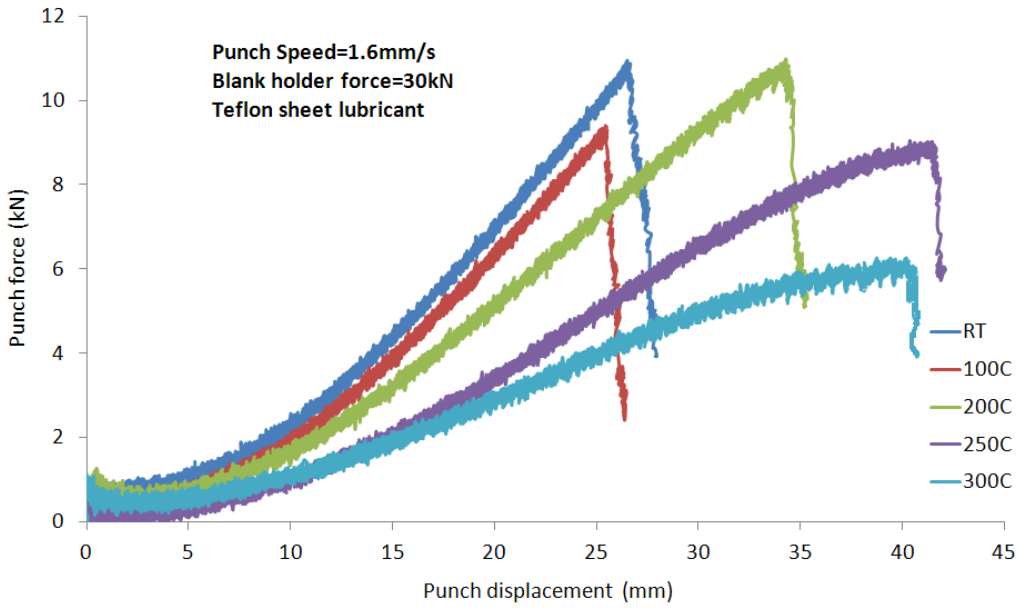

Figure 3.13 Punch force vs. punch displacement at different temperatures

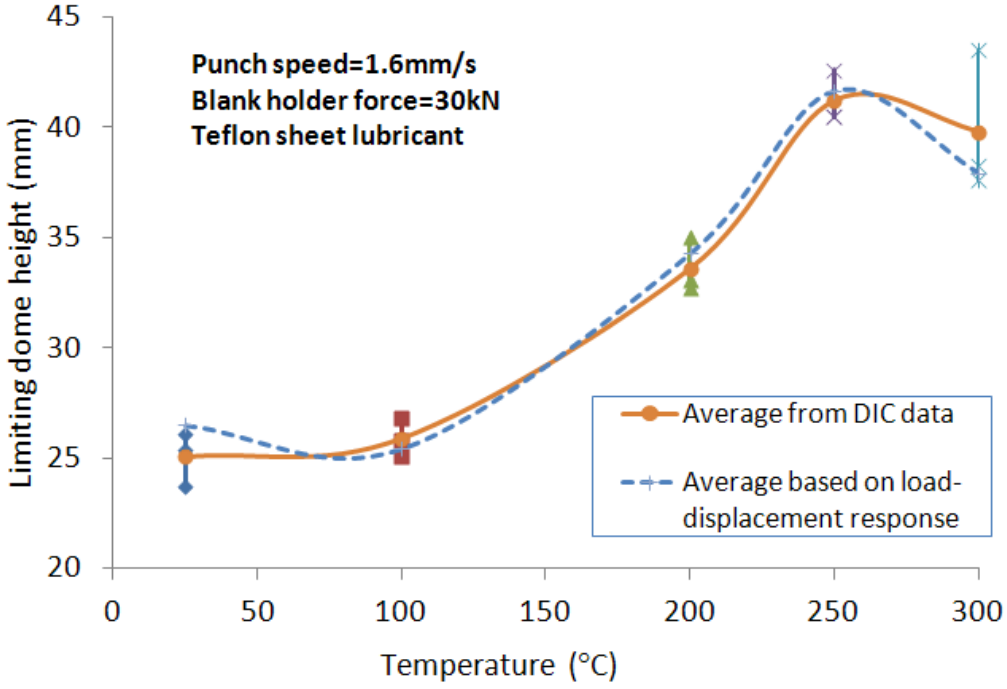

Figure 3.14 Effect of temperature on dome height. Average dome heights are shown based on DIC data and load-displacement response. Vertical lines at each temperature present the repeated measurements using DIC.

3.5.2 Effect of friction on LDH

In order to explore the effect of friction on LDH, LDH measurements were performed as described above, but in the absence of Teflon sheet lubricant. In all experiments: test specimens were 203.2mm×203.2mm, 0.5mm thick, the forming speed was 1.6mm/s, and a clamping force of 30kN was applied. All samples were cleaned before testing as described in Section 3.1.2. Figure 3.15 compares LDH values produced at different temperatures, with or without Teflon sheet lubricant. As can be seen, dome height decreased for dry-formed samples (no Teflon sheet lubricant); however, similar to lubricated samples, the dry samples demonstrated improved formability with increasing temperature. The average dome height of the dry samples decreased by approximately 27% relative to that of the lubricated samples for parts formed at temperatures between 100°C and 250°C. At room temperature, the LDH of unlubricated samples was 18% lower, whereas at 300°C, the unlubricated samples had a 23% reduction in LDH.

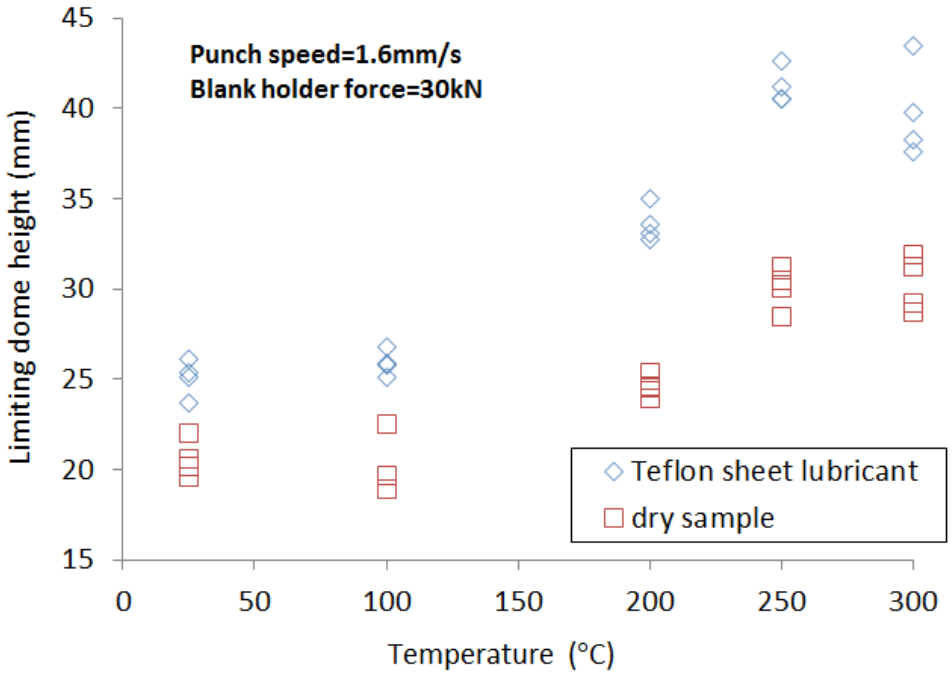

Figure 3.15 Effect of lubricant on LDH

3.5.3 Effect of forming speed on LDH

Experiments were performed to study the effect of forming speed on LDH. Again, 203.2mm×203.2mm, biaxial samples, 0.5mm in thickness, were used in each experiment. Teflon sheet lubricant was used and a 30kN clamping force was applied. Samples were tested at room temperature and 250°C, and at different forming speeds, including 0.32mm/s, 1.6mm/s, 8.0mm/s and 40mm/s. Dome heights were measured using punch force vs. punch displacement graphs. A sharp drop in punch force, where the maximum punch force is sensed, denoted necking and material failure. Measured LDHs agreed well with DIC results at lower forming speeds (Figure 3.16). At the highest forming speed, 40mm/s, the DIC system was unable to capture enough images during forming to identify the onset of necking. Each punch speed and temperature configuration was repeated four times and LDH values were measured using either DIC or punch force vs. punch displacement diagrams.

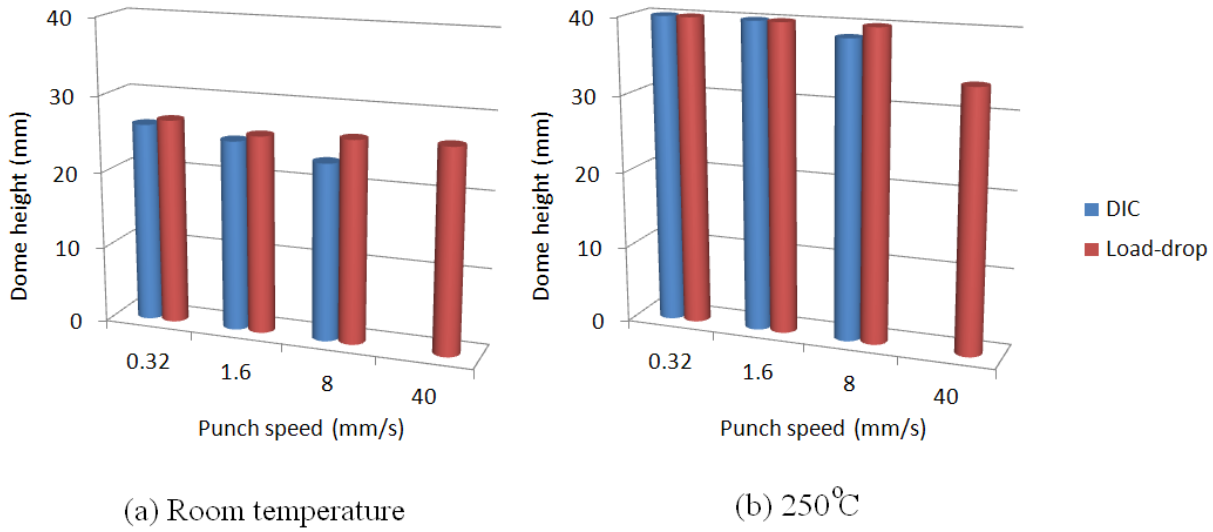

Figure 3.16 Average dome height using DIC method and load-drop technique. The DIC was unable to measure the safe dome height for a punch speed of 40 mm/s.

Figure 3.17 shows these results and compares the effect of forming speed at two temperature levels. As can be seen, the forming speed did not significantly affect LDH at room temperature. The LDH at room temperature varied from 24.9mm to 27.6mm, with an average value of 26.2mm (taking into account four punch speed levels (16 samples in total)). The lowest dome height of 24.9mm was produced at the highest forming speed, 40mm/s, while the maximum dome height, 27.6mm, was measured at the lowest forming speed, 0.32mm/s. The

effect of forming speed on formability was significant at 250°C; however, only at the highest (40mm/s) punch speed. On average, slower punch speeds, 0.32mm/s, 1.6mm/s and 8mm/s, produced dome heights of 41.2mm (four repeats at each forming speed, 12 samples in total). Samples formed with a punch speed of 40mm/s resulted in an average LDH of 33.3mm, which indicates a 20% decrease compared to the average LDH values at lower speeds. This drop can be attributed to the strain rate sensitivity of aluminum alloy sheet at higher temperatures. As discussed above, no significant rate dependency was observed at room temperature.

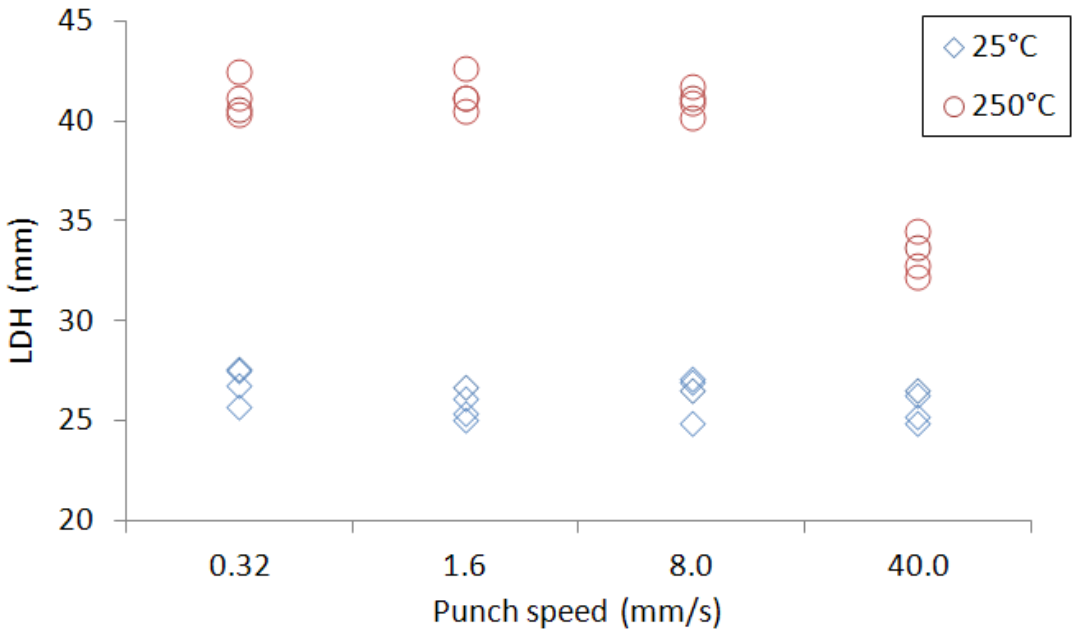

Figure 3.17 Effect of punch speed on LDH. LDH values were measured using load-drop technique.

3.5.4 Effect of Sample geometry

As mentioned in the Test Procedure section above (3.4), four test geometries were considered: dog-bones with 25.4mm, 50.8mm and 76.2mm minimum widths and 203.2mm×203.2 samples. In order to construct FLDs, LDH values were measured in response to a range of forming parameters; results corresponding to forming speeds of 1.6mm/s are presented here at different temperatures. As can be seen in Figure 3.18, dome height increased with decreasing sample width. This increase is attributed to enhanced material flow in the transverse direction and diffuse necking, which is greater for smaller sample widths. In addition, all geometries demonstrated a clear improvement in formability (in terms of LDH) with increased forming

temperature, up to 250°C. Further increases in temperature to 300°C had either no effect or a negative effect on measured dome heights. Negative effects were more significant for dog-bones of larger widths.

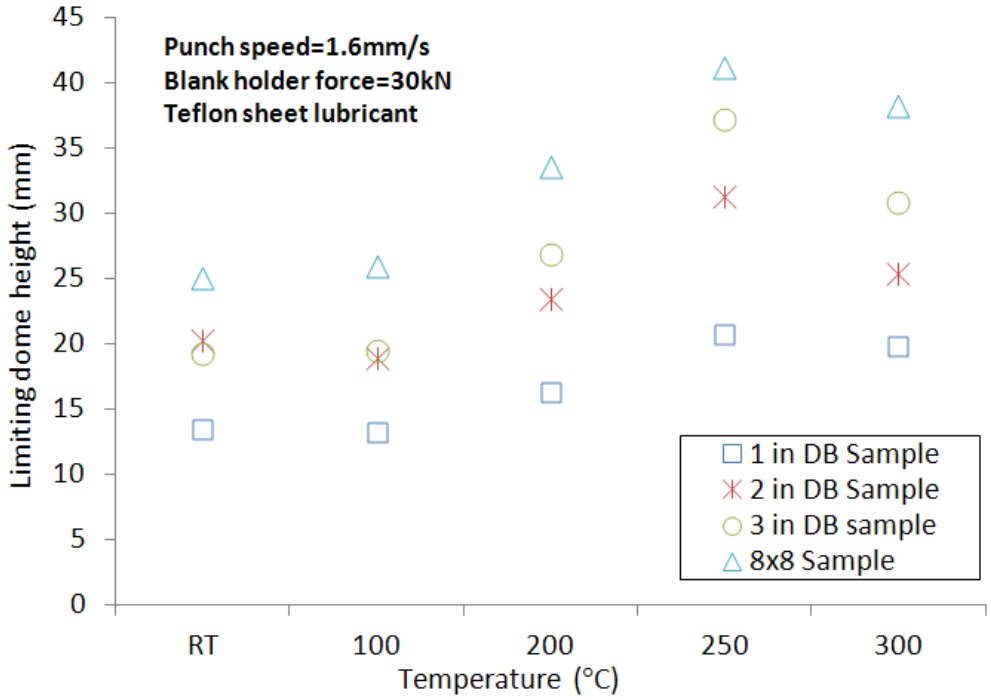

Figure 3.18 LDH using different test geometries across forming temperature

It has been reported that sheet orientation has very little effect on formability in the plane strain state, but can have large effects on uniaxial tension or in the drawing region, i.e. the negative minor strain region (Rees, 2001). To investigate this effect at elevated temperature, tests were performed using dog-bone samples cut in the rolling direction (RD) and transverse direction (TD) between room temperature and 250°C. Dog-bone specimens with minimum widths of 25.4mm, 50.8mm and 76.2mm (oriented in both the RD and TD) were used with Teflon sheet lubricant and stretched at a punch speed of 1.6mm/s and clamping force of 30kN. LDHs were measured by inspecting for necking within images captured by the DIC system and the results are presented in Figure 3.19.

As can be seen, dome heights were nearly the same for low temperature RD- and TD-oriented 76.2mm wide dog-bone samples measured in the plane strain region; however, a larger difference was observed at higher temperatures. Measured dome heights for TD-oriented specimens at room temperature and 100°C varied approximately 2% with respect to those of RD-oriented samples. However, dome heights of TD-oriented samples decreased by 0.04% and 10% compared to those of RD-oriented samples at 200°C and 250°C, respectively. In the negative minor strain region (25.4mm and 50.8mm wide specimens) the effect of sheet orientation was more evident. For example, RD-oriented 50.8mm wide samples showed better formability than their TD-oriented counterparts, with a minimum 10% and maximum 20% LDH improvement at room temperature and 250°C, respectively. Similar results were observed for 25.4mm width samples; sample orientation had a larger effect on formability at higher forming temperatures.

In general, rolling-oriented samples had higher limiting dome heights for strain states in the negative minor strain region. This effect can be attributed to aspect ratio of grains, for example, but could also be due to texture difference due to rolling effects. The effect of sheet orientation is more significant at higher temperatures. This agrees with the fact that a larger difference between R-values is found at higher temperatures for RD samples than TD samples.

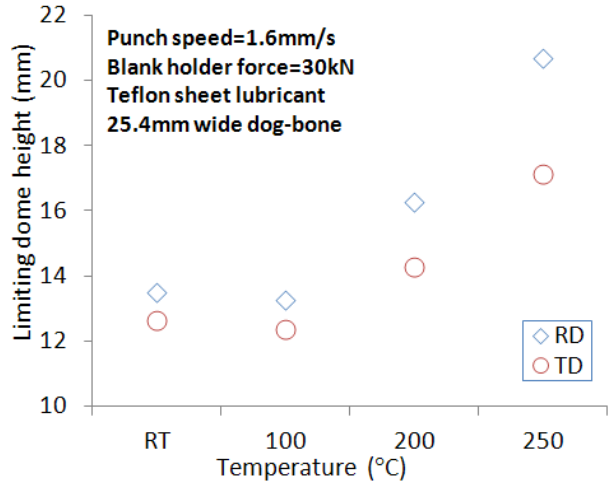

(a)

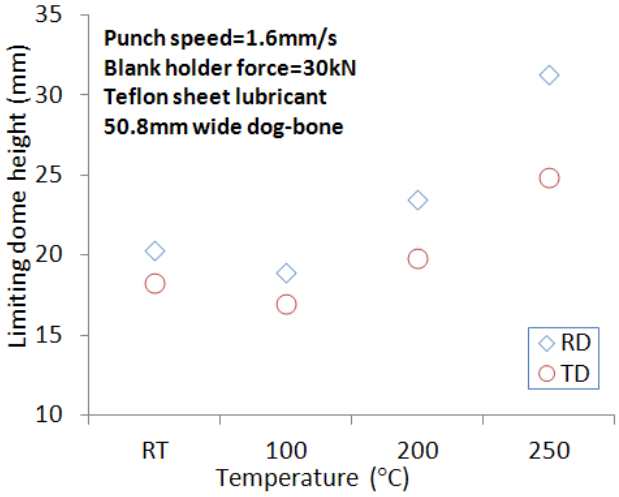

(b)

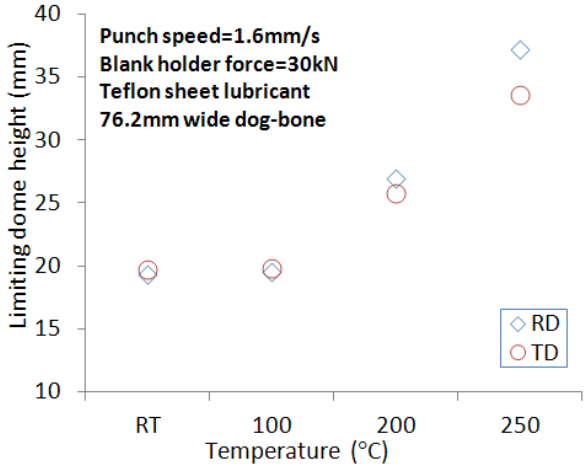

(c)

Figure 3.19 Effect of sample orientation. (a) 25.4mm, (b) 50.8mm, and (c) 76.2mm wide doge bone samples

3.5.5 Forming limit diagrams

Limiting strains were determined for 0.5mm thick AA3003 sheets under a range of forming conditions (strain states, temperatures and punch speeds). For each combination of forming speed and blank temperature, five different strain paths were obtained by forming three dog-bone samples of different widths and one full width sample (Figure 3.3) in the presence of Teflon sheet lubricant. The fifth path was obtained by forming a full width sample without lubrication. Figure 3.20 and Figure 3.21 show scatter plots of limiting strains using specimens formed with a punch speed of 1.6mm/s and clamping force of 30kN at room temperature and 250°C, respectively. For each test, the maximum major and minor engineering strains are plotted for safe points, as well as from necked and cracked areas. Measurements were performed using both the DIC and circle gridding method; however, only DIC results are presented in these figures (a comparison of forming limits obtained using these two techniques is provided below). In addition, typical strain paths are shown for each sample. It should be noted that with the *in situ* observation technique, strains are calculated using the images captured while the specimens are still loaded (i.e., the punch is still in contact with the specimen, hence the elastic strains are still present in the sheet). In the conventional circle gridding method, the specimen is removed from the tool and spring-back releases the elastic strains before measurement. The DIC method, which takes measurements based on images of loaded blanks, will produce higher strain measurements than the conventional method, in which the load is released. This results in forming limit curves that are less conservative (more realistic) than those obtained using the conventional CG method.

As can be seen from both temperature cases, the 76.2mm dog-bone samples presented the plane strain deformation mode in which the sheet is strained only in one direction and the minor strains are approximately zero. Full width samples (203.2mm×203.2mm), with or without lubrication, correspond to biaxial stretching. In cases where no lubrication was used, increasing the temperature to 250°C forced the strain path to move toward biaxial stretching with a lower minor-to-major strain ratio; i.e. closer to the plane strain path. For both temperature cases, applying the Teflon sheet lubricant forced the strain path to move toward equi-biaxial stretching; however, the ratio of minor-to-major strain was approximately 0.5. Narrower, 25.4mm dog-bone samples produced a strain path close to uniaxial tension in which the ratio of minor-to-major strain is close to -0.5. Safe points indicate limiting strains

and can be used to plot the FLD by drawing a trend line through the upper band of the data points (used in this research) or using average values. The maximum standard deviation of the measured safe points was calculated to be 0.016 strain. A potentially less conservative approach would be to draw the forming limit curve to lie just below the necked strain levels. The largest different between FLDs generated using the upper band of the safe points and the lower band of the necked points was observed for the plane strain samples and the no-lubricant biaxial stretch samples at room temperature which were measured to be 0.018 and 0.027, respectively. The maximum difference between the two methods in limiting strain values other than the plane strain sample was 0.006. The FLDs presented in the next sections are generated using the upper band of the safe points.

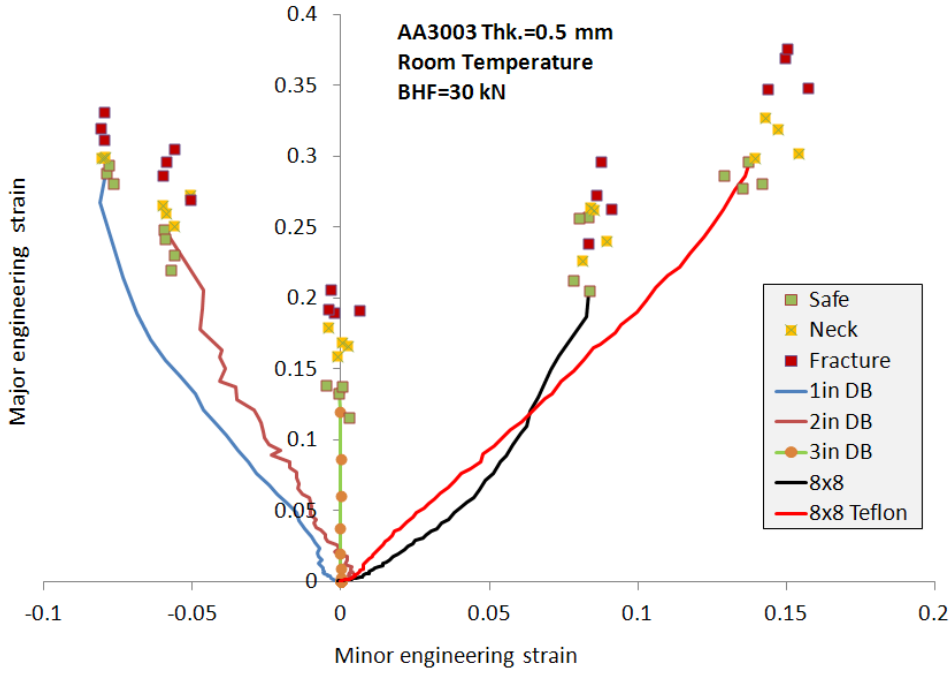

Figure 3.20 Major strain vs. minor strain scatter at room temperature

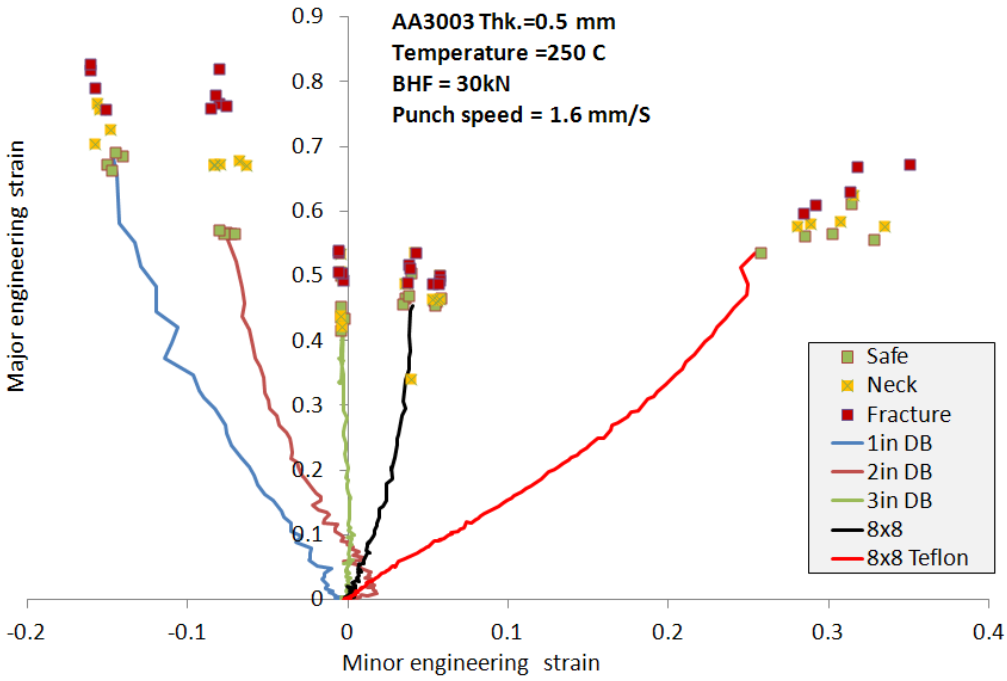

Figure 3.21 Major strain vs. minor strain scatter at 250°C

Figure 3.22 compares FLDs obtained using the DIC and circle gridding (CG) methods under identical forming conditions. In this figure, solid lines denote DIC results and individual points represent discrete limit strains measured within the safe area of the sample adjacent to the necked region using the CG method. In general, FLDs built from these methods are in good agreement, and it can be seen that they predict very similar limiting strains; however, when forming temperatures reached 250°C, the degree of scatter in the CG method increased significantly. The forming limit curves obtained using the DIC method are conservative since they tend to lie within the scatter of the "safe" CG measurements. Several factors can account for differences observed within FLDs obtained from these methods, such as reduced contrast in DIC images captured at higher temperatures, released elastic strains and thermal expansion (in elevated temperature experiments) when using the CG method, and difficulty with resolving the edge of the deformed grid used in conventional CG measurements. This comparison of the DIC method against the well-known conventional CG method shows that DIC experiments, as explained here, can be used to develop FLDs under different forming conditions. It should be noted that neither DIC nor CG methods were able to measure the limiting strains at forming speeds higher than 8m/s because it was not possible to stop the punch before necking. In addition, the DIC method was unable to capture sufficient images of

the sample during forming at this speed; hence, images corresponding to the onset of necking and safe dome height were not accessible.

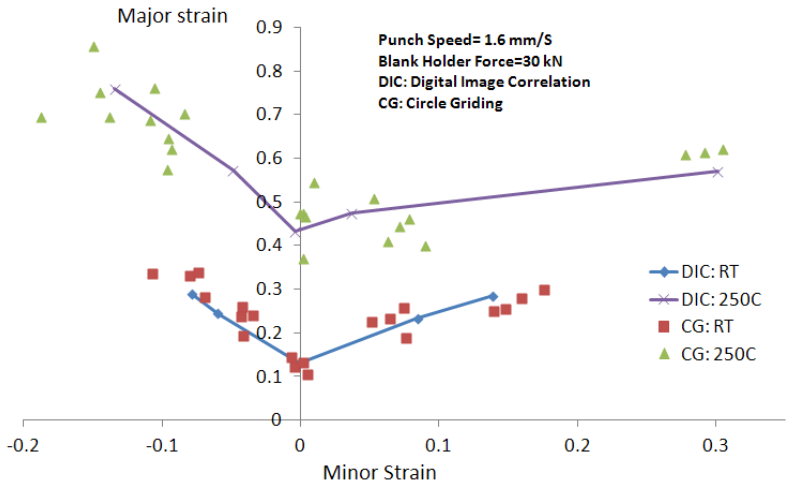

Figure 3.22 Comparison of DIC results against conventional method. CG data is obtained using safe points.

Figure 3.23 and Figure 3.24 show FLDs obtained with punch speeds of 1.6mm/s and 8mm/s, respectively. As can be seen from both graphs, formability (limiting strains) increased considerably with increasing test temperature; however, there is no significant effect below 100°C. FLD measurements at room temperature and 100°C resulted in very similar limiting strains under all forming conditions. There was a small difference between the limiting strains at room temperature and 100°C under plane strain conditions; however, a larger temperature effect was observed when the temperature was increased to 200°C or higher. The effect was less pronounced while moving toward the equal biaxial strain state.

Figure 3.25 compares the FLDs obtained using three forming speeds (0.32mm/s, 1.6mm/s and 8mm/s) at room temperature and 250°C. While formability improved at lower forming speeds, the rate effect is not as significant as the temperature effect, for the range of conditions considered. There was considerable improvement in the measured limiting strains as punch speed was decreased, for near-equi-biaxial strain states. While the last FLD point in the biaxial forming area, which corresponds to stretching 203.2mm×203.2mm samples using Teflon sheet lubricant, showed a considerable increase when forming speed was reduced to 0.32mm/s at 300°C, this effect was much less significant at lower temperatures.

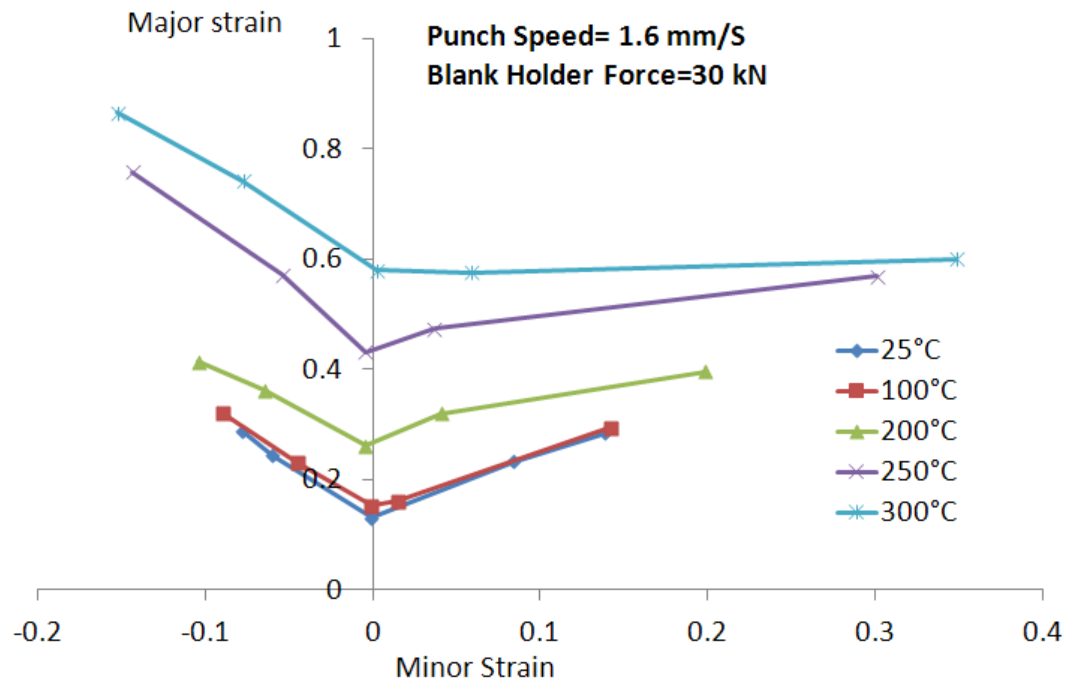

Figure 3.23 FLD of 0.5mm thick AA3003 at 1.6mm/s punch speed

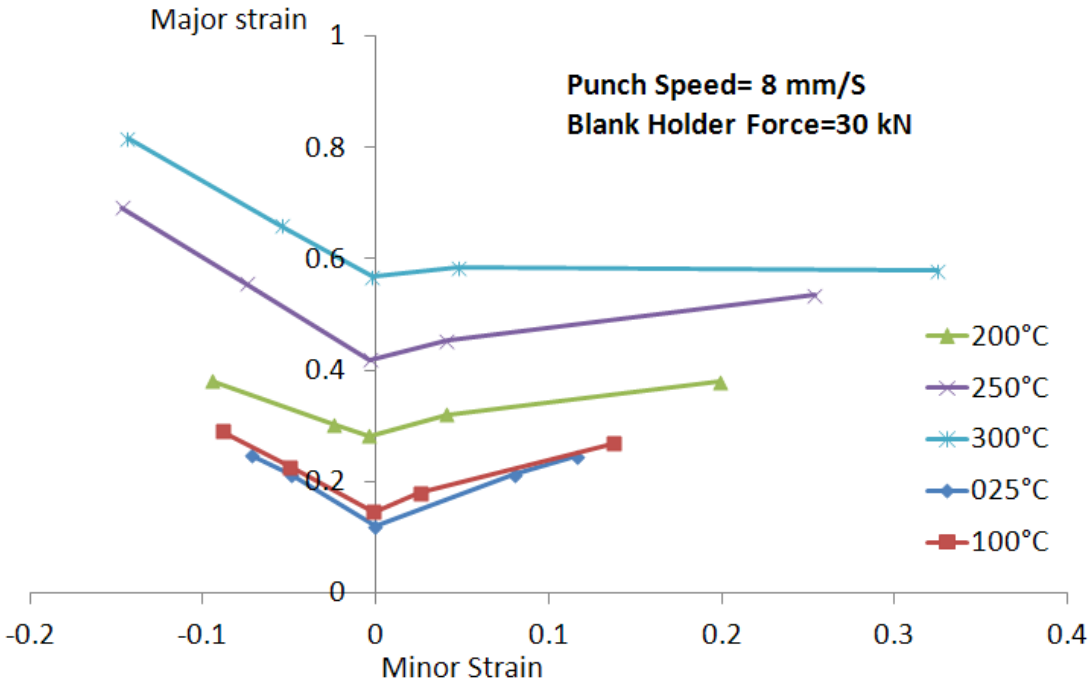

Figure 3.24 FLD of 0.5mm thick AA3003 at 8mm/s punch speed

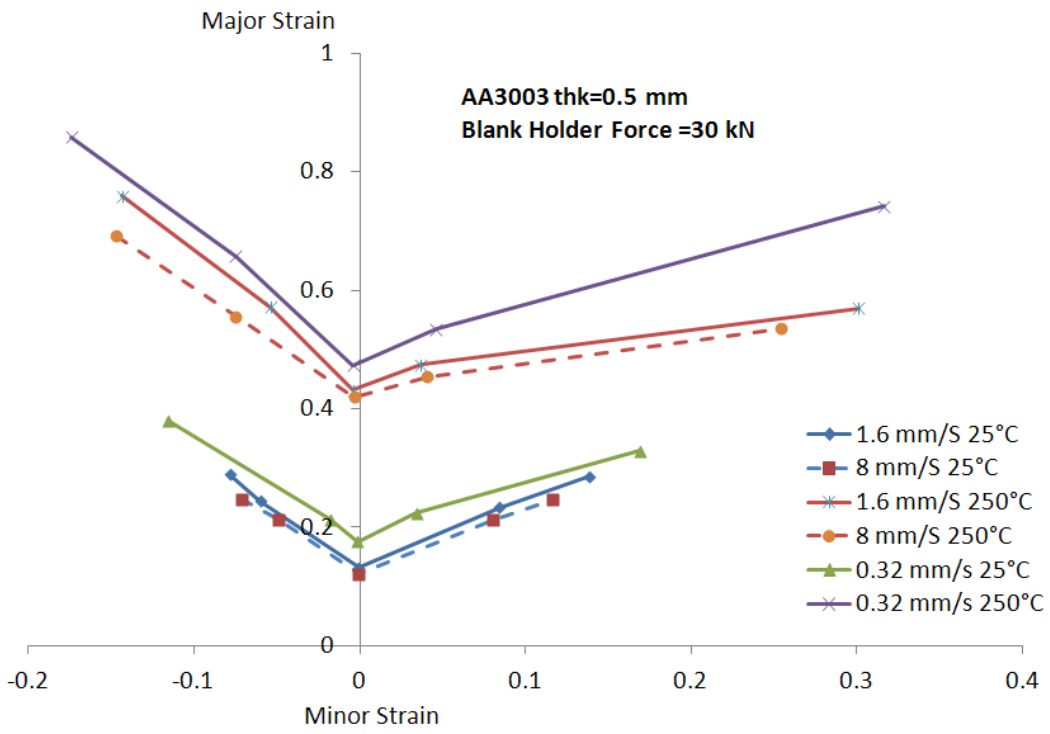

Figure 3.25 Effect of forming speed on FLD

The FLDs developed here show that temperature has a significant effect on formability, while rate effects are negligible within the range of forming speeds used in these experiments. Higher rate effects may be observed by increasing the forming speed; however, this would have required additional equipment, implementing a high speed camera set up with the DIC system, and was therefore outside the scope of this study. It is expected that increasing the forming speed would produce a negative effect on formability at elevated temperatures, but would show negligible effects at room temperature (Figure 3.17).

Limiting strains were extracted from the FLDs described in this chapter and used in simulations presented in Chapter 5 and Chapter 6 to predict failure during forming.

4 Numerical modeling of warm forming

This chapter presents the numerical model developed to simulate warm forming of AA3003 aluminum alloy sheet. At the heart of the modeling approach is a user material subroutine or "UMAT" that captures the material constitutive response, developed as part of this research. This umat incorporates a Bergstrom (1982) hardening law to account for the coupled thermal softening and rate sensitivity displayed by this alloy at elevated temperatures. In addition, the Barlat (2003) yield criterion is adopted to capture the anisotropy of this alloy. The Bergstrom (1982) and Barlat (2003) models and their constitutive parameter fits are presented in Chapter 2. This chapter opens with a description of the numerical integration scheme used for these models within the UMAT subroutine. Next, validation of the UMAT and finite element modeling approach is presented through simulation of two baseline experiments, the uniaxial tensile experiments described in Chapter 2 and the limiting dome height experiments in Chapter 3. After the validation work is presented, the balance of the thesis focuses on simulation of two warm deep drawing operations, a cylindrical cup draw and drawing of a heat exchanger component. These simulation efforts are presented in Chapters 5 and 6 of this thesis.

The finite element models developed in this research utilized the commercial finite element code, LS-DYNA (Hallquist, 2006). This code utilizes an explicit dynamic formulation that is well suited for simulation of intermittent, sliding contact problems such as in sheet metal forming. The code offers a coupled thermo-mechanical formulation to capture heat transfer during warm forming. A user-defined material subroutine option is available which allows the user to implement code capturing the desired constitutive behavior.

The mechanical behaviour of aluminum alloy sheet shows a complex dependence of flow stress on temperature and strain rate at elevated temperatures. None of the existing constitutive models implemented within LS-DYNA are able to model this material response accurately. As discussed in Chapter 1, the Barlat YLD2000 yield surface is able to describe the anisotropic behaviour of FCC aluminum alloys at elevated temperatures. Accordingly, a user-defined material subroutine embodying the Bergstrom model in conjunction with the Barlat YLD2000 yield function has been developed. This chapter presents the primary equations required within the UMAT developed for this project.

4.1 Numerical integration

There have been many efforts on numerical integration and stress update of plastic deformation (Tugcu and Neale, 1999; Hashiguchi, 2005). The anisotropic, temperature dependant yield function described in section 2.3 YLD2000, was implemented using rate-independent plasticity using an efficient integration algorithm originally developed by Oritz and Simo (1986). The incremental theory of plasticity as explained by Chung et al. (1993) and later by Yoon et al. (1999, 2003) is used for numerical integration. The algorithm is a cutting-plane method and is applied to bypass the need to compute the yield function and flow rule gradients using a point projection iterative method (Simo and Hughes, 1998). The stress integration algorithm for the YLD2000 yield function and its implementation as a UMAT into the explicit finite element code, LS-DYNA, are described here.

The strain increments, stress state and any history variables are recorded at each time step (stress update step) and will be taken to the next time step. The new strain increment is then assumed to be elastic and an elastic predictor "trial stress" state is calculated using elasticity relations. The cutting plane algorithm is used to re-calculate the actual stress state, and other plastic variables are calculated accordingly.

The basic steps in the numerical procedure for iterative integration of the elastoplastic constitutive equations for rate independent plasticity with the flow rule are summarized in Table 4.1.

Table 4.1 Basic steps in numerical integration

$\dot{\varepsilon}^{e}_{ij(n+1)} = \dot{\varepsilon}_{ij(n+1)}$	
$\dot{\sigma}_{ij} = C_{ijkl}\dot{\varepsilon}^{e}_{kl(n+1)}$	
$\dot{\varepsilon}^{p}_{ij} = \dot{\lambda}\frac{\partial \varphi}{\partial \sigma_{ij}}$	(Flow rule)
$\varphi \leq 0$	(Yield function)
$\dot{\lambda} > 0$	Normality parameter
$\dot{\lambda}\varphi = 0$	Kuhn-Tucker condition
$\dot{\lambda}\dot{\varphi} = 0$	Consistency condition

The normality rule is used to obtain the associated plastic strain. From the associative flow rule:

$$\dot{\varepsilon}^{p}_{ij} = \dot{\lambda}\frac{\partial \bar{\sigma}(\sigma_{ij})}{\partial \sigma_{ij}} \tag{4.1}$$

The numerical procedure used to update the stress state involves finding the unknown $\dot{\lambda}$ (normality parameter). At the end of the iteration all kinematics and stresses are updated using $\dot{\lambda}$. It should be noted that $\Delta\lambda = \Delta\bar{\varepsilon}^{p}$ as follows

$$\Delta\bar{\varepsilon}^{p} = \frac{\sigma_{ij}\dot{\varepsilon}^{p}_{ij}}{\bar{\sigma}(\sigma_{ij})} = \frac{\sigma_{ij}\Delta\lambda\frac{\partial \bar{\sigma}(\sigma_{ij})}{\partial \sigma_{ij}}}{\bar{\sigma}(\sigma_{ij})} = \frac{\Delta\lambda\ \bar{\sigma}(\sigma_{ij})}{\bar{\sigma}(\sigma_{ij})} = \Delta\lambda \tag{4.2}$$

where $\Delta\bar{\varepsilon}^{p}$ is the equivalent plastic strain increment and $\bar{\sigma}(\sigma_{ij})$ is a first order homogenous function, i.e. $\bar{\sigma}(\sigma_{ij}) = \bar{\sigma}(\sigma_{ij})\frac{\partial \bar{\sigma}(\sigma_{ij})}{\partial \sigma_{ij}}$.

To obtain $\Delta\bar{\varepsilon}^p$, $\bar{\sigma}$ and $\frac{\partial\bar{\sigma}}{\partial\sigma_k}$ must be calculated. Yoon et al. (2004) derived explicit forms of these terms for the Barlat YLD2000 yield function.

The strain increments, $\Delta\varepsilon_{ij(n+1)}$, the previous total stress state, σ_{ij}, and history variables are given by the FEM code at the beginning of each time step. The strain increment is initially assumed to be elastic; thus, a trial elastic stress state is calculated using previously converged values of the state variables.

$$\sigma_{ij(n+1)}^{(trial)} = \sigma_{ij(n)} + C_{ijkl}\Delta\varepsilon_{kl(n+1)} \tag{4.3}$$

If the new stress state lies outside the yield surface, this trial state must be corrected to calculate the plastic stress state. Using this trial stress value, the yield function, $\bar{\sigma}_{(n+1)}^{(trial)}$, and its derivative, $\frac{\partial\bar{\sigma}_{(n+1)}^{(trial)}}{\partial\sigma_{ij}}$ are calculated. The size of the yield locus, $\bar{\sigma}\left(\bar{\varepsilon}_{(n+1)}^{p}, \dot{\varepsilon}, T\right)$, is calculated using the hardening rule, as presented in Eq. (2.5). Next it is determined whether the calculated trial stress state lies inside the yield surface as

$$\emptyset\left(\bar{\sigma}_{(n+1)}^{(trial)}, \bar{\varepsilon}_{(n+1)}^{p}, \dot{\varepsilon}, T\right) = \bar{\sigma}\left(\sigma_{ij(n+1)}^{(trial)}\right) - \bar{\sigma}\left(\bar{\varepsilon}_{(n+1)}^{p}, \dot{\varepsilon}, T\right) \leq 0. \tag{4.4}$$

If this condition is met, the trial stress state is elastic and therefore reflects the material's actual stress state – this term should be returned to the FEM code. If the condition is not met, the material has yielded and the stress state is elastic-plastic. An iterative Newton-Raphson method is then used to return the trial stress state to the yield surface by calculating the normality factor, $\Delta\lambda$, using sub-steps m. Then, the stress state is updated for the next step as follows

$$\begin{aligned}\sigma_{ij(n+1)}^{(m+1)} &= C_{ijkl}\left[\varepsilon_{kl(n+1)} - \varepsilon_{kl(n+1)}^{p}\right] \\ &= C_{ijkl}\left[\varepsilon_{kl(n+1)} - \varepsilon_{kl(n)}^{p}\right] - C_{ijkl}\Delta\varepsilon_{kl}^{p}\end{aligned} \tag{4.5}$$

By combining Eq. (4.5) and Eq. (4.1), and knowing that $\sigma_{ij(n+1)}^{(m)} = \sigma_{ij(n+1)}^{(trial)}$, Eq. (4.5) becomes

$$\sigma_{ij(n+1)}^{(m+1)} = \sigma_{ij(n+1)}^{(m)} - \Delta\lambda\, C_{ijkl} \frac{\partial \bar{\sigma}_{(n+1)}^{(m)}}{\partial \sigma_{ij}} \tag{4.6}$$

The yield function and hardening rule are calculated using this new stress state and the yielding check is performed again.

$$\begin{aligned} &\emptyset^{(m+1)}\left(\bar{\sigma}_{(n+1)}^{(m+1)}, \bar{\varepsilon}_{(n+1)}^{p(m+1)}, \dot{\varepsilon}, T\right) = \\ &\bar{\sigma}\left(\sigma_{ij(n+1)}^{(m+1)}\right) - \bar{\sigma}\left(\bar{\varepsilon}_{(n+1)}^{p(m+1)}, \dot{\varepsilon}, T\right) \leq 0. \end{aligned} \tag{4.7}$$

The iteration procedure is repeated until plastic consistency is restored to within a defined tolerance, i.e. $\emptyset^{(m+1)}\left(\bar{\sigma}_{(n+1)}^{(m+1)}, \bar{\varepsilon}_{(n+1)}^{p(m+1)}, \dot{\varepsilon}, T\right) \leq \delta$ where δ is a small number. The graphical interpretation of this iterative procedure is shown in Figure 4.1. At each iteration, a tangent cut is defined on which the new variables are projected to initiate the next iteration; hence, the trial stress state is iteratively returned to the yield surface.

To solve for the normality parameter, $\Delta\lambda$, Eq. (4.4) is simplified using a Taylor expansion as follows

$$\begin{aligned} 0 = \emptyset^{(m)}\left(\bar{\sigma}_{(n+1)}^{(m)}, \bar{\varepsilon}_{(n+1)}^{p(m)}, \dot{\varepsilon}, T\right) + \frac{\partial \emptyset^{(m)}}{\partial \sigma_{ij}}\left(\sigma_{ij(n+1)}^{(m+1)} - \sigma_{ij(n+1)}^{(m)}\right) + \\ \frac{\partial \emptyset^{(m)}}{\partial \bar{\varepsilon}^{p}}\left(\bar{\varepsilon}_{(n+1)}^{p(m+1)} - \bar{\varepsilon}_{(n+1)}^{p(m)}\right) \end{aligned} \tag{4.8}$$

From Eq. (4.6) and Eq. (4.8) and knowing that $\bar{\varepsilon}_{(n+1)}^{p(m+1)} - \bar{\varepsilon}_{(n+1)}^{p(m)} = \Delta\lambda$, the normality factor, $\Delta\lambda$, is obtained as

$$\Delta\lambda = \frac{\emptyset^{(m)}\left(\bar{\sigma}_{(n+1)}^{(m)}, \bar{\varepsilon}_{(n+1)}^{p(m)}, \dot{\varepsilon}, T\right)}{\frac{\partial \bar{\sigma}_{(n+1)}^{(m)}}{\partial \sigma_{ij}} C_{ijkl} \frac{\partial \bar{\sigma}_{(n+1)}^{(m)}}{\partial \sigma_{kl}} - \frac{\partial R^{(m)}}{\partial \bar{\varepsilon}^{p}}} \tag{4.9}$$

At the end of each step, the thickness strain is calculated using a Secant iteration method and is returned to the FEM code. The procedure used to update the stress state is shown in Table 4.2

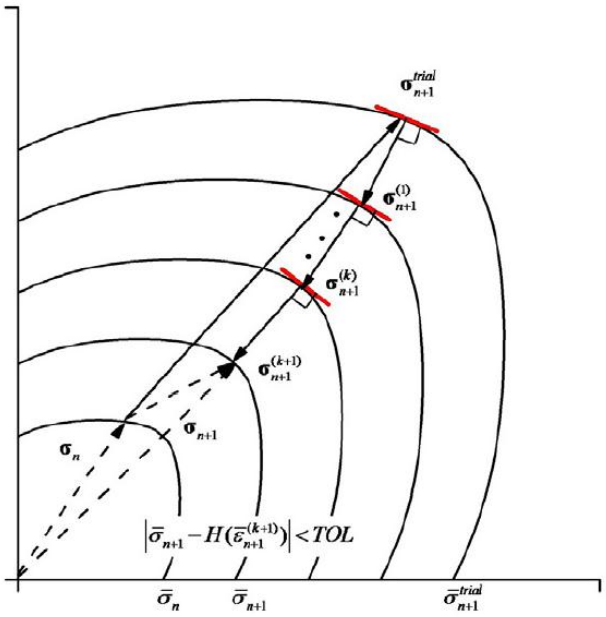

Figure 4.1 Geometric interpretation of the cutting-plane algorithm

The linearized yield function in Eq. (4.8) defines tangent cuts of the yield function until the stress state is completely returned to the yield surface. This implementation was quite fast and the solution converged within 2-5 iterations. The implementation of the constitutive equation is used along with LS-DYNA's explicit solver; hence calculation of a consistent tangent modulus is not needed. In order to check the accuracy of the developed user defined material subroutine according to the above implementation method, single element simulations performed to see if the UMAT is capable of reproducing the material anisotropy and stress-strain curves at different temperatures. Single element analysis and a comparison between calculated plastic anisotropy parameters and measured data was satisfactory. Validation of the developed UMAT against the tensile and stretch forming tests in Chapters 2 and 3 is presented in the following sections of this chapter.

Table 4.2 Stress update algorithm based on incremental theory of plasticity

1. Geometry update

$$\Delta\varepsilon_{ij(n+1)},\ \sigma_{ij(n)},\ \bar{\varepsilon}_n^p$$

2. Initialize

$$\text{m=0},\ \Delta\lambda = 0$$

3. Elastic predictor (compute trial state, flow stress and yield function)

$$\sigma_{ij(n+1)}^{(0)} = \sigma_{ij(n)} + C_{ijkl}\Delta\varepsilon_{kl(n+1)}$$

$$\bar{\varepsilon}_{(n+1)}^{p(0)} = \bar{\varepsilon}_{(n)}^{p}$$

$$\bar{\sigma}_{(n+1)}^{(0)} = \bar{\sigma}\left(\sigma_{ij(n+1)}^{(0)}, T\right)$$

$$R^{(0)} = \bar{\sigma}\left(\bar{\varepsilon}_{(n+1)}^{p(0)}, \dot{\varepsilon}, T\right)$$

$$\emptyset_{(n+1)}^{(0)} = \bar{\sigma}_{(n+1)}^{(0)} - R^{(0)}$$

4. Check yield condition

If $(\emptyset_{(n+1)}^{(0)} < 0)$ then material is elastic;

$$\varepsilon_{ij(n+1)}^{p} = \varepsilon_{ij(n+1)}^{p(0)}$$

$$\sigma_{ij(n+1)} = \sigma_{ij(n+1)}^{(0)}$$

$$\bar{\varepsilon}_{(n+1)}^{p} = \bar{\varepsilon}_{(n+1)}^{p(0)}$$

else material is plastic

$$\Delta\lambda = \frac{\emptyset^{(m)}\left(\bar{\sigma}_{(n+1)}^{(m)}, \bar{\varepsilon}_{(n+1)}^{p(m)}, \dot{\varepsilon}, T\right)}{\frac{\partial\bar{\sigma}_{(n+1)}^{(m)}}{\partial\sigma_{ij}} C_{ijkl} \frac{\partial\bar{\sigma}_{(n+1)}^{(m)}}{\partial\sigma_{kl}} - \frac{\partial R^{(m)}}{\partial\bar{\varepsilon}^{p}}}$$

$$\sigma_{ij(n+1)}^{(m+1)} = \sigma_{ij(n+1)}^{(m)} - \Delta\lambda\, C_{ijkl} \frac{\partial\bar{\sigma}_{(n+1)}^{(m)}}{\partial\sigma_{ij}}$$

$$\Delta\varepsilon_{ij(n+1)}^{p(m+1)} = \Delta\lambda \frac{\partial\bar{\sigma}_{(n+1)}^{(m+1)}}{\partial\sigma_{ij}}$$

$$\bar{\varepsilon}_{(n+1)}^{p(m+1)} = \bar{\varepsilon}_{(n+1)}^{p(m)} + \Delta\lambda$$

$$\bar{\sigma}_{(n+1)}^{(m+1)} = \bar{\sigma}\left(\sigma_{ij(n+1)}^{(m+1)}, T\right)$$

$$R^{(m+1)} = \bar{\sigma}\left(\bar{\varepsilon}_{(n+1)}^{p(m+1)}, \dot{\varepsilon}, T\right)$$

5. Check convergence

If $\left(\bar{\sigma}_{(n+1)}^{(m+1)} - R^{(m+1)}\right) \leq \delta$ then

$$\Delta\varepsilon_{ij(n+1)}^{p} = \Delta\varepsilon_{ij(n+1)}^{p(m+1)}$$

$$\sigma_{ij(n+1)} = \sigma_{ij(n+1)}^{(m+1)}$$

$$\bar{\varepsilon}_{(n+1)}^{p} = \bar{\varepsilon}_{(n+1)}^{p(m+1)}$$

else m=m+1 and go to (4.)

4.2 Numerical simulation of tensile tests

The first application used to validate the UMAT implementation is the tensile test work by McKinley (2010) as presented in Chapter 2 of this thesis. A simple model of this tensile test was built to confirm the ability of the UMAT constitutive model to reproduce the measured tensile data. Only one-quarter of the specimen is modeled due to symmetry. Three-node Belytschko-Tsay (Belytschko and Tsay, 1981) shell elements with 5 through-thickness integration points were used to generate the mesh. A mesh with 1.0mm elements is shown in Figure 4.2. A coarser mesh is used for the grip area. Symmetry boundary conditions are applied to the nodes on the left and bottom edges of the model.

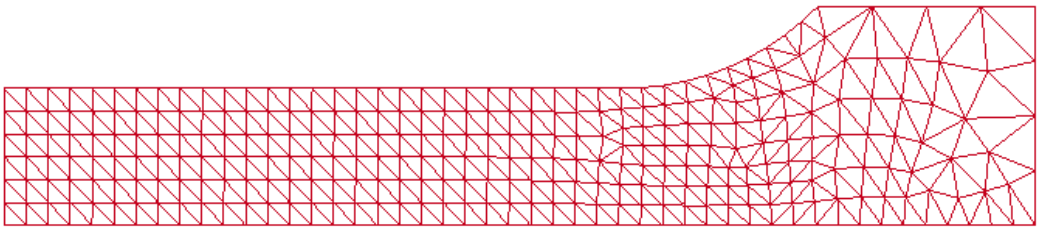

Figure 4.2 Mesh model of tensile test showing the fine mesh.

An explicit dynamic time integration scheme was adopted and the simulations were time scaled by a factor of 1000 to reduce the computation time. All tensile test simulations are isothermal. Velocity boundary conditions corresponding to nominal strain rates of $7 \times 10^{-2}, 7 \times 10^{-3}$ and $7 \times 10^{-4}\ s^{-1}$, were applied to the grip end.

In order to study the effect of mesh size, three different mesh models, with 4, 2, and 1 mm element sizes, were built to predict the deformed shapes of the tensile samples at 250°C and a strain rate of 0.07 s^{-1}, as shown in Figure 4.3. Figure 4.4 compares the predicted stress-strain curves using each mesh, with sample temperatures set at 200°C and the strain rate at $7 \times 10^{-2}\ s^{-1}$. As can be seen, mesh size does not have a significant effect on the material

hardening response; however, the onset of diffuse necking strongly depends on the size of the elements. All three meshes result in approximately the same maximum tensile stress values. The only difference can be seen in the strain values corresponding to the onset of localization. Simulations using fine, medium and coarse meshes need about 270, 43 and 5 minutes, respectively, to complete for the same temperature and strain rate condition. Based on required CPU times for each mesh size and the calculated stress-strain curves shown in Figure 4.4, the medium mesh size was used to validate the numerical results against the experimental data.

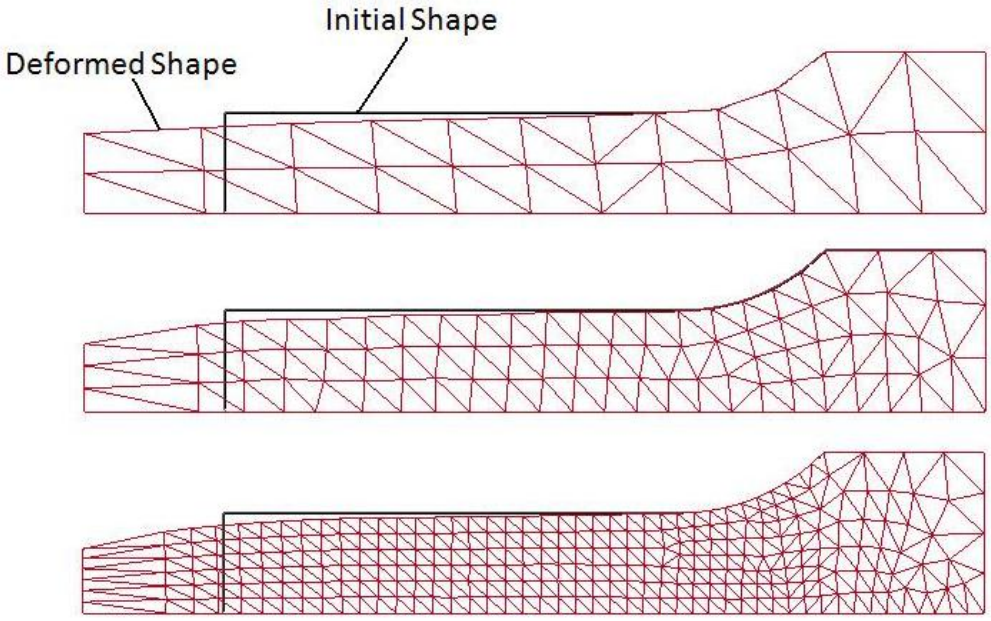

Figure 4.3 Deformed shapes of the tensile sample at 250°C and strain rate of 0.07 s^{-1} using three different mesh models.

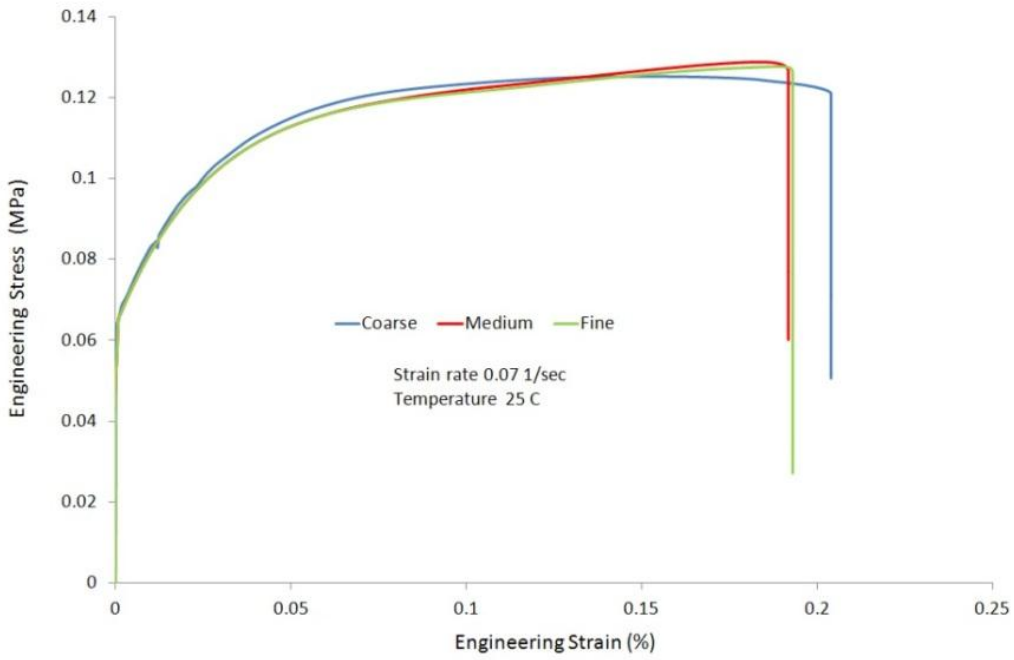

Figure 4.4 Effect of mesh size on numerical results for stress-strain curve.

Figure 4.5 compares the predicted tensile stress-strain response with measured data at 25, 200 and 250°C, and at different strain rates. It can be seen that the model predictions at different temperatures are in good agreement with the measured data. The model underestimates the stress values at strains lower than 10% for a strain rate of 0.07 s^{-1}. For all other cases, the predictions are in good agreement with or are slightly higher than the measured data. Models at room temperature predict post-uniform stresses reasonably accurately for different strain rates, although greater deviations are observed at higher temperatures. There is also a similar difference between the experimental and numerical results in the strain values corresponding to the onset of localization.

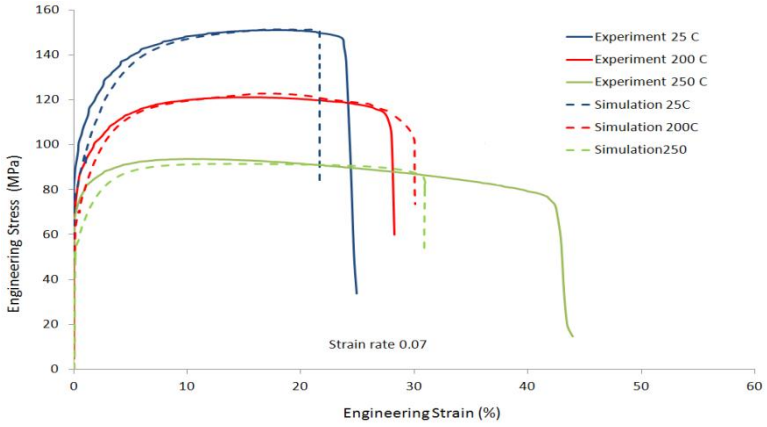

(a)

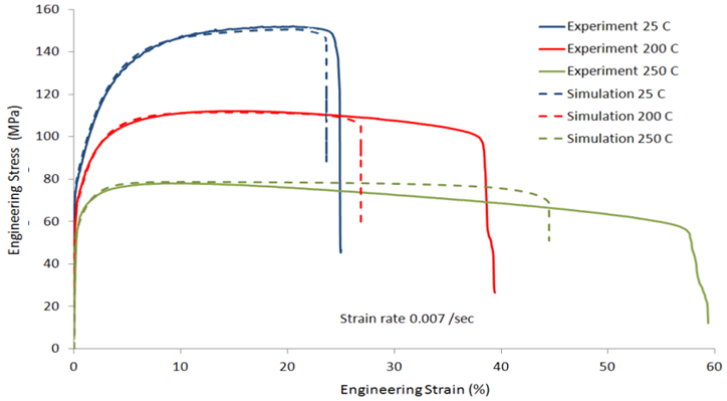

(b)

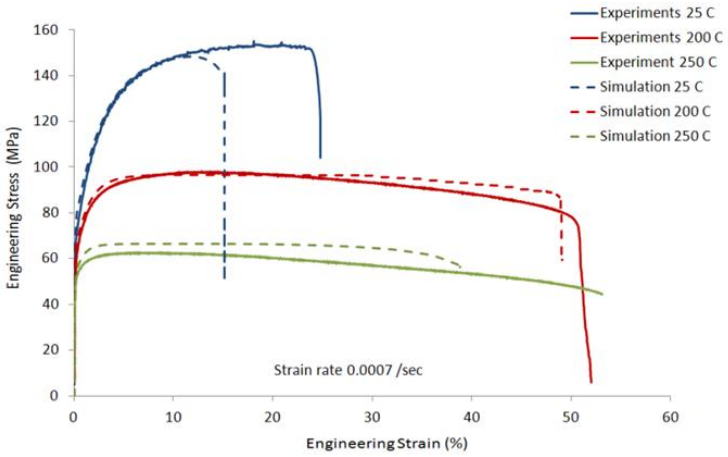

(c)

Figure 4.5 Comparison of numerical results with measured engineering stress-strain curves at (a) 0.07, (b) 0.007 and (c) 0.0007 s^{-1} strain rates.

Figure 4.6 provides numerical results that illustrate the effect of strain rate on the material response at room temperature and 250°C. The model captures both the low strain rate sensitivity induced at low forming temperature and the strong strain rate sensitivity at elevated temperatures.

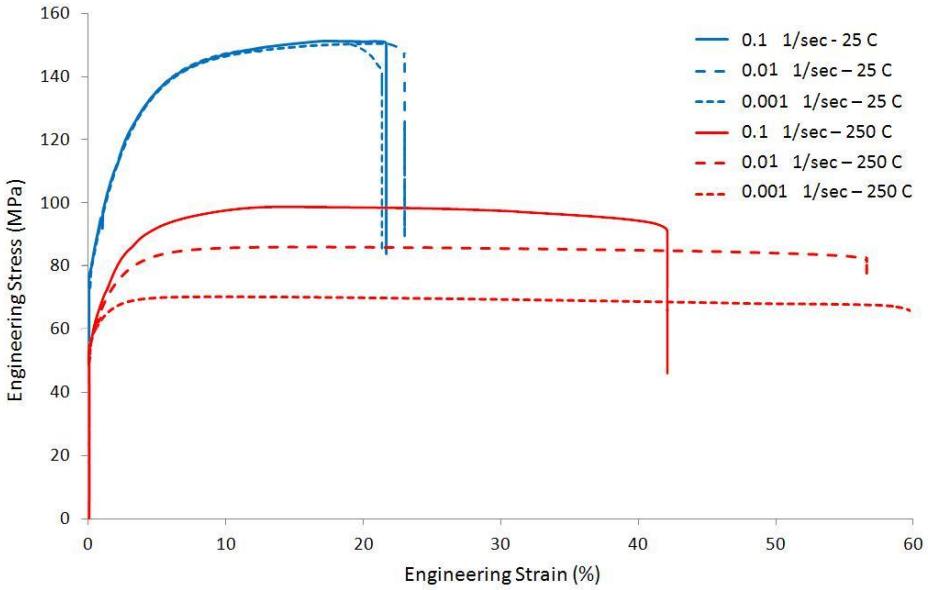

Figure 4.6 Effect of strain rate on predicted stress-strain response and rate sensitivity.

4.3 Numerical simulation of stretch forming with hemispherical punch

The hemispherical punch test results (Chapter 3) were also used to assess the numerical predictions of material behaviour. Isothermal forming process models that take into account varying forming speeds and sample temperatures were developed using the UMAT implemented within LS-DYNA. Predicted values of load-displacement response and strain distributions within formed parts were compared against experimental data to evaluate the material model accuracy.

4.3.1 Numerical models

Solid models of the tooling and blank were used to generate the mesh model using Altair HyperMesh. Due to the symmetry of the sample geometry and loading, only one-quarter of the geometry was meshed. Tools were modelled with four node rigid quadrilateral elements.

The test samples were modelled using Belytschko-Tsay elements (Belytschko and Tsay, 1981) with 7 through-thickness integration points. The tooling and blank meshes are shown in Figure 4.7 (a) and (b), respectively. A constant temperature was defined for the blank elements mimicking the conditions for the experiments which were approximately isothermal.

Symmetry boundary conditions were applied to the blank. The tooling constraints were applied through definition of rigid material; the die is fixed in all directions while the clamp and punch can move freely to close the lock-bead and form the blank. While the punch is under displacement control, the clamp is operated under load control. A constant force, matching that used in the experiments, is applied to the clamp die after an initial ramp-up. The punch then ramps up to a prescribed velocity. Coefficients of friction of 0.043 and 0.15 were used to describe sample-punch and sample-die contacts, respectively.

The actual simulations were time-scaled by a factor of 1000 to save computation time. Since there was no heat transfer between the contact surfaces, the only time-dependent material property that had to be scaled was strain rate sensitivity. Therefore, while the punch speed was increased by a factor of 1000, the strain rate was reduced by the same factor to mimic the real strain rate.

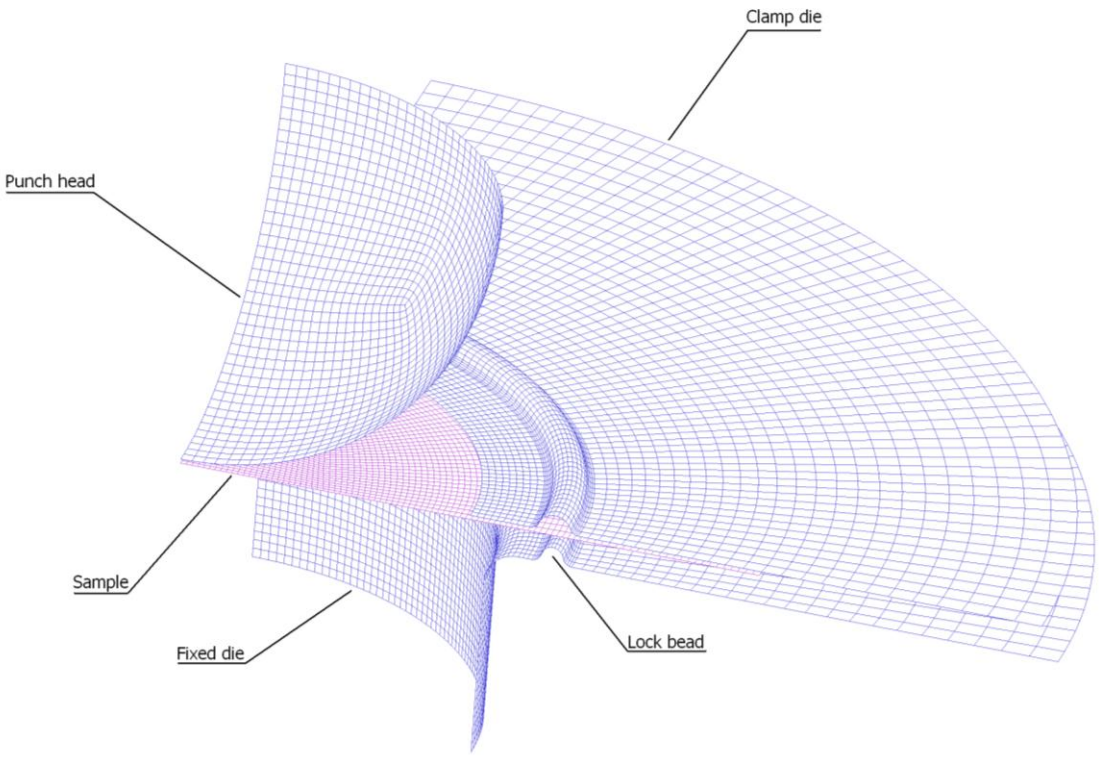

(a)

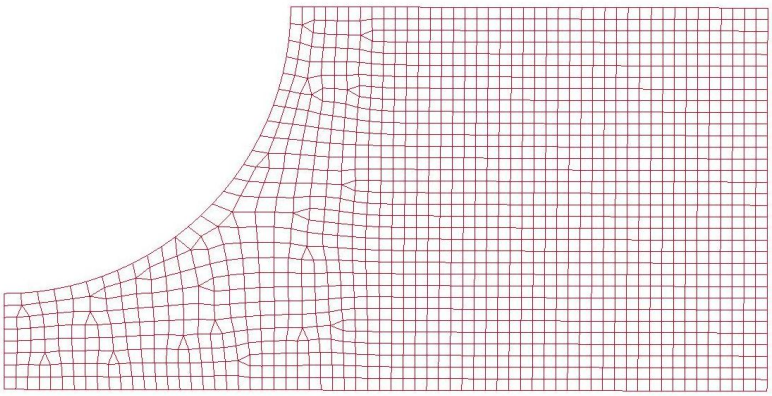

(b)

Figure 4.7 Mesh model of the quarter tooling and quarter blank (a) and the quarter of 25.4mm dog-bone sample (b)

4.3.2 Results

4.3.2.1 Predicted deformation and strains

Figure 4.8 through Figure 4.11 compare predicted and experimentally measured major and minor strain distributions experienced along the centerline (from pole to edge) of samples. Experimental results are shown at 10 measurement points and error bars are defined using the standard error definition. Both numerical and measured values are plotted for each sample geometry at "safe" dome heights for which necking was not yet observed. Room temperature distributions are plotted at 10mm, 20mm, 20mm and 25mm dome heights, while warm forming results (at 250°C) are presented for 15mm, 30mm, 35mm and 40mm, for 25.4, 50.8 and 76.2mm wide dog-bones and 203.2mm×203.2mm samples, respectively. All samples were formed using a punch speed of 1.6mm/s, a clamping force of 30kN and Teflon sheet lubricant at two different forming temperature levels, that is, room temperature and 250°C. The same forming conditions were considered in the numerical simulations.

The figures indicate that the predicted results agree quite well with experimental findings. In general, the models overestimate the major strain distributions at both temperatures; however, the difference is greater at room temperature. Specifically, the models predict that maximum major strain occurs closer to the pole (between 3~4mm closer to the pole) than the experimental results demonstrate. A smaller difference is shown between numerical and experimental results derived from plane strain samples (76.2mm wide dog-bones), where the location of the maximum major strain is predicted fairly well. The value of major strain at both temperature levels is over-estimated by roughly 15%.

The figures also show that predicted negative minor strain distributions obey the same trend observed in the experimental results; however, the magnitudes are somewhat overestimated, particularly in the area directly surrounding the pole. The 25.4mm wide dog bone model produced the least accurate estimation, overestimating the maximum minor strain value by nearly 40% (over experimental measurements). Some of this error could be associated with the friction coefficient since this controls the sample draw-in. Friction measurements are not available for high temperature conditions – this should be addressed in future research.

Since the predicted results generally overestimate both major and minor strains, the numerical model will likely predict limiting strains, and failure, at earlier forming steps than would

occur in reality. Furthermore, model predictions are likely to be less accurate at negative minor strain states.

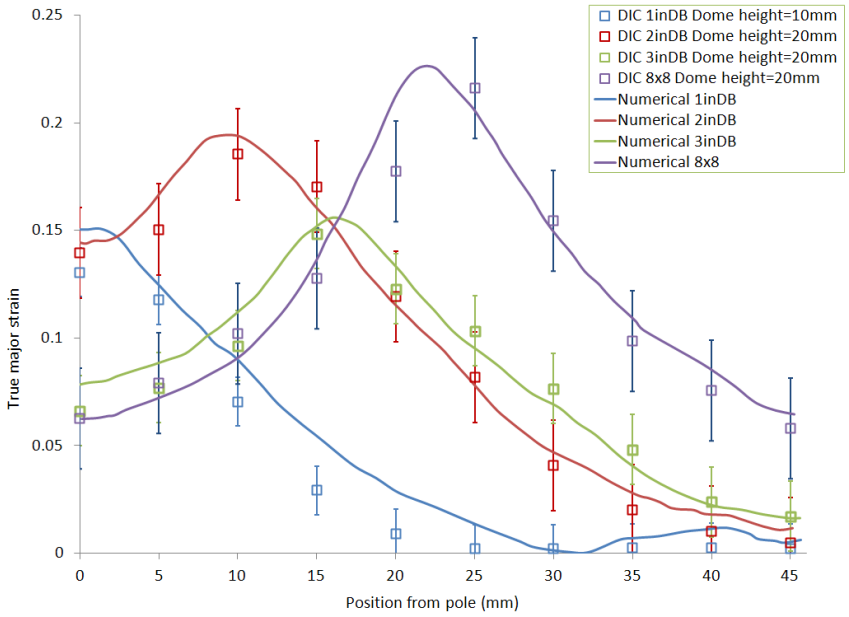

Figure 4.8 True major strain distribution vs. distance from the pole of samples stretched at room temperature with 1.6mm/s punch speed. Results are shown for dome heights of 10mm, 20mm, 20mm, and 25mm for 25.4mm, 50.8mm, and 76.2mm wide dog-bones and 203.2×203.2mm samples, respectively.

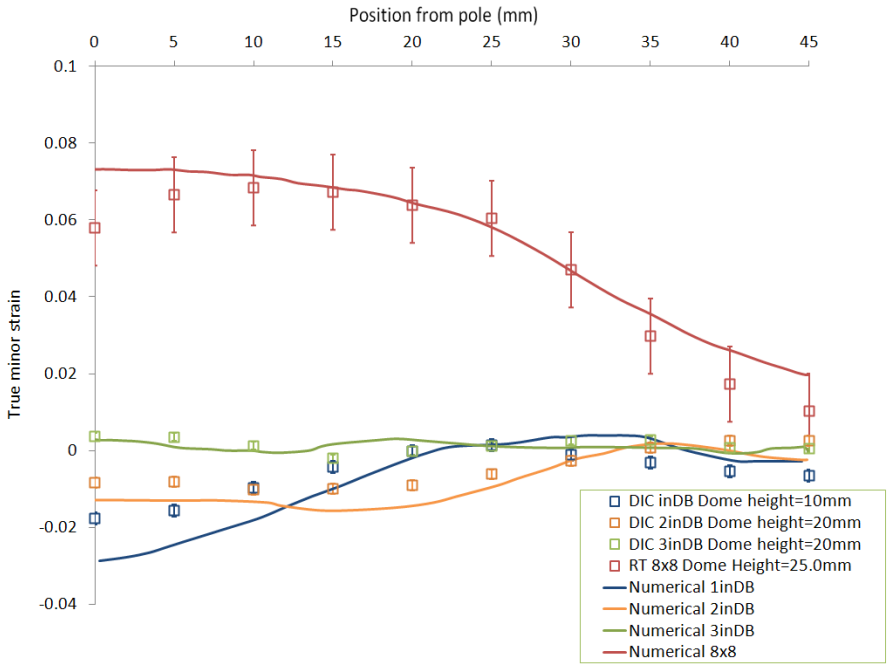

Figure 4.9 True minor strain distribution vs. distance from the pole of samples stretched at room temperature with 1.6mm/s punch speed. Results are shown for dome heights of 10mm, 20mm, 20mm, and 25mm for 25.4mm, 50.8mm, and 76.2mm wide dog-bones and 203.2×203.2mm samples, respectively.

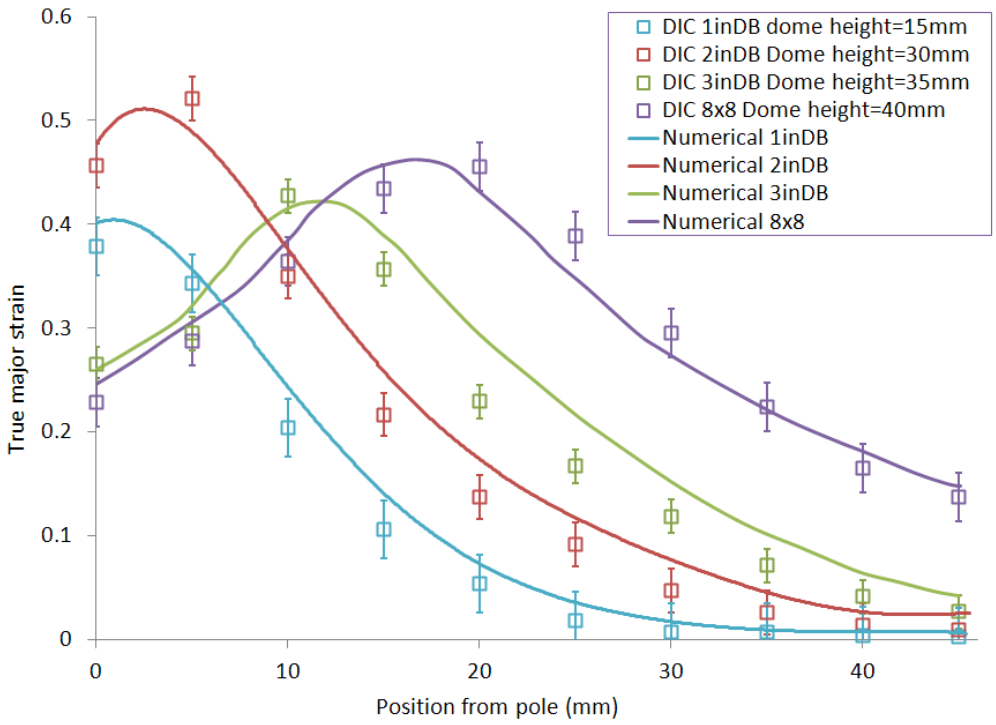

Figure 4.10 True major strain distribution vs. distance from the pole of samples stretched at 250°C with 1.6mm/s punch speed. Results are shown for dome heights of 15mm, 30mm, 35mm, and 40mm for 25.4mm, 50.8mm, and 76.2mm wide dog-bones and 203.2×203.2mm samples, respectively.

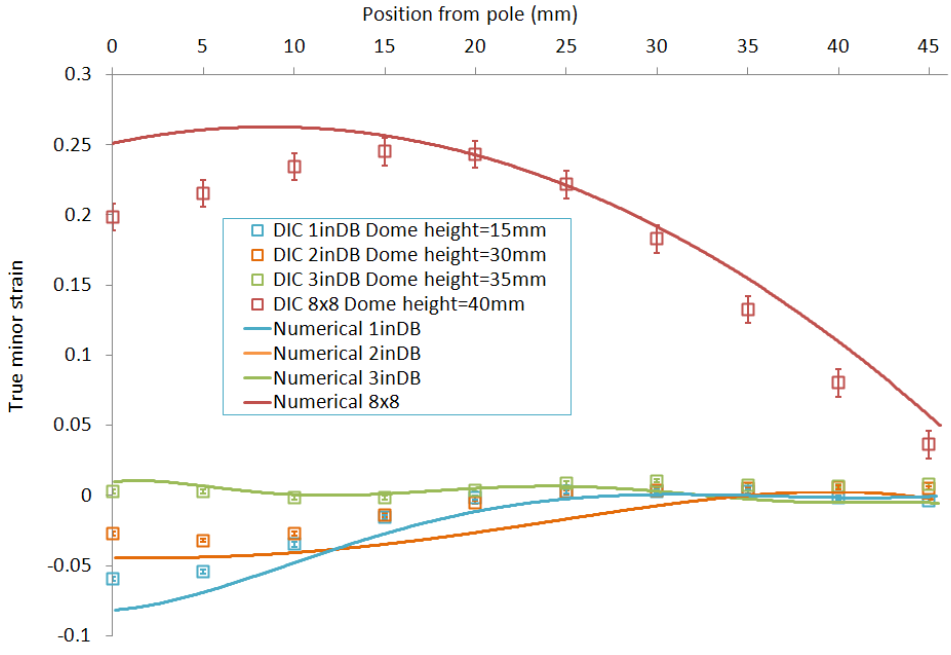

Figure 4.11 True minor strain distribution vs. distance from the pole of samples stretched at 250°C with 1.6mm/s punch speed. Results are shown for dome heights of 15mm, 30mm, 35mm, and 40mm for 25.4mm, 50.8mm, and 76.2mm wide dog-bones and 203.2×203.2mm samples, respectively.

4.3.3 Predicted punch force-displacement

Figure 4.12 compares the predicted and measured punch force vs. punch displacement results for 203.2×203.2mm Teflon sheet lubricated samples stretched at a punch speed of 1.6mm/s and clamping force of 30kN, at both room temperature and 250°C. As can be seen, the predictions agree well with measured data; however, the models are unable to capture the sharp drop in punch force that results from material failure. The predicted values are generally larger than the experimental results at earlier forming steps, but the experimental and numerical curves approach each other as the punch advances and the sample is formed. The decrease in punch force at 250°C is caused by material softening at elevated temperatures.

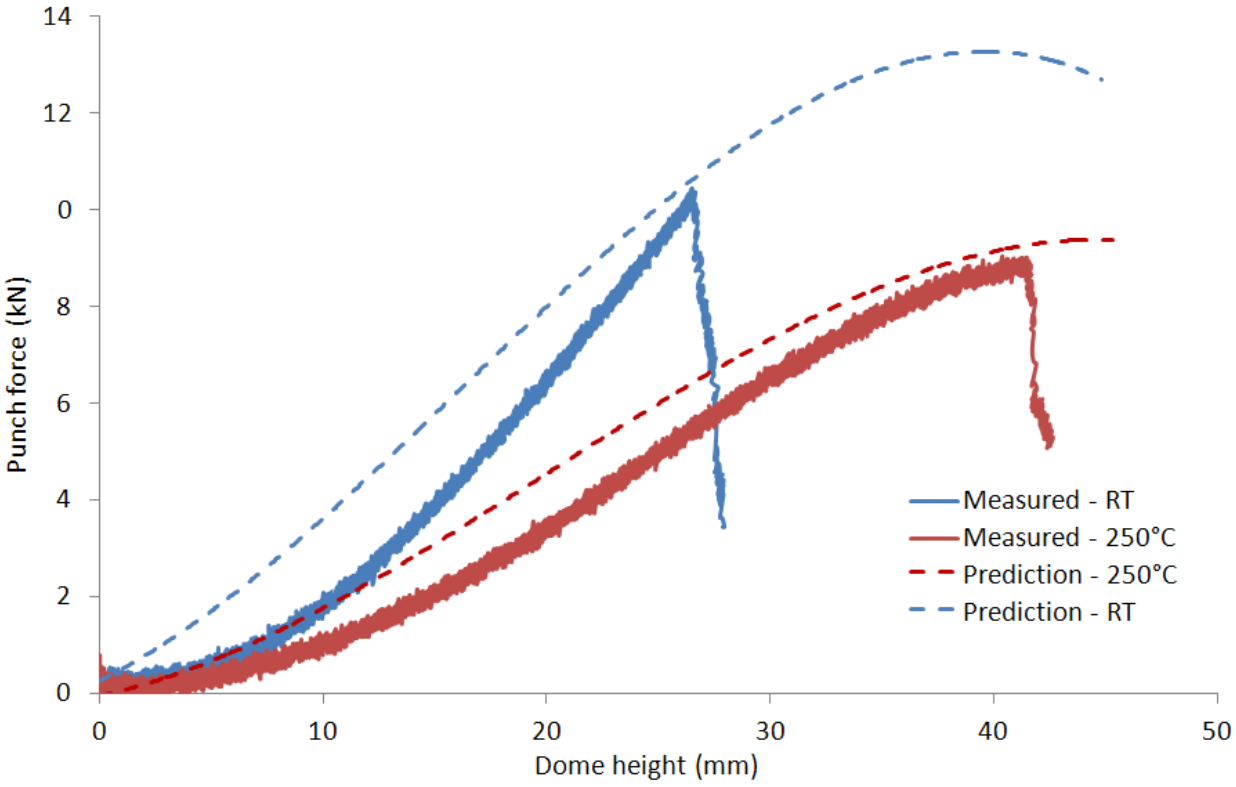

Figure 4.12 Punch force vs. punch displacement for deep drawing 228.6 mm using Teflon sheet lubricant and 8mm/s punch speed. Predicted results are compared against experimental data gathered at room temperature (RT) and 250°C.

4.3.4 Failure prediction

From the previous sections, it is evident that the finite element model is capable of predicting the strains during forming relatively well, however, the onset of failure is not predicted well, as seen in Figure 4.14, which indicates that additional localization or failure criteria are required. In the current work, the forming limit curves (FLCs) developed in Chapter 3 corresponding to the appropriate simulation temperature are used to assess whether the predicted strains in the finite element simulations of warm deep drawing exceed the material forming limits. This comparison is performed as a post-processing operation using the software Ls-Prepost. Numerical simulations were performed up to a dome height of 50mm and failure is predicted by comparing the calculated strains with the forming limit strains.

Figure 4.13 and 4.14 show isothermal stretch simulation results at room temperature and 250°C, respectively. Four different sample geometries are presented for each temperature level to evaluate the model's ability to predict failure at different strain paths. The major and minor strains of each element were projected onto the FLD shown on the right, while the failure location predicted by the analysis is shown schematically on the left. The data is shown for the time step at which the strains first exceed the forming limit curve which corresponds to the predicted onset of failure. In the contour plots (left figures) the elements whose strains lie below the FLC are coloured green, whereas elements coloured red have strains in excess of the forming limits.

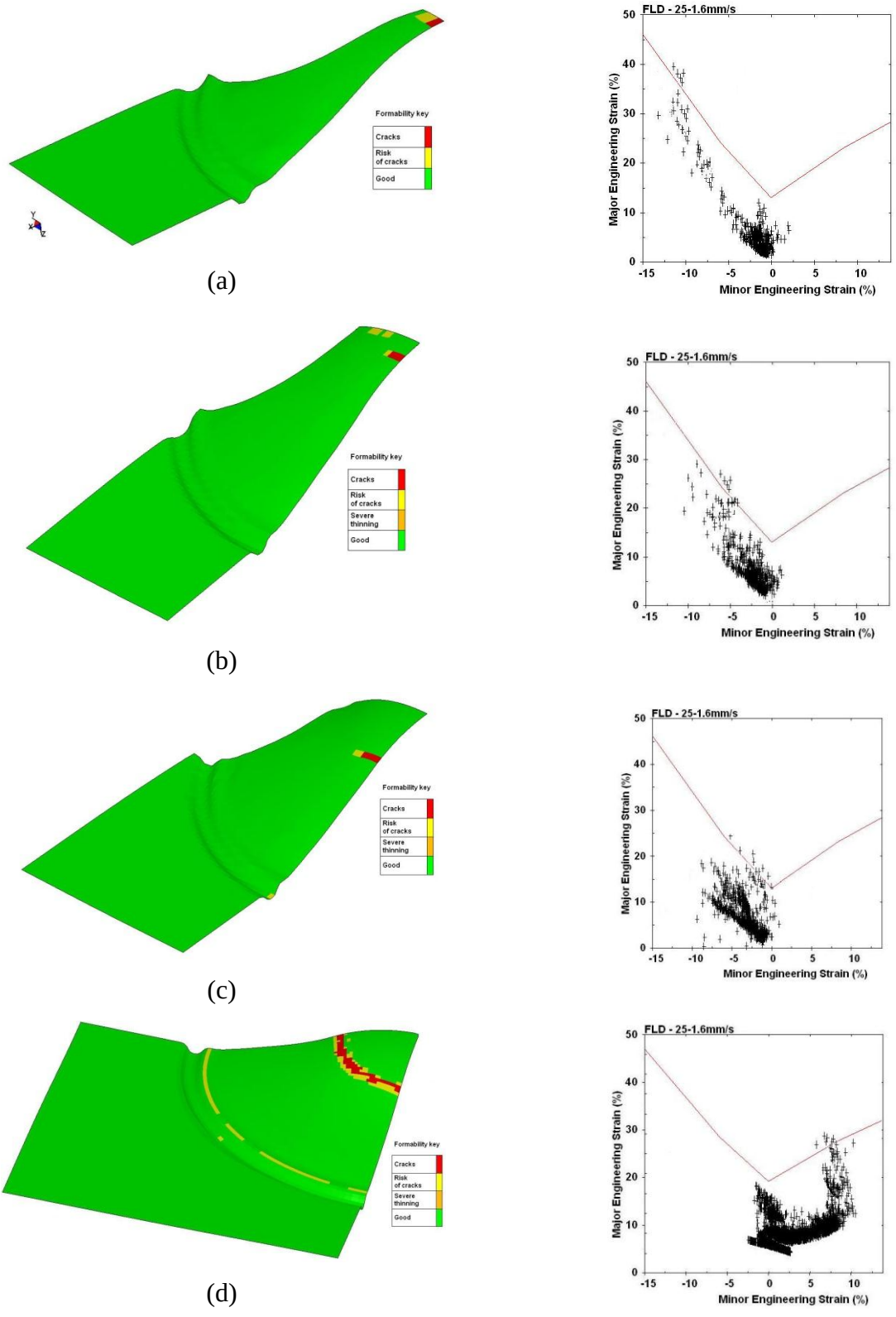

Figure 4.13 Failure prediction of stretching different sample geometries at room temperature with 1.6mm/s punch speed, 30kN clamping force and Teflon sheet lubricant at room temperature; (a) 25.4mm, (b)50.8mm, and 76.2mm wide dog-bones and 203.2×203.2mm sample

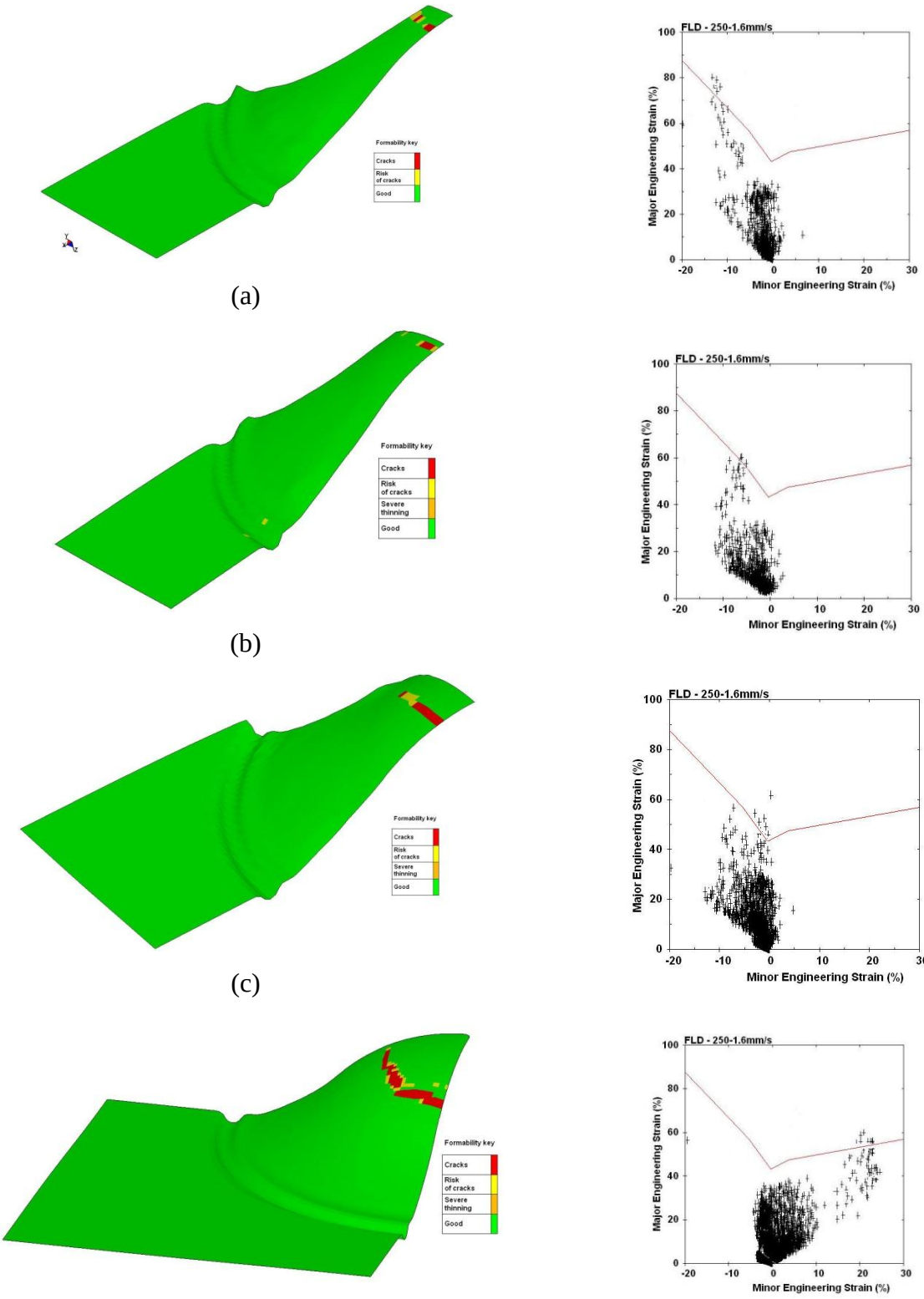

Figure 4.14 Failure prediction of stretching different sample geometries at 250°C with 1.6mm/s punch speed, 30kN clamping force and Teflon sheet lubricant at room temperature; (a) 25.4mm, (b)50.8mm, and 76.2mm wide dog-bones and 203.2×203.2mm sample

The corresponding punch depth at which the sheet is predicted to fail is shown in Table 4.3. The predictions compare well with the experimental data; although the predicted punch depths at failure lie roughly 1-3 mm below the measured values. This level of error is consistent with the differences in predicted versus measured major and minor strain distributions, as seen in Figures 4.8-4.11. The punch depths to failure predicted for room temperature and 250°C have been plotted on Figure 4.15, from which it is evident that the improvement in the predicted punch depth to failure is greatly improved through incorporation of the warm forming limit curve data to predict onset of failure. The error bars shown in Figure 4.15 are based on the standard deviation of measured values for each geometry at the specified forming temperature. As seen, the predictions underestimate the punch depth to failure for all cases. The predicted values at room temperature agreed well with measurements. The prediction error is larger at 250°C.

Table 4.3 Predicted and measured failure punch depths

	25.4mm wide		50.8mm wide		76.2mm wide		203.2mmx203.2mm	
	Prediction (mm)	**Measurement (mm)**	**Prediction (mm)**	**Measurement (mm)**	**Prediction (mm)**	**Measurement (mm)**	**Prediction (mm)**	**Measurement (mm)**
25°C	**12.6**	**13.5**	**19.2**	**20**	**18.3**	**19**	**22.9**	**25**
250°C	**18.5**	**20**	**29.1**	**31**	**36.0**	**37**	**37.1**	**40.2**

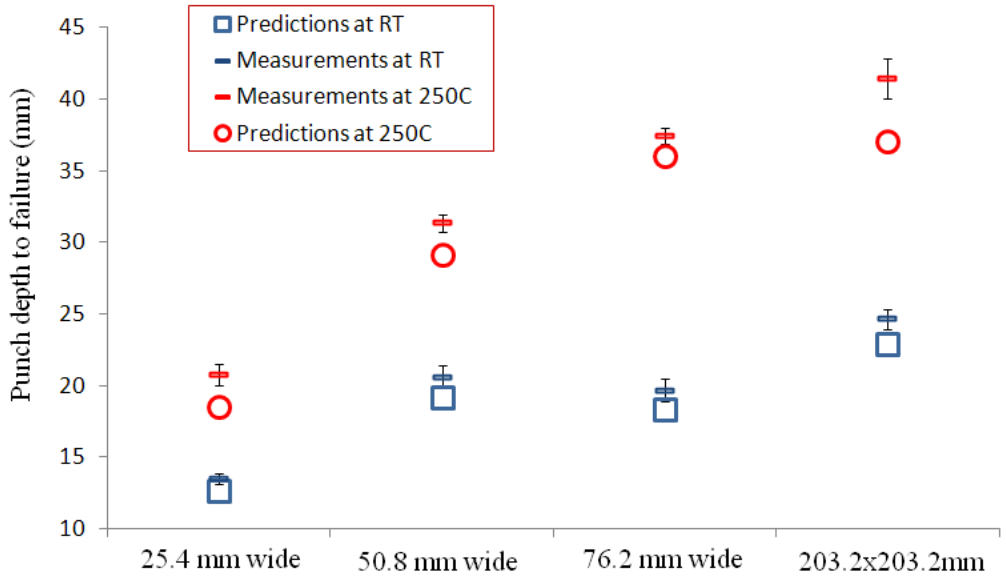

Figure 4.15 FLC-based punch depth to failure.

Figure 4.16 and 4.17 show the as-tested samples corresponding to the forming simulations at room temperature and 250°C, respectively. The location of failure is close to the pole of the 25.4mm wide dog bones, and moves towards the sample edge as sample width increases. Comparison of these figures with the predictions in Figures 4.13 and 4.14 reveals that the models also predict the location of failure fairly well at both temperature levels.

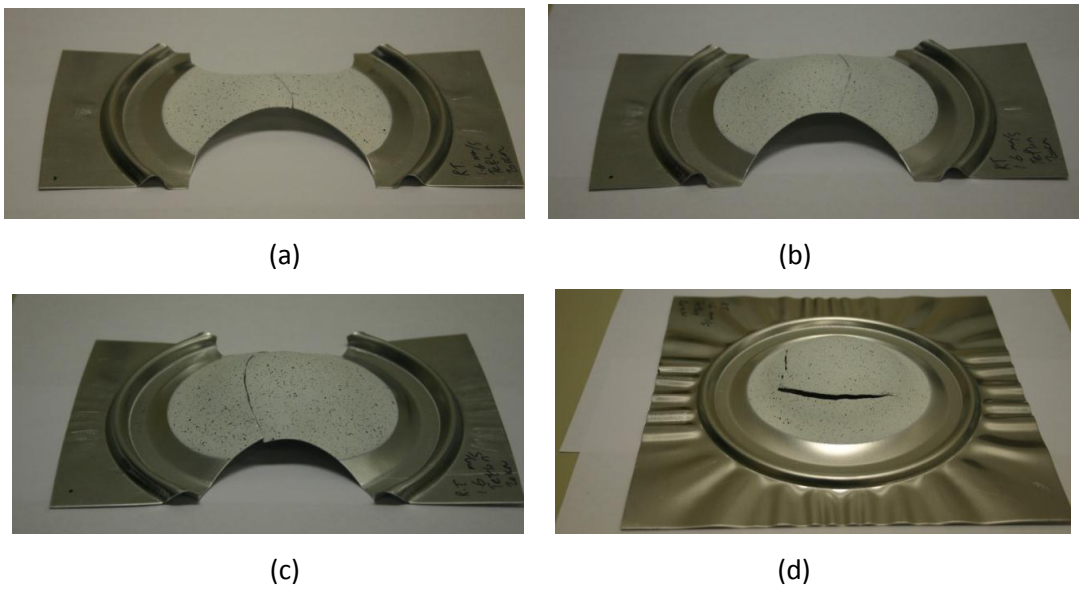

Figure 4.16 Experimental results of stretching different sample geometries with 1.6mm/s punch speed, 30kN clamping force and Teflon sheet lubricant at room temperature; (a) 25.4mm, (b)50.8mm, and 76.2mm wide dog-bones and 203.2×203.2mm sample

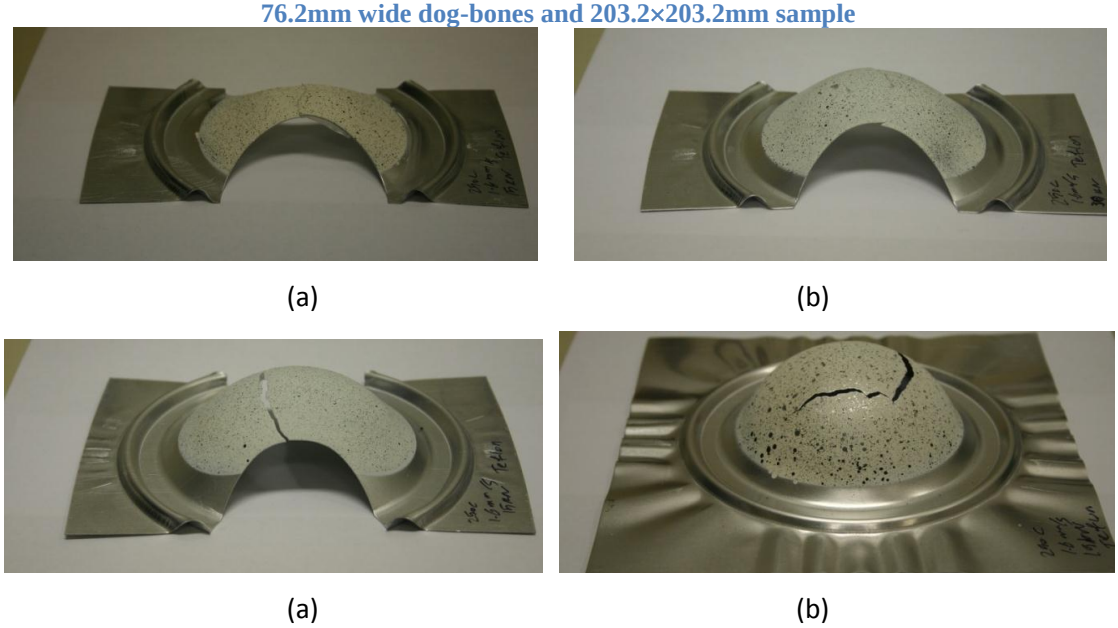

Figure 4.17 Experimental results of stretching different sample geometries with 1.6mm/s punch speed, 30kN clamping force and Teflon sheet lubricant at 250°C: (a) 25.4mm, (b) 50.8mm, (c) 76.2mm wide dog-bones and (d) 203.2×203.2mm sample

4.4 Summary

The preceding comparisons between the predicted and measured strains and load-displacement data over the range of temperatures considered provides an important validation of the developed Bergstrom-Barlat constitutive model and UMAT implementation. The good agreement between the predicted and measured dome heights to failure and the failure locations also supports the use of warm forming limit curves in FEM simulation of warm forming. It is important to note, that the experiments used to create the FLC data are the same experiments used here to assess the predictive ability of this failure criterion; thus, independent assessment of the FLC approach is necessary. Such an assessment is considered in the next chapter of this thesis which examines application of the constitutive model and failure criterion to two independent warm forming processes.

5 Simulation of the warm deep drawing of a circular cup

Two warm deep draw forming applications are considered as part of this research: (i) the warm deep drawing of a circular cup and (ii) the warm forming of an automotive heat exchanger component. Investigation of these two forming operations serves to further characterize the potential gains in formability of aluminum alloy sheet at elevated temperature using both isothermal and non-isothermal processes. Simulation of both forming operations is also undertaken to further assess the simulation framework presented in Chapter 4 of this thesis. The warm cup draw simulations are presented in this chapter, while the warm forming of the automotive heat exchanger component is presented in Chapter 6.

The warm cup draw experiments considered in this chapter were those performed by McKinley (2010) at the University of Waterloo. These experiments were simulated to validate the constitutive model and UMAT subroutine for isothermal and non-isothermal deep drawing applications. Predictions of the strain distribution and thinning within the deep drawn cups, as well as the predicted punch load versus displacement behaviour, were compared to measured data provided by McKinley (2010). Failure predictions based on the FLDs presented in Chapter 3 are also compared against McKinley's results.

5.1 Experimental setup

McKinley (2010) performed non-isothermal deep drawing of circular cups using a double acting servo-hydraulic press with 0.5 mm thick AA3003 aluminum alloy blanks with 203mm (8") and 229mm (9") diameter. A brief description of McKinley's experiments is provided below; the reader is referred to McKinley (2010) for a more detailed presentation of the experimental setup and results.

The tooling consists of a heated die and clamp that incorporate embedded cartridge heaters and a punch cooled by channels that circulate chilled water (Figure 5.1). A flat-bottomed cylindrical punch (101.5mm (4") diameter and 6.35mm punch corner radius), die, and clamp (229mm outer diameter and 6.35mm die entry radius without lock beads) were used. The clearance between the punch and the die was 2.38mm. The tooling material was H13 tool steel hardened to 52 Rockwell C. A schematic section of the tooling is shown in Figure 5.1 (a). Both the die and clamp contain four 867 Watt electrical resistance cartridge heaters. A

close up photo of the tooling is also provided in Figure 5.1 (b), showing the centering fixture used by McKinley (2010) to ensure proper positioning of the samples prior to forming. During testing, the die is held stationary while the punch and blank holder are moved using two hydraulic actuators controlled by MTS 407 controllers. Load cells were installed to measure tooling loads. Linear variable differential transformers (LVDTs) are used to measure the tooling displacements. The punch is displacement controlled and its maximum velocity is approximately 40 mm/s. The clamp is load controlled, so a constant blank holder force is maintained throughout the deep drawing process.

Embedded thermocouples were used to control the die and clamp temperature, between room temperature and 250°C. Chilled water at a constant temperature of 10°C was circulated through channels machined into the punch to maintain its temperature at about 14°C. The punch temperature was also monitored using embedded thermocouples. A data acquisition card attached to a PC was used to record the experimental data by means of a custom Labview program. The force and displacement of the punch and clamp, and the temperatures of the die, clamp and punch were also recorded.

Different configurations of die and punch temperatures and clamping force were considered by McKinley (2010); however, for the sake of brevity only a few were considered in the current simulation effort and are presented here. For all configurations, the punch temperature was kept at 14 °C while the die and clamp temperatures ranged from room temperature to 250 °C. Three levels of clamp force were considered, 13.3 kN (3000 lb), 17.8 KN (4000 lb) and 35.6 KN (8000 lb), and three punch speeds,1.6mm/s, 8mm/s, and 40mm/s. Two different lubricants, Teflon sheet and a siloxane emulsion lubricant (Dasco Cast), were applied during forming. The room temperature coefficient of friction of Teflon sheet and Dasco Cast were measured to be 0.043 and 0.08, respectively, using a twist compression friction test at the University of Waterloo. Unfortunately, elevated temperature friction data for these lubricants is not available.

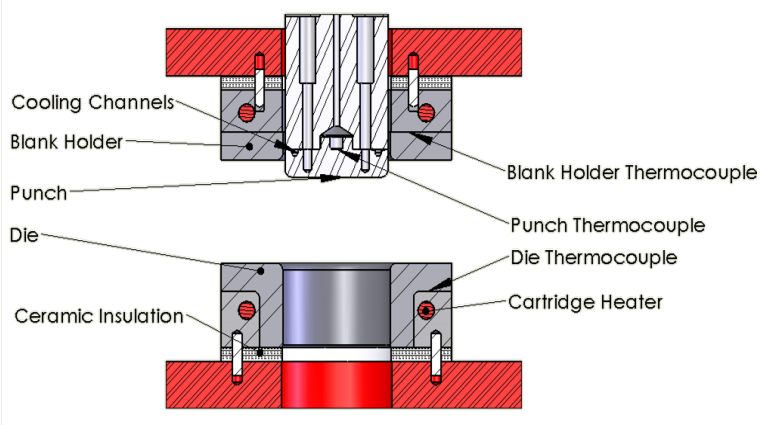

(a)

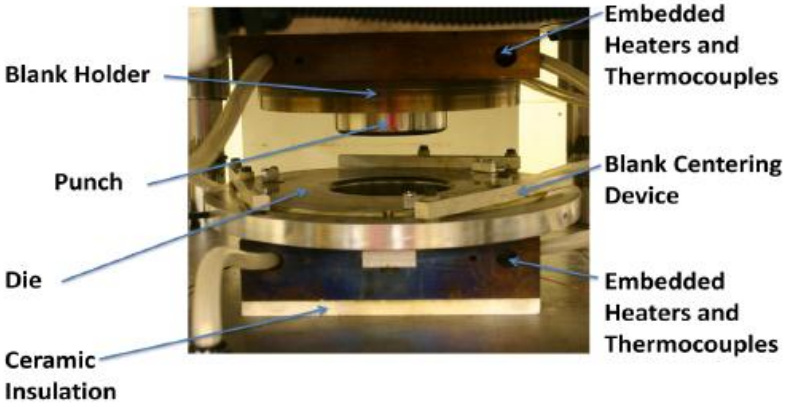

(b)

Figure 5.1 (a) Tooling cross section and (b) close up view of the tooling (b). From McKinley (2010)

5.2 Simulations

Solid models of the deep drawing tooling were imported into Altair HyperMesh from Solidworks. Only one-quarter of the geometry was meshed, taking advantage of symmetry to reduce computation time. The tools were modelled with four node rigid quadrilateral elements. The tooling solid model and the blank mesh are shown in Figure 5.2. A uniform mesh consisting of 1.0mm by 1.0mm elements was adopted for the blank. However, a coarser mesh was used for some regions of the tooling components which were modelled as rigid bodies. The blanks were modelled using Belytschko-Tsay elements (Belytschko and Tsay, 1981) with 7 through-thickness integration points. The tooling was held at a constant temperature throughout the simulations. The blank temperature was determined by heat

transfer from the tooling. The initial blank temperature was set at room temperature. Thermal contact is one of the least published aspects of warm forming simulations. The most commonly used thermal conductance for contact between the tool steel and the aluminum sheet is 1400 W/m^2K (Takuda, 2004) and was adopted for these simulations. Future work will consider direct measurement of the thermal conductance, in particular for the Teflon sheet.

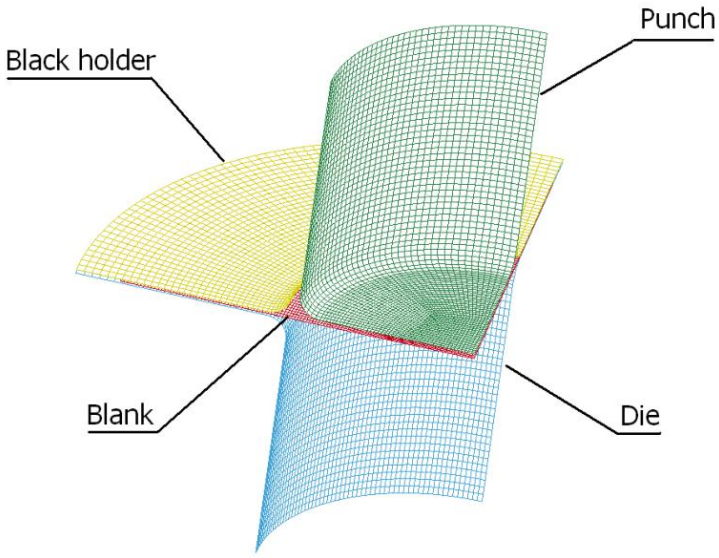

(a)

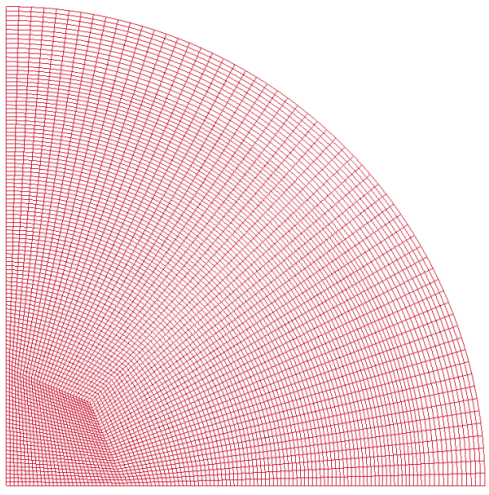

(b)

Figure 5.2 Mesh model for (a) the quarter tooling and (b) quarter blank mesh

The same boundary conditions as considered in the experiments were applied in the numerical simulations. The die is fixed in all directions while both the blank holder and punch are free to travel along the Z-axis. The blank holder is closed first, and then the punch descends. As in the experiments, the punch is operated under displacement control and the blank holder is under load control. A constant force is applied to the blank holder after an initial ramp-up. The punch contacts initially with the blank, after which the punch is held at a fixed position to allow heat transfer to occur between the punch and sheet. The punch is then ramped up to its prescribed velocity.

5.3 Numerical Results

Simulations were carried out using the developed UMAT (Chapter 4) within the LS-971 version of the explicit dynamic finite element code LS-DYNA. LS-DYNA employs a central difference method of dynamic explicit time integration. For coupled thermo-mechanical simulations, fully implicit thermal time steps (backwards difference) are performed between mechanical time steps. Explicit simulations require a small time step, which can result in computationally expensive simulations. The actual simulations are time-scaled by a factor of 1000 to save computation time. The inertial force, the force required to accelerate the blank to forming speeds, is kept below 0.1% of the total forming force to limit inertial effects due to time-scaling. All time-dependent material properties are scaled accordingly, namely strain rate sensitivity and thermal conductivity. Tooling velocities are increased by a factor of 1000 and the thermal conductivity is also increased by a time-scaling factor. The strain rate calculated within the constitutive model is divided by 1000 to correspond to the operative strain rate during the experiments.

Figure 5.3 (a) shows contour plots depicting the temperature distribution of one quarter, half, and fully drawn cups, while Figure 5.3 (b) shows the temperature distributions during the forming process at different draw depths. The simulation was done for a 203 mm Teflon sheet lubricated blank with a die temperature of 250°C and punch temperature of 14°C. The blank holder force was set to 13.3 kN, while the punch speed was set to 40 mm/sec. The temperature of the blank within the areas in contact with the hot dies equalized to the die temperature during forming.

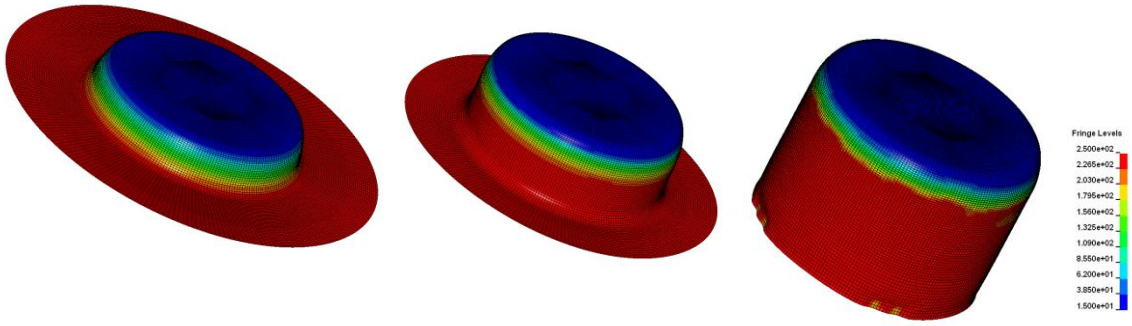

20 mm 40 mm 80 mm

(a)

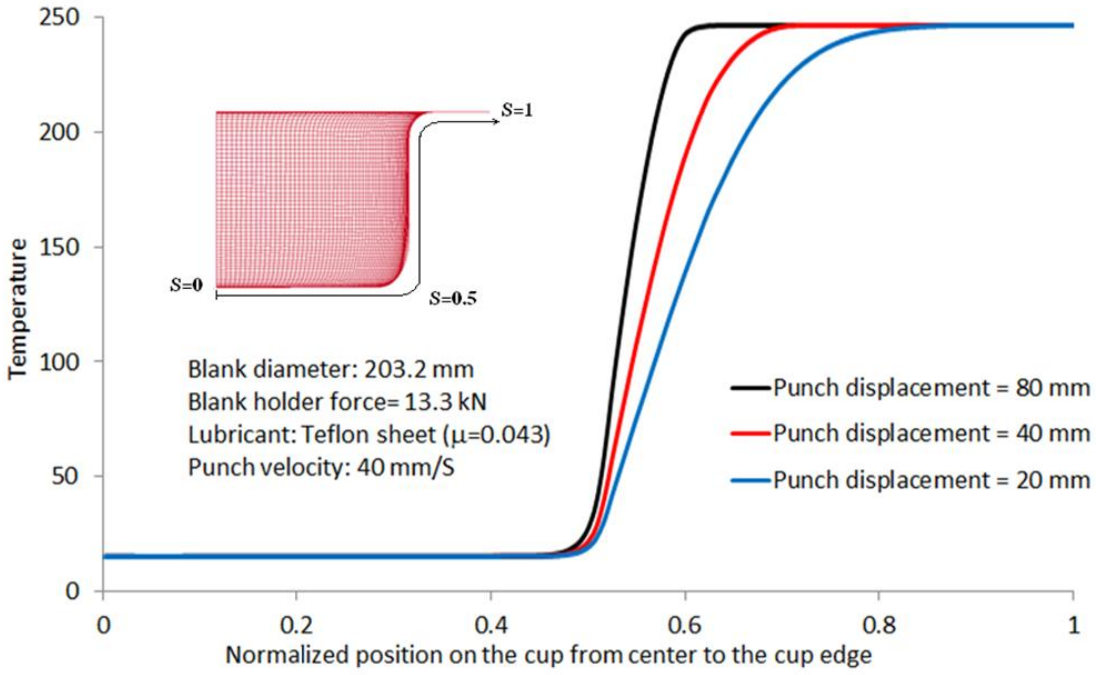

(b)

Figure 5.3 (a) Contour plot of temperature distribution for a deep drawn 203.2 mm blank, and (b) blank temperature versus normalized position on the cup wall from the centre to the cup edge for a full, one half and one quarter drawn cup

5.4 Predicted deformation and strain

Figure 5.4 shows the predicted normalized thickness (predicted thickness divided by initial thickness) distribution in the cup wall from the centre to the cup edge for partially drawn cups under isothermal forming conditions at room temperature and at 250°C, corresponding to punch depths of 23.5 and 38.2 mm, respectively. These punch depths correspond to time steps just prior to the onset of localization within the models. Also shown is the predicted thickness

distribution for a cup that was drawn fully under non-isothermal forming conditions with a cold punch at 14°C and warm dies at 250°C. Results are shown for 229mm Dasco Cast lubricated blanks with a friction coefficient of 0.08. The simulations predict a localization of strain at the punch profile radius for isothermal forming at room temperature, which leads to a sharp increase in strain at the punch profile radius for punch depths beyond 23.5mm. The onset of localization is delayed to 38.2 mm punch depth for the case of isothermal warm forming at 250°C. This improvement can be attributed to elevated strain rate sensitivity experienced at higher temperatures (Figure 4.6), which serves to delay localization. Non-isothermal forming has the important effect of reducing thinning at the punch profile radius due to the higher strength of the colder material at the punch compared to the material in the warm flange region of the blank (Figure 4.5), allowing the cup to be drawn fully without localization in the model. These trends in predicted draw depth are in general agreement with the experiments by McKinley (2010) and the models serve to demonstrate the relative benefits of elevated temperature and non-isothermal forming conditions. Note that more precise predictions of failure using the forming limit criteria in Chapter 3 are presented below.

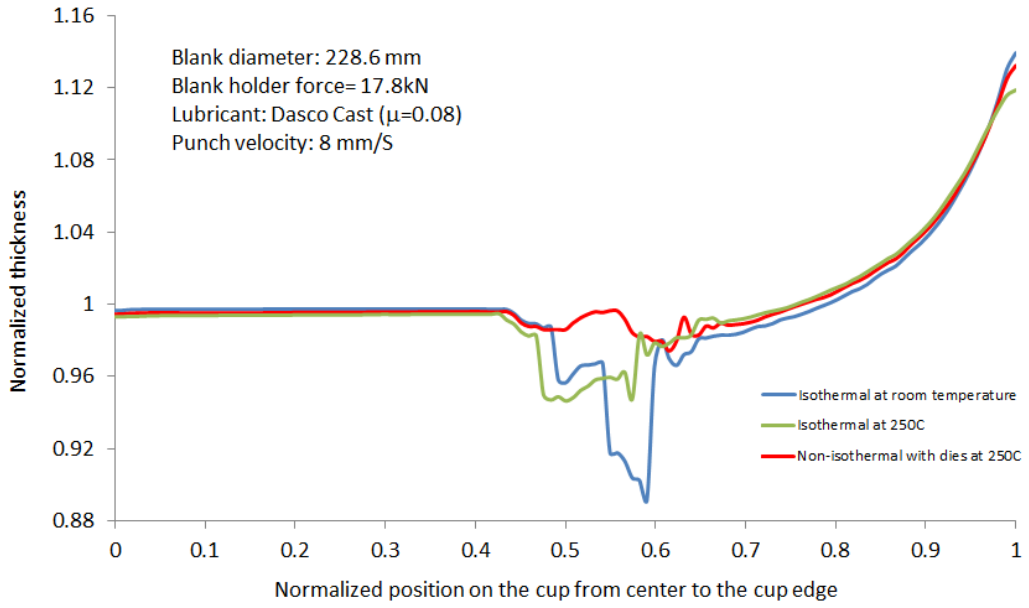

Figure 5.4 Comparison of predicted normalized thickness change versus normalized position (along radial direction) on the cup under isothermal conditions at room temperature and 250°C and non-isothermal forming with punch at 15°C and dies at 250°C

Figure 5.5 and Figure 5.6 show predicted and measured distributions of major vs. minor strains for 228.6mm blanks formed with 8mm/s punch speed, 17.8kN clamping force, 250°C dies and a 14°C punch along the blank rolling and transverse directions, respectively. Measured data were obtained from experimental results reported by McKinley (2010). Results are shown for Dasco Cast and Teflon sheet lubrication. The simulations used coefficients of friction of 0.08 and 0.043 representing Dasco Cast and Teflon sheet lubricants, respectively. As can be seen in both figures, the predicted strains are in good agreement with the experimental results; the largest difference for all cases occurs at the flange area where the highest compressive strain levels are observed (Point D in Figure 5.5 and Figure 5.6). This can be caused by errors in measuring the strains at the flange area, where wrinkling occurs. The circle gridding method cannot accurately measure strain in the presence of wrinkles, since the circles are barely readable and the local strain gradients are high. The strain state at the punch profile radius (Point B) is in a positive minor-major strain state (stretching), where low strain magnitudes were observed. Side-wall strain distributions (Point C) are largely compressive (around 45%), which denotes the possibility of wrinkles in the cup's side-wall area.

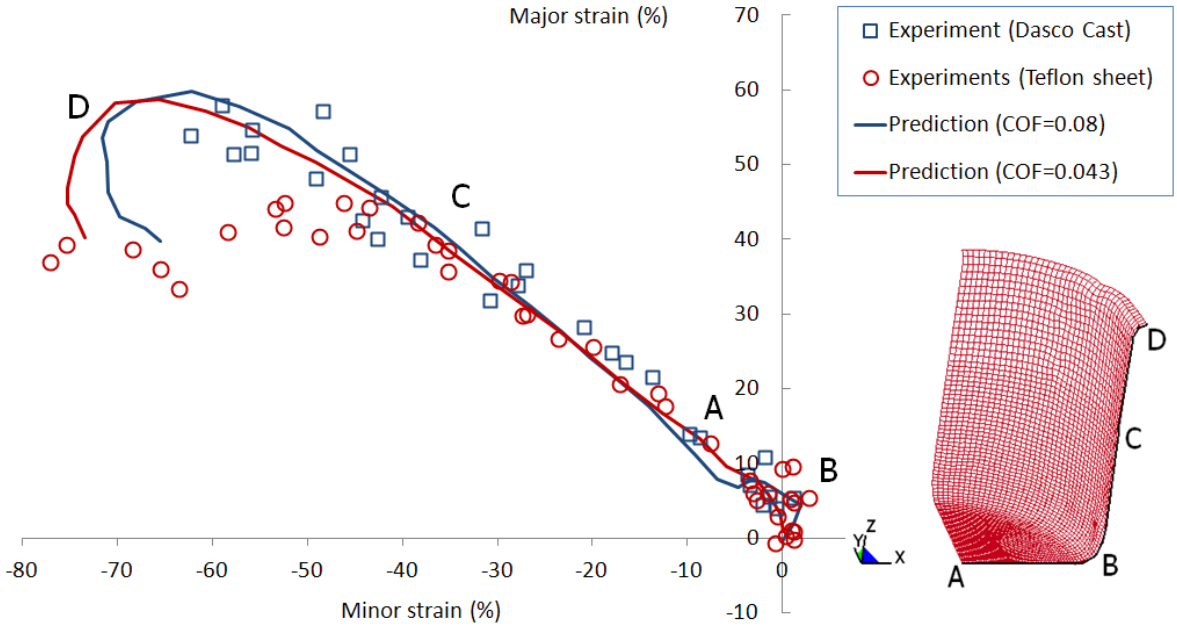

Figure 5.5 Major versus minor strain along x-axis (rolling direction) for experiments (McKinley, 2010) and simulations. 228.6mm (9") blank and 17.8kN clamping force

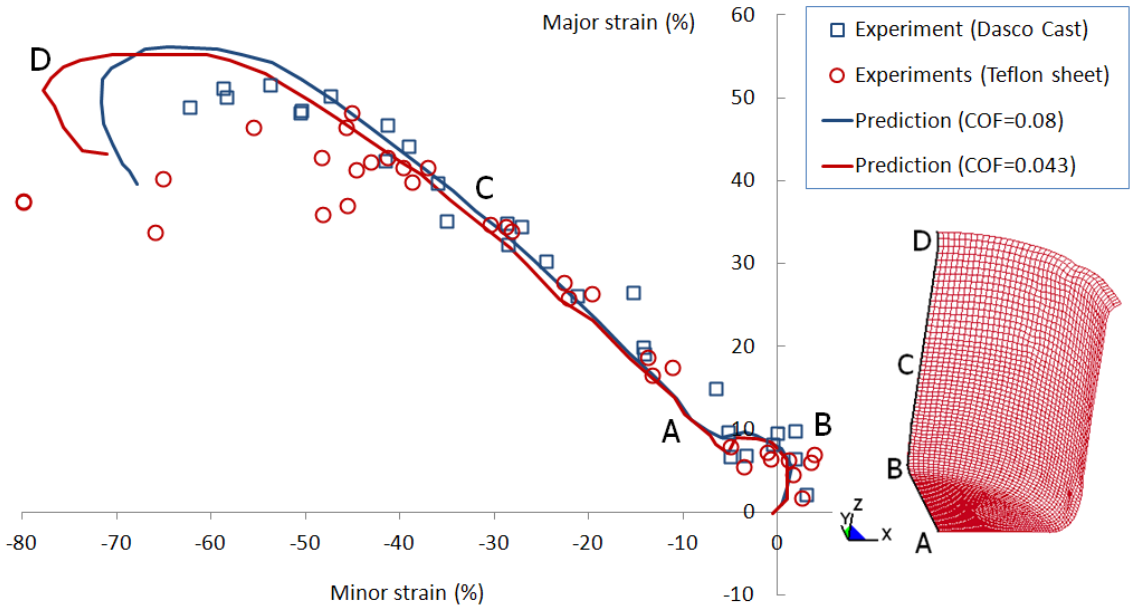

Figure 5.6 Major versus minor strain along y-axis (transverse direction) for experiments (McKinley, 2010) and simulations. 228.6mm (9") blank and 17.8kN clamping force

Figure 5.7 and Figure 5.8 show contour plots of major and minor strains, respectively, for cups formed under isothermal conditions at room temperature (a) and non-isothermal conditions with dies at 250°C (b). Figure 5.7(c) and Figure 5.8(c) plot these strains as a function of angular position for elements initially located along an arc of radius 93mm from the blank centre. As can be seen, the cup drawn at room temperature exhibits a stronger degree of in-plane anisotropy. This behaviour is expected when anisotropy parameters in Table 2.3 are considered, which shows α1 to α6 are closer to unity (isotropic condition) at 250°C compared to values taken at room temperature. (This is not the case for α7 and α8, which account for shear strains.) It can be seen that forming at higher temperature results in more uniform strain distributions due to the decrease in in-plane anisotropy. Negative strains in the contour plots shown in Figure 5.8 are responsible for the wrinkling at the edge of blank.

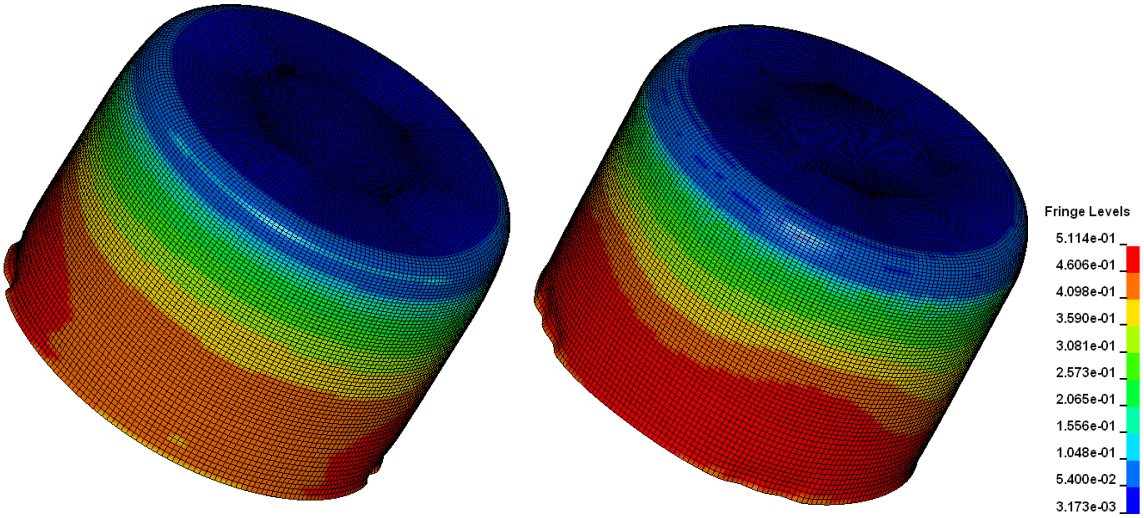

(a) Isothermal Room Temperature (b) Non-isothermal with dies at 250°C

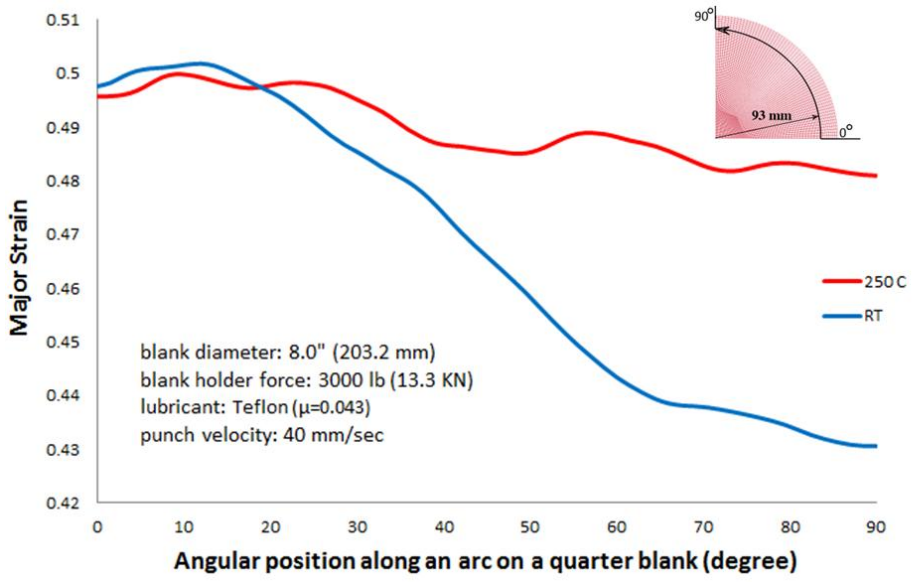

(c)

Figure 5.7 Contour plots of major strain for deep drawn 203mm blank under (a) isothermal conditions at room temperature and (b) non-isothermal conditions with dies at 250°C, (c) comparison between major strains for a row of elements initially located along an arc of radius 93mm from the centre of the blank

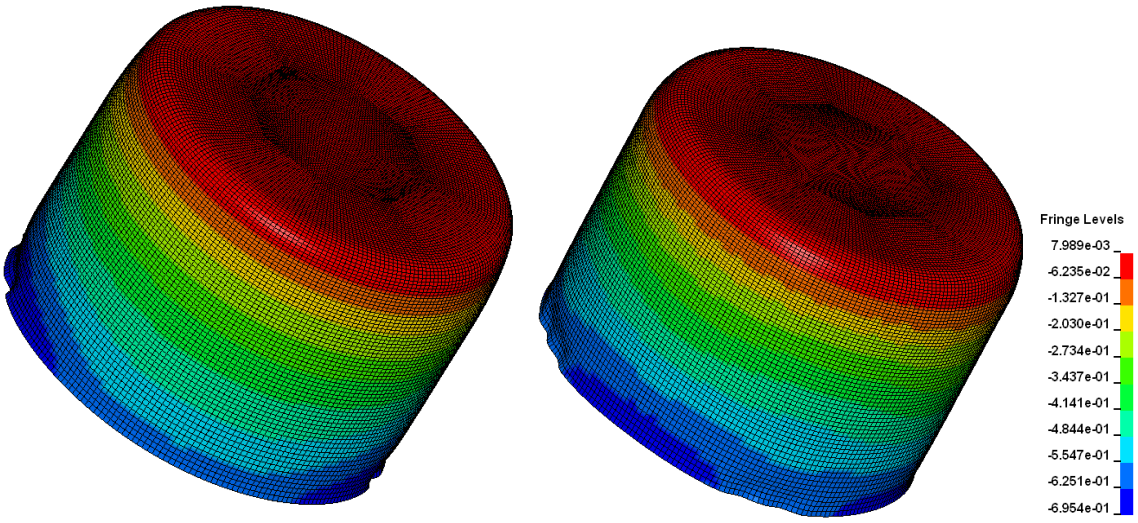

(a) Isothermal Room Temperature (b) Non-isothermal with dies at 250°C

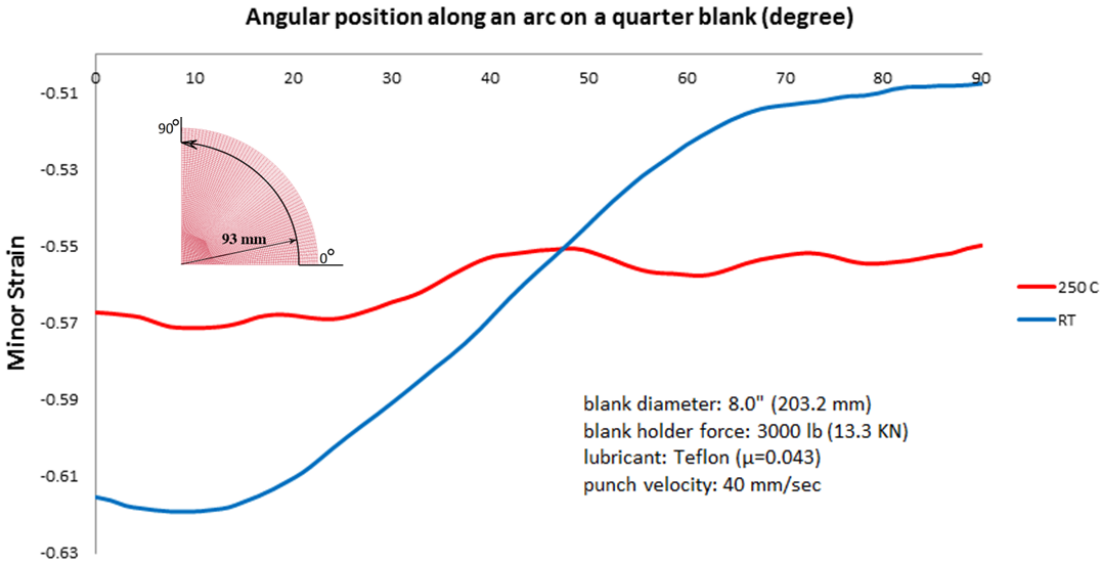

(c)

Figure 5.8 Contour plot of minor strain for deep drawing of 203mm blank under (a) isothermal conditions at room temperature and (b) non-isothermal conditions with dies at 250°C , (c)comparison between minor strains for a row of elements initially located along an arc of radius 93mm from the centre of the blank

To evaluate the ability of the numerical model to predict the deformed shape, two forming conditions resulting in wrinkled and fully drawn samples were considered. The numerical simulations were performed under the same experimental conditions reported by McKinley (2010). Figure 5.9 compares simulated and as-formed 203.2mm blanks produced under: (a) isothermal conditions at room temperature with a blank holder force of 6.6kN and (b) non-isothermal conditions with a cold punch at 14°C, warm dies at 250°C, and blank holder force of 17.8kN. Both models considered 8mm/s punch speed and a coefficient of friction of 0.08 (Dasco Cast lubricant). The room temperature model predicted wrinkles and subsequent failure of the part at a depth of 24 mm, while non-isothermal forming resulted in the desired shape.

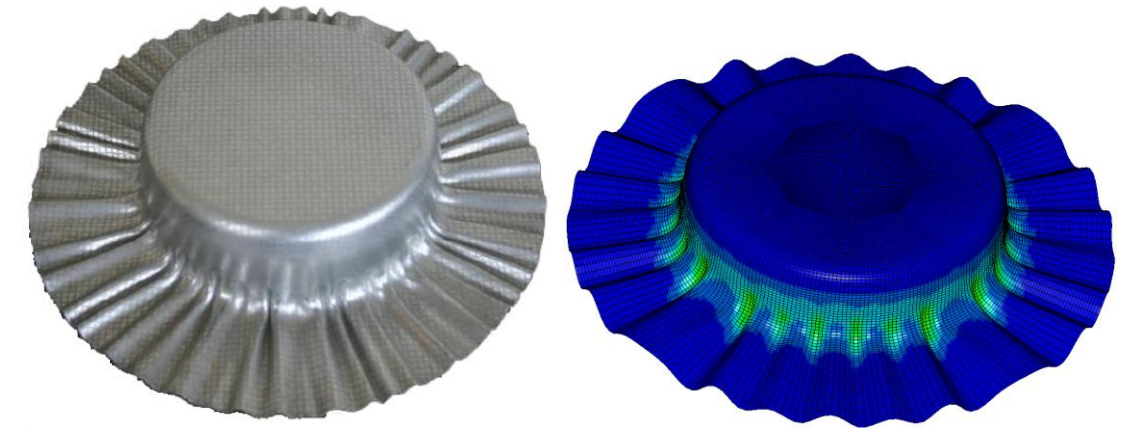

(a)

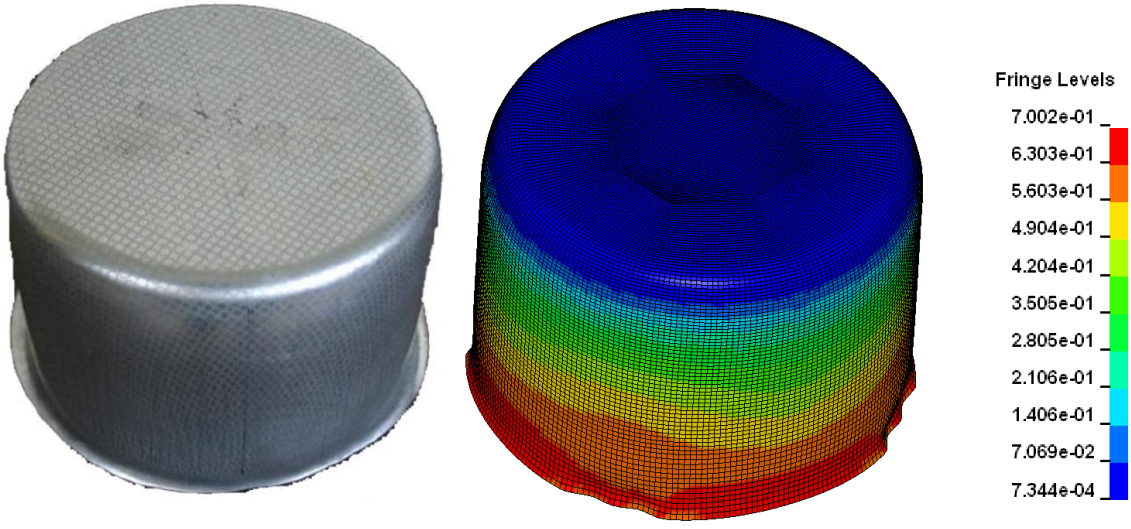

(b)

Figure 5.9 (a) Wrinkled isothermal and (b) fully drawn non-isothermal parts under different blank holder forces. The predicted effective plastic strain distributions are shown for both parts

5.5 Predicted punch force-displacement

Figure 5.10 through Figure 5.13 compare the experimental (McKinley, 2010) and numerical punch force versus displacement results at different temperatures, velocities, blank holder forces and lubricants. All simulations and experiments used 229mm diameter blanks.

Figure 5.10 shows the punch force versus punch displacement for deep drawn Teflon sheet lubricated blanks formed at different tooling temperatures. These experiments and simulations considered a blank holder force of 17.8kN, 8mm/s punch speed and a coefficient of friction of 0.043. The graph compares the punch force versus punch displacement for isothermal forming at room temperature and non-isothermal forming with a cold, 14°C punch and warm, 250°C dies. As expected, the punch force reduced dramatically at higher temperatures.

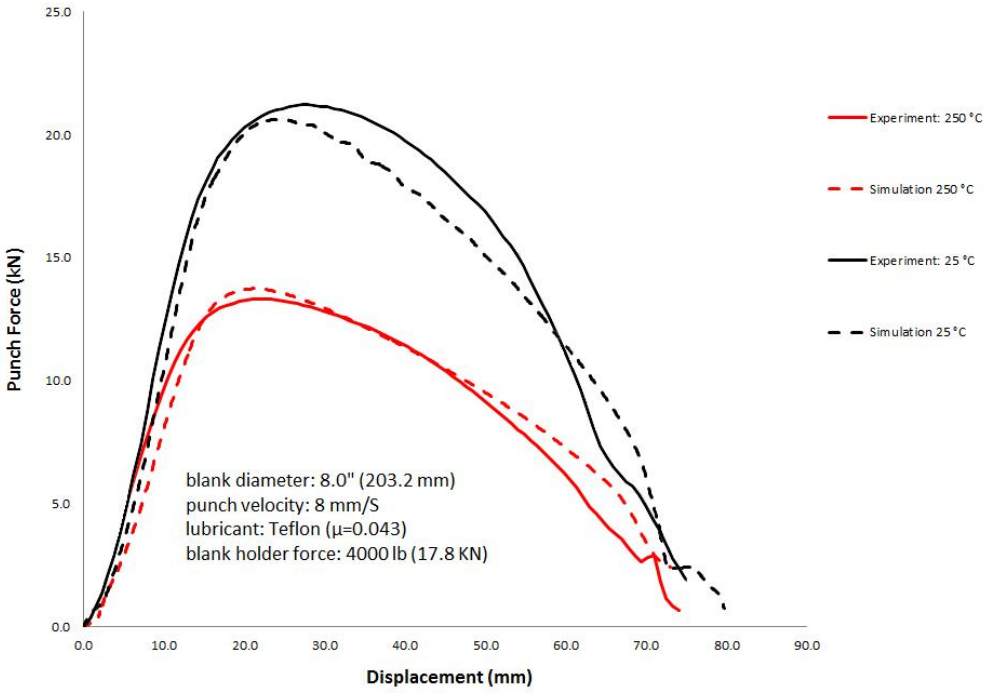

Figure 5.10 Punch force vs. punch displacement for deep drawn 228.6mm using Teflon sheet lubricant and 8mm/s punch speed, comparing results with experiments for room temperature forming and warm forming with dies at 250°C

Figure 5.11 illustrates the effect of forming speed on punch force for three levels of punch velocity (1.6, 8 and 40 mm/s). Both the die and blank holder were held at 250°C while the punch temperature was held at 14°C. Dasco Cast lubricant was used during experimentation, therefore a coefficient of friction of 0.08 was assumed in the models. A blank holder force of 35.6 kN was applied for all three punch velocities. The comparison shows good agreement between the experiments and numerical results. Increasing the punch velocity caused a significant increase in the maximum punch force, which is attributed to rate sensitivity experienced by the warm flange region of the cup or possibly a viscous response of the lubricant. Experiments (McKinley, 2010) performed using Teflon as the forming lubricant (not shown) exhibited a lower degree of rate sensitivity.

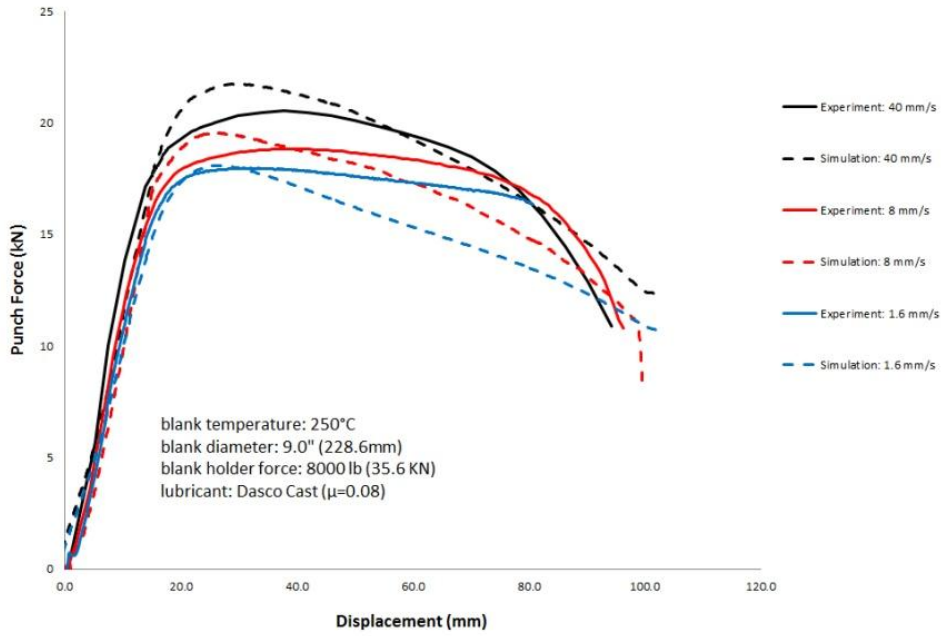

Figure 5.11 Punch force vs. punch displacement for deep drawn 228.6mm blank using warm dies and cold punch and Dasco Cast lubricant at different punch speeds

Figure 5.12 compares calculated punch force-displacement curves at two blank holder pressure levels, 17.8kN and 35.6kN, with those derived from the experimental results. Both the experiments and simulations considered warm dies at 250°C and a cold punch kept at 14°C. The punch speed was 8mm/s and Teflon sheet was used as the lubricant. Both the maximum punch force and general trends agree well with the experiments.

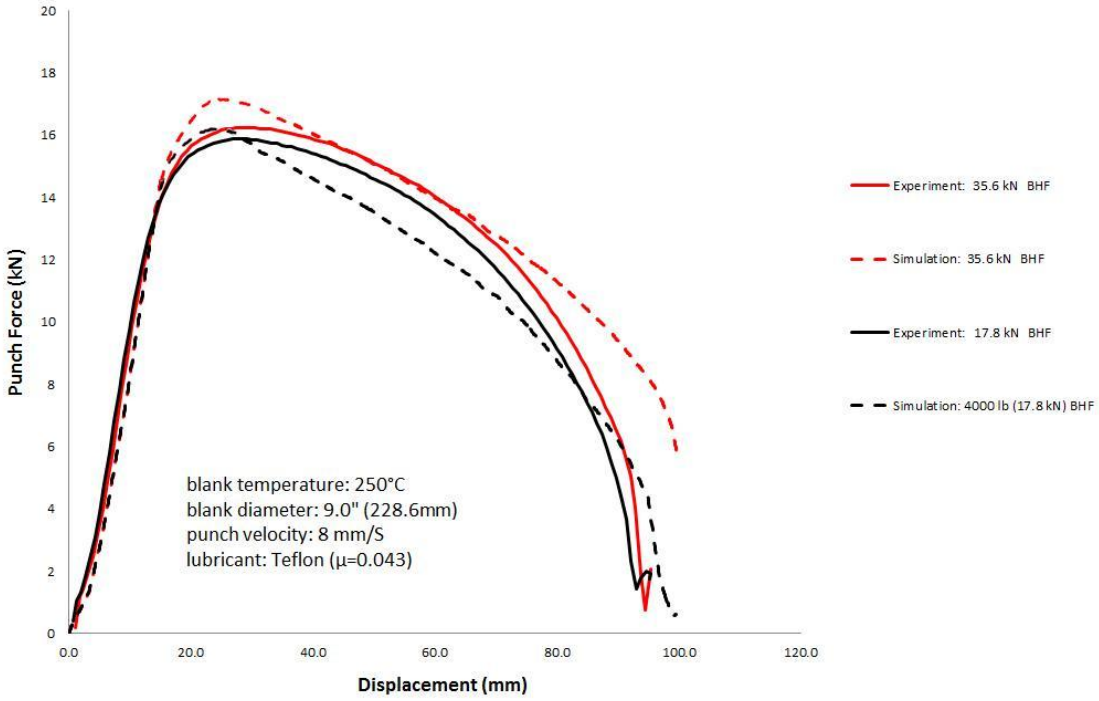

Figure 5.12 Punch force vs. punch displacement for deep drawn 228.6mm blank using Teflon sheet lubricant, comparing results against experimental data at two blank holder force levels

Figure 5.13 compares the experimental and numerical punch force versus displacement results for samples formed using two lubricants: Teflon sheet and Dasco Cast. Teflon's lower coefficient of friction reduces punch force - the models capture this trend relatively well.

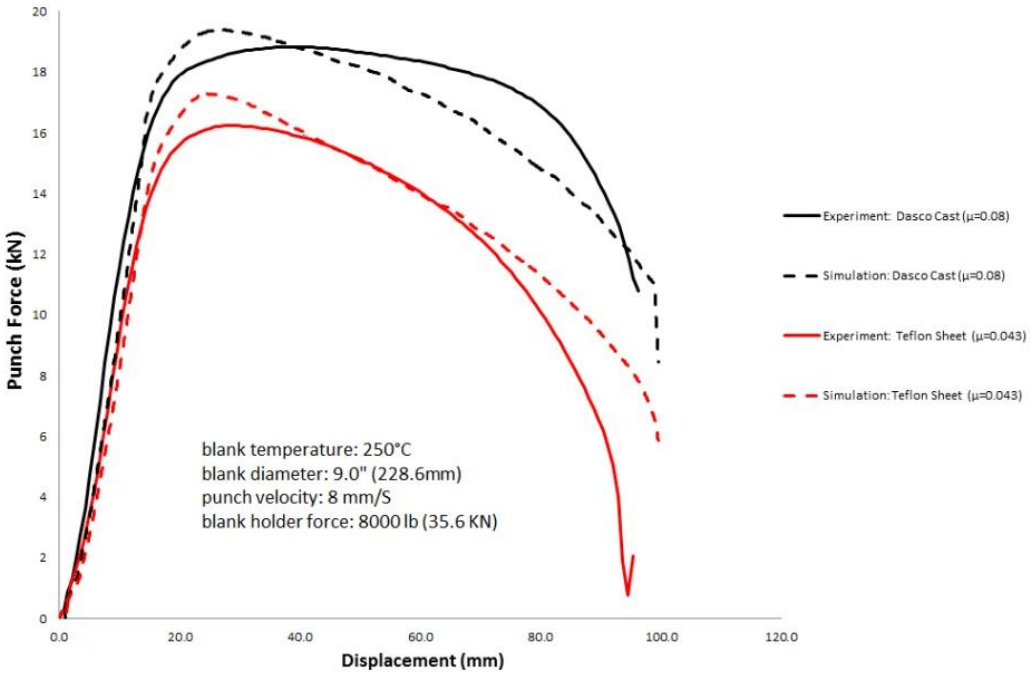

Figure 5.13 Punch force vs. punch displacement for deep drawn 228.6mm at 8mm/S punch speed, comparing results with experimental data for two different lubricants

5.6 Failure prediction

This section provides a comparison of measured punch depth at failure for the deep drawn cups (McKinley, 2010) and predictions using the warm forming limit data presented in Section 3.5.5 in conjunction with the current simulations. The predicted conditions at failure are essentially determined as a post-processing operation in which the measured forming limit curve (FLC) is read into LS-Prepost (the LS-DYNA post-processor) and the predicted strains for each time step are compared to the FLC. Punch depths for which the predicted strains on the middle plane of the elements (middle integration point through the thickness of the element) lie above the FLC are considered to correspond to "failed conditions". The mid-plane was used to eliminate the effect of bending strains that are manifest on the upper and lower surface of the elements.

5.6.1 Isothermal cases

Figure 5.14 shows a forming limit plot corresponding to a predicted failure (a) against McKinley's (2010) experimental results (b) for deep drawn 228.6mm blanks at room temperature, with 8mm/s punch speed, 4.4kN clamping force, and Dasco Cast lubricant (COF

= 0.08). In this case, the room temperature forming limit curve developed in Chapter 3 was entered into LS-Prepost and used as a failure criterion. As can be seen in Figure 5.14(a), the material is predicted to crack almost immediately along the punch profile radius at a punch depth of approximately 19.1mm. The failure depth from the load-displacement data reported by McKinley is approximately 22mm. The location of failure in the photograph (Figure 5.14(b)) agrees well with predictions. Figure 5.14(c) shows the predicted major and minor strains projected onto the room temperature FLD. As can be seen, the strains at the punch nose exceeded the limiting strains near the plane strain state.

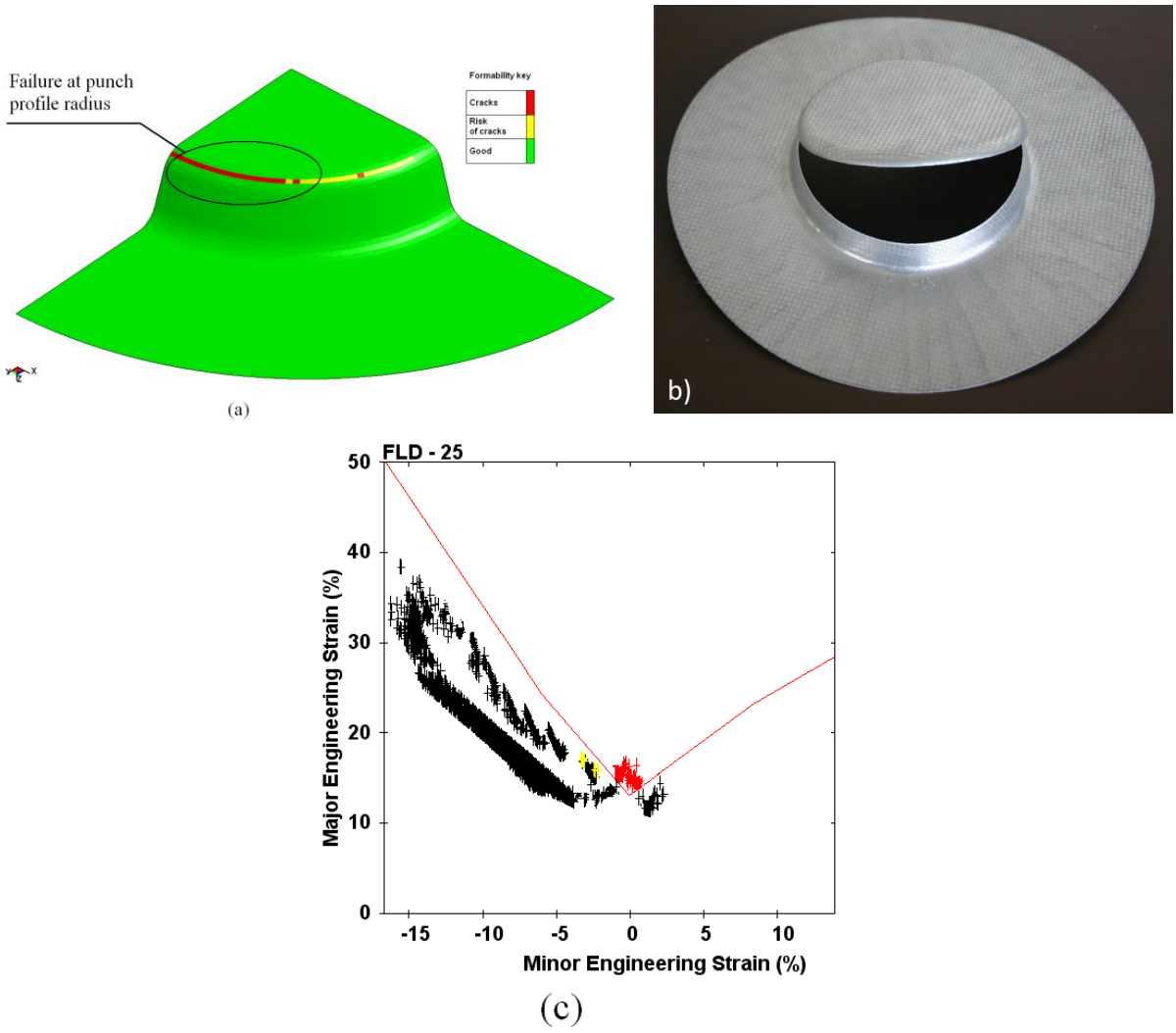

Figure 5.14 Failure prediction for deep drawing of 228.6mm blank at room temperature, 8mm/s punch speed, 4.4kn clamping force, and Dasco Cast lubricant (COF=0.08). Fracture occurs at punch radius. (a) Model prediction; (b) experimental results (McKinley, 2010); and (c) major and minor strains projected on the FLD

Figure 5.15 shows the predicted failure response for isothermal, deep drawing of 228.6mm blank at 250°C, with 8mm/s punch speed, 17.8kN clamping force, and Dasco Cast lubricant (COF=0.08). The simulation exhibited strain localization at the punch profile radius at a punch depth of 38.2mm. This was previously observed as a sudden decrease in calculated thickness of the blank (Figure 5.4). The 250°C-forming limit curve (FLC) was entered into LS-Prepost as limiting strains and used to predict failure. Using the FLC, the model predicts that failure initiates at a punch depth of 36.7mm, as shown Figure 5.15(a). Figure 5.15(b) shows projected major and minor strains on the 250°C-FLD. As seen, the strains exceed the limiting strains near the plane strain state at the punch profile radius. As per the model predictions, isothermal forming at elevated temperatures (250°C) produces greater drawability gains relative to room temperature processing; however, complete drawing is still not possible.

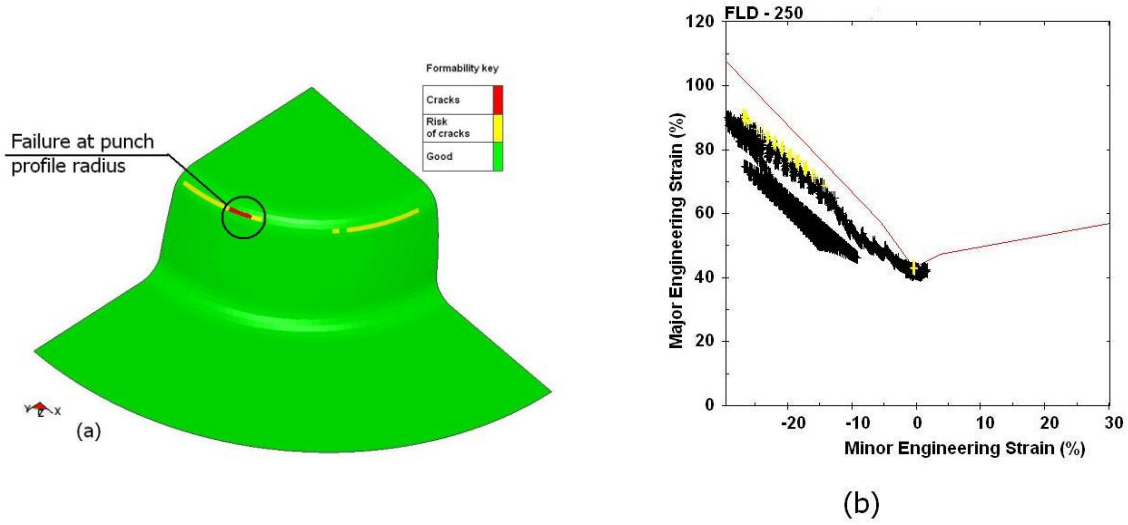

Figure 5.15 Failure prediction for isothermal deep drawing of 228.6mm blank with dies at 250°C, 8mm/s punch speed, 17.8kN clamping force, and Dasco Cast lubricant (COF=0.08). (a) Fracture happens at the die entry radius, at a punch depth of 37.5mm as predicted by model . (b) Major and minor strains are projected on 250°C-FLD

5.6.2 Non-isothermal cases

Figure 5.16 compares predicted failure with experimental results (McKinley, 2010) for non-isothermal deep drawing of 228.6mm blanks with dies warmed to 200°C and the punch cooled to 14°C. The simulation and experimental forming process considered a punch speed of 8mm/s, a clamping force of 22kN, and Dasco Cast lubricant (COF = 0.08).

Figure 5.16(a) shows the temperature distribution in the blank at 16mm punch depth (the failure assessment, as explained later, shows that the material fails at this punch depth). As can be seen, the blank develops three well-defined temperature zones: (1) under the punch and the punch profile radius, the blank temperature is 14°C, (2) the flange area and die entry radius are 200°C, and (3) the cup wall varies between 14°C and 200°C.

To assess failure of the cup in each of these three zones, the FLDs for temperatures of room temperature, 150°C, and 200°C were used, respectively. The FLDs were separately entered in LS-Prepost. Failure assessment using the 200°C-FLD revealed that severe thinning begins in the flange at a punch depth of 14mm and, by advancing the punch, the material fails at the die entry radius (punch depth of 16mm). Assessment of failure in the cup wall and punch profile radius areas using FLDs for room temperature and 150°C revealed no failure or severe thinning before the 16mm punch depth was reached. Formability plots of these areas, which were separately obtained using FLDs that directly correspond to the temperature of each area, were assembled together in a single plot (Figure 5.16(b)). Comparing these predicted values against the experimental results shown in Figure 5.16(d) shows that the model predicts the location of failure well. Again, McKinley did not report exact data indicating the failure punch depth; however, both experimental and simulation results show that the failure occurred early in the forming process.

Figure 5.16(c) shows projected major and minor strains on the 200°C-FLD. Only values corresponding to elements on the die entry radius and flange areas are shown. Red symbols represent nodes that have already failed, yellow symbols correspond to nodes with severe thinning and are at risk of cracking, and black symbols represent safe nodes.

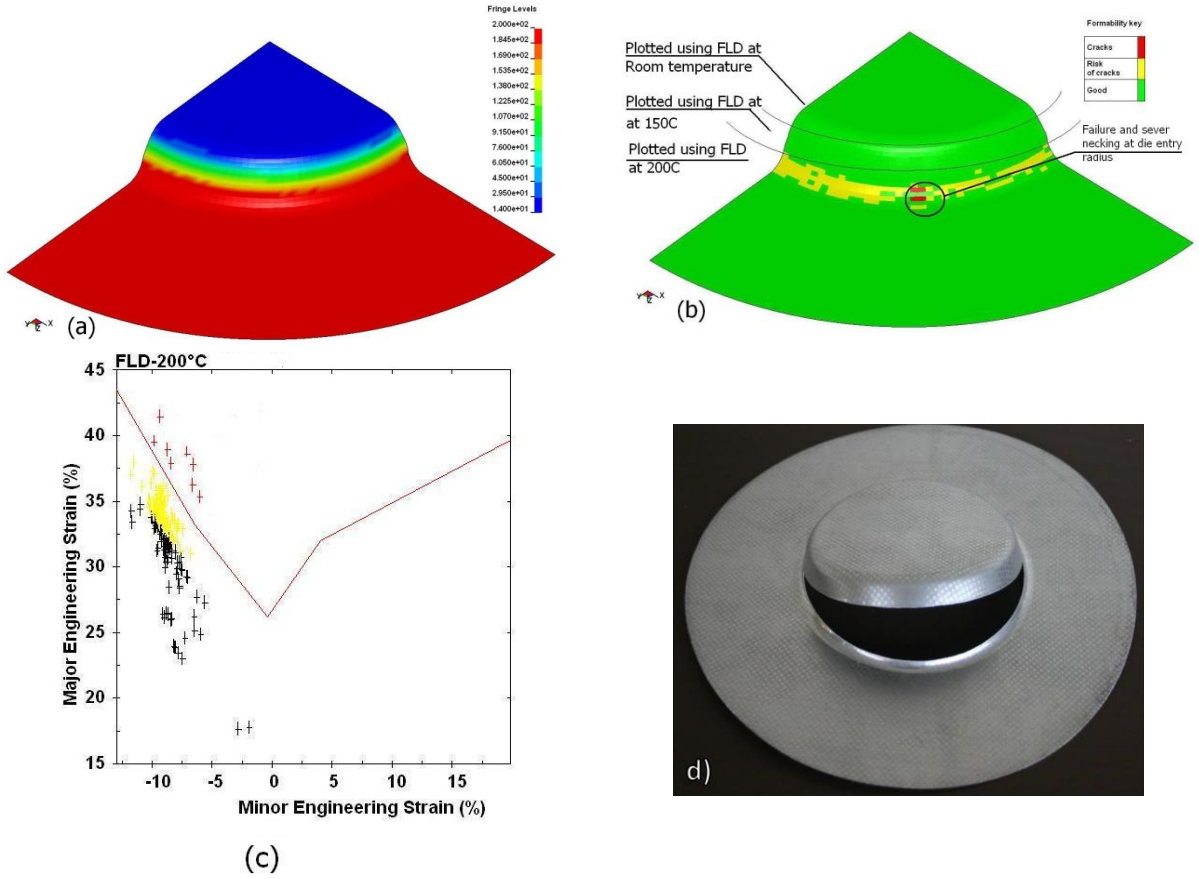

Figure 5.16 Failure prediction for deep drawing of 228.6mm blank with warm, 200°C dies, and a cold punch at 14°C, 8mm/s punch speed, 22.2kN clamping force, and Dasco Cast lubricant (COF=0.08). Fracture happens at the die entry radius. (a) Temperature distribution (b) model prediction (c) major and minor strains on the die entry radius, projected on 200°C-FLD and (d) experimental results (McKinley, 2010)

Figure 5.17 and Figure 5.18 illustrate the failure evaluation for a non-isothermal 228.6mm blank formed with warm dies (250°C) and a cold punch (14°C), 8mm/s punch speed, 17.8kN clamping force and Dasco Cast lubricant (COF=0.08). The experiments demonstrated that these conditions resulted in a successful deep draw. Figure 5.17 shows the predicted temperature distribution in the fully drawn cup, which varies between 14°C (under the punch bottom and on the punch profile radius) and 250°C (in the die and die entry radius). To predict material failure of the blank, FLDs were selected according to individual temperature distributions developed for each element.

Failure of the elements on the punch profile radius and under the punch bottom was evaluated by entering the room temperature FLD into LS-Prepost, where it was used as a failure criterion. The formability analysis showed that these elements do not experience limiting

strains, which is supported by a comparison of major and minor strains experienced by these elements at 25°C or colder, with limiting strains corresponding to the room temperature FLD.

In order to assess failure on the cup wall, FLDs corresponding to temperature levels experienced around the middle height of the cup (200°C) and close to the die entry radius (250°C) were used. Both analyses showed that the cup wall did not experience failure or severe necking; however, some wrinkling was observed in the blank edge (not shown here). Figure 5.18(b) and (c) compare major and minor strains experienced by elements located within 200°C and 250°C temperature zones. As can be seen, the strain distribution does not reach limiting strains, which confirms successful forming. This is in agreement with experimental results reported by McKinley (2010).

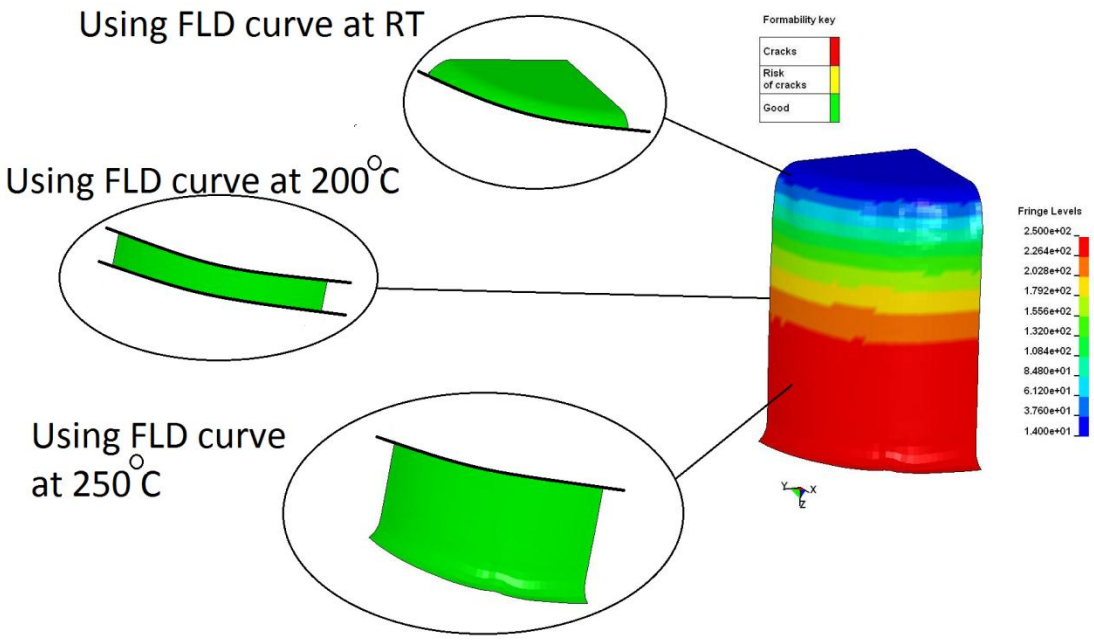

Figure 5.17 Failure evaluation for non-isothermal deep drawing of 228.6mm blank with warm dies at 250°C, Cold punch at 14°C, 8mm/s punch speed, 17.8kN clamping force, and Dasco Cast lubricant (COF=0.08). Each area was checked with the FLD curve corresponding to its temperature

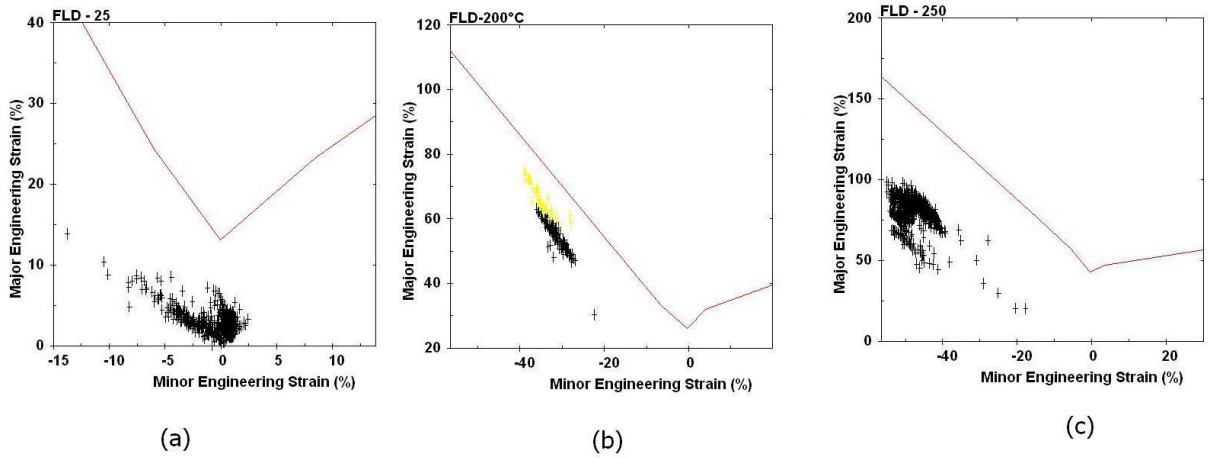

Figure 5.18 Minor and major strains of a fully drawn 228.6mm blank are projected on FLD curves for (a) elements under the punch head and on the punch profile radius, (b) elements on the cup wall which are at 200°C approximately, and (c) elements on the cup wall close to the cup opening which are at 250°C

In summary, the finite element predictions of the thinning, strain distributions and load-displacement response for the deep drawn cups agree well with the measured data of McKinley (2010). These results support the umat and constitutive model approach (Bergstrom-Barlat) adopted in this work. The forming limit curves also provide good predictions of failure when the curve for the appropriate temperature is matched to the material temperature in the deep drawn cup.

6 Heat exchanger core plate warm forming: experiment and simulation

The experimental characterization and numerical simulation of the forming of an automotive heat exchanger component is presented in this chapter. The experiments were performed as part of the current research and considered the warm forming of a simplified heat exchanger plate component with a cup shape feature that represents the fluid channel and manifold of an automotive heat exchanger. The effects of several forming parameters, temperature and temperature distribution, binder force and lubrication on the draw depth to failure of this component are studied. Numerical models of selected experiments were developed using the constitutive model described in Chapter 4 and the predictions are compared with measured data as a further assessment of the modeling framework.

The forming experiments considered a simplified heat exchanger plate geometry, representing a component within an automotive heat exchanger (Figure 6.1), as an exemplar structure. Each heat exchanger plate is 0.61mm thick, 580mm long, and 32mm wide, with a cup height of 6.8mm; however, a simplified 73mm long plate with a cup feature at one end of the plate was considered in this study (Figure 6.1). The part was fabricated from an aluminum brazing sheet that consisted of a modified AA3003 core and AA4045 clad. The sheet has a 10% clad layer on both sides, totalling 0.61mm across (thickness). In the current work, warm forming experiments were performed using this material.

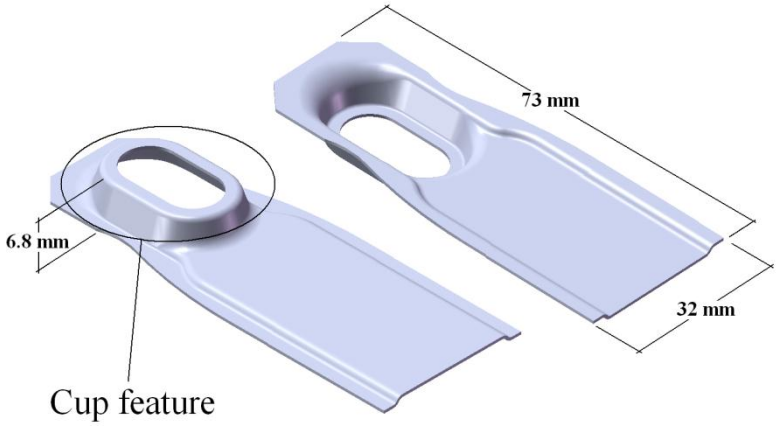

Figure 6.1 Schematic view of a simplified heat exchanger plate component incorporating the cup shape feature at the end. These plates are stacked and brazed together to form the manifold and fluid channel of an automotive heat exchanger

The heat exchanger plate tooling geometry was generated based on a tooling design provided by Dana Canada, which incorporates the cup feature within a foreshortened plate length (Figure 6.1). Conventional room temperature manufacturing requires multiple forming steps to achieve the necessary draw depth to form the cup feature within the heat exchanger plate geometry (Figure 6.2). Note that the hole in the deep drawn section of the cup is pierced after the forming step. The objective of this section is to determine whether warm forming, in particular non-isothermal warm forming with a cold punch and heated die, can reduce the heat exchanger plate forming process to a single draw step. The goal is to maximize the formability of the material and, ultimately, to form the part without inducing failure or necking. Numerical models of the non-isothermal forming process were performed using the UMAT presented in Chapter 4 and forming limit curves presented in Chapter 3, and the results are compared here against corresponding experimental data.

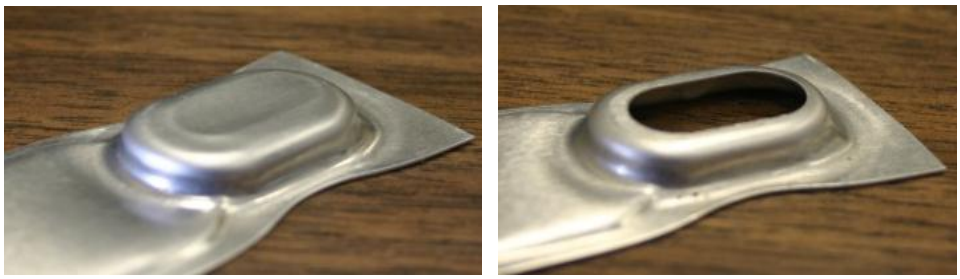

(a) (b)

Figure 6.2 Current heat exchanger plate component: (a) as formed and (b) after piercing the coolant channel.

6.1 Experimental setup

The heat exchanger plate components were formed using a specially designed toolset equipped with a heated die and blank holder, and a cooled punch (Figure 6.3), developed as part of this research. The punch and die entry radii were both 2.36 mm. The die and blank holder temperatures can be set to any temperature between 25°C and 300°C using PID controllers with thermocouple feedback. Internal water channels serve to chill the punch to approximately 15°C. The warm forming tooling was mounted in a double-acting servo-hydraulic press. While the tooling could accommodate punch speeds up to 40 mm/s, these

experiments utilized punch speeds of only 4 and 8 mm/s. Experimental variables are summarized in Table 6.1. The experimental setup was controlled by a Labview program that records punch and blank holder force, punch velocity, tooling temperatures, and, optionally, blank centre temperature.

Table 6.1 Heat exchanger plate forming process variables (for experiments and simulation)

Variable	Range
Die and blank holder temperature	up to 300°C
Punch temperature	15°C
Blank holder force	2.24 kN (500 lbf) to 6.72 kN (1,500 lbf)
Cup depth	up to 6.8 mm
Punch Speed	4 and 8 mm/s
Lubricants	Dasco Cast 1200 (μ=0.08) and Teflon sheet (μ=0.043)

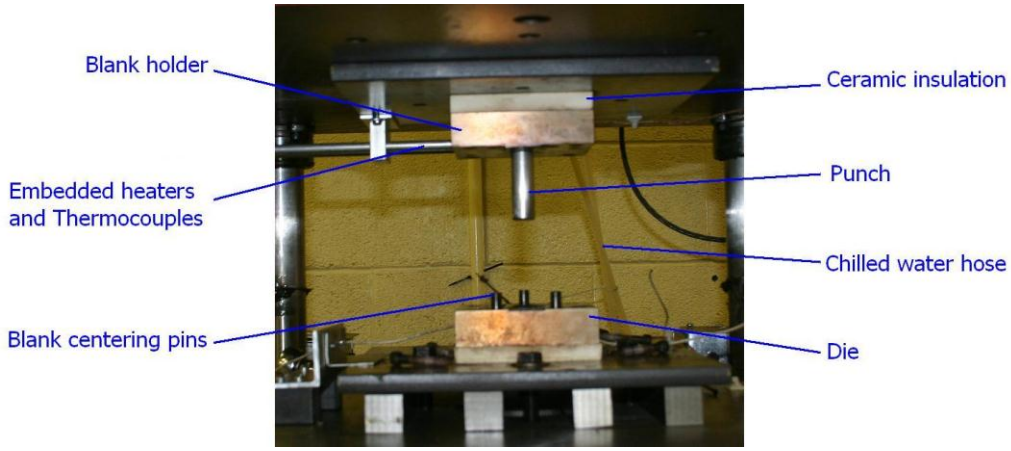

(a)

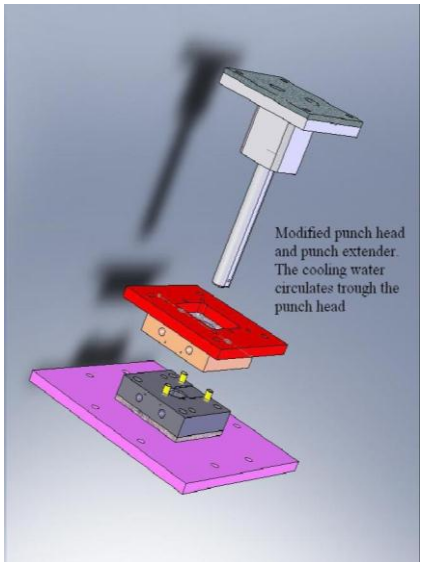

(b)

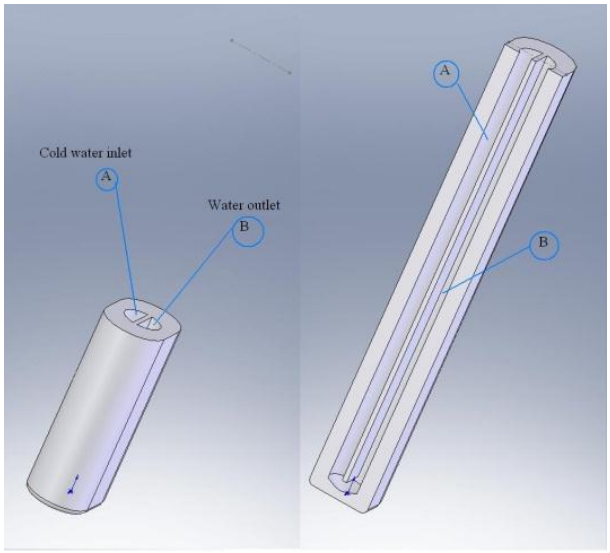

(c)

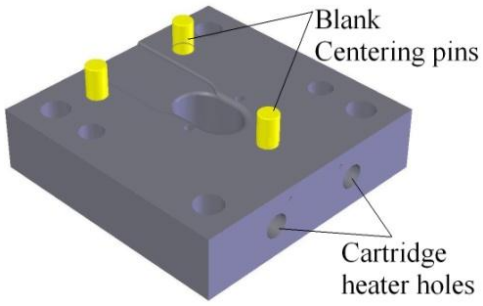

(d)

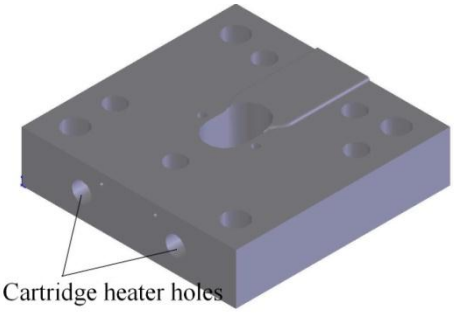

(e)

Figure 6.3 (a) Close up view of warm tooling, (b) CAD model of the tooling, (c) Section view of the punch head showing the cooling water channel, (d) CAD model of the die, and (e) blank holder

Different configurations were used to explore the effect of the die and punch temperatures, lubricity, punch speed, and clamping force on formability. For all non-isothermal configurations, the punch temperature was held constant at 15 °C, while the die and clamp temperatures ranged from room temperature to 300°C, and the clamping force was adjusted between 2.24kN and 6.72kN.

Prior to forming, the blanks were cleaned thoroughly and either Dasco Cast 1200 or Teflon sheet lubricant was applied. The forming process started by placing the blank on the previously heated (or non-heated) die. The clamp was closed and the blank was heated by the dies until it reacheds the die temperature. The punch then advanced to contact the blank, pushing the blank into the die cavity to a depth of 1 mm. This initial displacement was imposed to ensure that the surfaces are in contact and that heat is transferred between the die, punch and blank. The tooling was held stationary at this position for 30 seconds while the region of the cup feature under the punch was cooled by the punch. Finally, the punch movement was activated to force the blank into the die cavity, forming the bubble shaped part, with or without failure. Figure 6.4 shows the recorded and predicted temperature history at the centre of the cup feature under the punch prior to forming, for the case of 200°C dies, a 15°C punch and a clamping force of 2.24kN. The calculated heating and cooling rate is faster than that seen in the measurements, however both reach a steady state close to room temperature. This difference between the measured and predicted heating and cooling rates is attributed to the Teflon lubricant which is expected to have a lower heat transfer coefficient than conventional forming lubricants. Future work will consider characterization of the heat transfer coefficient between the workpiece and tooling for a range of lubricants.

The measurement shows that the temperature of the centre of the core plate bubble is steady at around 21°C after 42s while the model predicted a steady state at 18.8°C after 33s. It proved difficult to acquire transient temperature data during the actual forming operation since the thermocouple detached from the sheet surface, however, measurements such as those in Figure 6.4 were used to confirm the thermal conditions prior to forming and to determine the required wait time prior to activating the punch forming motion.

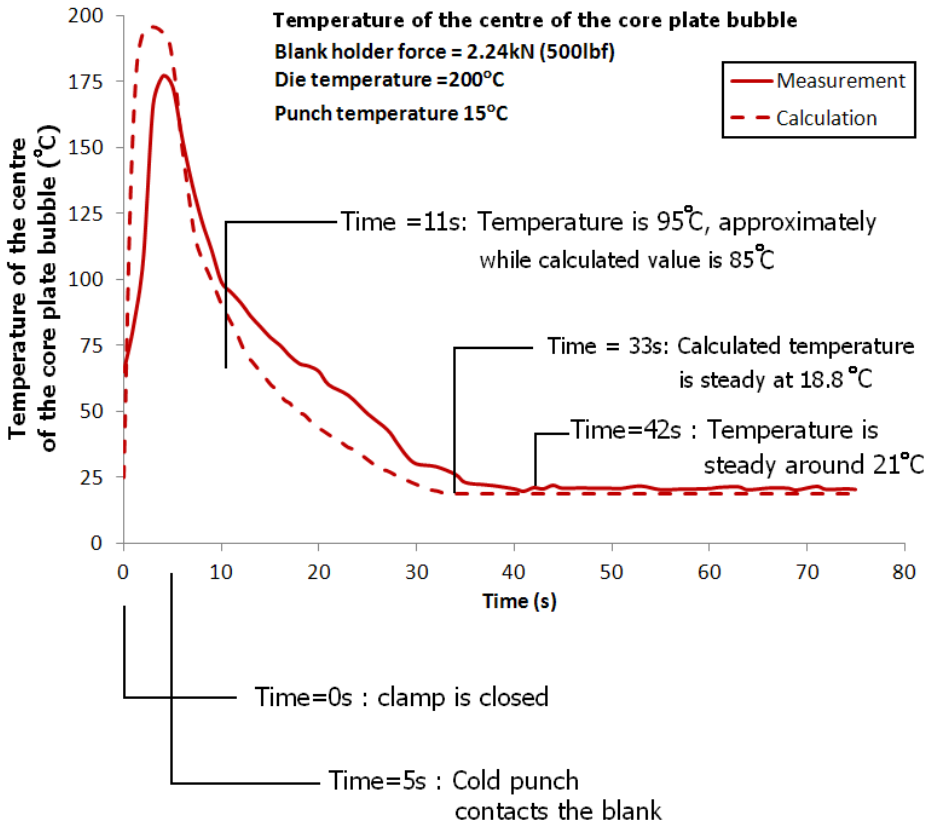

Figure 6.4 Temperature of the centre of the core plate bubble under the punch head

6.2 Experimental results

To study the effect of non-isothermal forming on formability, experiments considering three levels of die temperature, two levels of clamping force, two levels of punch speed and two different lubricants were performed. Each configuration was tested at least three times to ensure repeatability. Punch speed had no effect on the results, suggesting that strain rate sensitivity was not significant, at least over the range of velocities used in the current experiments (0.5 to 8 mm/s).

6.2.1 Dasco Cast lubricant Experiments

Figure 6.5 shows the specimen condition after a total draw depth of 5 mm for room temperature isothermal and non-isothermal forming with a punch speed of 8 mm/s using Dasco Cast lubricant. For all cases, the temperature of the centre of the blank under the punch was measured to be approximately 20°C prior to forming. The forming outcomes in the figure

correspond to the indicated blank holder force and die temperatures. It is evident from Figure 6.5 that applying a higher clamping force reduces the degree of wrinkling; however, the elevated clamping force may result in necking or failure (tearing). The use of the elevated temperatures causes the wrinkles to reduce dramatically. The room temperature samples failed for all configurations of clamping force and punch velocity; however, for the higher punch velocity and higher clamping force, the failure initiates at a lower drawing depth. Heating the dies to 300°C serves to prevent necking, but some wrinkles remain for a clamping force of 2.24 kN. When the clamping force is increased to 4.48kN, necking is observed at the die entry radius of the part.

For a given blank holder force of 4.48 kN the forming was performed at different temperature configurations with and without Dasco Cast as the lubricant. The draw depths at necking have been measured at the point of initiation of a sharp drop in punch force. A summary of these results is shown in Table 6.2.

Table 6.2 Draw depth at necking for different temperature settings with blank holder force of 4.48 kN and punch speed of 8 mm/s

Die Temperature (°C)	Punch Temperature (°C)	Bubble depth (mm)	
		Dasco Cast	No lubricant
25	25	**2.8**	**2.8**
150	15	**3.0**	**2.9**
200	15	**4.7**	**3.9**
250	15	**5.2**	**4.3**
300	15	**6.0**	**5.0**

The conditions summarized in Table 6.2 have been repeated with a punch speed of 4mm/s; however no significant change in the results was observed. The beneficial effect of temperature difference between the bubble centre under the punch and the die entry radius is evident from the results. Also, it can be seen that the lubricant (Dasco Cast) has an important

effect on formability at higher temperatures. For temperatures lower than 150°C, Dasco Cast does not function well as a lubricant.

	Die Temperature		
Clamp Force	**Room Temperature**	**250° C**	**300°C**
2.24kN	Failure, severe wrinkling 	Failure, severe wrinkling 	No failure, moderate wrinkling 
4.48kN	Failure, moderate wrinkling 	Failure, mild wrinkling 	Failure (necking), no wrinkling 

Figure 6.5 Summary of experimental results for 8mm/s punch speed, cold punch at 15°C for non-isothermal cases and total draw depth of 5 mm and Dasco Cast as lubricant

Figure 6.6 compares the maximum draw depth (without necking) for 2.24kN and 4.48kN blank holder force with a punch speed of 8mm/s under room temperature and non-isothermal forming conditions with heated dies and a cold punch at 15°C. As seen in the figure, the attainable draw depth increases as the blank holder force decreases. The maximum possible draw depth without necking at room temperature was observed to be 4.2 mm for a clamping force of 2.24 kN (500 lbf); however, there is significant wrinkling around the bubble. For dies

heated at 200°C, the part fails at a draw depth of 4.9 mm with a clamping force of 4.48 kN (1,000 lbf). By applying a clamping force of 2.24 kN, the part can be drawn fully without necking (Figure 6.5), however moderate wrinkling is observed.

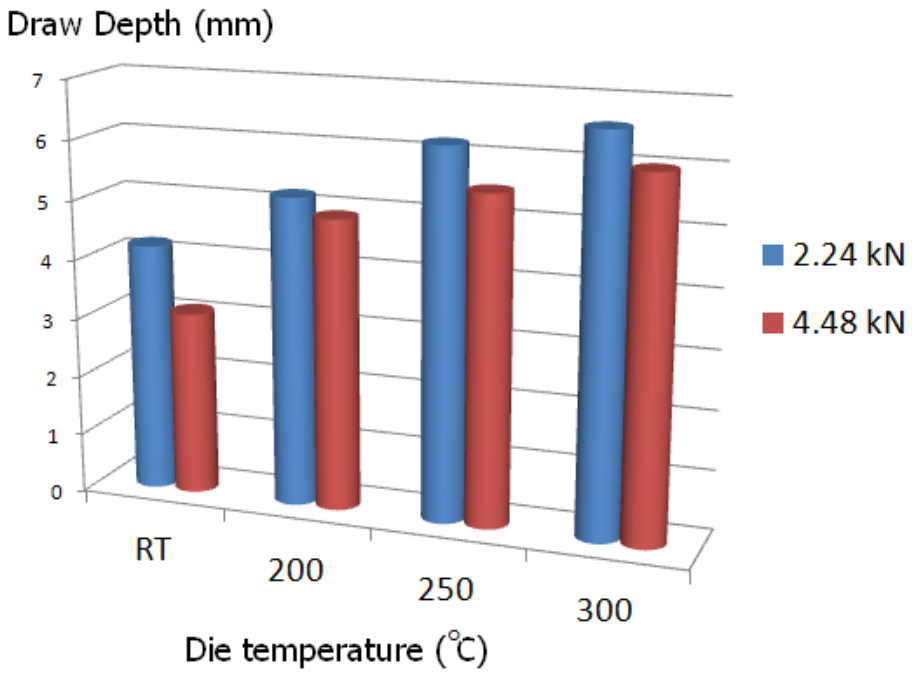

Figure 6.6 Maximum draw depth before fracture (punch speed of 8mm/s, cold punch at 15°C and Dasco Cast lubricant)

6.2.2 Teflon sheet lubricant Experiments

Experiments were also performed using Teflon sheet as a lubricant to overcome some of the undesirable effects of the Dasco Cast lubricant (elevated friction coefficient and build-up of residual lubricant). These experiments utilized a clamping force of 4.48 and 6.72 kN and three die temperature cases were considered: room temperature, 250°C and 300°C. All parts were drawn to full depth (6.8 mm). Figure 6.7 shows the formed parts. It can be seen that the use of Teflon sheet has improved the forming process. The forming at room temperature resulted in a broken part. Heating the dies up to either 250 or 300°C resulted in a formed part without failure though wrinkles still exist in both cases. The formed part at 300°C showed a smaller degree of wrinkling.

To eliminate the wrinkles, the clamping force was increased to 6.72 kN (1,500 lbf) using a die temperature of 300°C. The wrinkles disappeared although a small amount of necking was observed at the punch radius (Figure 6.8). It should be noted that the parts all show a feature that appears in the photograph to be a neck at the die entry radius. This is in fact not a neck, but a lighting artifact that proved difficult to eliminate.

Room Temperature	250° C	300°C
Failure 	Draw (severe wrinkling) 	Draw (mild wrinkling) 

Figure 6.7 Summary of experimental results for 8mm/s punch speed, 4.48kN clamping force, cold punch at 15°C for non-isothermal cases, and Teflon sheet as lubricant. All samples reached the required draw depth (6.8mm)

Figure 6.8 Forming using Teflon sheet as lubricant, 6.72 kN clamping force, heated dies at 300°C and cold punch at 15°C

Figure 6.9 summarizes the overall forming performance for samples without lubricant and with either Dasco Cast or Teflon lubrication at different temperatures. The draw depths for forming under different temperature settings, a punch speed of 8 mm/s and a clamping force

of 4.48 kN using Teflon sheet were measured and compared with those of no-lubricant forming (Table 6.2). The red-coloured portions indicate the improvement in formability using Dasco Cast and the green-coloured portions are the further improvement achieved using Teflon sheet, which is seen to be significant. As can be seen, the Dasco Cast has no effect at room temperature, however, it improves the draw depth by 20.5%, 20.9% and 20% under non-isothermal forming conditions with dies heated to 200°C, 250°C and 300°C, respectively. The ineffectiveness of Dasco Cast at room temperature was expected since it is designed for high temperature applications. The Dasco Cast is formulated to be sprayed on the hot surface of the tooling to establish a low-friction layer in contact with the hot tool. The Teflon sheet caused a significant increase in maximum draw depth at room temperature (42% more with respect to no-lubricant forming). The draw depths were increased by 30.1%, 58.2% and 56.3% under non-isothermal forming conditions with dies heated at 200°C, 250°C and 300°C, respectively. It was observed that the highest improvement of both lubricants (Dasco Cast and Teflon Sheet) was realized at 250°C; however, it was necessary to heat the tooling up to 300°C (using Teflon sheet) to draw the full depth without necking.

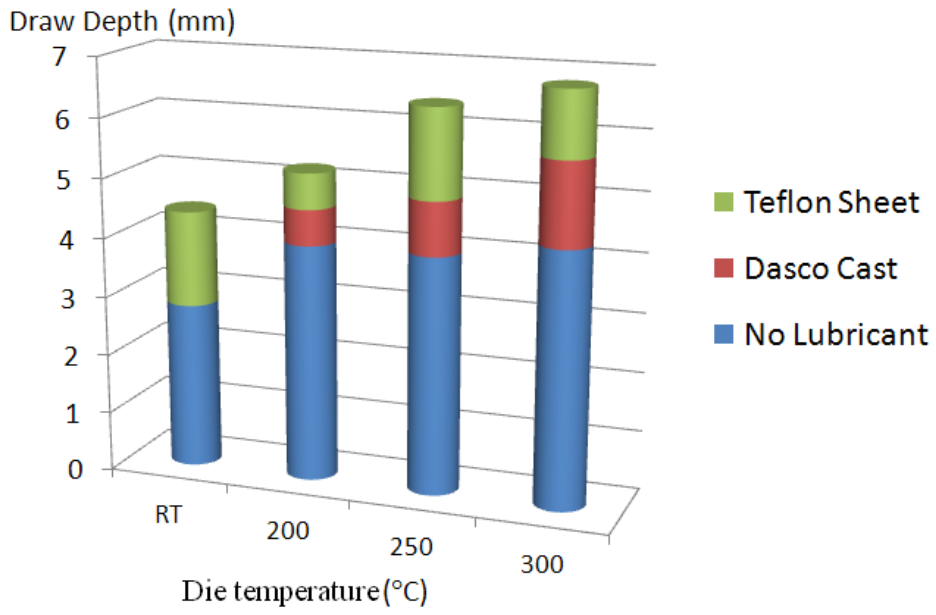

Figure 6.9 Forming improvement by using Dasco Cast and Teflon sheet at different die temperatures; cold punch at 15°C, clamping force of 4.48kN and punch speed of 8mm/s

6.3 Numerical Simulation

The solid tooling model was developed using SolidWorks and CAD surface descriptions of the tooling. The geometry model was imported into Hypermesh and simplified to retain only those surfaces necessary to generate a tooling surface mesh within the finite element model. An LS-DYNA-compatible mesh model was generated in Hypermesh, as seen in Figure 6.10. Due to the symmetry of the equipment and samples, only one-half of the part and tooling was modeled. The mesh was generated using 4-node Belytschko-Tsay shell elements (Belytschko and Tsay, 1981). The tooling was modeled using rigid surface elements. An overall element size of 0.5 mm was used for mesh generation, but a finer mesh was used in areas with a curved profile. In total, 4672 shell elements and 14,764 rigid elements comprise the blank and tooling meshes, respectively. Figure 6.10 shows the tooling and blank mesh model.

All surface contacts were modeled as thermal contacts within LS-DYNA to simulate heat transfer between the hot dies, cold punch and blank. The heat transfer conductivity of the contact surfaces with closed gaps is defined as 50,000 W/m^2K (Cengel and Boles, 2001). Intermittent mechanical contact is also enforced between the blank and tooling components utilizing a penalty function-based approach. Coefficients of friction for Dasco Cast and Teflon sheet lubricants, obtained by twist compression testing the applied lubricants and sheet material, were measured at 0.08 and 0.043, respectively. The loading mimics that in the experiments. After the clamp die was closed, the punch advanced to push the blank into the die cavity to a depth of 1 mm. As described in the experimental setup (Section 6.2.1), the punch was held in this position for a short period to enable heat transfer, then moved to the desired depth. An accelerated loading rate was used in the forming experiments to keep the explicit dynamic run times manageable. The punch speed was increased by a factor of 1,000. As a result, the heat conductance coefficients between the contact surfaces and within the blank were increased proportionally. This approach greatly reduces the required CPU time without introducing excessive dynamic effects in the simulations. Numerical simulations corresponding to all of the experiments have been performed. The forming process parameters used in each of the experiments have been simulated in a coupled thermo-mechanical model.

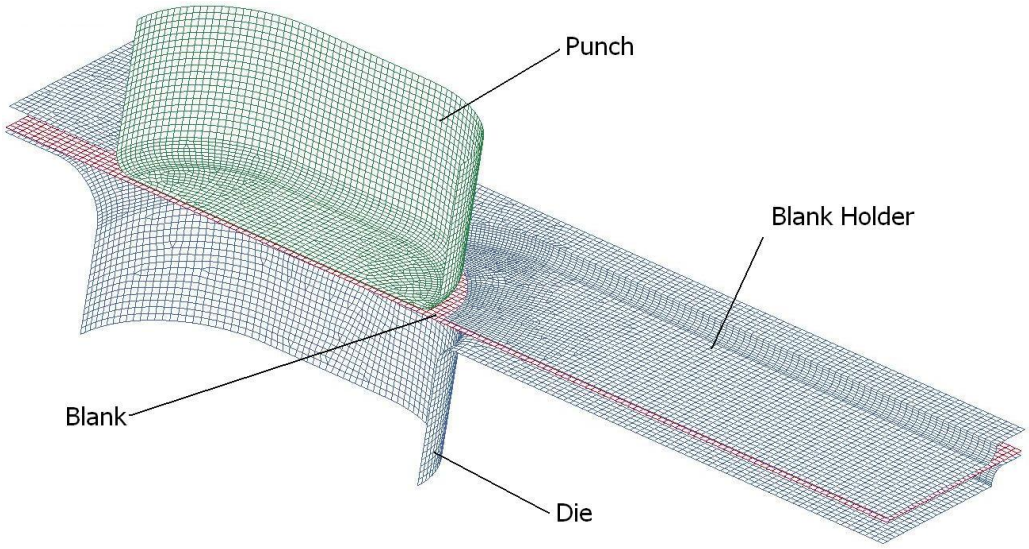

Figure 6.10 Mesh model of tooling and blank

6.4 Numerical Results

6.4.1 Temperature distribution

Figure 6.11 shows contour plots of temperature distribution at the start of draw, mid-draw and end of the forming for the case in which the die and blank holder temperature is 200 °C, a clamping force of 2.24kN is applied and the punch speed is 8mm/s. The simulation shows that after closing the clamp and initial contact of the punch (punch depth of 1mm), the temperature of the blank area in contact with the punch drops to approximately 19°C while the temperature of the rest of the blank reaches the die temperature of 200°C, very quickly. The predicted temperature-time history is plotted in Figure 6.4 and compares reasonably well with the measured data. Once the forming proceeds, the temperature of the blank under the punch increases to approximately 30°C at the intermediate forming step (punch depth of 3mm), likely due to loss of contact with the punch bottom once forming starts. By the end of forming, the punch cools down the region of the blank adjacent to the punch surface to 16°C while the area between the die and binder is heated to 200 °C.

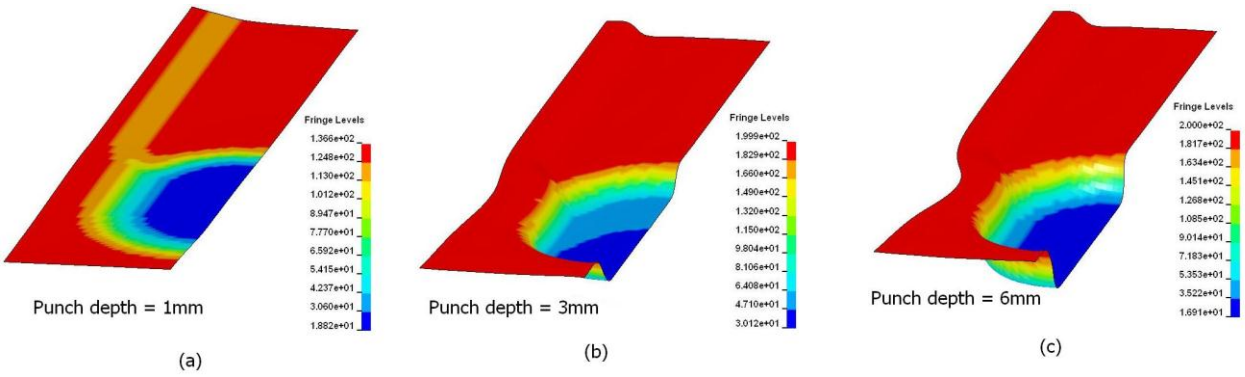

Figure 6.11 Temperature distribution in a formed part with tooling at 200 °C and cold punch at 15°C; (a) 1mm punch depth, (b) 3 mm punch depth, and (c) 6 mm punch depth

6.5 Predicted punch force

Figure 6.12 shows the effect of forming speed on punch force and serves to compare the experimental and numerical results. A clamping force of 2.24 kN with heated dies at 250°C and Teflon sheet (μ=0.043) as lubricant is used. In general, the agreement between the predicted and measured punch force is good. The measured punch force data is unfiltered and exhibits a fair level of scatter. This "noise" is attributed to the rather low punch force range needed to form the bubble feature (3,500 N) compared to the press capacity (896,000 N). Both experiments and simulations show that the forming speed with the studied range does not have a significant effect on punch force. Hence, for the rest of the simulations only a punch speed of 8 mm/s is considered.

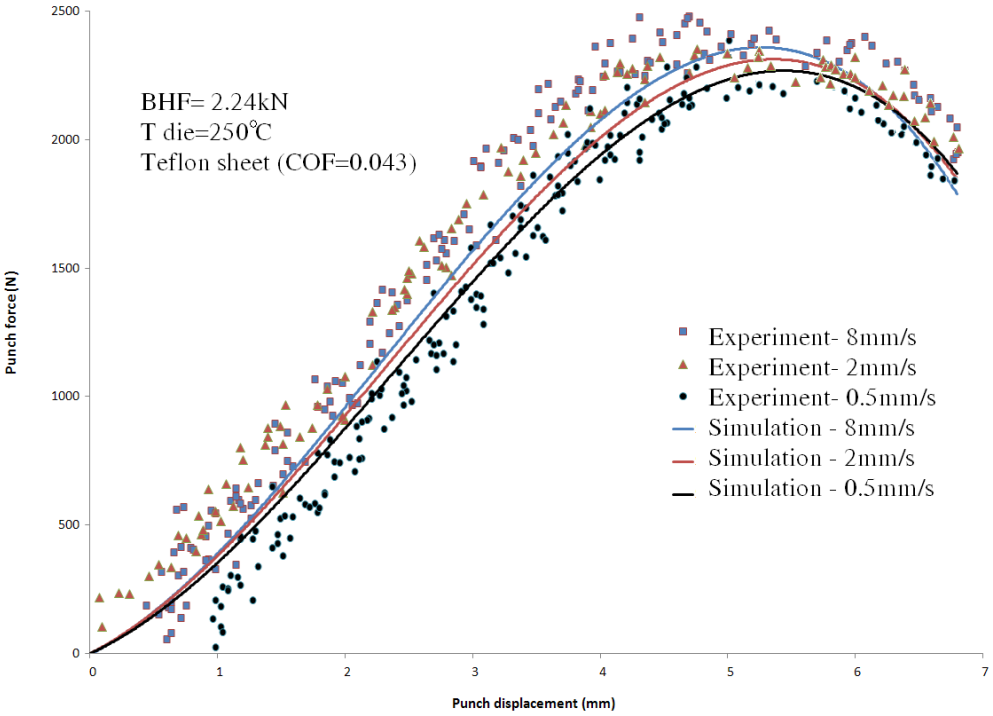

Figure 6.12 Punch force vs. punch displacement for different forming speeds. Experimental results are plotted with symbols and numerical results are plotted with solid lines.

Figure 6.13 to Figure 6.15 show the effect of temperature, lubricant and blank holder force on the forming force, comparing both experimental and numerical data. Figure 6.13***Figure 6.13*** shows the punch force variation for different die temperature settings. For all cases, the punch speed and blank holder force are set to 8 mm/s and 2.24 kN, respectively, and Teflon sheet lubricant is used. The increase in temperature results in a decrease in punch force. A 300°C die temperature lowers the punch force by 29% with respect to that of room temperature forming. Figure 6.14 is a comparison of punch force *versus* punch displacement for two different lubricants. In the simulations and experiments, the punch speed of 8 mm/s and a clamping force of 2.24 kN is used while the dies are heated to 250°C and the punch is kept cold at 15°C. Both cases follow the same trend with the lower friction resulting in lower punch force as expected. The effect of clamping force on punch force is shown in Figure 6.15. Two blank holder forces of 2.24 kN and 4.48 kN are compared. The figure shows a very good agreement between the experimental and numerical results. Forming with higher blank holding pressure requires a higher punch force.

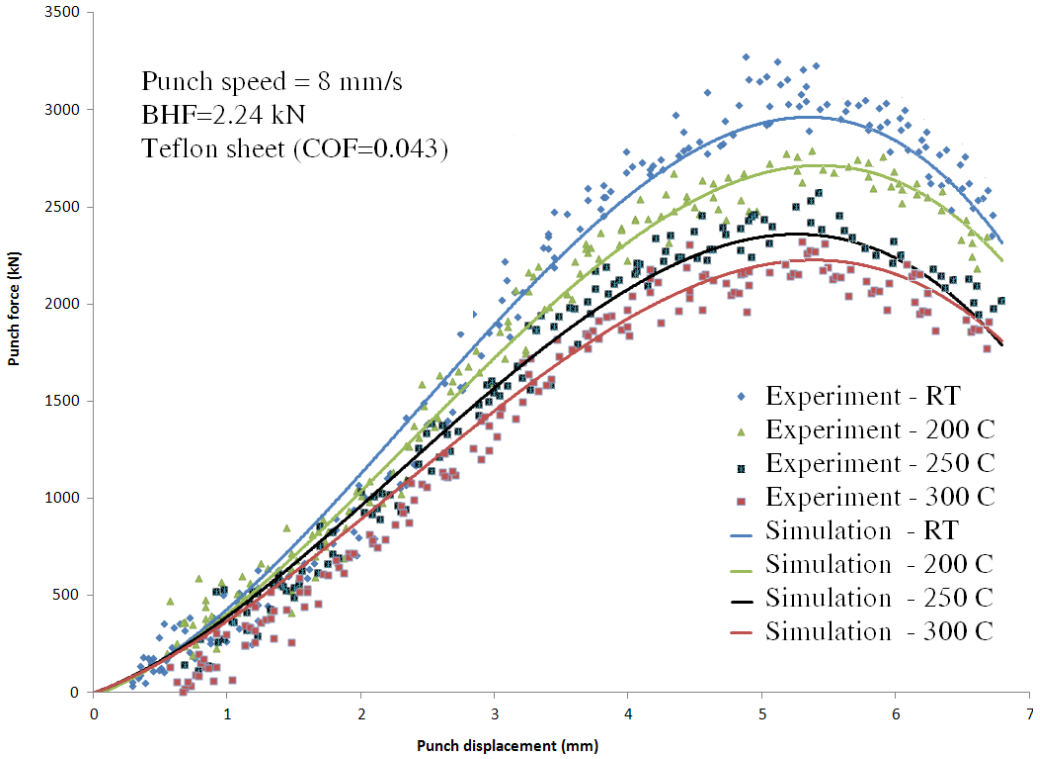

Figure 6.13 Comparison of punch load vs. punch displacement for different die temperatures. Experimental results are shown with symbols and numerical results are shown with solid lines.

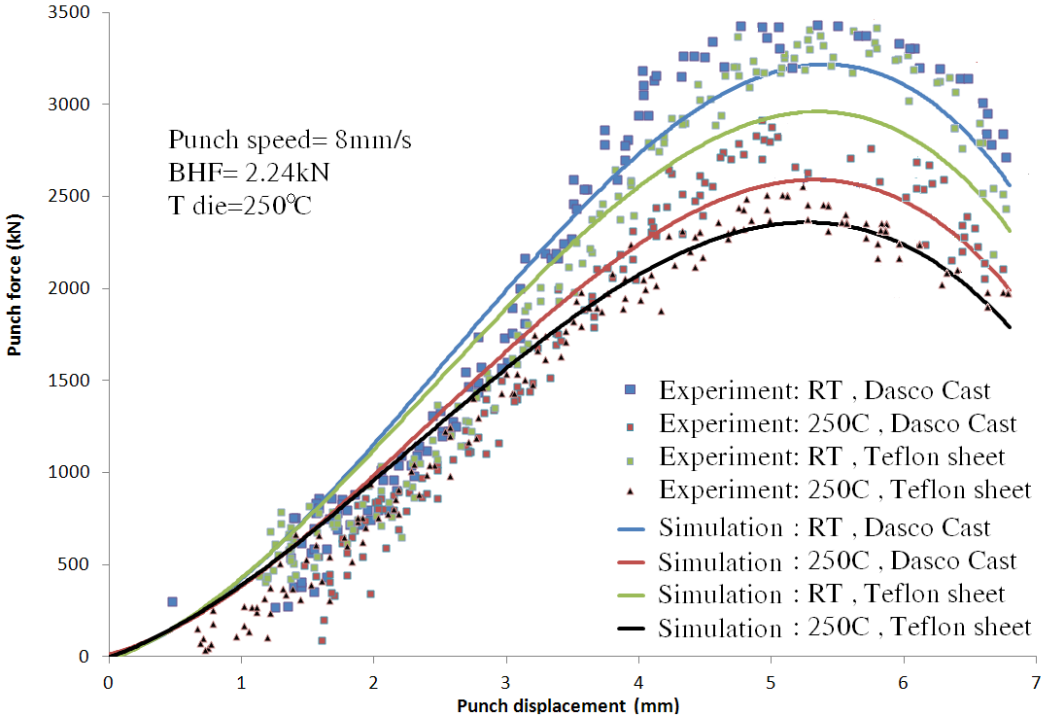

Figure 6.14 Comparison of punch load for samples formed with Teflon sheet and Dasco Cast lubricants. Experimental results are shown with symbols and numerical results are shown with solid lines.

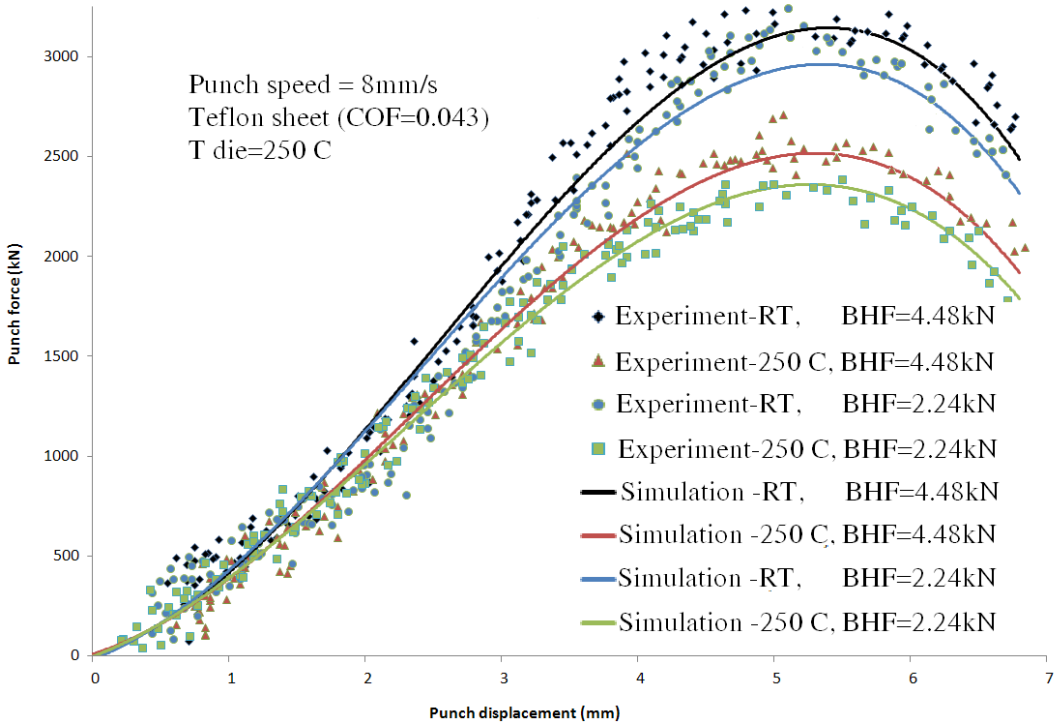

Figure 6.15 Effect of blank holder force on punch force. Experimental results are shown with symbols and numerical results are shown with solid lines.

6.5.1 Effect of temperature difference between the dies and the punch on thickness

The simulations show that a higher temperature gradient at the bubble wall results in less thickness reduction. Figure 6.16 compares the percentage thickness reduction at a draw depth of 5 mm for a clamping force of 2.24 kN, punch speed of 8 mm/s under isothermal forming conditions at (a) room temperature and (b) 300°C; and, non-isothermal forming with a cold punch at 15°C and dies at (c) 250°C and (d) 300°. A coefficient of friction equal to 0.08 is used in the simulations corresponding to the Dasco Cast lubricant. It can be seen that the maximum thinning occurs at the punch profile radius. The contours show that the non-isothermal parts formed at lower flange temperature experience higher thickness reduction at the punch profile radius. The parts formed isothermally at room temperature and 300°C both exhibited sharp thickness reductions. The effect of the temperature difference between the dies and the punch on formability of the part is clearly beneficial which is in agreement with the experimental observations (Figure 6.5 and Figure 6.7).

Figure 6.17 shows the predicted and measured thickness reduction as a function of die temperature. The data corresponds to a clamping force of 2.24 kN and punch speed of 8

mm/s. A coefficient of friction equal to 0.08 is used in the simulations corresponding to the Dasco cast lubricant. In general, the predictions agree well with the measurements.

One simplified design criterion often used in industrial practice is to specify a limit on the maximum thickness reduction, following the approach of Kim et al. (2006). In the current work, for example, if a maximum thickness reduction of 20% was specified, the data in Figure 6.17 indicates that a die temperature warmer than 200 °C would be required for successful forming.

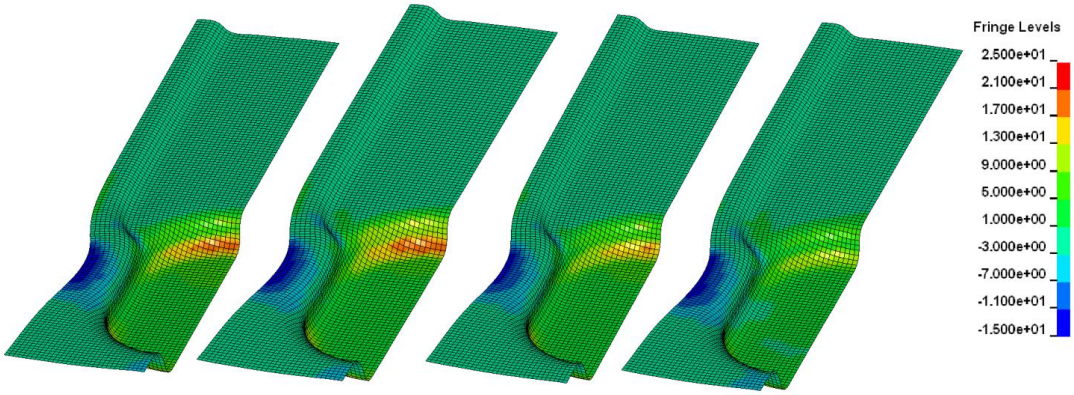

(a) Isothermal at room temperature (b) Isothermal at 300°C (c) Non-isothermal with dies at 250°C (d) Non-isothermal with dies at 300°C

Figure 6.16 Thickness reduction percentage under isothermal forming condition at (a) room temperature and (b) 300°C and non-isothermal forming condition with warm dies at (c) 250°C and (d) 300°C

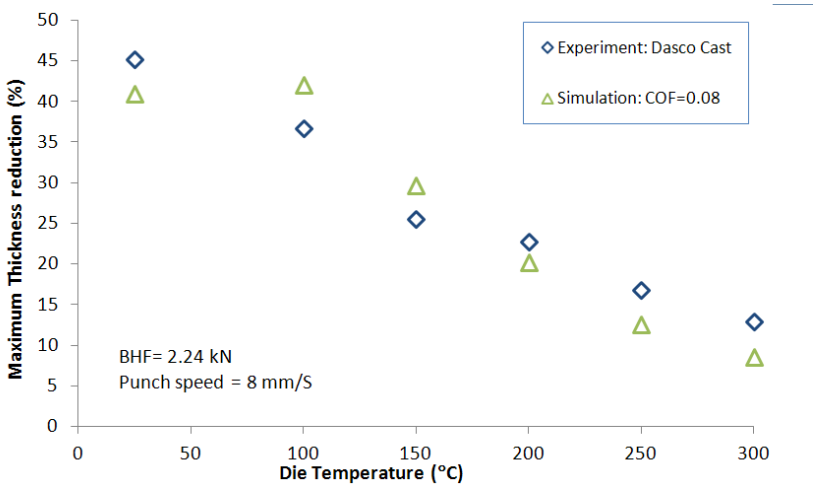

Figure 6.17 Maximum thickness reduction percentage for different die temperatures

6.5.2 Effect of forming parameters on thickness reduction predictions

Figure 6.18 shows the effect of different forming parameters on the predicted maximum thickness reduction for non-isothermal forming with dies at 250°C and a 15°C punch. All predictions are shown for a punch depth of 5.0mm. Simulations were also performed for isothermal forming at room temperature and 250°C; however, all of the isothermal models localized (failed, not shown) which indicates the importance of the non-isothermal process.

Figure 6.18(a) shows the effect of punch speed on thickness prediction. All simulations were performed with a blank holder force of 2.24kN and a coefficient of friction of 0.08. As seen, the forming speed has only a mild effect on predicted thickness reduction, the most significant change occurring for the increase in punch speed from 0.5 to 2.0mm/s. The maximum thickness reduction percentage was predicted as 12.5, 11.9, and 9.7% for punch speeds of 8, 2, and 0.5mm/s, respectively.

Figure 6.18(b) shows the predictions of maximum thickness reduction for parts formed with a punch seed of 8 mm/s and a coefficient of friction of 0.08. As can be seen, the blank holder force has an important effect on necking in the blank. The predicted maximum thickness reduction increased almost linearly with increases in the blank holder force. The predicted maximum thickness reduction using a blank holder force of 2.24kN was 12.5% for non-isothermal forming with dies at 250°C. Increasing the blank holder force from 2.24kN to 4.48kN and to 6.72 kN resulted in increases in thickness reductions of 26% and 35%, respectively.

Friction was also identified as an important factor in controlling localized necking. Figure 6.18(c) shows the predicted maximum thickness reduction using a punch speed of 8mm/s, blank holder force of 2.24kN, and three different coefficients of friction; i.e. 0.15, 0.08, and 0.043. The thickness reduction increased with increases in friction; the predicted values of thickness reduction were 9.1%, 12.5%, and 16% for coefficients of friction of 0.15, 0.08, and 0.043, respectively.

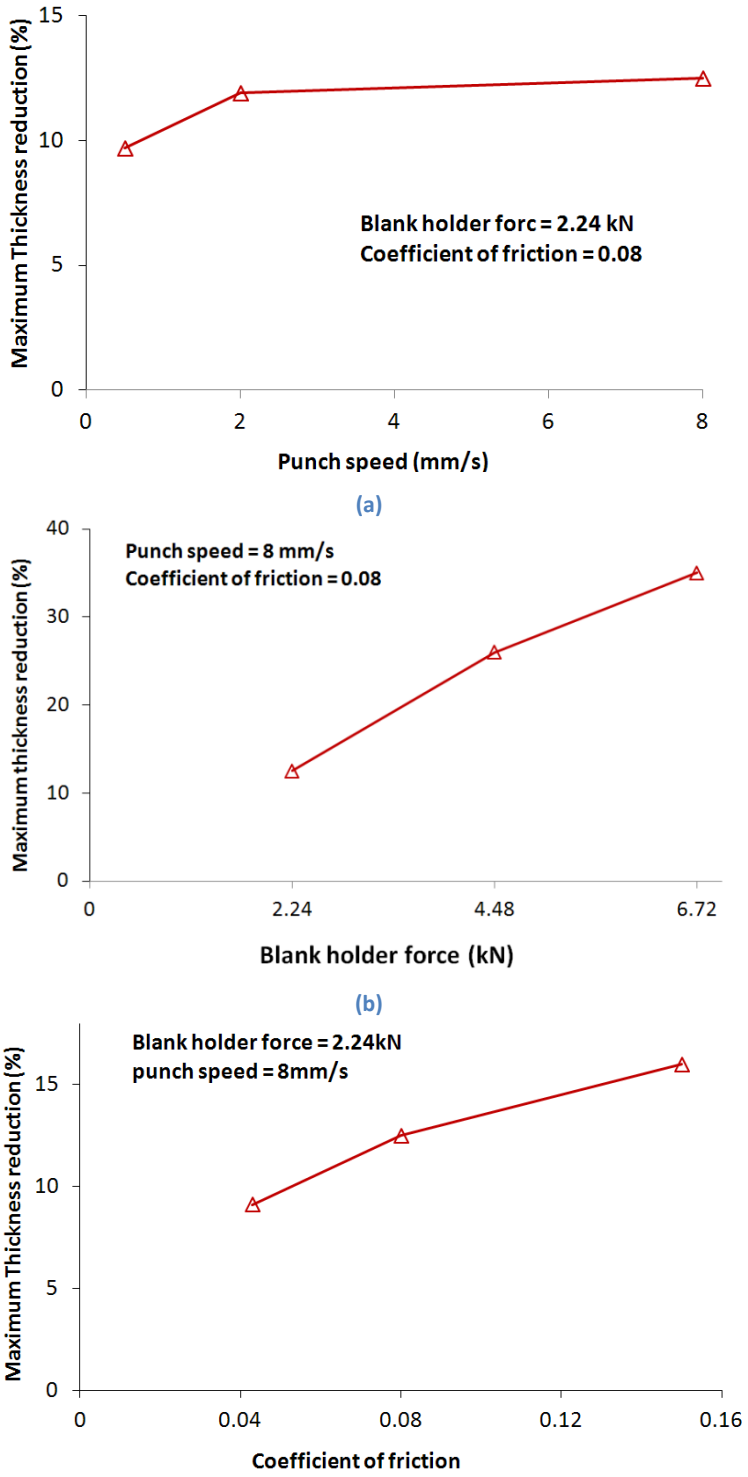

Figure 6.18 Effect of forming parameters on predicted maximum thickness reduction percentage for non-isothermal forming with warm dies at 250°C and cold punch at 15°C: (a) effect of punch speed, (b) effect of blank holder force, and (c) effect of friction

6.6 Failure prediction

In order to predict failure during the forming process, the appropriate FLD corresponding to a given forming temperature distribution is used as the limiting strain within LS-Prepost, the LS-DYNA post-processor. The predicted strain field at each time step is compared with the limiting strains. Each step is assessed sequentially until failure is predicted in the models, corresponding to a strain state lying about the forming limit curve. It must be noted that the FLDs for 0.61mm thick for AA3003 (actual thickness of the core plates) is not available, hence FLDs as described in Chapter 3 (using 0.5 mm thick samples) are used in this section. The use of FLDs from thinner material is expected to result in underestimation of failure depth; however, the available FLDs were used to obtain approximate predictions of failure using the FLD method.

Figure 6.19 and Figure 6.20 show the failure predictions for parts formed isothermally at room temperature and 300°C, respectively. Both simulations were performed using 2.24kN blank holder force, a punch speed of 8mm/s, and a coefficient of friction of 0.08. Failure was predicted at 2.8mm and 3.2mm punch depth for isothermal forming at room temperature and 300°C, respectively. The predicted failure depth for samples formed at room temperature is lower than that measured during experimentation (4.0 mm). This difference was somewhat expected because the FLDs used to predict these values were developed using 0.5mm thick samples, while the actual thickness of the blank used for the core plate samples was 0.61mm. In general, material formability will increase with sheet thickness. As seen from the predictions, isothermal forming at 300°C eliminated the wrinkles; however, it also caused necking to occur at earlier forming steps. Failure occurred at the punch profile radius and the strain state was in the positive minor strain regime. The same response was predicted for the room temperature condition, except that some elements failed in the negative minor strain regime.

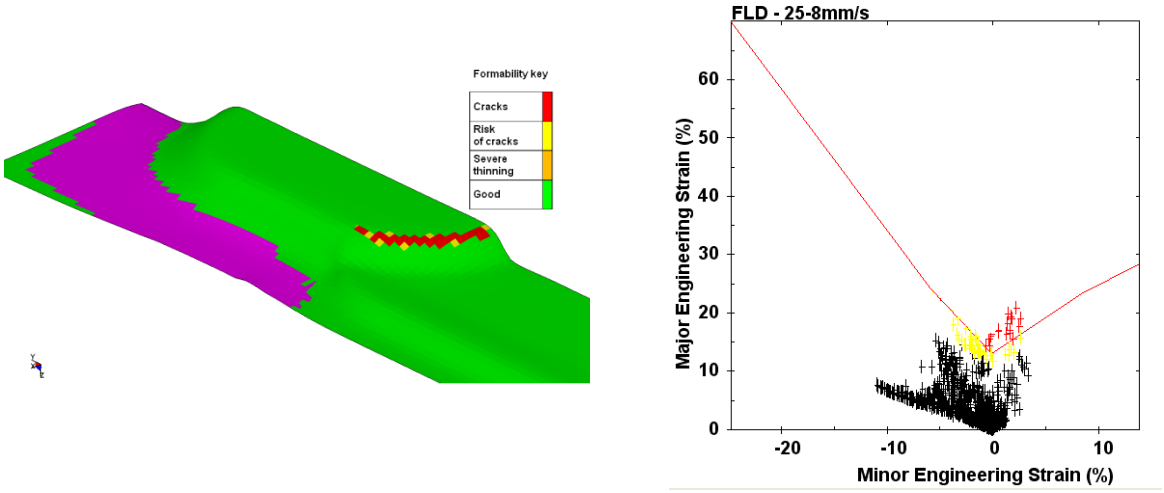

(a) (b)

Figure 6.19 Failure prediction for a part isothermally formed at room temperature with a 8mm/s punch speed, 2.24kN clamping force, and Dasco Cast lubricant (COF=0.08). Fracture occurs at a punch depth of 3.2mm, at the punch profile radius. (a) model prediction (b) Major and minor strains projected on the room temperature FLD

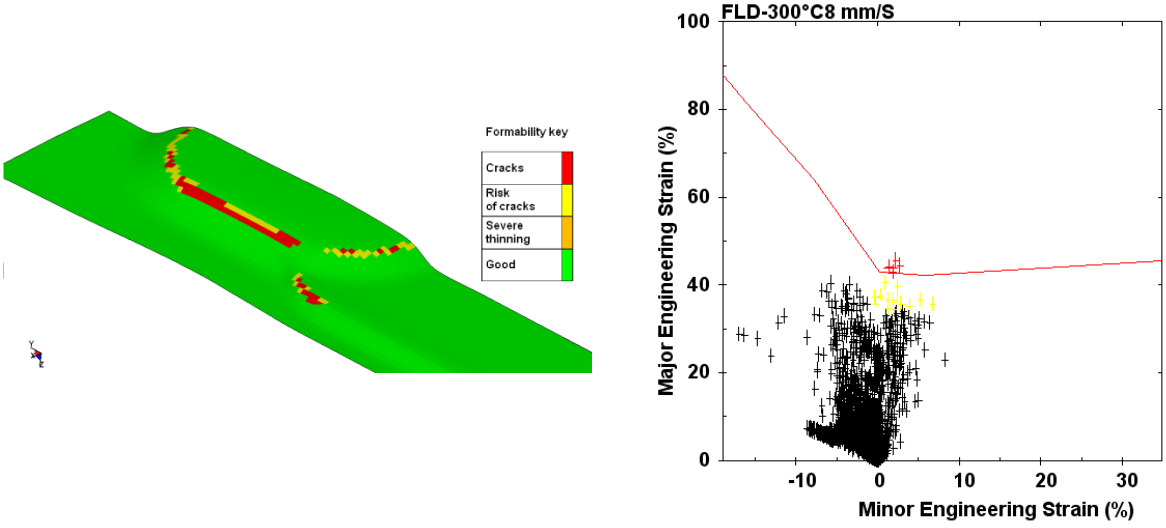

(a) (b)

Figure 6.20 Failure prediction for a part isothermally formed at 300°C, with a 8mm/s punch speed, 2.24kN clamping force, and Dasco Cast lubricant (COF=0.08). Fracture occurs at a punch depth of 2.8 mm at the punch profile radius (a) model prediction (b) Major and minor strains projected on the FLD at 300°C

Figure 6.21 shows the predicted failure of samples formed under non-isothermal conditions using 250°C dies, a 15°C punch, clamping force of 2.24kN, punch speed of 8mm/s, and a COF of 0.08. In order to check for failure, each element should be compared with the FLD corresponding to its temperature during forming. Figure 6.21(a) shows the temperature distribution in the sample. The elements at the punch profile radius and under the punch are formed at room temperature, whereas the elements in the flange area and adjacent to the die entry radius are heated to 250°C. In addition, there is a temperature gradient between the die entry and punch profile radii.

At present, the LS-Prepost software does not have the capability to assign different formability limits to different elements based upon element temperature. To work around this limitation, the predicted strains and temperatures were checked against all of the available forming limit curves (FLCs) for each time step. Failure is predicted for an element if the following criteria are met:

1. The element temperature is equal to or below the FLC;
2. The element strains lie above the FLC.

This comparison had to be performed manually, to account for the temperature gradient within the formed part. This assessment was performed for each time step until the formability criteria are met or the part is successfully deep drawn. To illustrate this process, forming limit plots generated using room temperature, 150°C, and 250°C FLCs are shown in Figure 6.21(b), (c), and (d), respectively, corresponding to a punch depth of 5.7mm (the temperature distribution is shown in Figure 6.21(a)). In Figure 6.21(b), the predicted strains are compared to the room temperature FLC which suggests that failure is likely to occur at both the punch nose and the die entry radius. The predictions are reasonable at the punch nose since the temperature under the punch is near to room temperature. However, the temperature of the die entry radius is 250°C, thus the FLC for this temperature should be used. This comparison is shown in Figure 6.21(d) which illustrates that failure at the die entry radius is unlikely. Thus the operative failure process occurs at the punch profile radius under room temperature conditions, as seen in Figure 6.21(b). The necking and fracture experienced at the die entry radius must be ignored since the temperature of the elements located in this area is

between 200°C and 250°C. The measured punch depth at failure is 6.2 mm, which lies 8.8% above the predicted values; this error is attributed to the thicker sheet material (0.61mm) used for the core plate forming experiments compared to that used for the FLC determination (0.5mm).

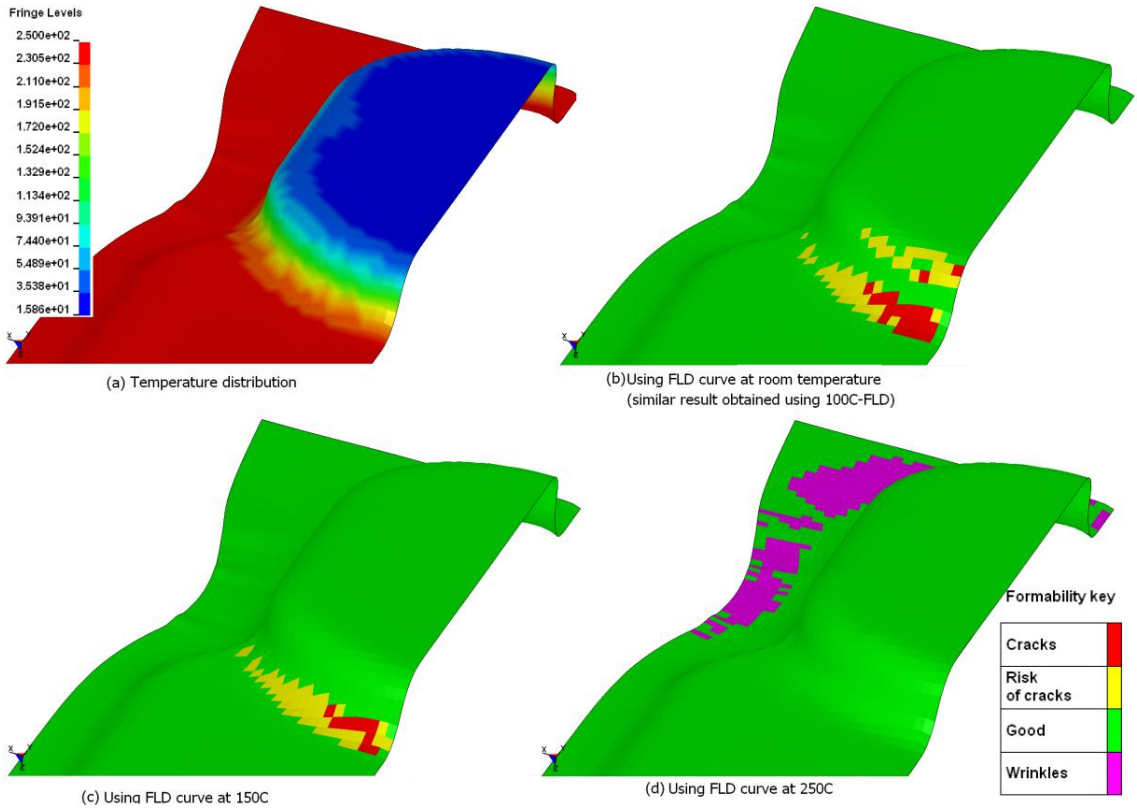

Figure 6.21 Failure prediction for a part non-isothermally formed with dies at 250°C, punch at 15°C, a 8mm/s punch speed, 2.24kN clamping force, and Dasco Cast lubricant (COF=0.08); (a) temperature distribution and failure prediction using FLD at room temperature (b), 150°C (c), and 250°C (d). Fracture is seen first using FLD at room temperature. Wrinkling prediction is only plotted in (d).

Table 6.3 and Figure 6.22 compare predicted punch depths at failure with measured data. As can be seen, the model underestimates the failure depth, which can be attributed to the use of FLCs developed for 0.5mm thick blanks. It should be noted that all predictions showed severe wrinkling in the flange area near the bubble feature. Implementation of techniques to better interpolate the FLCs as a function of temperature and also use of stress-based FLCs, for

example, which are strain path independent, within the UMAT may serve to more accurately predict the onset of failure.

Table 6.3 Predicted and measured draw depth before failure at different temperature settings, with a blank holder force of 2.24kN and punch speed of 8 mm/s

Die Temperature (°C)	Punch Temperature (°C)	Bubble depth (mm)	
		Measured	Predicted
25	25	**4.1**	**3.2**
200	15	**5.2**	**3.9**
250	15	**6.2**	**5.7**
300	15	**6.6**	**5.9**

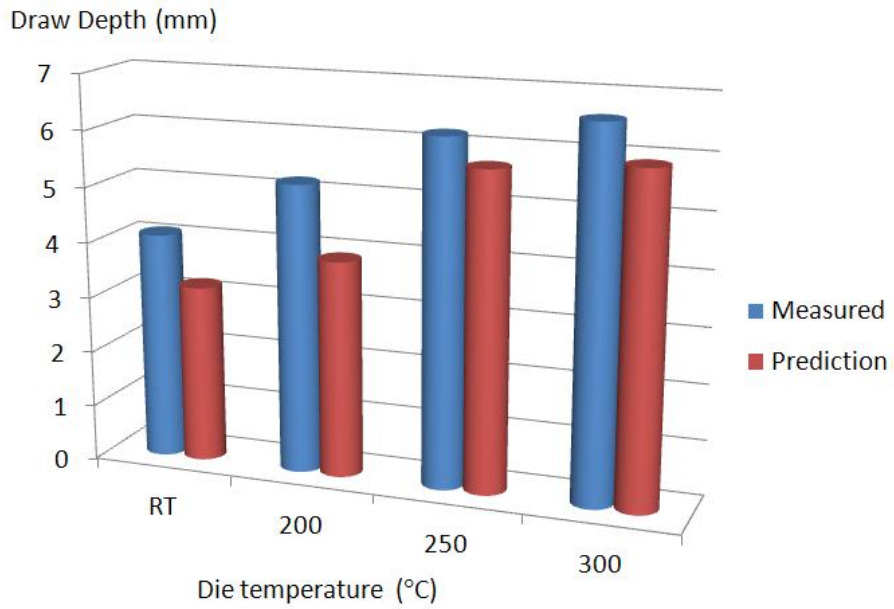

Figure 6.22 Predicted and measured draw depth before failure with a black holder force of 2.24kN and punch speed of 8mm/s for different temperature settings; isothermal room temperature and non-isothermal with a cold punch at 15°C

6.7 Summary

Experiments on warm forming of the heat exchanger core plate have shown that the application of independent die and punch temperature control increases the formability of AA3003 aluminum alloy sheet. Warm forming has an important effect on the thickness within the part sidewall and reduces thinning at the punch radius.

Numerical models using the UMAT and constitutive model approach (Bergstrom-Barlat) adopted in this work, were found to accurately predict the mechanical behaviour of AA3003. The simulations are capable of capturing load response and failure location for the studied material. The parametric study showed that the forming speed does not have a significant effect on localized necking for the range of punch velocities in this study while, both friction and blank holder force are identified as important forming parameters in controlling the thickness reduction in the blank.

The forming limit curves underestimate the failure depth (conservative), which is expected since the forming limit curves were measured using 0.5mm thick sheets while the thickness of the heat exchanger plate is 0.61mm. Additional work is required to implement a formal algorithm to interpolate forming limits based upon element temperature.

7 Conclusions and recommendation

7.1 Conclusions

1. A novel constitutive model combining the Barlat YLD2000 yield function (Barlat et al., 2003) and the Bergstrom hardening rule (Bergstrom and Hallen, 1982) has been developed. The stress-strain curves fit using the Bergstrom parameters showed good agreement with the experimental data for the range of temperatures and strain rates considered; however, the predicted values of stress for strain levels lower than 10% are not as accurate as those in the post uniform strain regime. This issue could be due to the strain rate-independent treatment of the yield point in the Bergstrom model.
2. The key factors controlling warm formability are the dramatic reduction in flow stress and increase in positive rate sensitivity at elevated (warm) forming temperatures. The increased rate sensitivity promotes significant increases in post-uniform elongation. In addition, the reduction in flow stress allows tailoring of the flow stress distribution within the part during non-isothermal forming to promote high strength and fracture resistance at the punch nose and lower strength and ease of flow in the flange.
3. Limiting dome height experiments using 0.5mm thick AA3003 sheet demonstrated that elevating the temperature beyond 100°C increases the limiting dome height and improves the material formability significantly. The maximum dome height measured at 250°C was 42.6mm which is 63% greater than that at room temperature (26.1mm). The orientation of the dog-bone samples did not significantly affect the measured limiting dome height, suggesting that the fracture anisotropy at the range of temperatures and forming speeds considered in this study is negligible.
4. Forming limit diagrams were developed at several temperatures. The material exhibited relatively low limit strains at room temperature; however, the limit strains increased significantly at temperatures above 100°C. Elevating the temperature to 200°C and 250°C increased the limiting strain for plane strain conditions by 99% and 229% compared to room temperature values, respectively. It was found that forming speed has very little effect on the FLC, at least for the punch speeds considered in this work. A slight increase in the limit strains was observed for the lowest punch speed of 0.32mm/s; however, lower punch speeds were not investigated.

5. Experiments on warm forming of the cup shape feature within the heat exchanger plates further demonstrated the increased formability of AA3003 aluminum alloy sheet under non-isothermal conditions. Increasing the flange temperature to 300°C also served to dramatically reduce the extent of wrinkling in the flange region which, in turn, improves formability and is expected to improve brazing performance. The heat exchanger plate experiments were unable to achieve full depth (6.8mm) in a single forming step; however, they were able to quantify the substantial gain in forming depth that could be achieved. The maximum draw depth using non-isothermal forming with dies at 300°C was measured to be 6.6mm while room temperature forming could achieve a depth of only 4.1mm. It is thought that further optimization of the tooling geometry may allow a single step, full depth cup shape feature to be formed under warm conditions; however, this effort is left for future work.
6. Lubrication has an important effect on formability since lower friction reduces thinning at the punch profile radius area but can cause a higher extent of wrinkling at the flange area. The Dasco Cast lubricant had poor room temperature performance, but was more effective at higher temperatures. Nonetheless, Teflon was a much superior lubricant over the entire range of temperatures tested.
7. Blank holder force was identified as an important forming parameter in controlling the thickness reduction in the blank. Lower blank holder force reduces the possibility of necking at the punch profile radius area; however, it increased the wrinkling level at the same time.
8. The ability to accurately simulate warm forming of AA3003 has been demonstrated utilizing the Bergstrom-Barlat user material subroutine (UMAT) developed as part of this research. Numerical models using the UMAT subroutine linked to LS-DYNA were able to reproduce the tensile stress-strain curves under a wide range of temperatures and strain rates. Also, the LDH simulations predicted punch force *versus* displacement as well as strain distributions that were in good agreement with the measured data.
9. The coupled thermo-mechanical finite element models of the cylindrical cup and heat exchanger plate deep drawing operations were found to be able to predict the punch force *versus* punch depth response for both isothermal and non-isothermal deep

drawing accurately, capturing the important effects of blank temperature, binder force and lubricant condition (friction coefficient) on punch loads. The models represent a general framework for simulation of the warm forming of aluminum alloy sheet that accounts for the temperature and strain rate dependency of the hardening response and yield surface shape.

10. Using the temperature dependent, strain-based FLD approach, the numerical models of the hemispherical dome forming, cylindrical cup deep drawing, and heat exchanger plate forming were able to predict both the location of failure and the punch depth at failure well.

7.2 Recommendations and future work

1. Determination of FLCs at higher forming speeds is needed to more accurately study the effect of strain-rate on formability at elevated temperature. This requires faster cameras to be used with the DIC system. The existing cameras are able to capture maximum 4 fps. A minimum of 40 fps is required for a forming speed of 40mm/s (maximum speed of the current press).
2. The determination of FLCs for samples with different thicknesses is required to understand the relation between the material thickness and limiting strains at elevated temperature.
3. A key issue limiting the deployment of non-isothermal forming techniques in industrial practice is the period of time to achieve the required initial temperature gradients. An effective process is needed to induce the required temperature distribution rapidly within the blank. One option might be to use pre-heated blanks in conjunction with a nitrogen/air chill inside the punch. A backup punch could also be used to increase normal force between the punch and sheet and to elevate the rate of heat transfer. Such processes need to be developed and demonstrated.
4. An investigation (search) for appropriate warm forming lubricants that display desirable lubricity without build up on forming dies is necessary. A warm friction testing capability should be developed, likely based upon the current twist

compression friction testing apparatus, to better characterize the warm performance of lubricants.

5. There is little or no information on the heat conductance coefficient between the contact surfaces at elevated temperatures. A more comprehensive understanding of the heat transfer between the tool, lubricant and blank is required and experimental measurement of heat conductance coefficient is recommended.
6. A more general implementation of failure criteria at warm temperatures will be important. Such an effort may require calculation of stress-based FLDs using the measured strain-based FLDs at warm temperatures. Stress-based forming limits may also be beneficial, particularly to capture strain path change effects.
7. There is a need to improve the friction model treatment to account for temperature, interface pressure and sliding distance (lubricant breakdown).
8. Biaxial tensile testing should be performed to find the biaxial yield strength, σ_b. Since this data was unavailable, the current work considered $\sigma_b = (\sigma_{90} + \sigma_{45})/2$.
9. The current Bergstrom model assumes the yield point to be strain rate-independent. The current tensile data indicates that the yield point may be rate sensitive and modifications to the constitutive model to account for this effect should be considered.

Bibliography

Abedrabbo, N., Pourboghrat, F., and Carsley, J., 2006. Forming of aluminum alloys at elevated temperatures - part 1: material characterization. Int. J. Plasticity 22 (2), 314-341.

Abedrabbo, N., Pourboghrat, F., Carsley, J., 2007. Forming of AA5182-O and AA5754-O at elevated temperatures using coupled thermo-mechanical finite element models. Int. J.Plast. 23, 841–875.

Altan, T., 2002. Warm forming of aluminum alloys-academic exercise or practical opportunity? Stamping J. 14, 58–59. ASM Metal Handbook, 1988. Volume 14 Forming and Forging. 9th ed. ASM International, Metals Park, Ohio, pp. 791–804.

Ambrogioa, G., Filicea, L., Palumbob, G., Pintob, Prediction of formability extension in deep drawing when superimposing a thermal gradient, Journal of Materials Processing Technology Volumes 162-163, 15 May 2005, Pages 454-460

Ayada, M., Higashino, T., and Mori, K., Central bursting in extrusion of inhomogeneous materials, Adv. Technol. Plast. **1** (1987), pp. 553–558

Ayres, R.A., Brewer, E.G. , Holland, S.W., 1979. Trans. SAE, 88 (1979), pp. 2630–2634

Bagheriasl, R., Ghavam, K., Worswick, M.J., 2011a. Formability analysis of aluminum alloy sheets at elevated temperatures with numerical simulation based on the M-K method, Proc. of ESAFORM, Belfast, Ireland.

Bagheriasl, R., Ghavam, K., Worswick, M.J., 2011b. Stress Analysis of a Deep Drawn Cup with Plastic Anisotropy and Rate Sensitivity at elevated Temperatures, 15th International Conference IDDRG, Bilbao, Spain

Bagheriasl, R., Ghavam, K., Worswick, M.J., 2011c. Effect of strain rate and temperature gradient on warm formability of Aluminum alloy sheet, NUMISHEET, Seoul, Korea.

Barlat, F., Chung, K., 1993. Anisotropic potentials for plastically deforming metals Model. Simul. Mater. Sci. Eng., 1 (1993), pp. 403–416

Barlat, F., Lian, J., 1989. Plastic behavior and stretchability of sheet metals. Part I. A yield function for orthotropic sheets under plane stress conditions. Int. J. Plast. 5, 51–66.

Barlat, F., Lege, D.J., Brem, J.C., 1991. A six-component yield function for anisotropic materials. Int. J. Plast. 7, 693–712.

Barlat, F., Maeda, Y., Chung, K., Yanagawa, M., Brem, J.C., Hayashida, Y., Lege, D.J., Matsui, K., Murtha, S.J., Hattori, S., Becker, R.C., Makosey, S., 1997. Yield function development for aluminum alloy sheets. J. Mech. Phys. Solids 45 (11/12), 1727–1763.

Barlat, F., Brem, J.C., Yoon, J.W., Chung, K., Dick, R.E., Lege, D.J., Pourboghrat, F., Choi, S.H., Chu, E., 2003. Plane stress yield function for aluminum alloy sheets. Part 1. Theory. Int. J. Plast. 19, 1297–1319.

Barlat, F., Aretz, H., Yoon, J.W., Karabin, M.E., Brem, J.C., Dick, R.E., 2005. Linear transformation-based anisotropic yield functions. Int. J. Plast. 21 (5), 1009–1039.

Barlat, F., Yoon, J.W., Cazacu, O., 2007. On linear transformations of stress tensors for the description of plastic anisotropy. Int. J. Plasticity 23 (6), 876-896.

Belytschko, T. and Tsay, C.S., 1981. Explicit algorithms for nonlinear dynamics of shells. AMD, ASME (48) 209-231.

Belytschko, T.,W. K. Liu and B. Moran (2006), Nonlinear finite elements for continua and structures, Wiley, Chichester.

Bergstrom, Y., Hallen, H., 1982. An improved dislocation model for the stress-strain behavior of polycrystalline α-Fe. Mat. Science and Eng. 55, 49-61.

Cengel, Y.A., and Boles, M.A., 2001. Thermodynamics: An Engineering Approach. McGraw-Hill, 4th ed.

Bolt, P.J., Lamboo, N.A.P.M., Rozier, P.J.C.M., 2001. Feasibility of warm drawing of aluminum products. J. Mater. Process. Technol. 115, 118–121.

Bragard, A., 1989. Forming Limit Diagrams: Concepts, Methods, and Applications, TMS, Warrendale, PA (1989), pp. 9–19

Brozzo, .P., DeLuka, B., Rendia, R., 1972. A new method for the prediction of formability in metal sheets, Proceedings of the Seventh Biennial Conference on Sheet Metal Forming and Formability IDDRG (1972)

Carle, D., Blount, G., 1999. The suitability of aluminum as an alternative material for car bodies Mater. Des., 20 (1999), pp. 267–272

Choi, H., Koc¸ , M., Ni, Jun., 2007. A study on the analytical modeling for warm hydro-mechanical deep drawing of light weight materials. Int. J. Mach. Tool Manuf. 47, 1752–1766.

Cockcroft, M.G. , and Latham, D.J. , 1968, Ductility and the workability of metals, J. Inst. Met. **96** (1968), pp. 33–39

Cole, G.S., Sherman, A.M., 1995. Light weight materials for automotive applications, Mater. Charact., 35, pp. 3–9

Crisfield, M. A. (1997), Non-linear finite element analysis of solids and structures, Vol. 2: Advanced Topics, J. Wiley & Sons, New York

Demeri, M.Y., 1981. The Stretch-Bend Forming of Sheet Metals, J. Appl. Metal working, 2, (1), 1981, pp 3-10. 2

Desmorat, R. and Marukk, R., 2011. Non-quadratic Kelvin modes based plasticity for anisotropic materials. Int. J. Plasticity 27, 328-351

Dinda, S., James, K.F., Keeler, S.P., Stine, P.A., 1981. How to Use Circle Grid Analysis for Die Tryout, ASM, Metals Park, OH

Doege, E., Melching, R., Kowallick, G., 1978. Investigations into the behavior of lubricants and the wear resistance of die materials in hot and warm forging. J.ofMech. Working Tech., 2(1978) 129-143

Farrokh, B., Khan, A.S., 2009. Grain size, strain rate, and temperature dependence of flow stress in ultra-fine grained and nanocrystalline Cu and Al: synthesis, experiment, and constitutive modeling. Int. J. Plasticity 25, 715-732.

Fourmeau, M., Borvki, T., Benallal, A., Lademo, O.G., Hopperstad, O.S., 2011. On the plastic anisotropy of an aluminum alloy and its influence on constrained multiaxial flow. Int. J. Plasticity 27, 2005-2025

Freudenthal, A.M., 1950, The inelastic behaviour of engineering materials and structures, Wiley, New York (1950)

Fukui S, Yoshida K, Abe K, 1960. Correlation among experimental values obtained in various formability tests. Scientific Papers of the Institute of Physical and Chemical Research 54:199–205

Ghavam, K., Bagheriasl, R., Worswick, M.J., 2011a. Numerical modeling of hemispherical dome testing of aluminum alloy sheet at elevated temperatures, Int. Symp. of Plasticity, Puerto Vallarta, Mexico.

Ghavam K., Bagheriasl R., Worswick M.J., 2011c, Stress analysis of non-isothermal deep drawing with induced anisotropy and rate sensitivity at elevated temperatures, Submitted to Int. J. Plast.

Gavas, M., Izciler, M., 2007. Effect of blank holder gap on deep drawing of square cups. Mater. Des. 28, 1641–1646.

Ghosh, A.K., 1975. The Effect of Lateral Drawing- In On Stretch Formability, Metals Engineering Quarterly, 15 (3) (1975) pp. 53-64

Goodwin, G.M., 1968. Application of strain analysis to sheet metal forming problems in the press shop Trans. Soc. Automot. Eng., 77 (1968), pp. 380–387

Hallquist, J.O. 2006. LS-DYNA Theory Manual, Livermore Software Technology Corporation, Livermore, California, USA

Hanna, M.D., 2009. Tribological evaluation of aluminum and magnesium sheet forming at high temperatures. Wear 267 (2009) 1046–1050

Harvey, D.N. , Optimizing patterns and computational algorithms for automatic, optical strain measurement in sheet metal, efficiency in sheet metal forming, in: Proceedings of the 13th Biennial Congress, Melbourne, Australia, International Deep Drawing Research Group, 1984, pp. 403–414.

Hecker, S.S., 1974. Met. Eng. Quarterly, 14 (1974 Nov.), p. 30

Hecker, S.S., Gosh, A.K., Gegel, H.L., 1978. Formability: Analysis, Modeling, and Experimentation, AIME, New York, pp.150-182.

Hershey, A.V., 1954. The plasticity of an isotropic aggregate of anisotropic face centred cubic crystals. J. Appl. Mech. 21 (1954) 241-249

Hill, R.: A theory of the yielding and plastic flow of anisotropic metals. Proc. Roy. Soc. London A193 (1948) 281–297

Hill, R.: On discontinous plastic states, with special reference to localized necking in thin sheets. J. Mech. Phys. Sol. 1 (1952) 19-30

Hill, R.: Theoretical plasticity of textured aggregates. Math. Proc. Cambridge Philos. Soc. 85 (1979) 179–191

Hill, R.: Constitutive dual potential in classical plasticity. J. Mech. Phys. Solids 35 (1987) 23–33

Hill, R.: Constitutive modelling of orthotropic plasticity in sheet metals. J. Mech. Phys. Solids 38 (1990) 405–417

Hill, R.: A user-friendly theory of orthotropic plasticity in sheet metals. Int. J. Mech. Sci. 35 (1993) 19–25

Hutchinson, J.W., Neale, K.W., 1985. Wrinkling of curved thin sheet metal, plastic instability. In: Proceedings of the Considere Memorial Symposium, Presses Ponts et Chaussees, Paris, pp. 71–78.

Jain, M., Allin, J., Bull, M.J., 1998. Deep drawing characteristics of automotive aluminum alloys. Mater. Sci. Eng. A-Struct. 256, 69–82.

Jinta, M., Sakai, Y., Oyagi, M., Yoshizawa, S., Matsui, K., Noda, K., 2000. Press forming analysis of aluminum auto body panel: wrinkle behavior in 5000 and 6000 series aluminum alloy sheet forming. JSAE Rev. 21, 407–409.

Keeler, S.P, Backofen, W.A, 1963. Plastic instability and fracture in sheets stretched over rigid punches

Trans. ASM, 56 (1963), pp. 25–48

Kapij, M.I., Lee, D., 1990. Tribological factors in the stamping of coated and uncoated steel sheets, 16th Biennal Congress of the IDDRG, Borlänge

Karafillis, A.P., Boyce, M.C.: A general anisotropic yield criterion using bounds and a transformation weighting tensor. J. Mech. Phys. Solids 41 (1993) 1859-1886

Kaufman, J. (2000). Introduction to aluminum alloys and tempers. ASM International. pp. 116–117. ISBN 087170689X. Retrieved Nov 9, 2011.

Kaya, S., Spampinato, G. & Altan, T. 2008, "An Experimental Study on Nonisothermal Deep Drawing

Process Using Aluminum and Magnesium Alloys", *Journal of Manufacturing Science and Engineering*, vol. 130, no. 6.

Keeler, S., "Statistical Deformation Control for SPQC Monitoring of Sheet Metal Forming," SAE Technical Paper 850278, 1985, doi: 10.4271/850278.

Kelly, J.F., Cotterell, M.G., 2002. Minimal lubrication machining of aluminum alloys. J. Mater. Process. Technol. 120, 327–334.

Keum, Y.T., Ghoo, B.Y., Wagoner, R.H., 2001. 3-dimentional finite element analysis of nonisothermal forming processes for non-ferrous sheets. In Simulation of Material Processing: Theory, Methods and Applications, ed. Ken-ichiro Mori, A.A. Balkema, Lisse, The Netherlands, pp. 813

Khan, A.S., and Liang R., 1999. Behavior of three BCC metal over a wide range of strain rates and temperatures. Int. J. Plasticity, 15, 1089–1109

Khan, A.S., Baig, M., 2011. Anisotropic response, constitutive modeling and the effect of strain-rate and temperature on the formability of an aluminuma lloy. Int. J. Plasticity 27, 522-538

Kim, H.S., Koc¸ , M., Ni, J., Ghosh, A., 2006. Finite element modeling and analysis of warm forming of aluminum alloys-validation through comparisons with experiments and determination of a failure criterion. J. Manuf. Sci. Eng. Trans. ASME 128, 613–621.

Kurukuri S., van den Boogaard A.H., Mirox A., Holmedal B., 2009. Warm forming simulation of Al-Mg

sheet, J. Mat. Processing Tech. in press.

Kurukuri, S., Miroux, A., Wisselink, H.H., Boogaard, A.H., 2011. Simulation of stretch forming with intermediate heat treatments of aircraft skins - a physically based modeling approach. Int. J. of Mat. Form. 4 (2), 129–140.

Li, D., Ghosh, A., 2003. Tensile deformation behavior of aluminum alloys at warm forming temperatures. Mater. Sci. Eng. A-Struct. 352, 279–286.

Li, D., Ghosh, A., 2004. Biaxial warm forming behavior of aluminum sheet alloys. J. Mater. Process. Technol. 145, 281–293.

Lian, J., Barlat, F., Baudelet, B., 1989. Plastic behaviour and stretchability of sheet metals. Part II. Effect of yield surface shape on sheet forming limit. Int. J. Plast. 5, 131–147.

Lin, Z., Wang, W., Chen, G., 2007. A new strategy to optimize variable blank holder force towards improving the forming limits of aluminum sheet metal forming. J. Mater. Process. Technol. 183, 339–346.

Logan, R.W., Hosford, W.F.: Upper-bound anisotropic yield locus calculations assuming pencil glide. Int. J. Mech. Sci. 22 (1980) 419–430

Marciniak, Z. & Kuczynski, K. 1967, "Limit strains in the processes of stretch-forming sheet metal",

International Journal of Mechanical Sciences, vol. 9, no. 9, pp. 609-612, IN1-IN2, 613-620.

Maslennikov, N.A., 1957. Russian developed punchless drawing. Metalwork Prod. 16, 1417–1420.

McKinley, J., Abedrabbo, N., Worswick, M.J., Kozards, M., 2008. Effect of independent die and punch temperature control on the formability of 3003 aluminum alloy in warm deep drawing. Proc. of the 7th Int. Conf. Numisheet, Interlaken, Switzerland.

McKinley, J., Simha, C.H.M., Worswick, M.J., 2009. Constitutive Modeling of Aluminum Clad Sheet for Warm Forming, Proceedings IDDRG 2009 Conference, Golden, Colorado, June 1-3, 2009

McKinley, J., 2010. Warm forming of aluminum brazing sheet. MSc thesis, University of Waterloo.

Mellor, P.B.: Sheet metal forming. Int. Metals Review 1 (1981) 1–20

Meuleman, D., Sues, J., and Zoldak, J., "The Limiting Dome Height Test for Assessing the Formability of Sheet Steel," SAE Technical Paper 850005, 1985, doi:10.4271/850005

Meiler, M., Pfestorf, M., Geiger, M., Merklein, M., 2003. The use of dry film lubricants in aluminum sheet metal forming. Wear 255, 1455–1462.

Nadai, A. Theory of Flow and Fracture of Solids, 1950, McGraw-Hill, London

Naka, T., Yoshida, F., 1999. Deep drawability of type 5083 aluminum–magnesium alloy sheet under various conditions of temperature and forming speed. J. Mater. Process. Technol. 89/90, 19–23.

Naka, T., Torikai, G., Hino, R., Yoshida, F., 2001. The effects of temperature and forming speed on the forming limit diagram for type 5083 aluminum–magnesium alloy sheet. J. Mater. Process. Technol. 113, 648–653.

Naka, T., Nakayama, Y., Uemori, T., Hino, R., Yoshida, F., 2003. Effects of temperature on yield locus for 5083 aluminum alloy sheet. J. Mater. Process. Technol. 140, 494–499.

Nakazima, K.,Kikuma, T., Hasuka, K., 1968. Technical report 264. Yawata Iron & Steel Co. Sep 1968, P.141

Namoco Jr., C.S., Iizuka, T., Narita, K., Takakura, N., Yamaguchi, K., 2007. Effects of embossing and restoration process on the deep drawability of aluminum alloy sheets. J. Mater. Process. Technol. 187/188, 202–206.

Nes, E., 1998. Modelling of work hardening and stress saturation in FCC metals. Progress in Materials Science, 145, pp.129-193.

North American Deep Drawing Research Group, 1987. Recommended Referee Practice for the Limiting Dome Height (LDH) Test (1987 October 27)

Oritz, M., Simo, J.C., 1986. An analysis of new class of integration algorithms for elastoplastic constitutive relations. Int. J. Num. Meth. Eng. 23, pp.353-366

Palumbo, G., Tricarico, L., 2007. Numerical and experimental investigations on the warm deep drawing process of circular aluminum alloy specimens. J. Mater. Process. Technol. 184, 115–123.

Paquet, D., Dondeti, P., Gosh, S., 2011. Dual-stage nested homogenization for rate-dependant anisotropic elsto-plasticity model of dentritic cas aluminum alloys. Int. J. Plasticity 27, 1677-1701

Picu, R.C., Vincze, G., Ozturk, F., Gracio, J.J., Barlat, F., Maniatty, A.M., 2005. Strain rate sensitivity of the commercial aluminum alloy AA5182-O. Mater. Sci. Eng. A-Struct. 390, 334–343.

Rees, D.W.A, Factors influencing the FLD of automotive sheet metal, Journal of Materials Processing Technology, Volume 118, Issues 1–3, 3 December 2001, Pages 1-8

Sakata, K., Daniel, A., Jonas, J.J., Bussiere, J.F., 1990. Acoustic determination of the higher order orientation distribution function coefficients up to l=12 and their use for the on-line prediction of r-value. Met. Trans., 21A (1990), P.697

Samuel, M., 2002. Influence of drawbead geometry on sheet metal forming. J. Mater. Process. Technol. 122, 94–103.

Schey, J.A., 1992. Formability determination for production control. J.of Mater.Process.Tech, 32, 207-221.

Schmoeckel, D., 1994. Temperaturgefu¨ hrte Prozeßsteuerung beim Umformen von Aluminiumblechen. EFB-Forschungsbericht Nr. 55.

Schmoeckel, D., Liebler, B.C., Speck, F.D., 1995. Grundlagen und Modellversuche—Temperaturgefu¨ hrterStoffffluß beim tiefziehen von Al-blech-realversuche. B¨ander Bleche Rohre 36, 14–21.

Schwarz, H.G., Briem, S., Zapp, P., 2001. Future carbon dioxide emissions in the global material flow of primary aluminum, Energy, 26 (2001), pp. 775–795

Shehata, F., Painter, M.J., Pearce, R., 1978. Warm forming of aluminum/magnesium alloy sheet. J. Mech. Work Technol. 2, 279–291.

Simo, J.C., Hughes. T.J.R., 1998. Computational Inelasticity. Springer, New York, pp.143-149.

Simo, J. C. and T. J. R. Hughes (2000),Computational inelasticity, interdisciplinary applied mathematics, Springer, New York

Smerd, R., Winklera, S., Salisburya, C., Worswicka, M., Lloydb, D., Finn, M., 2005. High strain rate tensile testing of automotive aluminum alloy sheet. Int. J. Impact Eng. 32, 541–560.

Spigarelli, S., Ciccarelli, D., Evangelista, E., 2004. Compressive deformation of An Mg–Al–Si–RE alloy between 120 and 180 ◦C. Mater. Lett. 58, 460–464.

Story, J.M., 1982. Variables Affecting Dome Test Results, J. Applied Metalworking, 2, 1982, pp. 119-125

Takuda, H., Mori, K., Masuda, I., Abe, Y., Matsuo, M., 2002. Finite element simulation of warm deep drawing of aluminum alloy sheet when accounting for heat conduction. J. Mater. Process. Technol. 120, 412–418.

Tebbe, P.A., Kridli, G.T., 2004. Warm forming of aluminum alloys: an overview and future directions. Int. J. Mater. Prod. Technol. 21, 24–40.

Tugcu, P., Neale, K.W., 1999, On the implementation of anisotropic yield functions into finite strain problems of sheet metal forming, Int. J. Plasticity 15, 1021, 1999.

Tugcu, P., Wu, P.D., Neale, K.W., 2002, On the predictive capabilities of anisotropic yield criteria for metals undergoing shearing deformations, Int. J. Plasticity 18, 1219, 2002.

Ungureanu, C.A., Das, S., Jawahir, I.S., 2007. Life-cycle Cost Analysis: Aluminumversus Steel in Passenger Cars. TMS, 11–24.

Van den Boogaard, A.H., Hu´ etink, J., 2004. Modelling of aluminium sheet forming at elevated temperatures. Materials Processing and Design: Modeling, Simulation and Applications, NUMIFORM 2004. In: Proceedings of the 8th International Conference on Numerical Methods in Industrial Forming Processes, vol. 712, AIP Conference Proceedings, pp. 893–898.

Van den Boogaard, A.H., Hu´ etink, J., 2006. Simulation of aluminum sheet forming at elevated temperatures. Comput. Methods Appl. 195, 6691–6709.

Van den Boogaard, A.H., Werkhoven, R.J., Bolt, P.J., 2001. Modeling of Al–Mg sheet forming at elevated temperatures. Int. J. Form. Process. 4, 361–375.

Van den Boogaard, A.H., Meinders, T., Hu´ etink, J., 2003. Efficient implicit finite element analysis of sheet forming processes. Int. J. Numer. Methods Eng. 56, 1083–1107.

Vegter, H., Dane, C.M., 1985. Proc. 15th Bienn. Congr. IDDRG, Amsterdam (1985)

Vogel, J.H., Lee, D., 1989. J. Mater. Shaping Technol., 6 (1989), pp. 205–216

von Mises, R., 1913. Mechanik der Festen Korper im plastisch deformablen Zustand. Göttin. Nachr. Math. Phys., vol. 1, pp. 582–592

Wagoner, R.H., Nakamachi, E., Germain, Y., 1988. Analysis of sheet forming operations using the finite element method. In: Proceedings of IDDRG working groups, Toronto, p. 1.

Wang, H., LUO, Y., Friedman, P., Chen, M., GAO, L., 2012. Warm forming behavior of high strength aluminum alloy AA7075. Transactions of Nonferrous Metals Society of China, Volume 22, Issue 1, January 2012, Pages 1–7

Wilson, D.V., 1988. Aluminum versus steel in the family car-The formability factor. J. Mech. Work Technol. 16, 257–277.

Worswick, M.J., Finn, M.J., 2000, The numerical simulation of stretch flange forming, Int. J.Plasticity 16, 701, 2000.

Wu, H., Chio, C., Wang, J., Lee, S., 2006. Effect of lubrication on deformation characteristics of a superplastic 5083 Al alloy during bi-axial deformation. Mater. Sci. Eng. A-Struct. 427, 268–273.

Xi, W., Jian, C., 2000. An analytical prediction of flange wrinkling in sheet metal forming. J. Manuf. Process. 2, 100–107.

Yamashita, M., Hattori, T., Nishimur, N., 2007. Numerical simulation of sheet metal drawing by Maslennikov's technique. J. Mater. Process. Technol. 187/188, 192–196.

Yoon, J.W., Barlat, F., Dick, R., Chung, K., Kang, T.J., 2004. Plane stress yield function for aluminum alloy sheets. Part II. FE formulation and its implementation. Int. J. Plast. 20 (3), 495–522.

Yoon, J.W., Dick, R.E., Barlat, F., 2011. A new analytical theory for earing generated from anisotropic plasticity. Int. J. Plasticity 27, 1165-1184

Yoshihara, S., Nishimura, H., Yamamoto, H., Manabe, K., 2003a. Formability enhancement in magnesium alloy stamping using a local heating and cooling technique: circular cup deep drawing process. J. Mater. Process. Technol. 142, 609–613.

Yoshihara, S., Yamamoto, H., Manabe, K., Nishimura, H., 2003b. Formability enhancement in magnesium alloy deep drawing by local heating and cooling technique. J. Mater. Process. Technol. 143/144, 612–615.

Yoshihara, S., Mac Donald, B., Hasegawa, T., Kawahara, M., Yamamoto, H., 2004. Design improvement of spin forming of magnesium alloy tubes using finite element. J. Mater. Process. Technol. 153/154, 816–820.

Yu, Z., Lin, Z., Zhao, Y., 2007. Evaluation of fracture limit in automotive aluminum alloy sheet forming. Mater. Des. 28, 203–207.

Zhang, Z., Couture, A., Luo, A., 1998. An investigation of the properties of Mg–Zn–Al alloys. Scripta Mater. 39, 45–53.

Zienkiewicz, O. C. and R. L. Taylor (2005), The Finite Element Method, volume 2: Solid Mechanics, Butterworth–Heinemann, 6th edn